Communauté
UNIVERSITÉ Grenoble Alpes

THÈSE

Pour obtenir le grade de

DOCTEUR DE LA COMMUNAUTÉ UNIVERSITÉ GRENOBLE ALPES

Spécialité : Physique Subatomique et Astroparticules

Arrêté ministériel du 25 mai 2016

Présentée par

Felix KANDZIA

Thèse dirigée par **François MONTANET**, UGA
et codirigée par **Torsten SOLDNER**, ILL

Préparée au sein de **l'Institut Laue Langevin (ILL)**
dans **l'École Doctorale de Physique**

Recherche de neutrino stérile par l'expérience STEREO : Optimisation du blindage et calibration de l'échelle d'énergie

Search for a sterile neutrino with the STEREO experiment: Shielding optimisation and energy calibration

Thèse soutenue publiquement le **Lundi 11 décembre 2017**,
devant le jury composé de :

Elsa MERLE	Prof.	Grenoble INP, LPSC	Présidente
José BUSTO	Prof.	Univ. Aix Marseille, CPPM	Rapporteur
Lothar OBERAUER	Prof.	Technische Univ. München	Rapporteur
Muriel FALLOT	Maître de conf.	Univ. Nantes, SUBATECH	Examinatrice
Antoine KOUCHNER	Prof.	Univ. Paris 7 Diderot, APC	Examinateur

Abstract

Light sterile neutrinos are currently a topic actively discussed in neutrino physics. One indication of their possible existence and their participation in neutrino oscillations is the Reactor Antineutrino Anomaly, which states a deficit of about 6% between predicted and observed antineutrino fluxes in short baseline reactor neutrino experiments. The STEREO experiment addresses this anomaly by searching for neutrino oscillations at baselines of 8.9-11.1 m from the compact core of the research reactor of the Institut Laue Langevin (ILL), Grenoble, France. For this purpose a Gd-loaded liquid scintillator detector was designed with an active target mass of about 2 t. The target volume is subdivided in six optically separated cells along the line of propagation of the neutrinos. The electron antineutrinos emitted from the reactor are detected via the inverse beta decay on hydrogen nuclei, where a positron and a neutron are created. These two particles are detected in the scintillator in delayed coincidence, with the prompt signal from the positron and a delayed signal from neutron capture. The scintillation light created in the processes is read out by photomultiplier tubes (PMTs) on top of the detector cells. The detector is completed by a gamma catcher and a muon veto.

This manuscript covers parts of the preparation and the commissioning of the STEREO experiment. As basis for the design process of the magnetic shielding for STEREO's PMTs a series of finite element simulations was performed. The studies of different general layouts and required material qualities as well as of details of the final design are summarised. Under consideration of these studies the collaboration opted for a shielding design, a double layer setup with an outer soft iron and inner mumetal layer, which has the required shielding efficiency to reduce the magnetic field at the position of the detector PMTs below 60 μT for all known external magnetic field configurations. This limits the maximum PMT gain change due to variations of the external magnetic fields to $< 2\%$.

Furthermore different studies have been performed concerning the on-site background situation. A mapping of the γ-ray background was conducted with high purity germanium detectors and a NaI scintillator detector, in order to validate the efficiency of the installed shielding. The focus lied on the characterisation of the count rate in the neutron capture energy window. An estimation of the background rate is presented and compared to the rate obtained in STEREO. At the current state of the analysis the background of accidental coincidences in STEREO is a minor contribution compared to the muon induced correlated background. In addition a series of MCNP simulations was performed to determine the impact of a beamtube removal in the vicinity of STEREO on the overall reactor-related background situation. The beamtube was closed by a dedicated shielding, optimised for background reduction for STEREO, which could not be reinstalled after removal of the tube. A new shielding at the end of the former beamtube was proposed by the ILL. Its shielding effect was studied with MCNP and compared to the previous configuration in order to assess whether the new shielding suffices or needs to be improved. According to these simulations the background situation is expected to improve.

Finally a procedure is proposed and applied for the analysis of the energy calibration of the STEREO detector. The procedure is designed to be applicable to all available calibration sources and to minimise systematic uncertainties. It can be used to adjust parameters in the existing Geant4-based simulation of the detector, developed by the collaboration, by comparison to measured data and later to determine the energy scale with the required precision of $\leq 2\%$.

Keywords: Neutrino oscillations, sterile neutrinos, reactor antineutrino anomaly, STEREO experiment.

Résumé

La recherche de neutrinos stériles et légers est, à l'heure actuelle, l'un des enjeux majeurs de la physique des neutrinos. Une indication de leur existence résulte de l'anomalie des antineutrinos de réacteur. Cette anomalie découle du déficit de 6% entre les taux prédits et les taux observés par les expériences à courte distance de réacteurs. Ce déficit peut être interprété comme une oscillation à courte distance des neutrinos. L'objectif de l'expérience STEREO, situé auprès du réacteur de recherche de l'Institut Laue Langevin (ILL), à Grenoble, France, est d'étudier cette oscillation. La cible du détecteur de neutrinos est placée entre 8,9 et 11,1 m du cœur compact du réacteur d'ILL. Le détecteur consiste d'environ 2 t d'un scintillateur liquide, dopé avec du Gd. Le volume actif est séparé dans le sens de la longueur en six cellules. Les antineutrinos sont détectés par la désintégration bêta inverse, où ils interagissent avec un proton libre (ion H^+) et produisent un positron et un neutron. Les deux particules sont détectées dans le scintillateur par une coïncidence retardée où le positron crée un signal prompt et le neutron est capturé après un temps de modération. La lumière produite par le scintillateur est mesurée par les photomultiplicateurs (PM) installés au-dessus des cellules. Le détecteur est complété par un "gamma catcher" qui entoure la cible et par un veto à muons.

Ce manuscrit présente des études concernant la préparation et la mise en exploitation de l'expérience STEREO. La conception du blindage magnétique des PM a été menée sur la base de simulations par éléments finis afin d'examiner différentes options, d'étudier en détail les performances de l'option retenue ainsi que de déterminer la qualité nécessaire des matériaux utilisés. Sur la base de ces études, la collaboration a retenu un plan de blindage en deux couches: une couche de fer doux à l'extérieur, couvrant le détecteur et le veto à muons, et une couche de mu-métal autour de la cible. Ce blindage réduit les champs magnétiques externes à la position des PM de la cible à moins de 60 μT pour toutes les configurations connues de champs externes. Ceci réduit à moins de 2% une variation de l'amplification des PM induite par des changements des champs magnétiques.

D'autre part, des études du bruit de fond sur le site de STEREO ont été menées. Une cartographie du bruit de fond du rayonnement gamma a été effectuée avec des détecteurs au germanium et un scintillateur NaI, afin de valider l'efficacité du blindage installé sur le site. Une estimation du taux de bruit de fond est présentée et comparée au taux mesuré avec STEREO. Dans l'état actuel de l'analyse des données, le bruit de fond de coïncidences fortuites est inférieur au bruit de fond corrélé induit par les muons cosmiques. Après une première phase d'exploitation de STEREO, un "doigt de gant" en fin de vie situé à l'avant de STEREO a dû être retiré. Un bouchon était adapté à l'extrémité de ce doigt de gant afin de réduire le bruit du fond pour STEREO. Ce dispositif n'ayant pas pu être réinstallé à la suite l'enlèvement du doigt de gant, un nouveau blindage a été proposé par l'ILL. Une série des simulations neutroniques et photoniques (MCNP) a été effectué pour étudier l'effet de ce changement sur le bruit de fond autour de STEREO et pour décider si le blindage proposé était suffisant. Les deux scénarios avant et après l'enlèvement ont été comparés et selon cette simulation, la situation du bruit de fond devrait être améliorée.

Enfin une procédure a été proposée et appliquée pour analyser les données de calibration de l'échelle d'énergie de STEREO. La procédure a été élaborée pour être applicable pour toutes les sources de calibration disponibles et pour minimiser les incertitudes systématiques. Le résultat peut être utilisé pour ajuster les paramètres de la simulation Geant4 du détecteur développée par la collaboration, par comparaison avec des données mesurées et après pour déterminer l'échelle de l'énergie avec la précision requise de $\leq 2\%$.

Mots Clés: oscillations des neutrinos, neutrinos stériles, anomalie des antineutrinos de réacteur, expérience STEREO.

Contents

Chapter 1

Fundamentals of Neutrino Physics

1.1 Neutrinos in the electro-weak Standard Model

1.1.1 Discovery of Neutrinos

At the beginning of the 20th century there was a strong activity in investigating natural radioactivity. Experiments on α and γ radiation showed sharply defined energies which could be explained with the energy difference between initial and final state of decaying nuclei. The β-decay on the other hand did not follow this model and the emitted electrons show a wide energy distribution between basically zero and the mass difference of the participating nuclei, where Ellis *et al.* could show that this is a fundamental property arising from the decay itself [Ell27].

Another discrepancy emerged when Pauli introduced the concept of particle spins. With the electron being emitted as the only spin-1/2 particle and the nucleon changing its spin in integer values the overall spin would not be conserved. Both problems were solved in 1930 by Pauli postulating an additional spin-1/2 particle being emitted in β-decay and carrying away the missing energy and spin [Pau91]. Considering charge conservation this additional particle had to be electrically neutral, hence he named it "Neutron".

Based on Pauli's assumptions Fermi developed a quantum-mechanical description of β-decay [Fer34] and successfully obtained a quantitative description of the electron spectra. Since in the mean time Chadwick discovered the today's "Neutron" in 1932 [Cha32], as heavy, electrically neutral nucleon, Fermi introduced the term "Neutrino" for a smaller neutral particle.

The direct experimental confirmation of the existence of neutrinos was long pending and was achieved only in 1956 by the experiment of Cowan, Jr and Reines [Cow56]. In their experiment the nuclear reactor of the Savannah River Power Plant, U.S., served as source of anti-electronneutrinos and a liquid scintillator detector as target for the inverse beta decay (IBD) reaction

$$\bar{\nu}_\mathrm{e} + p \rightarrow \mathrm{e}^+ + n \ . \tag{1.1}$$

The target volume consisted of three stacked tanks in which the energy deposition of the positron was observed. Intermediate tanks containing $CdCl_2$ dissolved in water were installed to capture the neutrons after a certain moderation time. This delayed coincidence signal is a typical IBD signature used in many reactor experiments, see Sec. 2.2.6. The neutrino reaction rate observed in the experiment was in agreement with the predicted cross section in the order of 10^{-20} barn.

In 1962 Lederman, Schwartz and Steinberger established the principle of "neutrino beams" as alternative sources. In their experiment neutrinos are produced in two steps, by first focussing a 15 GeV proton beam onto a beryllium target and then guiding the produced charged mesons, mainly pions and kaons, into a decay tunnel. By decay in flight of the mesons a neutrino beam is produced: $\pi^\pm \rightarrow \mu^\pm + \overset{(-)}{\nu}_\mu$. A spark chamber was used as detector for the reaction $\nu_l \rightarrow l$, where l denotes a charged lepton. From the fact that only muons were observed in the final state

Lederman *et al.* concluded that neutrinos participating in the reaction are different from those observed by Cowan and Reines and thus that at least two different kinds of neutrinos exist [Dan62]. By this the doublet structure of leptons (charged lepton and corresponding neutrino) was established.

In 1975 evidence for an unknown charged particle, later identified as the τ lepton, was found by Perl *et al.* [Per75]. Following the lepton doublet structure this led to the postulation of a third type of neutrino. From there it took another 26 years until the DONUT collaboration finally could observe ν_τ interactions [DON01]. Here again a neutrino beam was used, created by 800 GeV protons on a tungsten target. The main production channel for ν_τ (85%) was

$$\begin{aligned} \mathrm{D}_S \rightarrow \quad & \tau \quad + \bar{\nu}_\tau \\ & \tau \quad \rightarrow l + \bar{\nu}_l + \nu_\tau \ , \end{aligned} \tag{1.2}$$

where $l = e,\ \mu$. Tau neutrinos were detected by τ-lepton production in charged current interactions and its subsequent decay. With this also the third generation of the currently known neutrinos was established.

The strongest limit on the question whether more types of neutrinos exist was set by experiments at the Large Electron Positron collider, LEP. The number of light neutrinos ($m_\nu < m_\mathrm{Z}/2$) is constraint by the precision measurement of the decay width of the Z-boson Γ_Z [ALE06]. This is the sum of the partial widths of the single decay branches

$$\Gamma_\mathrm{Z} = \Gamma_\mathrm{had} + \Gamma_{ll} + \Gamma_\mathrm{inv} \ , \tag{1.3}$$

where the hadronic partial decay width Γ_had includes all reactions with a decay to quarks $\mathrm{Z} \rightarrow \mathrm{q\bar{q}}$, the leptonic partial width Γ_{ll} all productions of charged lepton pairs $\mathrm{Z} \rightarrow l^+ l^-$ under assumption of lepton universality, and the invisible width the decays into light neutrinos $\Gamma_\mathrm{inv} = N_\nu \Gamma_{\nu\bar{\nu}}$, with N_ν the number of neutrino generations. By comparing the measured ratio $R_\mathrm{inv} = \Gamma_\mathrm{inv}/\Gamma_{ll}$ to Standard Model predictions, assuming that all invisible Z decays produce only neutrinos which couple according to the Standard Model, N_ν can be calculated [ALE06]:

$$R_\mathrm{inv} = \left(\frac{12\pi \Gamma_\mathrm{had}/\Gamma_{ll}}{\sigma^0_\mathrm{had} m^2_\mathrm{Z}} \right)^{1/2} - \frac{\Gamma_\mathrm{had}}{\Gamma_{ll}} - 3 = N_\nu \cdot \left(\frac{\Gamma_\mathrm{inv}}{\Gamma_{ll}} \right)_\mathrm{SM} \ , \tag{1.4}$$

where the mass of the Z-boson m_Z and the total hadronic cross section σ^0_had are obtained from the centroid and maximum of the Z-resonance in the $e^- e^+ \rightarrow$ hadrons reaction, see Fig. 1.1. In [ALE06] the number determined for the light neutrino generations, coupling to the Z-boson is 2.9840 ± 0.0082. The existence of more or fewer generations would change the magnitude of the cross section at the resonance significantly, see Fig. 1.1.

This, however, does not exclude the existence of heavier neutrinos, with $m_\nu > m_\mathrm{Z}/2$, or light neutrinos which do not participate in weak interactions and are therefore called sterile. Findings of recent reevaluations of reactor neutrino experiments may be interpreted as indications for the existence of the latter, which is described in more detail in Section 2.2. The confirmation or refutation of this hypothesis is the aim of the STEREO experiment.

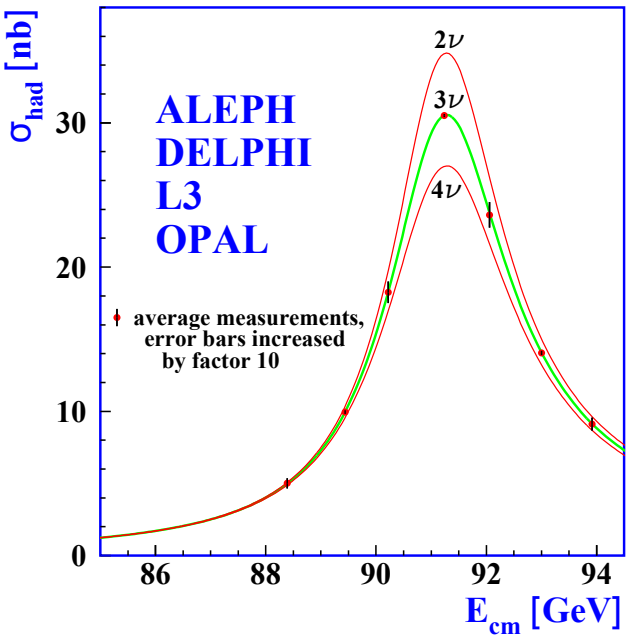

Figure 1.1: Combined result of the cross section measurement in $e^-e^+ \rightarrow$ hadrons reactions of the four LEP detectors at energies around the Z resonance. Assumptions of different numbers of light neutrinos ($m_\nu < m_Z/2$) coupling via standard model couplings to the Z-boson would change the magnitude of the resonance significantly. From [ALE06].

1.1.2 The GWS Formalism

The Standard Model of particle physics is a quantum field theory, describing the strong, the weak and the electromagnetic interaction. It is a gauge theory constructed as the direct product of the groups $SU(3)_c \otimes SU(2)_L \otimes U(1)_y$. The $SU(3)_c$ group describes the strong interaction in between quarks, characterised by the colour charge c, and is not considered in the following. The electroweak interactions are described by the $SU(2)_L \otimes U(1)_y$, where the L denotes that only left-handed particles can couple, via the weak isospin I_w, and y is the hypercharge, the quantum number of the U(1). This subset is also called the Glashow-Weinberg-Salam (GWS) model, according to their pioneering contributions in the development of its structure [Gla61, Sal59, Wei67]. For the following explanations the notation of Bjorken is adapted [Bjo64]

$$\gamma_0 = \begin{pmatrix} \mathbb{1}_2 & 0 \\ 0 & -\mathbb{1}_2 \end{pmatrix} , \quad \gamma_k = \begin{pmatrix} 0 & \sigma_k \\ -\sigma_k & 0 \end{pmatrix} , \quad \gamma_5 = i\gamma_0\gamma_1\gamma_2\gamma_3 = \begin{pmatrix} 0 & \mathbb{1}_2 \\ \mathbb{1}_2 & 0 \end{pmatrix} , \tag{1.5}$$

where $\mathbb{1}_2 = \begin{pmatrix} 1 & 0 \\ 0 & 1 \end{pmatrix}$ is the 2×2 unit matrix, 0 a 2×2 matrix of zeros and the σ_i denote the 2×2 Pauli matrices

$$\sigma_1 = \begin{pmatrix} 0 & 1 \\ 1 & 0 \end{pmatrix} , \quad \sigma_2 = \begin{pmatrix} 0 & -i \\ i & 0 \end{pmatrix} , \quad \sigma_3 = \begin{pmatrix} 1 & 0 \\ 0 & -1 \end{pmatrix} . \tag{1.6}$$

One characteristic feature of weak interactions is parity violation. Parity, a symmetry transformation achieved by inversion of space coordinates at the origin, was thought to be a fundamental conservation law. In fact no contradiction was observed in electromagnetic and strong interactions. The violation in weak interactions, however, was proven by Wu *et al.* [Wu57] from an asymmetry of electron emission from the β-decay of polarised nuclei. This implies that the helicity $\mathcal{H}$ of particles, defined as the projection of the particle's spin onto its momentum

$$\mathcal{H} = \frac{\sigma p}{|p|} , \tag{1.7}$$

has a defined value in this interaction. The helicity of the neutrinos was later measured explicitly by GOLDHABER *et al.* [Gol58], where it was found that the result of the experiment was compatible with 100% negative helicity of the neutrinos. With neutrinos considered massless this corresponds to the interaction of only left-handed neutrinos, where the handedness, or chirality, is defined as the eigenvalue to the γ_5 matrix (introduced in Eq. (1.5)):

$$\gamma_5 \phi_\mathrm{R} = +1 \cdot \phi_\mathrm{R} \ , \quad \gamma_5 \phi_\mathrm{L} = -1 \cdot \phi_\mathrm{L} \ , \tag{1.8}$$

where $\phi_{\mathrm{R/L}}$ is a right-/left-handed 4-component Dirac spinor. For an arbitrary spinor ϕ the left- and right-handed components can be separated with the projectors

$$P_\mathrm{R}\phi = \frac{1}{2}(1+\gamma_5)\phi = \phi_\mathrm{R} \qquad P_\mathrm{L}\phi = \frac{1}{2}(1-\gamma_5)\phi = \phi_\mathrm{L} \ . \tag{1.9}$$

It was thus found that the weak interaction is maximally parity violating, and that only left-handed (L) particles and right-handed (R) anti-particles participate. The elementary particles can then be arranged in left-handed doublets and right-handed singlets, according to their weak isospins, or its third component I_3:

$$\begin{array}{cccccccc} & & & & & & & \mathrm{I}_3 \\ \begin{pmatrix} u \\ d' \end{pmatrix}_\mathrm{L} & \begin{pmatrix} c \\ s' \end{pmatrix}_\mathrm{L} & \begin{pmatrix} t \\ b' \end{pmatrix}_\mathrm{L} & \begin{pmatrix} \nu_e \\ e \end{pmatrix}_\mathrm{L} & \begin{pmatrix} \nu_\mu \\ \mu \end{pmatrix}_\mathrm{L} & \begin{pmatrix} \nu_\tau \\ \tau \end{pmatrix}_\mathrm{L} & & +1/2 \\ & & & & & & & -1/2 \\ u_\mathrm{R} \quad d_\mathrm{R} & c_\mathrm{R} \quad s_\mathrm{R} & t_\mathrm{R} \quad b_\mathrm{R} & e_\mathrm{R} & \mu_\mathrm{R} & \tau_\mathrm{R} & & 0 \ . \end{array} \tag{1.10}$$

Here $u,\ d,\ c,\ s,\ t,\ b$ are the quarks and $'$ indicates the weak eigenstate.

All of those are Fermions which can be described by the Dirac equation. Considering free Dirac particles in vacuum the corresponding Lagrangian is

$$\mathcal{L} = \bar{\psi}\left(i\gamma_\mu \frac{\partial}{\partial x_\mu} - m_\mathrm{D}\right)\psi \tag{1.11}$$

where the first term describes the kinetic energy and the second the Dirac mass m_D of the particle. The spinor ψ can be split in its chiral right-handed and left-handed components

$$\psi = \psi_\mathrm{L} + \psi_\mathrm{R} \qquad \bar{\psi}_\mathrm{L}\psi_\mathrm{L} = 0 \qquad \bar{\psi}_\mathrm{R}\psi_\mathrm{R} = 0 \tag{1.12}$$

and the Dirac mass term then writes as

$$\mathcal{L} = m_\mathrm{D}(\bar{\psi}_\mathrm{L}\psi_\mathrm{R} + \bar{\psi}_\mathrm{R}\psi_\mathrm{L}) \tag{1.13}$$

with the Hermitian conjugates $\bar{\psi}_\mathrm{R}\psi_\mathrm{L} = (\bar{\psi}_\mathrm{L}\psi_\mathrm{R})^+$. A mass term of the form (1.13) can be written for all quarks and the charged leptons, for neutrinos the right-handed neutrino is missing in the Standard Model.

An alternative formulation was proposed by MAJORANA [Maj37]. In contrast to the Dirac formalism, particle and anti-particle would not be regarded as different particles, but as two appearances of the same state. This could be applied to the electrical neutral neutrinos and would allow to include also anti-particle components ψ^c in the formulation of the mass term. When explicitly considering left- and right-handed particles those can be formulated as (see e.g. [Zub12])

$$\mathcal{L}^\mathrm{L} = \frac{1}{2} m_\mathrm{L}(\bar{\psi}_\mathrm{L}\psi^\mathrm{c}_\mathrm{R} + \bar{\psi}^\mathrm{c}_\mathrm{R}\psi_\mathrm{L}) \tag{1.14}$$

$$\mathcal{L}^\mathrm{R} = \frac{1}{2} m_\mathrm{R}(\bar{\psi}^\mathrm{c}_\mathrm{L}\psi_\mathrm{R} + \bar{\psi}_\mathrm{R}\psi^\mathrm{c}_\mathrm{L}) \tag{1.15}$$

with the Majorana masses $m_{\mathrm{L,R}}$. Together with the Dirac mass term in Eq. (1.13) this results in

$$2\mathcal{L} = (\bar{\psi}_\mathrm{L}, \bar{\psi}^\mathrm{c}_\mathrm{L}) \begin{pmatrix} m_\mathrm{L} & m_\mathrm{D} \\ m_\mathrm{D} & m_\mathrm{R} \end{pmatrix} \begin{pmatrix} \psi^\mathrm{c}_\mathrm{R} \\ \psi_\mathrm{R} \end{pmatrix} + \text{Hermitian conjugated} \ . \tag{1.16}$$

This is a more generalised mass term and its interpretation depends on the values of the mass parameters $m_{\mathrm{D,L,R}}$:

In the case $m_{\mathrm{L}} = m_{\mathrm{R}} = 0$ only the Dirac component remains and has the form of Eq. (1.13).

If $m_{\mathrm{D}} = 0$ the pure Majorana case is obtained, with two different mass terms, one for left- and one for right-handed particles, which can be formulated as in Eq. (1.15). This describes the complete mixing of the particles ψ_{L} and ψ_{R} and their anti-particles $\psi_{\mathrm{R}}^{\mathrm{c}}$ and $\psi_{\mathrm{L}}^{\mathrm{c}}$.

In the special case that $m_{\mathrm{R}} \gg m_{\mathrm{D}}$ and $m_{\mathrm{L}} = 0$ the result are two different masses for each flavour:

$$m_\nu = \frac{m_{\mathrm{D}}^2}{m_{\mathrm{R}}} \quad \text{and} \quad m_{\mathrm{N}} = m_{\mathrm{R}}\left(1 + \frac{m_{\mathrm{D}}^2}{m_{\mathrm{R}}^2}\right) \approx m_{\mathrm{R}} \ . \tag{1.17}$$

This could explain the small masses of the observed neutrinos m_ν and would at the same time predict additional neutrinos with large masses m_{N}. In this "seesaw" mechanism, where lighter masses m_ν are related to heavier m_{N}, the heavy neutrinos m_{N} may not be observable due to their large masses.

One remaining difficulty for the description of massive particles within the Standard Model is the requirement of gauge invariance. Considering the elementary fermions (Eq. (1.11)) the right-handed singlets do not participate in weak interactions which means they do not transform under SU(2) transformations, but the left-handed doublets do. Thus a term as $\bar{\psi}\psi = (\bar{\psi}_{\mathrm{L}}\psi_{\mathrm{R}} + \bar{\psi}_{\mathrm{R}}\psi_{\mathrm{L}})$ would not be gauge invariant under SU(2)×U(1) transformations, which forbids mass terms as in Eq. (1.13), and the fundamental fermions and bosons of the Standard Model would remain massless.

Gauge invariant masses can be generated via the so-called Higgs-mechanism, developed by Brout, Englert, Higgs and Kibble [Eng64, Hig64b, Hig64a, Kib67]. For this in the simplest way a doublet of a charged and a neutral complex scalar field is introduced, with weak isospins $\mathrm{I}_3 = 1/2$ and $\mathrm{I}_3 = -1/2$, respectively:

$$\Phi = \begin{pmatrix} \phi^+ \\ \phi^0 \end{pmatrix} \ . \tag{1.18}$$

In order to obtain a vacuum state which is different from zero and allows for non-zero particle masses the mechanism of symmetry breaking is used by adding the following to the Standard Model Lagrangian:

$$\mathcal{L}_{\mathrm{Higgs}} = (\partial\mu\Phi)^+(\partial^\mu\Phi) - \underbrace{\mu^2\Phi^+\Phi - \lambda(\Phi^+\Phi)^2}_{V(\Phi)} \ . \tag{1.19}$$

If now $\lambda > 0$, necessary to have a lower bound of the potential, and $\mu^2 < 0$, the potential has a minimum at

$$(\Phi^+\Phi) = \frac{-\mu^2}{2\lambda} = \frac{v^2}{2} \tag{1.20}$$

with $v = \sqrt{-\mu^2/\lambda}$ called the vacuum expectation value. Thus the vacuum state, the ground state of the potential, has a value different from zero and in fact there is not one single ground state, but all points in the complex plane with a radius of $v/\sqrt{2}$ are degenerate ground states. Each of them has a local symmetry but does not reflect the original symmetry of the potential anymore. From this infinite number of points that one is chosen where

$$\Phi_0 = \frac{1}{\sqrt{2}}\begin{pmatrix} 0 \\ v \end{pmatrix} \ . \tag{1.21}$$

The upper, charged scalar field needs to be zero to guarantee an electrically neutral vacuum. Excitations in the potential are given by

$$\Phi_0 = \frac{1}{\sqrt{2}}\begin{pmatrix} 0 \\ v + H(x) \end{pmatrix} \ , \tag{1.22}$$

where the field $H(x)$ describes the Higgs boson.

The fermions gain their masses by coupling to the Higgs field, described by the Yukawa coupling, e.g. for electrons e

$$\begin{aligned}\mathcal{L}_{\text{Yuk}} &= -c_e \cdot \bar{e}_{\text{R}} \Phi_0^+ \begin{pmatrix} \nu_{e,\,\text{L}} \\ e_{\text{L}} \end{pmatrix} + (\bar{\nu}_{e\,\text{L}}, \bar{e}_{\text{L}}) \Phi_0 e_{\text{R}} \\ &= -c_e \frac{v}{\sqrt{2}} \bar{e} e \end{aligned} \tag{1.23}$$

where c_e is the Yukawa coupling constant for the electron, defining its mass as $m_e = c_e v/\sqrt{2}$. This mechanism works for all charged leptons and quarks, with the corresponding Yukawa couplings c_i, but not for neutrinos as right-handed neutrinos are not present within the Standard Model. Thus they remain massless. In the simplest extension of the Standard Model right-handed neutrinos are included as sterile (not weakly interacting) neutrinos and neutrino masses are generated in the same way as for all other fundamental fermions. Their small masses would then only result from the small Yukawa coupling constants.

Using the covariant derivative in Eq. (1.19) instead of the normal derivative the coupling of the Higgs field with the gauge fields is obtained, from which their masses can be obtained, see e.g. [Giu07]

$$m_{\text{W}}^2 = \frac{e^2 v^2}{4 \sin^2 \theta_{\text{W}}} \tag{1.24}$$

$$m_{\text{Z}}^2 = \frac{e^2 v^2}{4 \sin^2 \theta_{\text{W}} \cos^2 \theta_{\text{W}}} \tag{1.25}$$

where e is the elementary charge and θ_{W} is the Weinberg angle.

1.2 Neutrino Oscillations

Neutrino oscillations have first been observed by the Super-Kamiokande experiment, by measuring charged current interactions of atmospheric (muon-)neutrinos in a 50 kton water Cherenkov detector. A zenith angle dependent deficit of muon events, but not of electron events, was observed relative to expectations [Fuk98]. This occurred dominantly for high energies and upward-going muons, where the neutrinos had to cross the Earth before the interaction. For all energies and zenith angles the deficit was found in agreement with neutrino oscillations from $\nu_\mu \to \nu_\tau$.

Another direct evidence resulted from the Sudbury Neutrino Observatory (SNO) by solving the long-standing solar neutrino problem, which describes a 2/3 deficit in observed versus predicted solar neutrino fluxes. SNO measured the electron neutrino flux as well as the flavour-independent neutrino flux from the sun, showing that about two thirds of the solar neutrinos reach the Earth with a changed flavour [Ahm02]. Neutrino oscillations arise from the fact that the weak (or flavour) eigenstates $|\nu_\alpha\rangle$ and mass eigenstates $|\nu_k\rangle$ of the neutrinos are not identical. They are connected via a unitary mixing matrix $\mathbf{U}$:

$$|\nu_\alpha\rangle = \sum_k \mathbf{U}_{\alpha k} |\nu_k\rangle \qquad |\nu_k\rangle = \sum_\alpha \mathbf{U}^*_{\alpha k} |\nu_\alpha\rangle \ . \tag{1.26}$$

From this a general oscillation formalism can be derived, which is briefly summarised here, following the description in [Zub12]. Considering neutrinos as highly relativistic particles emitted at coordinate $x = 0$ with momentum p the mass states can be described as stationary states, transforming according to

$$|\nu_k(x,t)\rangle = e^{ipx} e^{-E_k t} |\nu_k(0,0)\rangle \ , \tag{1.27}$$

where $E_k = \sqrt{p^2 + m_k^2}$ is the energy of the mass state. For relativistic particles the following approximation can be made

$$E_k = \sqrt{m_k^2 + p_k^2} \simeq p_k + \frac{m_k^2}{2p_k} \simeq E + \frac{m_k^2}{2E} \ . \tag{1.28}$$

With Eqs. (1.26), (1.27) and (1.28) the transition amplitude from one flavour state to another can be calculated as

$$\begin{aligned} A(\alpha \to \beta)(t) = \langle \nu_\beta | \nu_\alpha(x,t) \rangle &= \sum_k \mathbf{U}^*_{\beta k} \mathbf{U}_{\alpha k} e^{ipx} e^{-iE_k t} \\ &\overset{(1.28)}{\simeq} \sum_k \mathbf{U}^*_{\beta k} \mathbf{U}_{\alpha k} \exp\left(-i \frac{m_k^2 L}{2E}\right) = A(\alpha \to \beta)(L) \ . \end{aligned} \tag{1.29}$$

From this the transition probability P can be calculated:

$$P(\alpha \to \beta) = |A(\alpha \to \beta)|^2 = \sum_k |\mathbf{U}_{\alpha k} \mathbf{U}^*_{\beta k}|^2 + 2 \ \mathrm{Re} \left(\sum_{l>k} \mathbf{U}_{\alpha k} \mathbf{U}^*_{\alpha l} \mathbf{U}^*_{\beta k} \mathbf{U}_{\beta l} \exp\left(-i \frac{\Delta m^2_{kl} L}{2E}\right) \right) \tag{1.30}$$

with $\Delta m^2_{kl} = m^2_k - m^2_l$. If now the mass states are not all exactly degenerated and the off-diagonal elements of $\mathbf{U}$ are non-zero oscillations can occur.

For three flavour oscillations the corresponding mixing matrix is the 3×3 Pontecorvo-Maki-Nakagawa-Sakata (PMNS) matrix. The nine matrix entries can be fully parametrised by three mixing angles, θ_{12}, θ_{13} and θ_{23}, and one CP-violating Dirac phase δ and, in case neutrinos are Majorana particles, two additional CP-violating phases λ. The PMNS matrix in its standard parametrisation writes as

$$\mathbf{U}_{\mathrm{PMNS}} = \underbrace{\begin{pmatrix} 1 & 0 & 0 \\ 0 & \mathrm{c}_{23} & \mathrm{s}_{23} \\ 0 & -\mathrm{s}_{23} & \mathrm{c}_{23} \end{pmatrix}}_{\text{atmospheric}} \underbrace{\begin{pmatrix} \mathrm{c}_{13} & 0 & \mathrm{s}_{13} e^{-i\delta_{13}} \\ 0 & 1 & 0 \\ -\mathrm{s}_{13} e^{i\delta_{13}} & 0 & \mathrm{c} \end{pmatrix}}_{\text{reactor}} \underbrace{\begin{pmatrix} \mathrm{c}_{12} & \mathrm{s}_{12} & 0 \\ -\mathrm{s}_{12} & \mathrm{c}_{12} & 0 \\ 0 & 0 & 1 \end{pmatrix}}_{\text{solar}} \underbrace{\begin{pmatrix} 1 & 0 & 0 \\ 0 & e^{i\lambda_{21}} & 0 \\ 0 & 0 & e^{i\lambda_{31}} \end{pmatrix}}_{\text{Majorana phases}} , \tag{1.31}$$

where c_{ij} and s_{ij} denote $\cos\theta_{ij}$ and $\sin\theta_{ij}$, respectively. Experimentally three different mixing angles and two independent Δm^2 have been determined, which means that the mass states of the known neutrinos are not degenerated and at least two are different from zero. Since oscillation experiments are only sensitive to the differences of squared masses the absolute mass scale cannot be determined from oscillations. In addition with $\Delta m^2_{13} \simeq \Delta m^2_{23} \gg \Delta m^2_{12}$ the ordering of the mass states, the hierarchy, could so far not be resolved and two scenarios are possible, see Fig. 1.2. This topic will be addressed by upcoming experiments such as the Jiangmen Underground Neutrino Observatory (JUNO) [JUN15], which aims to resolve the subleading oscillation with reactor neutrinos, or KM3NeT-ORCA [Cap17], by exploiting hierarchy-dependent matter effects in atmospheric neutrino oscillations in the Earth.

The currently best values under assumption of a three flavour mixing scheme are [Pat16]:

$$\begin{aligned} &\sin^2(\theta_{12}) = 0.307(13) && \Delta m^2_{21} = 7.53(18) \cdot 10^{-5}\,\mathrm{eV}^2 && \\ &\sin^2(\theta_{23}) = 0.51(4) && |\Delta m^2_{32}| = 2.45(5) \cdot 10^{-3}\,\mathrm{eV}^2 && \text{normal hierarchy} \\ &\sin^2(\theta_{23}) = 0.50(4) && |\Delta m^2_{32}| = 2.52(5) \cdot 10^{-3}\,\mathrm{eV}^2 && \text{inverted hierarchy} \\ &\sin^2(\theta_{13}) = 2.10(11) \cdot 10^{-2} && && \end{aligned} \tag{1.32}$$

A sterile neutrino could be included by adding one mass state at lower masses (1+3 scenario) or higher masses (3+1) and extending the PMNS matrix to a 4×4-matrix. The current best fits would point towards a $\Delta m^2_{\mathrm{new}} \sim 1\,\mathrm{eV}^2$, see Sec. 2.2. Thus the oscillation lengths for oscillations from known flavours to sterile neutrinos would all be similar, as $\Delta m^2_{\mathrm{new}} \simeq \Delta m^2_{14} \simeq \Delta m^2_{24} \simeq \Delta m^2_{34}$, but the oscillation amplitudes $\sin\theta_{k4}$ may differ for $k = 1, 2, 3$.

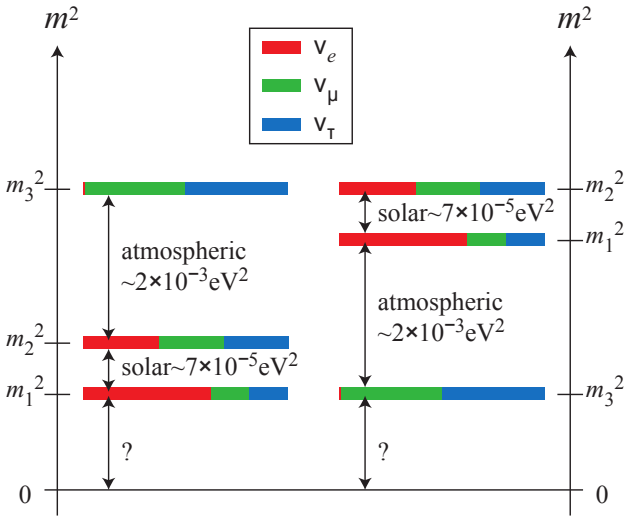

Figure 1.2: Scheme of the possible mass orderings, left: normal hierarchy, right: inverted hierarchy. From [Moh04].

Chapter 2

Neutrinos from nuclear Reactors

2.1 Reactor Neutrino Spectra

Nuclear reactors represent powerful artificial neutrino sources. Most fission products are unstable, heavy nuclei and are always neutron rich. Thus they decay only via β^- decays towards the line of stability, emitting a pure flux of electron antineutrinos. On average six transitions are necessary to reach a stable isotope which results in a flux of about about $2 \cdot 10^{17}\,\nu/(\mathrm{s{\cdot}MW_{therm}})$ emitted isotropically. Power reactors work with low enriched uranium (LEU) containing only a few percent of ^{235}U which is fissile by thermal neutrons. The main isotope is ^{238}U which mainly undergoes fission by fast neutrons. Through neutron captures on ^{238}U and subsequent β decays also ^{239}Pu and in a smaller amount ^{241}Pu are produced, which both are fissionable by thermal neutrons. The Pu-content increases with the burnup over the fuel cycle of a reactor. During normal operation the fission products of ^{235}U, ^{238}U, ^{239}Pu and ^{241}Pu produce more than 99% of the emitted neutrinos, where ^{238}U and ^{241}Pu contribute together to about 10%. The fission fractions of ^{235}U and ^{239}Pu can become comparable so that the burnup has to be taken into account. In fact power reactors are usually operated in a three batch mode, where about one third of the fuel is fresh, one third once irradiated and one third twice irradiated, with a usual duty cycle in the order of one year in between replacements. In this case there is always a contribution from all four isotopes present. Some research reactors on the other hand run with highly enriched uranium fuel (HEU) with $> 90\%$ ^{235}U and shorter run periods ($< 100\,\mathrm{d}$) than power reactors. Here the burnup effect is small and mostly negligible.
Being the most powerful artificial neutrino sources a number of experiments have been performed at reactors in order to study neutrino oscillations. To be sensitive to any oscillation pattern it is either necessary to measure the neutrino spectrum or flux directly at different distances and determine the relative changes, or alternatively to compare the data with precise predictions of expected spectra. The latter also increases the sensitivity of multi-detector setups to fast oscillations which might not be resolvable in the detector or have been averaged out over the source to detector distance. Predictions of neutrino spectra can in principle be made in two ways:

1. **Conversion method**: the accumulated β spectra of all fission products and their daughter nuclei of the four main fissile isotopes are measured and converted into corresponding neutrino spectra.

2. **Ab initio calculations**: the neutrino spectra are calculated from nuclear databases by successively adding up the individual β spectra of all fission products and their daughter nuclei, weighted by their fission yields.

In both cases predictions are made per fissile isotope and then added up according to the fission fractions of the considered reactor.

2.1.1 The Conversion Method

The primary requirement for this method is the precise knowledge of the accumulated β spectra. Those have been measured for the thermal fission isotopes ^{235}U, ^{239}Pu and ^{241}Pu by Schreckenbach *et al.* at the ILL research reactor, Grenoble, France [Sch81, vF82, Sch85, Hah89]. More recently also the spectrum of the fast fission of ^{238}U was measured by Haag *et al.* [Haa14] at the FRM II in Garching, Germany. For the ILL measurements the magnetic spectrometer BILL [Mam78] was used. The target, a sandwich of the fissile material and two thin Ni-foils ($7\,\mathrm{mg/cm^2}$), was exposed to a fully thermalised neutron flux of about $3 \cdot 10^{14}$ neutrons/($\mathrm{cm^2}$·s) at a distance of about 80 cm from the compact reactor core. The fission products were stopped in the Ni-foils and thus contained at the irradiation position while the electrons could exit the sample basically unaffected. After travelling through a ≈ 13 m long evacuated tube a double focusing magnet system guided the electrons onto the detector. This allowed to perform the measurements online, in an energy range of 1.5-9 MeV. The data was taken after irradiation times of ≈1 d, which was estimated to be sufficient to bring the β activities above 3 MeV into equilibrium. The statistical uncertainty on the β spectra for bins of 250 keV is between 0.5-3% (0.5-20%, 1-9%) for ^{235}U (^{239}Pu, ^{241}Pu) in the energy range from 2-8 MeV. The dominant error is the additional absolute normalisation uncertainty of the spectrum, quoted at 2.8% and 3.1% at 1.3 MeV and 7.4 MeV, respectively [Sch85].

For the FRM II measurement [Haa14] foils of natural uranium (99.3% ^{238}U, 0.7% ^{235}U) were used as samples. They were irradiated once in a thermal neutron beam (only ^{235}U fission) and once in a fast neutron beam (mainly ^{238}U fission) by adding converters of highly enriched uranium and thermal neutron absorbers in the thermal beam, without changing the setup otherwise. In order to suppress systematic uncertainties, e.g. from uncertainties in the detector efficiency and response and the neutron beam profile, the ^{235}U measurement was normalised to the more precise BILL data and the same normalisation function was then applied to the ^{238}U measurement. This normalisation fully correlates the measured ^{238}U spectrum with the BILL spectrum of ^{235}U. For the ^{238}U cumulative β spectrum an uncertainty below 3% below 4.5 MeV was achieved, increasing up to 28% at 7 MeV, not including an uncertainty of the absolute normalisation of 2.1% from the present measurement and an additional 1.8% resulting from the normalisation to the BILL data.

Once the experimental cumulative β spectra are available they need to be converted into the corresponding neutrino spectra. This process comprises several additional sources of uncertainties. The ILL spectra have been converted [Sch85] by fitting virtual β branches to the measured distribution. For this purpose each electron spectrum N_β was divided into 30 energy intervals. Then, starting from the highest energy, the data points of each interval i were used to fit a β branch according to the general function

$$N_\beta = \sum_i N_\beta^i = \sum_i a_i \cdot g_i'(E_e, E_0^{(i)}) \cdot S_i(E_e, E_0^{(i)}, \bar{Z}(E_0^{(i)})) \ , \tag{2.1}$$

where a_i is a weighting factor, g_i' a radiative correction term for real and virtual photon exchange of the contributing particles at first order of α_{QED}, calculated by Sirlin [Sir67], and S_i the spectral shape according to the Fermi theory as function of the electrons's kinetic energy E_e and in dependence of the endpoint energy of the β branch $E_0^{(i)}$ and its mean proton number $\bar{Z}$. For the S_i only allowed transitions were assumed. The function $\bar{Z}(E_0)$ was obtained from an empirical fit to available data of fission products. After fitting a branch its contribution was subtracted from the measured spectrum and the procedure was successively repeated for all remaining energy intervals. The neutrino spectrum was obtained by summing up the virtual branches and substituting E_e with $E_\nu = E_0 - E_e$ and omitting the radiative correction g' which is much smaller for neutrinos than for electrons since they do not themselves participate in electromagnetic interactions. For the full neutrino spectrum an effective Coulomb correction for the deviation of the extended nucleus from the point like Fermi theory and a correction for the weak magnetism were applied. Here a combined, approximated correction for both effects was

used, as derived by VOGEL [Vog84]:

$$\Delta N_\nu^{\mathrm{C,W}}(E_\nu) \simeq 0.65(E_\nu(\mathrm{MeV}) - 4)\% \ . \tag{2.2}$$

The converted neutrino spectra and their uncertainties are given between 2-9 MeV in bins of 250 keV for ^{235}U in [Sch85] and for ^{239}Pu and ^{241}Pu in [Hah89]. The total uncertainties in the neutrino spectra are 4.2-6% (4.3-35%, 3.9-11%) for ^{235}U (^{239}Pu, ^{241}Pu) between 2-8 MeV.

For the ^{238}U spectrum this procedure could not be applied, due to the poor statistics in the high energy region of the measured spectrum. An empirical method, as proposed in [Sch85], was used instead: Given that the electron and neutrino spectra are the sums of many individual decays their shapes are fairly similar for relativistic cases ($E_e \gg m_e c^2$) and when compared at energies E_ν and $E_e + m_e c^2$. An additional shift of 50 keV has to be applied to account for the average Coulomb attraction of the electron by the nucleus. The electron-to-neutrino-spectrum conversion is then given by

$$N_{\bar{\nu}}(E_\nu) = N_\beta(E_\nu - 511\,\mathrm{keV} - 50\,\mathrm{keV}) \cdot k(E_\nu) \ , \tag{2.3}$$

where $k(E)$ accounts for all further corrections, which are in the range of 5%. In [Haa14] the correction function was calculated as $k(E_\nu) = N_\beta^{\text{U-235}}/N_\nu^{\text{U-235}}$ with spectra from MUELLER *et al.* [Mue11] (details in section 2.1.2). With those spectra it was also shown that $k^{\text{U-235}}$ and $k^{\text{U-238}}$ agree within $\sim 1\%$. The converted ^{238}U neutrino spectrum between 3 MeV and 7.5 MeV is given with uncertainties in bins of 250 keV in [Haa14]. The relative uncertainties range from 3.5% at 3 MeV to 14.1% at 7 MeV, not including a 3.3% error for the global absolute normalisation, resulting from the ^{238}U measurement, the uncertainty in the BILL data and the electron-to-neutrino spectrum conversion.

More recently HUBER performed a refined conversion for the ^{235}U, ^{239}Pu and ^{241}Pu spectra [Hub11], with the original data from [vF82, Sch85, Hah89] and the same method of applying virtual branches. In order to improve the predictions more detailed shape correction factors have been taken into account than previously (compare Eq. (2.1)), including some subleading order effects. The β-spectrum is described in the form:

$$N_\beta(E_e) = K \underbrace{\mu p_e^2 (E_e - E_0)^2}_{\text{phase space}} \underbrace{F(Z,E_e)}_{\text{Fermi function}} \underbrace{L_0(Z,E_e)C(Z,E_e)}_{\text{finite size}} \underbrace{S(Z,E_e)}_{\text{screening}} \underbrace{G_\beta(Z,E_e)}_{\text{radiative}} \underbrace{(1+\delta_{\mathrm{WM}}E_e)}_{\text{weak magnetism}} \ , \tag{2.4}$$

where E_e and p_e are the electron's energy and momentum, respectively, E_0 the endpoint energy and K a normalisation constant. The neutrino spectrum is obtained by substituting $E_e \to E_\nu = E_0 - E_e$ and $G_\beta \to G_\nu$. The prefactor μ in front of the phase space factor of Fermi's theory describes a correction for forbidden decays ($\mu = 1$ for allowed decays). For forbidden decays $\mu = \mu(p_e, p_\nu)$ is symmetric between electron and neutrino momentum and thus, when neglecting the electron mass ($E \gg m_e c^2$) also in their energies. In [Hub11] it was argued that, given that the electron spectrum is fixed by the measurements, any factor symmetric in E_e and E_ν would not change the resulting neutrino spectrum. For this reason the influence of μ has been found to be small and was omitted, although there are many forbidden decays contributing to the reactor spectrum. The next contribution in Eq. (2.4) is the Fermi function which corrects for the attraction of the electron in the field of the nucleus under the assumption of a point like and infinitely heavy nucleus. To take into account its actual finite size two correction functions, L_0 and C for the electromagnetic and the weak interaction, respectively, were introduced. Approximations for both are given by WILKINSON [Wil90]. The function $S(Z, E_e)$ accounts for screening effects of the nucleus' charge by the electrons of the atomic shell. The G_α ($\alpha = e, \nu$) term accounts for first order radiative corrections ($\sim \alpha_{\mathrm{QED}}$). For electrons the same correction as in the previous analysis has been used, as calculated by SIRLIN [Sir67], who now has also derived expressions for neutrinos [Sir11]. The last term, the weak magnetism, is a coupling which is not present in the original Lagrangian but arises from interferences of vector

and axial vector currents and is accounted for by the correction $(1 + \delta_{\mathrm{WM}} E_e)$. The size of this correction depends on the exact matrix element of the transition and in a discussion in [Hub11] it was concluded that this could vary significantly and affect the neutrino rate at $\mathcal{O}(1)\%$. It was identified as one of the major sources of theory uncertainty in the prediction of neutrino spectra.

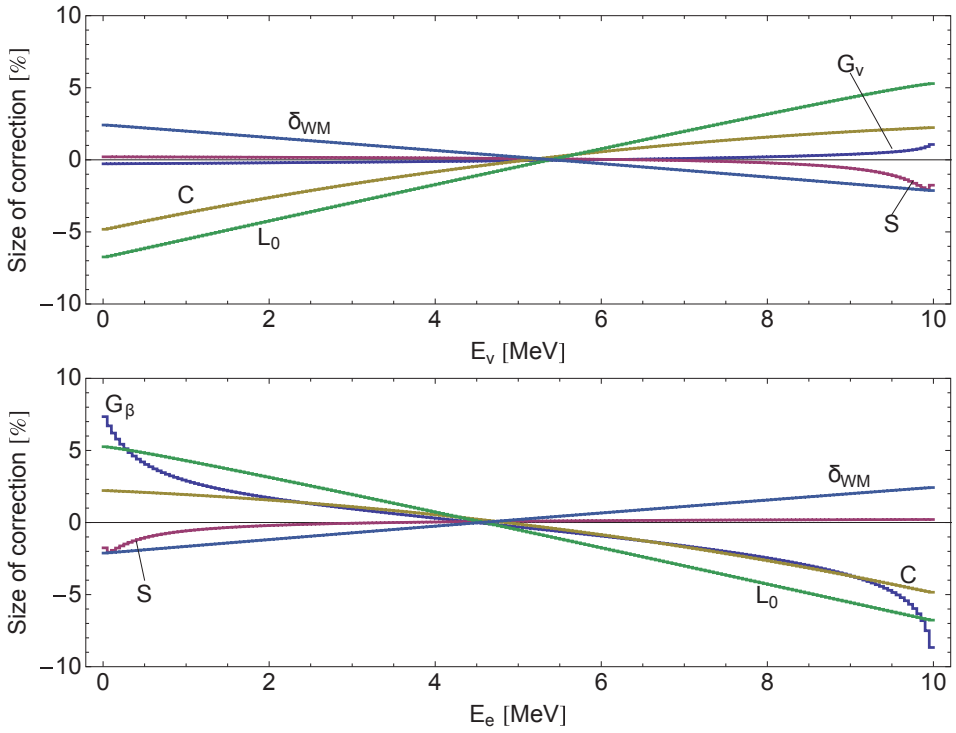

Figure 2.1: Relative size of the correction factors of Eq. (2.4) to the antineutrino (top) and electron spectrum (bottom) for a hypothetical β-decay with $Z = 46$, $A = 117$ and $E_0 = 10\,\mathrm{MeV}$. From [Hub11].

The impact of the single correction factors and their uncertainties have been studied with a generic β sum spectrum, built entirely from data from the ENSDF library [ENS17]. The relative contributions of the corrections are shown in Fig. 2.1.
The spectra conversion followed the procedure described earlier, of subsequently fitting 30 virtual branches to the electron spectrum. In contrast to the previous conversion [Sch85] all corrections are applied on the level of single virtual branches instead of averaged, overall corrections to the neutrino spectrum. An additional improvement was made by defining a new $\bar{Z}$ by fitting a second-order polynomial to the $Z(E_0)$ distribution of the fission products of each fissile isotope, where the individual contributing isotopes are weighted by their fission yields.
The new conversion results in a 2-3% higher neutrino flux than the previous predictions. This effect was originally first observed in [Mue11], described in the next paragraph. The reason for the shift was found to be twofold. At energies below 4 MeV the main effect is the implementation of the shape correction on the single branch level. Above 4 MeV a large contribution to the shift originates from the recalculated effective nuclear charge $\bar{Z}$. At high energies also the finite size and screening corrections gain a significant weight. As a crosscheck the same expression for $\bar{Z}$ as in [Sch85] was used and all corrections were applied only as effective corrections on the full spectrum. In this case the result from [Sch85] was reproduced. The deviation from the first conversion is not constant but increases from 2% (5%, 3%) at 3 MeV to 8% (6%, 13%) at 7 MeV for ^{235}U (^{239}Pu, ^{241}Pu). The total integrated flux change relative to the ILL conversion is +2.4% (2.9%, 3.2%) with a significance of 3.7σ (3.9σ, 4.0σ) for ^{235}U (^{239}Pu, ^{241}Pu). When convoluted with the cross section of the inverse β decay, which increases quadratically with energy, the difference in the expected event rates would be 3.7% (4.2%, 4.7%) with a significance of 2.4σ (2.8σ, 3.0σ). The reduced significance for the latter results from the convolution with the IBD

cross section, which gives a larger weight to high energies where the uncertainties are larger. The obtained antineutrino spectra are shown in Fig. 2.2. The stated relative uncertainties for the ^{235}U (^{239}Pu, ^{241}Pu) spectrum range from around 1.8% (2.6%, 2.5%) at 2 MeV to 7% (29%, 13%) at 8 MeV.
Huber also points out that for some particular isotopes the weak magnetism correction can be anomalously large. If a small fraction of fission products would show such a behaviour this could already revert a major part of the observed flux shift.

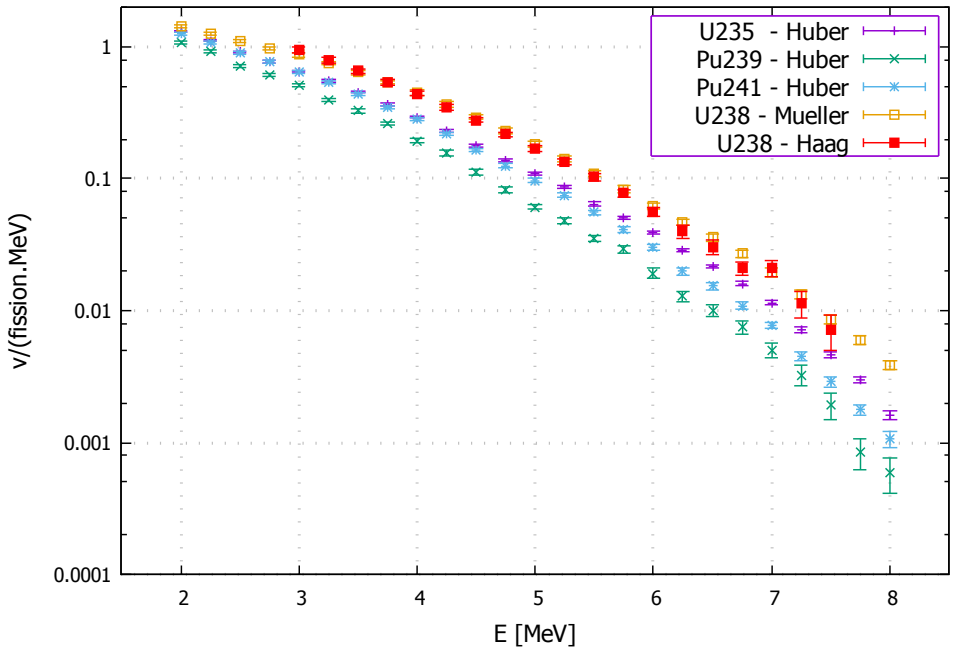

Figure 2.2: Predicted cumulative antineutrino spectra of the fission products of the four main fissile isotopes in a nuclear reactor. The ^{235}U, ^{239}Pu and ^{241}Pu spectra are taken from [Hub11], the ^{238}U spectrum is shown as predicted by Haag *et al.* [Haa14] and by Mueller *et al.* [Mue11]. The Huber and Haag spectra are obtained by conversion of electron spectra, the Mueller spectrum from an ab-initio calculation. The fission products of ^{238}U (^{241}Pu) have more neutrons than those of ^{235}U (^{239}Pu) which is mostly correlated with higher Q-values. In addition more decays are required to reach the line of stability. For these reasons the ^{238}U (^{241}Pu) spectrum per fission is higher in magnitude and energy.

2.1.2 Ab-initio method

The principle of this method is to consecutively sum up all neutrino spectra emitted in β decays of fission products and their daughter nuclei. This requires a huge amount of data such as the fission yields of each product, the branching ratios for all possible β decay branches (decays to ground states or excited states), the respective Q-values and the type of the transition (Fermi/Gamow-Teller, allowed/forbidden). The advantages of this method are that the conversion itself as well as corrections e.g. for finite size and weak magnetism effects can be applied on the level of single transitions instead of virtual branches or averaged correction factors of the full spectrum. In addition the impact of different corrections and the contribution of single isotopes can be studied in detail. Given that the electron and antineutrino spectra can be calculated at the same time, the cumulative electron spectra can still be compared to the measured ones.

Several calculations have been performed in the past, one of the most detailed in recent years by Mueller *et al.* [Mue11] which in the following is used as reference to describe the method. The total β spectrum S_{tot} from a reactor is composed of the integrated spectra of the fissile

isotopes

$$S_{\mathrm{tot}}(E_e) = \sum_k \alpha_k \left(\sum_{f=1}^{N_f} \mathcal{A}_f^k(t) S_f(E_e) \right) \ . \tag{2.5}$$

The index k runs over all fissile isotopes (^{235}U, ^{238}U, ^{239}Pu, ^{241}Pu), the index f over all N_f fission products. α_k is the fission fraction of the kth isotope at a given time, which in general slowly evolves over a reactor cycle. $\mathcal{A}_f^k(t)$ is the activity of the fth fission product produced by isotope k and normalised to one fission of the mother isotope. The time dependence here originates from the time required to reach the equilibrium activity of the given isotope. The spectrum of each fission product $S_f(E)$ is in itself the sum of N_f^b β decays. Each decay can either lead from the ground state or an isomeric state of the mother nucleus to the ground state or an excited state of the daughter nucleus

$$S_f(E_e) = \sum_{b=1}^{N_f^b} \mathrm{BR}_f^b S_f^b(Z_f, A_f, E_{0f}^b, E_e) \ , \tag{2.6}$$

where BR_f^b is the branching ratio (=probability) for the decay branch b to occur and S_f^b the corresponding β spectrum. The latter is a function of the proton and mass numbers Z_f and A_f of the parent nucleus and the endpoint energy E_{0f}^b. This general scheme is true for electrons and for neutrinos with $E_e \to E_\nu = E_{0f}^b - E_e$. In principle the individual β spectra S_f^b can be calculated according to Eq. (2.4), where Mueller *et al.* took into account the shape factor μ but not the weak interaction finite size correction $C(Z, E_e)$ and the screening correction $S(Z, E_e)$.

The Coulomb correction for the finite size of the nucleus (L_0) and the weak magnetism correction (δ_{WM}) were taken from Vogel [Vog84]:

$$L_0 = -\frac{10}{9} \frac{Z\alpha R}{\hbar c} \ , \tag{2.7}$$

where R is the nuclear radius and

$$\delta_{\mathrm{WM}} = -\frac{4}{3} \frac{\kappa_p - \kappa_n - 1/2}{M_{\mathrm{N}} \lambda} \ , \tag{2.8}$$

with $\lambda = g_{\mathrm{A}}/g_{\mathrm{V}}$ the ratio of the axial-vector and vector coupling constants, M_{N} the nucleon mass (in the considered cases only neutrons, $M_n = 939\,\mathrm{MeV}$) and κ_{p} and κ_{n} the anomalous magnetic moments of the proton and the neutron, respectively.

The formulas given above allow to build up the total neutrino spectrum emitted from a reactor, where all shape and correction factors can be applied on the level of single β transitions. In addition the uncertainties of the input parameters can be propagated to the final spectrum. The difficulty is that for each fissile isotope data of > 800 isotopes and ~ 10000 β-branches is required. This approach was followed in [Mue11] based on data from the Evaluated Nuclear Structure Data File (ENSDF) [ENS17]. By using only ENSDF data the residua of the calculated electron spectra relative to experimental data were found to oscillate in between $\pm 10\%$ around the measurement (dash-dotted line in Fig. 2.3). In order to improve the agreement a few corrections were made to the input data:
At first the so-called pandemonium effect has to be taken into account, which describes an overestimation of the intensity of high energetic β branches in the decay of a single nucleus. This can occur when branching ratios are based on measurements of the emitted γ-rays following the decay to an excited state of the daughter nucleus. For transitions to highly excited states, corresponding to low β energies, the following high energetic γ-ray or parts of the γ-ray cascade could be missed and thus the intensity of the transition underestimated. As a consequence a too high weight is assigned to higher energetic β transitions. To correct for this effect some data from the ENSDF was replaced by data from β spectra measurements (Tengblad *et al.* [Ten89]) and data measured by total absorption gamma spectroscopy (TAGS) (Greenwood *et*

al. [Gre92]). TAGS setups provide a large gamma detection efficiency and solid angle coverage with respect to the sample so that the pandemonium effect can be prevented.

About 90 pandemonium affected nuclei were replaced leading to a clear reduction of the electron spectrum at high energies (dashed line in Fig. 2.3). The calculations now show negative residua over the full energy range which are strongly increasing towards higher energies. This is associated with contributions from unknown, exotic nuclei which in general are short lived and have high Q-values. This missing data was partly filled up with predictions from the Japanese Evaluated Nuclear Data Library (JENDL) [JEND17]. Still missing data was approximated by fitting and extrapolating endpoint and branching ratio distributions from the ENSDF database.

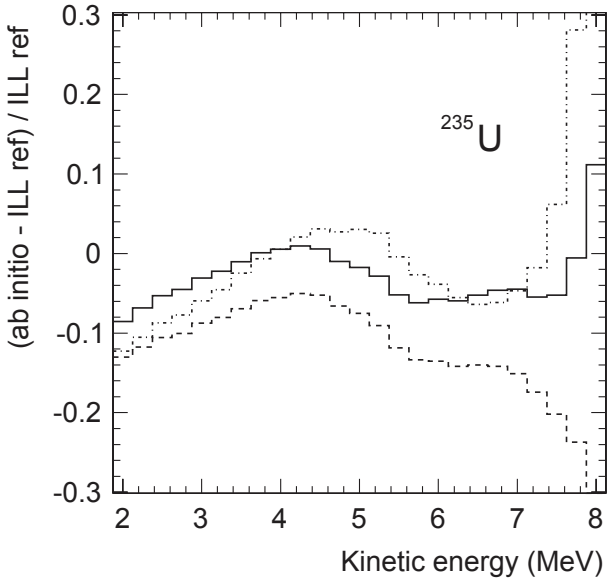

Figure 2.3: Residua of the cumulative electron spectrum of the fission products of ^{235}U obtained in an ab-initio calculation by Mueller *et al.* [Mue11], relative to the spectrum measured at the ILL by Schreckenbach *et al.* [Sch85]. The dash-dotted line corresponds to a calculation with only ENSDF data. For the dashed line some input was replaced by pandemonium corrected data. For the solid line missing information about some nuclei was added from theoretical calculations (JENDL data). From [Mue11].

The residuals of the final electron spectrum including all corrections are shown as the black line in Fig. 2.3. With the currently available data the highest accuracy which could be achieved in this theoretical approach is at the 10% level. Given the large amount of experimental data required for these predictions this is a remarkable result, but not sufficient to make precise predictions for reactor neutrino spectra.

To improve the data situation will require time as about 800 fission products contribute to the spectrum of each fission isotope, but ab-initio calculations may help to indicate which effects or isotopes need to be studied preferentially. The procedure of [Mue11] was revised later by Fallot *et al.* [Fal12] where it was shown that the correction of pandemonium affected data is indeed essential for more precise predictions. The used method was similar to [Mue11] but seven more pandemonium corrected nuclei of the ENDF library were replaced by data measured with total absorption spectroscopy (TAS) by Algora *et al.* [Alg10]: ^{102,104,105,106,107}Tc, ^{105}Mo, ^{101}Nb. When comparing the calculated antineutrino spectra with the results of [Hub11] the ratio lies still within a 10% envelope, which corresponds to the precision of this method stated before [Mue11], but when comparing cumulative spectra of the four main fission isotopes with and without the correction there is a decrease of up to 1.5% (4%, 8%) of the neutrino flux in the energy range from 2-6 MeV for ^{235}U (^{238}U, ^{239,241}Pu). The magnitude of the impact depends on the cumulative fission yield of the corrected isotopes. The affected energy range is of particular interest for reactor neutrino experiments. When folding the spectra with the IBD cross section

[Vog99] the correction of only those seven pandemonium affected isotopes in the database decreases the expected IBD-rate for pure fission of ^{235}U, ^{238}U, ^{239}Pu and ^{241}Pu to 99.1%, 98.09%, 94.53% and 94.76% of the uncorrected values, respectively.

The conclusion of MUELLER *et al.* drawn from their calculation was that the precision of the ab-initio method with the currently available data is not competitive with that of the conversion method, even compared to the original ILL conversion [Sch85]. Considering the known deficiencies of the conversion method it was argued in [Mue11] that the best way to improve the spectrum predictions is to chose a combined method. In [Mue11] the final approach is to start with the ab-initio calculations, including only the ENSDF and the pandemonium corrected data, which allows to include all spectrum corrections at the single transition level. The remaining difference to the measured electron spectrum was then fitted by five virtual β-branches with a proton number of $Z = 46$ (average of the fission products) and assuming allowed transitions. Afterwards all calculated plus the five fitted branches are converted into neutrino branches. This new conversion was found to be in good agreement with the previous conversion [Sch85] in terms of spectral shape, but had a mean normalisation shift of about +3%. For neutrino energies below $\sim 4\,\mathrm{MeV}$ the main reason was the implementation of the L_0 and δ_{WM} correction. While in [Mue11] the corrections at branch level (Eqs. (2.7) and (2.8)) are almost zero for low neutrino energies the effective linear approximation applied to the total neutrino spectrum in [Sch85] (Eq. (2.2)) is a negative correction below $E_\nu = 4\,\mathrm{MeV}$. At higher energies the normalisation shift results mainly from the parametrisation of the mean proton number in dependence of the endpoint energy of β branches, which was used in [Sch85] for the virtual branches, while in [Mue11] the underlying ab-initio calculation allowed to use the actual atomic numbers. These conclusions are in agreement with those of HUBER [Hub11].

This mixed approach has the advantage with respect to the conversion method that fewer approximations for averaged effects are required for spectrum shape corrections. In addition a precise uncertainty calculation per energy bin as well as correlations in between different bins is possible. Given that the larger fraction of the spectrum is known from the ab-initio calculations the time evolution of the spectrum during a reactor cycle can be calculated in a more reliable fashion. This includes the change in isotope activities over time, originating from the accumulation of long lived fission products and the build-up of new isotopes by neutron capture on the fuel material. This is important for power reactors with typical fuel element cycles of about one year.

While the spectra of ^{235}U and the two plutonium isotopes could be adjusted to the measured ILL spectra no data was published at that time for ^{238}U. The ab-initio calculation was therefore used to provide a new prediction for this spectrum. Although the uncertainty lies between 10% at 2 MeV and 20% at 8 MeV this gives a new reference. Experiments today mostly use the conversion of HUBER [Hub11] as predictions for ^{235}U, ^{239}Pu and ^{241}Pu and either the predictions of MUELLER *et al.* [Mue11] or the conversion from HAAG *et al.* [Haa14] for ^{238}U. The predictions are then called the HUBER-MUELLER model and the HUBER-HAAG model, respectively.

2.1.3 Comparison of the Spectra Predictions

Comparing the two newer neutrino spectra predictions from HUBER [Hub11] and MUELLER *et al.* [Mue11], performed by independent groups and with largely complementary methods they consistently show an upward shift of the predicted neutrino flux of about 3%. Both find that the main reason is the implementation of the weak magnetism and finite size corrections at the level of single β branches instead of an overall, averaged correction to the full neutrino spectrum, and a more precise consideration of the mean proton number $\bar{Z}$ of the fission products. There is, however, a difference in such that the MUELLER spectrum results in an overall shift while HUBER obtains a shift which increases with energy, see Fig. 2.4. The shift of the normalisation of the neutrino spectrum of about +3% together with a +2% increase of the calculated IBD cross-section over the last years (see Ch. 2.2) leads to a ∼5% increase of the predicted IBD rate

in reactor neutrino experiments. This led to the so-called Reactor Antineutrino Anomaly, which will be discussed in Chapter 2.2.

In response to the two new predictions HAYES *et al.* performed an independent study of systematic uncertainties of the predicted spectra [Hay14]. The main focus of this study was the influence of forbidden decays, which are stated to produce about 30% of the neutrino flux. In contradiction to HUBER, who considered the impact of forbidden decay shape corrections to be negligible, it is found that they have an impact on the neutrino spectrum in both, the conversion and the ab-initio method.

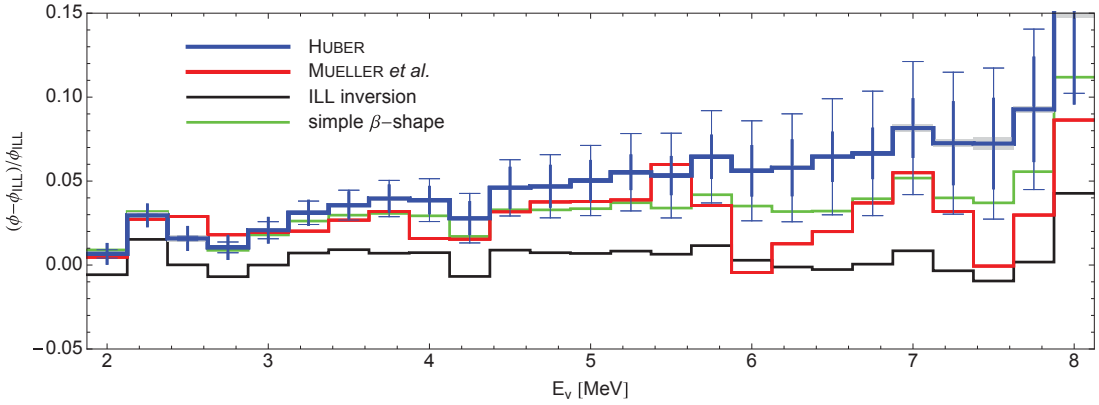

Figure 2.4: Comparison of different antineutrino spectrum predictions for ^{235}U relative to the ILL conversion [Sch85]. The blue line shows the results of HUBER [Hub11] which predict a clearly higher flux, increasing with energy. The thin error bars correspond to uncertainties from the effective nuclear charge $\bar{Z}$ and the weak magnetism correction, the thick error bars are statistical errors propagated from the electron spectrum. The red line is the deviation of MUELLER's prediction [Mue11] from the ILL conversion, which is consistent with HUBER's results up to 5.5 MeV but shows some oscillating behaviour for higher energies. The black line is a conversion from HUBER, performed with the effective charge and averaged spectrum corrections from [Sch85], which reproduces the original result. The green curve is obtained by HUBER by performing a conversion with the β decay description from MUELLER *et al.*, which produces a spectrum close to MUELLER's prediction. Adapted from [Hub11].

HAYES *et al.* calculated shape correction factors and weak magnetism corrections for allowed and first forbidden Gamow-Teller transitions and showed that both corrections do not only depend on the forbiddenness of the transition but on the exact matrix element which mediates between initial and final state. In some cases the weak magnetism correction can even become zero. In order to determine the resulting uncertainty in the spectra prediction the ILL ^{235}U electron spectrum [Sch85] is fitted by 40 virtual β branches first without a treatment of the forbidden decays and then with several different distributions of the forbidden decays among the 40 branches. In all cases the electron spectrum was well described by the fit but the converted neutrino spectra varied by as much as 4%, depending on the distribution of forbidden decays. Corrections for higher orders of forbiddeness have not been calculated. With these findings HAYES *et al.* suggested that the uncertainty of the predicted spectra should be at least 4%.

2.1.4 Corrections to Reactor Neutrino Spectra

The cumulative neutrino spectra are predicted for each fissile isotope individually. For any given reactor these have to be weighted and summed up according to the actual fission fractions, which are monitored by the reactor operator. For each experiment some additional contributions or corrections may be necessary, which will be briefly described here.

Off-equilibrium Corrections

The ILL spectra have been measured after 12 h and 38 h of irradiation for ^{235}U and the Pu isotopes, respectively [Sch85, Hah89], the ^{238}U spectrum after 11 h [Haa14]. For power reactors the irradiation time is usually around 1 yr, which gives time for the accumulation of long lived fission products. About 10% of them have a halflife sufficiently long to need several days to reach equilibrium. In addition at the ILL irradiation position the neutron flux was fully thermalised while a reactor core has more epithermal and fast neutron contributions. All this was taken into account by Mueller *et al.* [Mue11] in simulations of the fuel inventory of pressurised water reactor (PWR) cores for fuel cycle times from the given 12 h up to 450 d with the 'MCNP Utility for Reactor Evolution' (MURE [MUR17]). Based on the ab-initio calculations energy dependent relative correction factors for the time evolution have been calculated and are listed in [Mue11]. The corrections above the IBD threshold (∼1.8 MeV) for 450 d irradiation compared to the 12 h reference are about 6% (2%) at 2 MeV for ^{235}U (^{239,241}Pu), decreasing with the neutrino energy. Above 3.5 MeV the correction becomes negligible. The antineutrino spectrum is stable at the 1% level for all energies only after about 100 d.

Non-linear Effects

It was shown by Huber *et al.* [Hub16] that also neutron capture on fission products can have an impact on the antineutrino spectrum. In the case that a fission product P has a large cumulative fission yield, a long halflife and a sufficiently large neutron capture cross section another isotope N can be produced in a large amount by the reaction $P(n,\gamma)N$. In a few identified cases N would otherwise not have been part of a decay chain. If N in turn decays fast and its β endpoint energy is above the threshold of the detection reaction (i.e. >1.8 MeV for the inverse beta decay) it can reach a significant activity and influence the measured antineutrino spectrum.

The fission rate in a reactor and thus the population of the fission products (in equilibrium conditions) depends linearly on the neutron flux ϕ. Likewise the neutron capture rate on stable or long lived isotopes is linear in ϕ. As a result, in a simplified picture, the contribution of isotope N depends quadratically on the neutron flux. This means that not only the rate, but also the shape of the neutrino spectrum is a function of the neutron flux and thus also of the reactor power. Four main of these "non-linear" isotopes have been identified by Huber *et al.*: ^{100}Tc, ^{104}Rh, ^{110}Ag and ^{142}Pr, all with endpoint energies below 3.2 MeV. Mueller *et al.* [Mue11] studied neutron capture effects in general, but found them to be negligible. The more detailed study by Huber *et al.* shows that for a three-batch PWR (one third each of fresh, once irradiated and twice irradiated fuel) the correction can reach 0.9%, comparable to the non-equilibrium effects ($\sim 1-4\%$) and spent fuel contributions ($\sim 1\%$, see below). For other civil use reactors the contribution is smaller. For research reactors using HEU fuel and cycle durations of a few 10 d the correction is negligible ($\leq 0.1\%$). This correction can be relevant for precision reactor neutrino experiments such as the Daya Bay experiment [An16c] and the upcoming JUNO [JUN15] but even more for measurements of geoneutrinos or solar neutrinos which are detected by neutral current interactions. These reactions do not have an energy threshold and the concerned neutrinos have generally low energies. For these studies the low energy reactor neutrinos have to be subtracted as background.

Spent Fuel Contribution

At the end of a reactor fuel cycle some part of the reactor inventory needs to be replaced, in the case of the ILL this is the complete fuel element, in case of a power reactor usually one third of the fuel. This spent nuclear fuel (SNF) is stored in cooling water pools nearby the reactor to avoid risks during transportation. Given its high activity SNF contributes to the antineutrino spectrum seen by a neutrino detector and has to be taken into account for precision measurements. To cause a relevant contribution for reactor neutrino experiments the Q value of an isotope, or its daughter isotopes, should be larger than the IBD threshold of 1.8 MeV, the cumulative fission yield high enough to generate a high activity and the halflife of the isotope or

its mother should be sufficiently long, e.g. longer than $\sim 10\,\mathrm{h}$. Zhou *et al.* [Zho12] studied this effect for the Daya Bay experiment. Twelve isotopes were identified which fulfill the criteria, listed in Tab. 2.1. Once the isotopes are known their activity at the end of the irradiation of the fuel can be obtained from nuclear inventory simulations, normally performed by the reactor operator, or calculated explicitly with knowledge of the neutron flux in the reactor core and input from nuclear databases. The initially dominating contributions from ^{91}Sr, ^{93}Y and ^{97}Zr decay fast, leading to a reduction of the SNF spectrum by about a factor of two during the first day. At energies below 3 MeV the SNF spectrum remains at the percent level compared to the normal reactor spectrum, but given the comparatively low energy the contribution to the total IBD rate in a detector is lower. The leading contribution originates from ^{144}Pr which is produced by the decay of its mother isotope ^{144}Ce for a long period.

The actual contribution of spent fuel has to be assessed for each experiment individually. It depends on the reactor type, its fuel composition and burnup history and for very short baselines also on the location of the SNF. For example in the case of Daya Bay the total IBD rate caused by SNF was estimated to be 0.3%, with a conservative 100% uncertainty [An16a].

Table 2.1: Relevant isotopes for the spent nuclear fuel neutrino spectrum where either the mother M or daughter nucleus D has a long halflife and a high Q-value. From [Zho12].

M	$T_{1/2}$	Q [MeV]	D	$T_{1/2}$	Q [MeV]
^{90}Sr	28.78 a	0.546	^{90}Y	64.1 h	2.282
^{91}Sr	9.63 h	2.699	^{91}Y	58.51 d	1.544
^{93}Y	10.18 h	2.874	^{93}Zr	$1.53{\cdot}10^{6}$ a	0.091
^{97}Zr	16.9 h	2.685	^{97}Nb	72.1 min	1.934
^{106}Ru	373.6 d	0.039	^{106}Rh	29.8 s	3.541
^{112}Pd	21.03 h	0.288	^{112}Ag	3.13 h	3.956
^{125}Sn	9.64 d	2.364	^{125}Sb	2.758 a	0.767
$^{131\mathrm{m}}$Te	30 h	0.182	^{131}Te	25 min	2.233
^{132}Te	3.2 d	0.493	^{132}I	2.295 h	3.577
^{140}Ba	12.75 d	1.047	^{140}La	1.678 d	3.762
^{144}Ce	284.9 d	0.319	^{144}Pr	17.28 min	2.997
^{159}Sm	9.4 h	0.722	^{159}Eu	15.19 d	2.451

2.1.5 Direct Measurements of the Reactor Antineutrino Spectrum

A number of neutrino experiments was performed at nuclear reactors in the past, where one goal was to investigate possible neutrino oscillations with reactor neutrinos. From those experiments a set of flux and spectra measurements is available. However, the most precise measurements nowdays originate from the present large scale experiments designed to measure the mixing angle $\theta_{1,3}$, Double Chooz [Abe14], Daya Bay [An16c] and RENO [Ahn10]. They are all based on the same principle of having a near detector, at baselines of a few hundred meters, and a far detector at distances longer than one kilometer. The mixing angle can then be determined from the ratio of the spectra seen by the near and the far detector.

Before these experiments published their first data on θ_{13}, all in spring 2012 (DC [Abe12a], DB [An12], RENO [Ahn12]), only strong limits, e.g. from CHOOZ [Apo03], and indications of a non-zero value existed, e.g. from KamLAND [Gan11]. The mixing angle was thus presumably very small, so that a high experimental precision was required for its determination. On the one hand this requirement triggered the recent re-evaluation of the reactor neutrino spectra by Mueller *et al.* [Mue11] and by Huber [Hub11]. On the other hand the experiments' locations were chosen to have a high $\bar{\nu}_e$ flux and the detectors designed to have a large volume and a good energy resolution. This also allows to perform precision studies of the antineutrino spectrum in general. The most precise measurements are obtained by the Daya Bay experiment, China. For

this six commercial PWRs with a nominal power of 2.9 GW_{th} each serve as antineutrino sources. Always two are grouped at the Daya Bay reactor complex and at two complexes in Ling Ao, close by. For both reactor sites an underground near detector hall was built, containing two 20 t, liquid scintillator antineutrino detectors, with flux-weighted effective baselines of 512 m and 561 m. One far experimental hall with four antineutrino detectors of the same type was build at an effective baseline of 1579 m [An16a].

The first results of an antineutrino spectrum study were published after 217 d of data taking with the data of the near detectors only [An16a]. One detector in the far hall and one in the Ling Ao near hall were not installed at that time but already a total of about 300 000 inverse beta decay candidates were recorded. An update with data of the full configuration, with increased statistics and more detailed explanations of the analysis is given in [An17a]. For the spectrum analysis the effects of the θ_{13}-driven oscillation have been corrected for, the other oscillations are negligible for the near detectors. The data is compared to two models, called the ILL-Vogel model (^{235}U, ^{239}Pu,^{241}Pu based on the ILL conversion method [Sch85, Hah89] and ^{238}U predictions from Vogel *et al.* [Vog81]) and the Huber-Mueller model (^{235}U, ^{239}Pu,^{241}Pu conversion from [Hub11] and ^{238}U predictions from [Mue11]). Daya Bay measured an IBD yield of $(5.92 \pm 0.14) \cdot 10^{-43}$ cm^2 fission^{-1}. While the data is in agreement with the ILL-Vogel predictions it confirms the deficit with respect to the Huber-Mueller model, leading to a global averaged ratio between measured and predicted IBD rates of $R = 0.943 \pm 0.008(\text{exp}) \pm 0.025(\text{model})$ [An16a].
From the data an antineutrino spectrum is computed, corrected for all detector effects. When compared to the predicted shape it deviates slightly for most energies, but exhibits a significant excess of about 10% ($\sim 4\sigma$) between 5 MeV and 7 MeV neutrino energy[1], see Fig. 2.5. This excess was found to be time independent and correlated with the reactor power. Given that this was also observed in Double Chooz [Abe14, Abe15] and RENO [Cho16] it seems unlikely to be due to a detector effect, but rather a deficit in the predictions. The excess around 5 MeV and the general flux deficit do not necessarily have the same origin and are generally discussed independently.

Investigation of the 5 MeV Excess by Hayes et al.

Hayes *et al.* [Hay15] studied different possibilities of the origin of the antineutrino excess between 5 MeV and 7 MeV, based on ab-initio calculations. Both libraries, the ENDF/B-VII.1 [END17] and JEFF-3.1.1 [JEF17], were compared including total absorption gamma-ray spectroscopy data. Five different scenarios were considered which could contribute to the shoulder in the antineutrino spectrum.
(1) *Non-fuel reactor materials*
MCNP simulations were performed for a CANDU reactor, including all possible neutron reactions on the coolant, cladding and structural materials. The neutrino spectra obtained from the produced unstable isotopes were well below the 5 MeV range and although other reactors can contain different materials it is not expected that those produce higher energetic spectra. For this reason this option was excluded.
(2) *Spectral shape corrections of forbidden decays*
As Hayes *et al.* pointed out before [Hay14] some correction factors have been treated too generally in the Huber-Mueller model, i.e. the shape corrections for forbidden transitions (neglected by Huber [Hub11]) and the weak magnetism corrections. Both depend on the forbiddeness of the transition (i.e. on the nuclear operator connecting initial and final state) and the latter can even be zero for some forbidden decays, but, when applied nevertheless reduces the higher end of the neutrino spectrum. This is the case for several top contributors of the high energy part of the cumulative neutrino spectrum: ^{96,98}Y, ^{90,92}Rb and ^{142}Cs. By comparing ab-initio calculations only based on ENDF/B-VII.1 data with and without consideration of the

[1] In some publications the spectra are given in prompt energy instead, which refers to the energy deposited by the IBD positron. The two are related by $E_\nu = E_{\text{positron}} + 782$ keV. Thus the excess appears for $E_\nu \in 5 - 7$ MeV or $E_{\text{positron}} \in 4 - 6$ MeV.

aforementioned effects, the corrected version led to an increase of less than 1% in the 5-7 MeV region and thus cannot account for a significant fraction of the excess (which is about 10% above the predictions).

(3) *^{238}U as source of the excess*

Compared to ^{235}U the fission products of ^{238}U have more neutrons and are further away from the line of stability, thus the ^{238}U neutrino spectrum per fission is larger and harder than that of ^{235}U. The difference reaches about a factor of two in the 4-6 MeV region. The pure ENDF/B-VII.1 and JEFF-3.1.1 libraries both predict a shoulder in that region compared to Mueller's prediction [Mue11], which might be partly due to the pandemonium corrections included therein. Based on the magnitude of the excess from the libraries compared to that in Daya Bay and RENO and their respective ^{238}U fission fractions, Hayes *et al.* concluded that based on the JEFF-3.1.1 (ENDF/B-VII.1) library ^{238}U could contribute to 25% (50%) to the excess. To be solely responsible the fission yields in the libraries would have to be on average off by a factor of four (two). But even so ^{238}U could account for a significant fraction of the excess.

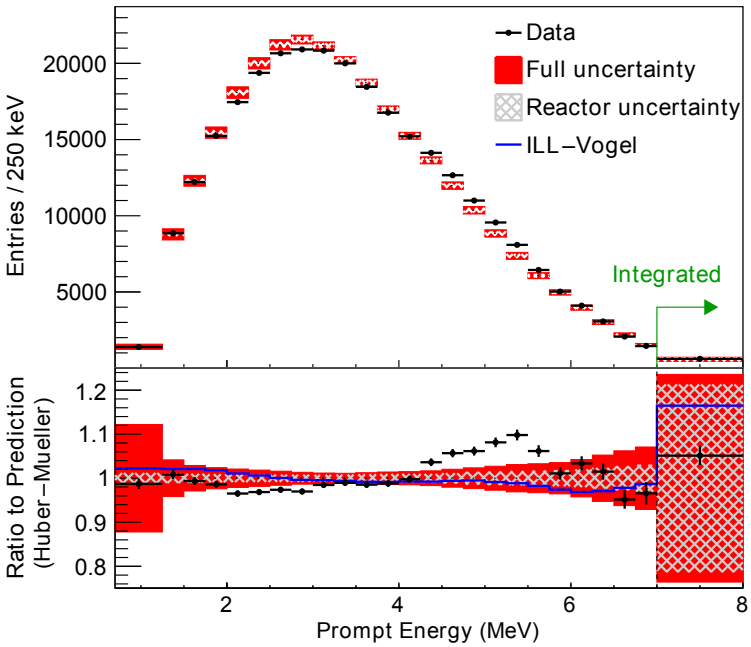

Figure 2.5: Top panel: predicted and measured prompt-energy spectra at Daya Bay. Bottom panel: ratio of the two. The predictions are normalised to the number of events in order to compare only the shape. The error bars on the data points include only statistical uncertainties. The gray hatched and red areas represent the reactor related and the full (reactor, detector and background) systematic uncertainties, respectively. The blue curve shows the ratio of the ILL-Vogel model to the Huber-Mueller model. From [An16a].

(4) *A harder neutron spectrum in PWRs*

The measurements by Schreckenbach *et al.* [Sch85, Hah89] were conducted in a fully thermalised neutron environment while in the core of a reactor a high contribution of epithermal neutrons is present. When surveying experiments measuring the change in fission yields for different neutron energies it was found that for rare isotopes (in the valley of the double peaked mass distribution of the fission products) the yield can change by as much as a factor of two, but for high yield fission products (on the peaks of the mass distribution, e.g. ^{96}Y, ^{92}Rb) the data is inconclusive. From a theoretical perspective a change of up to 20% cannot be ruled out. The effect is generally larger for ^{239}Pu, given a large resonance in the fission cross section at neutron energies of 0.3 eV. This would be in tension with the smaller ^{239}Pu fraction but higher shoulder in the neutrino spectrum in RENO compared to Daya Bay, but does not rule out this scenario.

(5) *Error in the ILL β spectrum measurement*
This assumption was mainly based on the shoulder around 5 MeV obtained in the antineutrino as well as in the electron spectrum in ab-initio calculations with the ENDF/B-VII.1 data by Dwyer *et al.* [Dwy15], when compared to the Schreckenbach data and conversion. This tension seems to be largely resolved by corrections to anomalous values and updates of isomeric ratios of fission yields and decay data in the ENDF/B-VII.1 proposed by Sonzogni *et al.* [Son16].

In conclusion, if the shoulder at 5 MeV and the Reactor Antineutrino Anomaly (RAA) are correlated this could be due to scenarios (4) or (5), but still it is possible that these are unrelated phenomena. Given the uncertainties and missing information in the databases a solution of both problems by improved predictions only is not possible at the moment. Considering that the observation of the RAA triggered a new series of very short baseline neutrino experiments at different reactor types, these can also help to address the problem of the 5 MeV shoulder. First analyses based on the new generation of experiments have already been proposed and performed and will be discussed in the following.

Experimental Analysis of the 5 MeV Excess

With NEOS the first very short baseline experiment published its data [Ko17]. The detector was a 1 t, single volume, Gd-loaded liquid scintillator detector at about 24 m from the core of a 2.8 GW_{therm} commercial power reactor at the Hanbit power plant, South-Korea (the same reactor complex which serves as source for RENO). The results of NEOS' sterile neutrino oscillation search will be discussed later in more detail, see Sec. 2.2.6. The NEOS data set of about 300 000 IBD events was also analysed by Huber in comparison with the Daya Bay spectrum in order to set constraints on possible sources of origin of the 5 MeV shoulder [Hub17]. The analysis is based on the fact that the reactors of the two experiments show different effective fission fractions. For Daya Bay the fission fractions of ^{235}U, ^{238}U, ^{239}Pu and ^{241}Pu are given as 0.561, 0.076, 0.307 and 0.056 [An17a] while for NEOS they are cited as 0.655, 0.072, 0.235 and 0.038, respectively. Both experiments published the ratio R of their spectra with respect to the predictions from the Huber-Mueller model. In [Hub17] at first a correction is applied to the NEOS data set to normalise both experiments to the same fission fractions, where the correction is based on the Huber-Mueller model. This allows to obtain a model-independent measure by taking the double ratio $R_{\mathrm{NEOS}}/R_{\mathrm{Daya\ Bay}}$, which cancels the model contributions while preserving the differences in the 5 MeV bump in the experiments, which is in both data sets a deviation from the model predictions. The correction to the NEOS data increases linearly with energy from 1% at 2 MeV to 5% at 7 MeV, without any features. However, a small model-dependent uncertainty remains in the double ratio, originating from the renormalisation of the fission fractions, but has been found to be negligible (i.e. a 10% uncertainty on a 5% correction, resulting in $\leq 0.5\%$ uncertainty in the double ratio). The double ratio still yields a bump around 5 MeV prompt energy of the IBD signal, see Fig. 2.6. In order to set constraints on the possible origin of this peak it was fitted with gaussian distributions of different amplitudes while keeping the position fixed at $E_{\mathrm{prompt}} = 4.9$ MeV. The uncertainties of both experiments have been considered in the fit. Conclusions can be extracted from the goodness of fit for the different bump amplitudes. Five hypotheses have been tested, each of which would have caused a different amplitude of the bump in the double ratio, defined only by the ratios of the fission fractions: the bump is only due to ^{235}U, ^{238}U, ^{239}Pu or ^{241}Pu or equally caused by all four isotopes. The expected amplitudes and the corresponding fit results are listed in Table 2.2.

From this analysis the plutonium isotopes are disfavoured as the single source of the bump by 3-4 standard deviations. The other three hypotheses are nearly equally likely, where ^{235}U as main contributor is slightly, but not significantly, preferred. The RENO collaboration has also seen a small positive correlation between the size of the 5 MeV bump and the ^{235}U fission fraction, which supports, but not establishes this trend [Joo16].

To further restrain the possible sources of the shoulder the new generation of very short baseline experiments at research reactors will be helpful. In case of STEREO the reactor fuel is 93% enriched in ^{235}U, which effectively delivers a pure ^{235}U spectrum. A similar study as above has already been proposed for a comparison of STEREO and the Double Chooz near detector [Buc17a], which is located at a commercial reactor with LEU fuel. The expected ratio of the spectra is shown in Fig. 2.7 for the scenarios: event excess only in ^{235}U, equally in all isotopes or not in ^{235}U. A sensitivity study was performed for the projected final data sets of both experiments. In the case of no excess in ^{235}U (excess only in ^{235}U) a significance of 4.9σ (3.7σ) could be reached. For these calculations only the anticipated detector resolution was considered, other detector related systematic uncertainties will weaken the constraints.

Table 2.2: Expected amplitudes of the bump in the double ratio of the NEOS and Daya Bay spectra for different hypotheses of the primarily responsible isotope (see text for explanations). The χ^2 values of the gaussian fit to the bump with a mean value at $E_{\text{prompt}} = 4.9\,\text{MeV}$, see Fig. 2.6, serve as a measure for the likelihood of each hypothesis. The number of degrees of freedom is 57-1. The minimal χ^2 is 46.7 at an amplitude of the double ratio of 1.022. From [Hub17].

Isotope/Hypothesis	^{235}U	^{238}U	^{239}Pu	^{241}Pu	equal
$R_{\text{NEOS}}/R_{\text{DayaBay}}$ exp.	1.021	0.993	0.971	0.960	1.000
χ^2	46.9	51.6	60.3	66.0	49.9

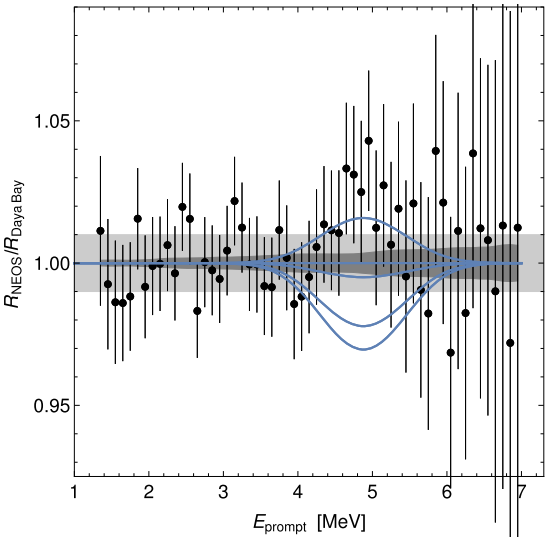

Figure 2.6: Double ratio of the NEOS and Daya Bay antineutrino data sets. The error bars include NEOS' statistical uncertainties and uncertainties from matching the more coarsely binned Daya Bay data to the NEOS data. The blue lines correspond to different predictions of the bump. The light gray band originates from uncertainties in the NEOS detector response, the dark grey band from the renormalisation of the fission fractions. From [Hub17].

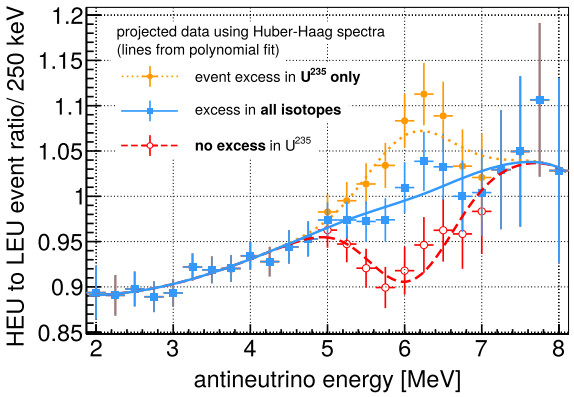

Figure 2.7: Anticipated ratio of STEREO (HEU) and Double Chooz near detector (LEU) data sets after two years of data taking. Reference spectrum is the Huber-Haag model. The error bars include statistical uncertainties and uncertainties from the model. The detector response is not included. From [Buc17a].

2.2 Reactor Antineutrino Anomaly

The new predictions of antineutrino spectra from reactors led to a shift of the expected neutrino flux of about +3%, first stated by MUELLER *et al.* [Mue11] and independently confirmed by HUBER [Hub11]. MENTION *et al.* who also worked on [Mue11] subsequently reviewed a number of reactor neutrino experiments performed in the 1980s and 1990s in view of the new spectra predictions [Men11]. Not only the expected spectra had to be changed but also the cross section of the IBD ($\bar{\nu} + p \rightarrow e^+ + n$) had to be revised, which is the fundamental antineutrino detection process used in all the experiments. The cross section for a reaction with a free proton (H^+-ion) is used in the form

$$\sigma_{\mathrm{IBD}}(E_e) = \sigma_0 p_e E_e (1 + \delta_{\mathrm{recoil}} + \delta_{\mathrm{wm}} + \delta_{\mathrm{rad}}) \ , \tag{2.9}$$

where p_e and E_e are the positron momentum and energy and the δ terms corrections for the energy dependent recoil, the weak magnetism and radiative effects. Since the standard model couplings to the IBD vertex are the same as for the β-decay of the free neutron the normalisation can be determined from that [Vog99]:

$$\sigma_0 = \frac{2\pi^2 \hbar^3}{m_e^5 c^7 f^{\mathrm{R}} \tau_n} \ , \tag{2.10}$$

with the electron mass m_e, the neutron lifetime τ_n and the phase space factor for the neutron β-decay f^{R}. The measured neutron lifetime evolved over the last decades from 926 s used in the first of the considered short baseline (SBL) experiments at the ILL in 1981 [Kwo81] to 885.7 s at the time of the publication of [Men11] in 2011 to the current PDG average value [Pat16] from 2016 of (880.2 ± 1.0) s. Most of the neutron lifetime measurements included in the current average are based on storage of ultra cold neutrons in material bottles. A better understanding of associated systematic corrections affected most of these experiments and systematically decreased the neutron lifetime over the last years. This in return increased the calculated IBD cross section by about +2% and thus the number of expected events.
The quantity which is compared among the different experiments is the cross section per fission

$$\sigma_f = \int_0^\infty S_{\mathrm{tot}}(E_\nu) \sigma_{\mathrm{IBD}}(E_\nu) \mathrm{d}E_\nu = \sum_k \alpha_k \sigma_{f,k} \ , \tag{2.11}$$

where the total neutrino spectrum S_{tot} is the sum of the neutrino spectra of the single fissile isotopes k weighted with their respective fission fractions α_k. For the conversion from positron to antineutrino energy in the cross section function it can be used that with only two particles in the IBD final state their energies follow a well defined relation, described in more detail in Sec. 2.2.6. In [Men11], in total 19 experiments with baselines between 9 m and 95 m at different types of reactors were considered. For each experiment at first the original results were reproduced from the published data, the previous spectra predictions (except for ^{238}U) and the respective neutron lifetimes used in the original analyses. These reproduced results were used as reference and were found to be in agreement with the original publications. The ratios of the experimental σ_f^{exp} and previously predicted $\sigma_f^{\mathrm{pred,\ old}}$ cross sections per fission were all in agreement with unity, except for the ILL experiment [Kwo81]. Compared with the new predictions, here only those from MUELLER *et al.* [Mue11], most experiments now deviate more or less significantly from unity with an average ratio of observed to predicted rates of $R = 0.943 \pm 0.023$ corresponding to a deviation from unity at 98.6% C.L., which is called the Reactor Antineutrino Anomaly (RAA). This was confirmed by the recent precision antineutrino flux measurement with the near detectors of Daya Bay [An16a], where a value of $R = 0.946 \pm 0.022$ was obtained relative to the HUBER-MUELLER model.
Possible explanations for this anomaly could for example be erroneous predictions or unknown systematic detector effects. Against the latter stands the fact that different IBD detection methods with different systematic effects were deployed in the experiments, for example only detecting the IBD neutron (e.g. Rovno integral type σ_{IBD} measurements), detecting positron and neutron in Li-(or Gd-)doped liquid scintillator or detecting IBD neutrons in ^{3}He-filled proportional

counters. An argument against the deficit being only caused by erroneous predictions is that the anomaly was observed with comparable magnitude at reactors with HEU fuel (difference to a pure ^{235}U spectrum <1.5%) and reactors with mixed fuel. Another explanation could be oscillations towards one (or more) sterile neutrinos with $|\Delta m^2_{\text{new}}| \sim 1\,\text{eV}^2$. For kinetic energies of 2-10 MeV the resulting oscillations would be at the meter scale and would be averaged out at distances $> 15\,\text{m}$, causing only a global deficit in the flux, especially for an extended source such as the core of a power reactor. In order to investigate this possibility MENTION *et al.* performed an analysis based on a 3+1 neutrino scheme, assuming a $|\Delta m^2_{\text{new}}| \gg 10^{-2}$. In the short baseline approximation, where the oscillations driven by the atmospheric and solar mixing angles are negligible ($L < 100\,\text{m}$), the electron antineutrino survival probability is given as [dG09]:

$$P_{ee} = 1 - \cos^4\theta_{\text{new}} \sin^2(2\theta_{13}) \sin^2\left(\frac{\Delta m^2_{31} L}{4E_{\bar{\nu}_e}}\right) - \sin^2(2\theta_{\text{new}}) \sin^2\left(\frac{\Delta m^2_{\text{new}} L}{4E_{\bar{\nu}_e}}\right) . \tag{2.12}$$

The most stringent limit on the new oscillation parameters originates from the Bugey-3 experiment [Ach95]. Two neutrino detectors had been installed at 15 m and 40 m distance from a $2.8\,\text{GW}_{\text{therm}}$ power reactor. Based on the ratio of the spectra of the two detectors, which shows no shape distortion, the oscillation parameters can be excluded in $0.06 < \Delta m^2_{\text{new}} < 1\,\text{eV}^2$ for $\sin^2(2\theta_{\text{new}}) > 0.05$. To obtain stronger limits the 19 selected SBL experiments were analysed in a combined analysis. For this purpose correlations between single experiments, which for example have been performed with the same detector or at the same reactor have been taken into account. Then a raster scan was performed in the Δm^2 - $\sin^2(2\theta)$ plane where for each set of oscillation parameters the expected rates in the experiments were simulated. In this way certain parameter ranges which disagree with the experiments can be excluded at a given confidence level, see Fig. 2.8. Combining the data of all considered reactor oscillation experiments the no-sterile-oscillation hypothesis is disfavoured at 96.5% C.L., with $\Delta m^2_{\text{new}} > 0.23\,\text{eV}^2$ and $0.02 < \sin^2(2\theta_{\text{new}}) < 0.21$.

Although the RAA alone does not clearly prove the existence of sterile neutrinos, even so the analysis was performed with the underestimated uncertainties in the reactor spectra predictions, there is a similar anomaly, observed in the calibration runs of the gallium solar neutrino experiments GALLEX and SAGE with strong radioactive sources, which could be explained by the same oscillation behaviour. Another anomaly not fully resolved is an event deficit in the MiniBooNE neutrino beam experiment. Both effects are described in the following sections.

2.2.1 The Gallium Anomaly

From 1990 onward two gallium-based experiments were measuring the low energy solar neutrino flux: SAGE (Russian (Soviet)-American Gallium Experiment) and GALLEX (GALLium EXperiment, 1991-1997) with its successor collaboration GNO (Gallium Neutrino Observatory, 1997-2003). Their aim was to measure the neutrino flux originating from the proton-proton fusion in the sun $p + p \rightarrow {}^2\text{H} + e^+ + \nu_e$ which produces about 90% of the sun's neutrinos but with energies below 420 keV. One possibility to probe such low energies is the reaction

$$^{71}\text{Ga}(\nu_e, e^-)^{71}\text{Ge}, \tag{2.13}$$

with a threshold of 233 keV. The experiments used large masses of gallium as target, 30 t gallium as $GaCl_3$-HCl in GALLEX/GNO and about 50 t metallic gallium in SAGE. The product of reaction (2.13), ^{71}Ge, is an unstable isotope and decays via electron capture back to ^{71}Ga with a halflife of 11.43 d. In regular intervals it is chemically extracted from the detection volume, synthesised into germane (GeH_4) and finally directly added to the counting gas in a proportional counter to measure the activity and determine the production rate.
In order to calibrate the detector response GALLEX and SAGE performed each two series of dedicated runs where intense ^{51}Cr and ^{47}Ar sources (∼PBq) were placed near the center of

the detectors [Ham98, Kae10], [Abd99, Abd06, Abd09]. Both isotopes decay only via electron capture, emitting several monoenergetic neutrinos at energies around 750 keV and 430 keV and around 810 keV, respectively.

The cross section for the detection reaction (2.13) has been calculated by several authors. For the analysis of the experiments the values of BAHCALL [Bah97] were used. The ground state to ground state cross section of reaction (2.13) can be calculated with good precision from the measured rate of the inverse process, the electron capture decay of ^{71}Ge. But in general also excited states of ^{71}Ge can contribute to the reaction. Information on those was inferred from $^{71}\mathrm{Ga}(p,n)^{71}\mathrm{Ge}$ measurements [Kro85] which yield large uncertainties especially for the lowest excited states of ^{71}Ge, which are the most important for the reaction cross section of (2.13). However, the total contribution of excited states in the source runs is only 5% [Bah97]. Based on these cross section calculations the ratios R of measured and expected Ge-production rates are:

$$\begin{aligned} R_{\mathrm{Cr1}}^{\mathrm{GALLEX}} &= 0.95 \pm 0.11 \text{ [Kae10]} & R_{\mathrm{Cr2}}^{\mathrm{GALLEX}} &= 0.81^{+0.10}_{-0.11} \text{ [Kae10]} \\ R_{\mathrm{Cr}}^{\mathrm{SAGE}} &= 0.95 \pm 0.12 \text{ [Abd99]} & R_{\mathrm{Ar}}^{\mathrm{SAGE}} &= 0.79^{+0.09}_{-0.10} \text{ [Abd06]} \end{aligned} \tag{2.14}$$

with an overall average of

$$R^{\mathrm{Ga}} = 0.87 \pm 0.06 \text{ [Kae10]} \tag{2.15}$$

which deviates about 2.2σ from unity. Under the hypothesis that this deficit is also caused by oscillations to sterile neutrinos MENTION *et al.* [Men11] performed a fit of the source experiments, using Eq. (2.12) without the θ_{13}-driven oscillation, given the short average baselines of $\langle \mathrm{L} \rangle_{\mathrm{GALLEX}} = 1.9\,\mathrm{m}$ and $\langle \mathrm{L} \rangle_{\mathrm{SAGE}} = 0.6\,\mathrm{m}$ [Giu12]. The obtained oscillation parameters are $\Delta m^2_{\mathrm{new}} > 0 - 3\,\mathrm{eV}^2$ and $\sin^2_{\mathrm{new}}(2\theta) \sim 0.26$, which is in agreement with the reactor antineutrino anomaly, assuming CPT conservation.

2.2.2 Combined Analysis of the RAA and Ga-Anomalies

Given the good agreement of the individual studies of the Ga and RAA anomalies MENTION *et al.* [Men11] performed a combined analysis. The Ga-anomaly alone excludes the no-sterile-oscillation hypothesis at 96.1% C.L., comparable to the RAA result of 96.5% C.L. The combined analysis, however, sets stronger limits of $\Delta m^2 > 1.45\,\mathrm{eV}^2$ and $0.05 < \sin^2(2\theta) < 0.22$ excluding the no-sterile-oscillation hypothesis at 99.7% C.L. The allowed parameter space in the $\Delta m^2 - \sin^2(2\theta)$-plane for the combined analysis is shown in Fig. 2.8.

2.2.3 Other Anomalies and Current Searches

A first anomalous behaviour was observed by the Liquid Scintillator Neutrino Detector (LSND) [Agu01] which was a short baseline neutrino beam experiment, running in the 1990s. The detector was a 167 t liquid scintillator volume equipped with PMTs for signal readout. To produce neutrinos a $\sim 800\,\mathrm{MeV}$ proton beam was focussed on a target, where at these energies mainly π^+/π^- are produced. Negative pions are largely stopped and absorbed in the beamstop. Positive pions can propagate and decay. The neutrino production channels are then $\pi^+ \to \mu^+ + \nu_\mu$ and $\mu^+ \to e^+ \nu_e \bar{\nu}_\mu$. In the detector at about 30 m distance from the target an excess of IBD events with prompt energies of 20-60 MeV was observed. Given that the main neutrino production channels do not produce $\bar{\nu}_e$ this excess could be explained by $\bar{\nu}_\mu \to \bar{\nu}_e$ oscillations with a Δm^2 in 0.2-10 eV^2 [Agu01].

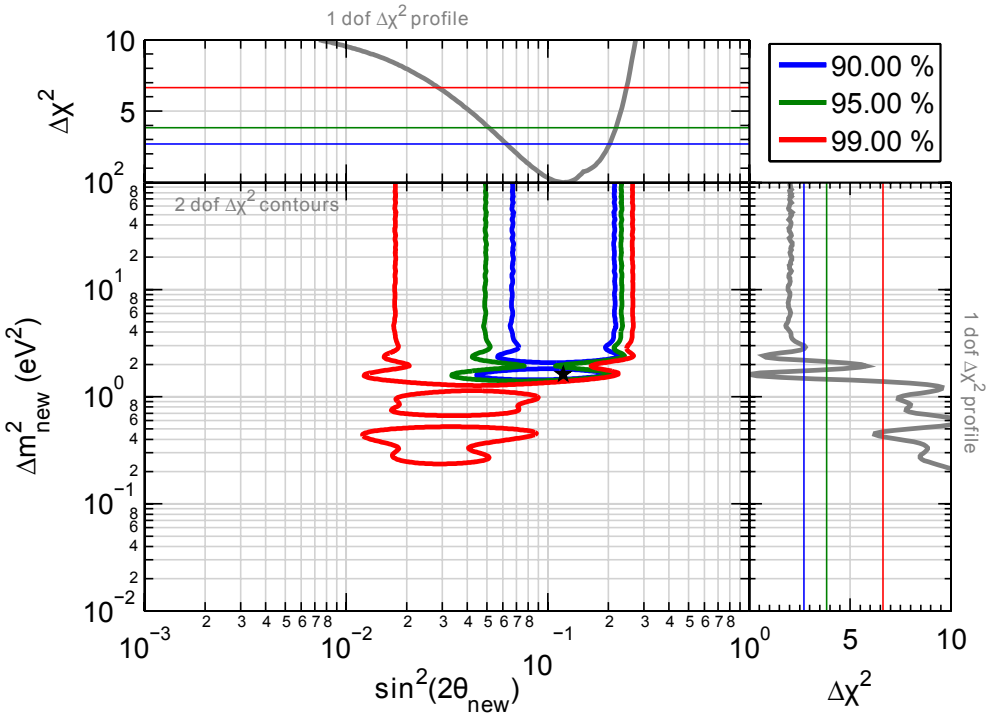

Figure 2.8: Allowed parameter space and marginal χ^2 distributions for an oscillation to sterile neutrinos for different confidence levels of exclusion, obtained from a combined analysis of the reactor and gallium anomalies. The best fit point is denoted by a star. From [Men11].

This observation could neither be confirmed nor definitely excluded by other experiments at the time. In order to solve this question the MiniBooNE experiment was build. The detector was a 800 t mineral oil volume with PMT readout at 540 m from the target. Neutrinos were produced by focussing a 8 GeV proton beam on a target and guiding the produced charged pions and kaons into a 50 m long decay tunnel where they could decay in flight. The higher energy of the produced neutrinos allowed for the longer baseline. MiniBooNE performed an oscillation analysis in the $\bar{\nu}_\mu \to \bar{\nu}_e$ and $\nu_\mu \to \nu_e$ channels. Neutrinos were detected in charged current interactions. In both channels an excess of $\overset{(-)}{\nu}_e$ induced signals was observed [AA13]. The excess is more significant in the $\bar{\nu}_\mu \to \bar{\nu}_e$ channel. The best antineutrino fit yields $\Delta m^2 = 0.043\,\mathrm{eV}^2$, $\sin^2(2\theta) = 0.88$, but parameters in the range up to $\Delta m^2 = 0.8\,\mathrm{eV}^2$, $\sin^2(2\theta) = 0.004$ are nearly equally likely. This oscillation would include two components of the unitary rotation matrix (extended PMNS matrix, see Sec. 1.2) describing the oscillations: $\sin^2(2\theta) = 4|\mathbf{U}_{e4}|^2|\mathbf{U}_{\mu 4}|^2$.

In recent years many results of searches for sterile neutrinos have been published e.g. by MINOS [Ada16], Daya Bay [An16b] and IceCube [Aar16]. The Daya Bay analysis is based on a relative comparison of the antineutrino spectra and rates in the three experimental halls and is sensitive to $\sin^2(2\theta_{14})$. The results improve the exclusion of oscillation parameters with respect to the Bugey-3 results [Ach95] only for $\Delta m^2 \lesssim 0.2\,\mathrm{eV}^2$.

The IceCube experiment, a neutrino telescope at the South Pole, performed a search for sterile neutrino signatures in data of charged current interactions of (upward going) atmospheric muon neutrinos in the energy range 320 GeV to 20 TeV. By crossing the Earth muon antineutrinos would experience a strongly enhanced oscillation due to resonant matter effects. This would differ for different path lengths through the Earth. By scanning over various zenith angles without finding any indication for an anomalous $\overset{(-)}{\nu}_\mu$ disappearance, a parameter space which extends to $\sin^2(2\theta_{24}) \leq 0.02$ at $\Delta m^2 \sim 0.3\,\mathrm{eV}^2$ is excluded [Aar16]. Assuming a global best-fit value at the time of $|\mathbf{U}_{e4}|^2 = 0.023$ [Kop13], also the oscillation parameter space proposed to explain the MiniBooNE excess is disfavoured.

Following these findings COLLIN *et al.* performed a global analysis to set first constraints on all entries of the 3+1 mixing matrix [Col16]. The range of mass splittings considered is $0.1 < \Delta m^2 < 100\,\mathrm{eV}^2$. The fit takes into account short baseline neutrino beam experiments, Bugey [Ach95] as reactor neutrino experiment, the Gallium Experiments and the aforementioned results of IceCube. This global analysis strongly limits the possible parameter space for a sterile-neutrino mass splitting to a narrow region around 1-2 eV^2, where the RAA best-fit value is still compatible.

2.2.4 Cosmological Limits on Sterile Neutrinos

The evolution of the early universe depends on the effective number of (neutrino) species which can be thermally excited, also called relativistic degrees of freedom N_{eff}. Those have an impact on the speed of the expansion of the universe and thus on the freeze-out of other particles (e.g. big bang nucleosynthesis) and the formation of cosmological structures. In return, from information about the evolution of the universe it is possible to set constraints on N_{eff}. During the last years the Planck satellite precisely mapped the cosmic microwave background, the remaining radiation from the moment when the universe became transparent for electromagnetic radiation. From a recent Planck data analysis [Pla16] the parameter is determined as $N_{\mathrm{eff}} = 3.15 \pm 0.23$. Already the three known active neutrino flavours require a value of 3, which would prohibit further neutrino types. In literature several theories exist explaining how sterile neutrinos could nevertheless be accommodated. One starting point is that the Planck result is based on the assumption that all neutrino types have been fully thermalised at the time of decoupling. For example a particle-antiparticle asymmetry, which is not ruled out for neutrinos, could have prevented this [Han12, Sav13]. Another hypothesis is a new gauge boson which also couples to sterile neutrinos. This could allow for sterile neutrino interactions and, depending on the interaction strength, delay their thermalisation, resulting in only a fractional relativistic degree of freedom in the early universe [Han14].

2.2.5 Study on Reactor Antineutrino Flux Evolution at Daya Bay

The Daya Bay experiment provides the most precise direct reactor antineutrino spectrum measurements to date, as described before in Sec. 2.1.5. Recently a study was performed, investigating the variation of the antineutrino flux and spectrum in dependence of the reactor fuel composition [An17c]. Since the beginning of data taking multiple fuel cycles have been measured for each of the six power reactors which are used as antineutrino sources. The effective fission fractions seen by each of the four near antineutrino detectors is the weighted sum over the fission fractions of all six reactors, taking into account the distance and the mean survival probability of the neutrinos. The values are identical within $< 0.1\%$ for the detectors in the same underground hall. The fission fractions change over a reactor cycle, due to the build-up of the plutonium isotopes. Effective ^{239}Pu fission fractions F_{239} between 0.25 and 0.35 have been measured with in total $2.2 \cdot 10^6$ IBD events. The averaged total IBD event yield $\bar{\sigma}_f$ shows a deficit of 5.1% with respect to the HUBER-MUELLER model, which is consistent with the RAA. For a more detailed analysis the data was grouped in eight bins with respect to F_{239} and the dependence of the neutrino flux was studied. A first investigation was the evolution of the total IBD yield

$$\sigma_f = \sum_\alpha F_\alpha \sigma_\alpha \ , \quad \alpha = (\ ^{235}\mathrm{U},\ ^{238}\mathrm{U},\ ^{239}\mathrm{Pu},\ ^{241}\mathrm{Pu}) \tag{2.16}$$

as a function of F_{239}. It was found that σ_f decreases with increasing contribution of ^{239}Pu, which is expected from the predicted spectra, see Fig. 2.2, but the change is less pronounced than predicted by the HUBER-MUELLER model, see Fig. 2.9. The predicted slope $\mathrm{d}\sigma_f/\mathrm{d}F_{239}$ differs by 3.1σ from the measurements. In order to investigate the origin of this discrepancy a χ^2 test of Eq. (2.16) over the eight F_{239} bins was performed. The results of this, shown in Fig. 2.10, show an agreement within uncertainties of σ_{239} for the data set and the HUBER-MUELLER model, but a σ_{235} value which is lower by 7.8% (compared to 2.7% experimental

uncertainty). The spectral shape evolution in dependence of F_{239} was found to be consistent with the HUBER-MUELLER model. Based on this analysis the hypothesis that the RAA is caused solely by an overprediction of the ^{235}U flux is favoured over the hypotheses of an equal deficit in all isotopes, which would be the case if sterile neutrino oscillations would cause the RAA, or an ^{239}Pu-only deficit by 2.8σ and 3.2σ, respectively [An17c].

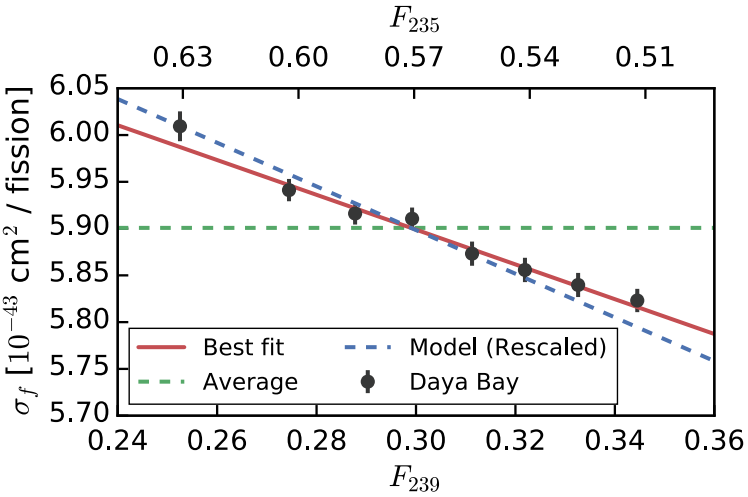

Figure 2.9: Average total IBD yield σ_f in dependence of the ^{239}Pu (lower axis) or ^{235}U (upper axis) fission fraction. The errorbars include only statistical uncertainties, which are dominating. The lines represent best fits for a constant yield (green), a variable yield (red) and the predicted evolution from the HUBER-MUELLER model (blue), rescaled for the difference in the total yield. From [An17c].

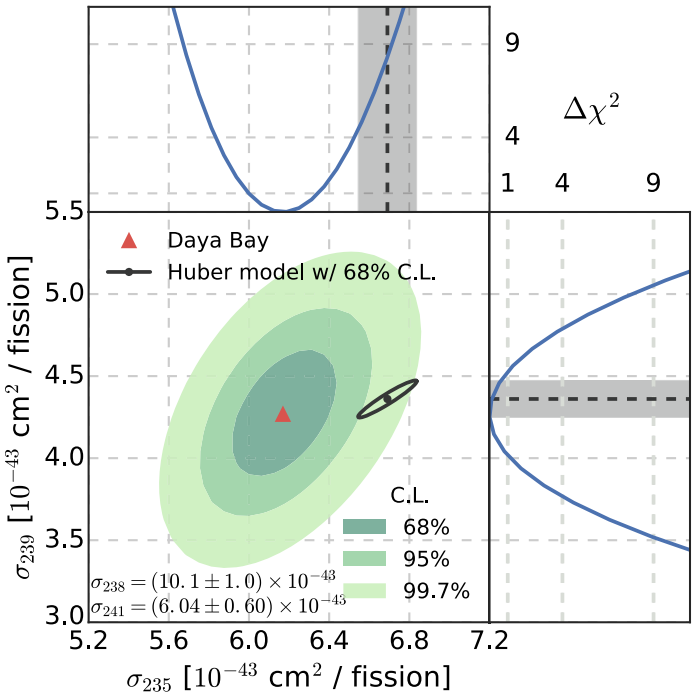

Figure 2.10: Combined evaluation of the IBD yields per fission of ^{235}U and ^{239}Pu, σ_{235} and σ_{239}. The red triangle marks the best fit point, the green contours the 1σ, 2σ and 3σ allowed regions. The minor fission isotopes ^{238}U and ^{241}Pu were weakly constraint to the predictions of the HUBER-MUELLER model, given in the lower left panel. The predictions for ^{235}U and ^{239}Pu and the 1σ allowed ranges are shown as black contours. The side panels show the marginal χ^2 profiles. While σ_{239} is in agreement between predictions and measurements σ_{235} deviates by 7.8%. From [An17c].

The strong disagreement of measurements and predictions for the ^{235}U IBD yield shows that the RAA is at least partially caused by an overprediction of reactor antineutrino fluxes. However, this measurement alone is not decisive yet on whether ^{235}U is the only source of the anomaly and experiments at reactors running with HEU fuel, with $F_{235} \sim 1$, can help to strengthen this analysis. In order to decisively address the question of sterile neutrino oscillations, which are not ruled out by these findings, a direct measurement of the L/E dependence of the neutrino flux at short baselines is required. If the spectra are measured over different baselines the hypothesis of short baseline oscillations can be addressed independently of any flux predictions. The current experiments directly investigating the RAA at short baselines are described in the next section.

2.2.6 Experiments investigating the RAA

Neutrino Detection

The electron antineutrinos emitted from the reactor core are detected via the inverse beta decay (IBD) on (quasi-)free protons (hydrogen nuclei)

$$\bar{\nu} + \mathrm{H}^+ \rightarrow e^+ + n \ . \tag{2.17}$$

Considering the mass difference in the initial and final state of Eq. (2.17) a minimum neutrino energy is required for the reaction, which in the rest frame of the proton amounts to:

$$\frac{(m_n + m_{e^+})^2 - m_p^2}{2m_p} = 1.806\,\mathrm{MeV} \ . \tag{2.18}$$

The IBD has a two-particle final state and given the large mass ratio of the positron and neutron the positron will obtain virtually all kinetic energy of the neutrino minus the threshold energy. The detectable prompt energy in a large detector on the other hand includes also the positron annihilation with an electron of the detector medium, thus, when neglecting the neutron recoil

$$E_{\mathrm{prompt}} \simeq E_{\bar{\nu}} - 1.806\,\mathrm{MeV} + 2m_e \simeq E_{\bar{\nu}} - 0.782\,\mathrm{MeV} \ . \tag{2.19}$$

The expected neutrino spectra, see Fig. 2.2, above the IBD threshold of 1.8 MeV decrease rapidly with energy up to $\sim$ 10 MeV, with negligible higher energetic contributions. The IBD cross section on the other hand increases with $\sim E^2$, Eq. (2.9). The detectable neutrino energy spectrum results from the convolution of the emitted spectrum with the cross section. It rises from the threshold at 1.8 MeV to a maximum at around 3.5 MeV and then decreases with a high energy tail up to $\sim$ 10 MeV, see Fig. 2.11.

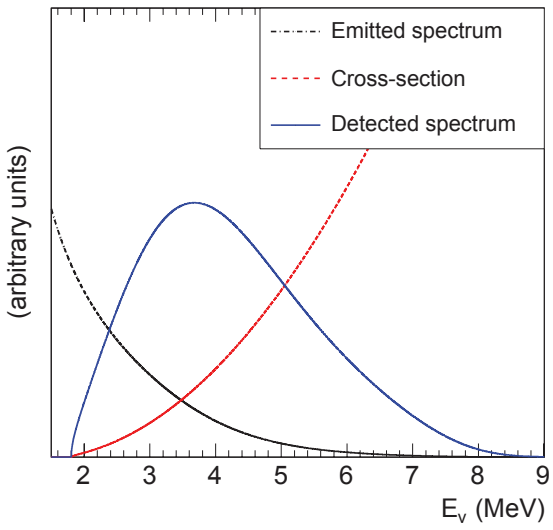

Figure 2.11: The detectable neutrino energy distribution in reactor neutrino experiments (blue, solid line) results from the convolution of the emitted neutrino spectrum (black, dash-dotted line) with the IBD cross section (red, dashed line. From [Mue11].

Different methods are used for the detection of the positron and the neutron produced in the IBD. For the positron detection usually plastic or liquid scintillators are deployed, as those can easily and comparatively inexpensively be produced in large quantities and contain a large number of hydrogen atoms as IBD targets. In principle the positron alone carries all information about the neutrino flux and spectra, but the coincident detection of the neutron helps to strongly suppress the background. The neutrons need some moderation time, in the order of microseconds, before they can be detected via a capture on an isotope with a high reaction cross-section, commonly ^{3}He, ^{6}Li or Gd. ^{3}He undergoes the reaction

$$^3\mathrm{He} + n \rightarrow\ ^3\mathrm{H} + p + 764\,\mathrm{keV}\ , \tag{2.20}$$

with a cross-section for thermal neutrons of $\sigma_{\mathrm{therm}}^{\mathrm{He\text{-}3}} = 5.3\,\mathrm{kbarn}$ [END17]. As helium is a noble gas it cannot directly be dissolved in the scintillator. For this reason ^{3}He-containing gas proportional counters in form of tubes or planar multi-wire chambers, interlaced with the scintillating volume have been used in some experiments. This implementation of distinctive neutron and positron detection volumes may lead to lower total detection efficiencies, due to the large surface to volume ratio of the individual detector parts, and longer neutron drift times, which in return requires longer coincidence time windows and increases the rate of accidental coincidences of background events.

^{6}Li has a high thermal neutron cross-section of $\sigma_{\mathrm{therm}}^{\mathrm{Li\text{-}6}} = 0.94\,\mathrm{kbarn}$ [END17] for the reaction

$$^6\mathrm{Li} + n \rightarrow \alpha +\ ^3\mathrm{H} + 4.79\,\mathrm{MeV}\ . \tag{2.21}$$

As both reaction products have a high ionising power and thus short ranges it is favourable to use the ^{6}Li either in a surface coating in contact with a scintillator or directly bound in the scintillator. The latter can be achieved either as Li-doping of an anorganic scintillator, e.g. as ^{6}LiF:ZnS(Ag) as deployed in SoLiD, see below, or by dissolving a Li-complex in a liquid scintillator, e.g. used in PROSPECT, see below. The high ionising power can be exploited by use of scintillators which have a pulse shape discrimination capability for this type of events.

Natural gadolinium contains two isotopes with very high neutron capture cross-sections, ^{155}Gd and ^{157}Gd. Their relevant properties are listed in Table 2.3. After neutron capture energy of about 8 MeV is emitted via γ-ray cascades. A 2 MeV γ-ray in a typical liquid scintillator (density $\sim 0.9\,\mathrm{g/cm^3}$, $N_{\mathrm{C}}/N_{\mathrm{H}} \sim 1.2$) has a mean free path of 23 cm. This can be an advantage when the Gd is component of a surface coating, e.g. in DANSS, as the γ-rays can easily reach the detection volume. On the other hand there is the disadvantage that a larger volume is required to detect the full energy of the reaction than e.g. for ^{6}Li, which can lead to a reduced detection efficiency.

Table 2.3: Properties of the Gd isotopes relevant for neutron detection. Data from [END17].

Isotope	Abundance [%]	$\sum E_\gamma$ [MeV]	σ_{therm} [kbarn]
^{155}Gd	14.80	8.54	60.7
^{157}Gd	15.65	7.94	252.9

To investigate the RAA experimentally some requirements have to be considered for the reactor and the detector layout and performance. A detailed study of the impact of the most important parameters can be found in [Hee13] and is briefly summarised here. The important reactor characteristics for this type of studies are:

(i) *Accessibility.–* With an expected $\Delta m^2_{\mathrm{new}}$ around 1 eV and reactor neutrino energies of $\mathcal{O}(1)$ MeV the resulting oscillation lengths are on the scale of a few meters, which requires access at baselines of ≤ 10 m.

(ii) *Reactor power.–* A high reactor power is an advantage as the total neutrino flux is proportional to it. This can help to achieve a good signal to background ratio and good total statistics.

(iii) *Core dimensions.*– A compact fuel element is favourable, to avoid that the source point distribution, which is assumed to be homogeneously distributed over the reactor fuel, washes out the oscillation signal. This makes research reactors with a generally compact design a preferential choice compared to commercial reactors.

(iv) *Duty cycle.*– While a high duty cycle allows to gain the required statistics in a shorter period, shutdowns allow to disentangle reactor related background and to measure the cosmic background distribution.

(v) *Fuel type.*– Some research facilities are operated with HEU fuel. This limits the fissioning isotopes to ^{235}U, which has the smallest uncertainties in the neutrino flux predictions and avoids uncertainties from the fission fraction determination. Furthermore the use of HEU fuel also allows to investigate the origin of the neutrino spectrum distortion around 5 MeV, as described in Section 2.1.5.

The important features of the detector design are:

(i) *Fiducial mass.*– The number of IBD events is proportional to the number of free target protons.

(ii) *Detector length.*– Length or displacement allow to measure over a large fraction of one expected antineutrino oscillation length, which increases the sensitivity for small amplitudes ($\sin^2\theta_{\text{new}}$) or longer oscillation lengths (Δm^2). In addition if measurements are performed at different baselines the ratio of spectra allows to constrain the oscillation parameters independently from flux predictions.

(iii) *Detector cross-section.*– The cross-section facing the neutrino source defines the count rate per position bin in the radial direction.

(iv) *Position and energy resolution.*– In order to resolve the expected oscillation pattern the spatial resolution, by vertex reconstruction or subdivision of the detector, should be in the range of a few tens of centimeters. The energy resolution should be about 10% or better for the energy range of interest (∼2-8 MeV), which has been reached before [Kwo81, Ach95], in order to reach the highest sensitivities. On the other hand the spatial resolution does not need to be significantly smaller than the extension of the source.

(v) *Signal to background ratio.*– The signal rate should at least be at about the same magnitude as the background rate, since otherwise the oscillation signature may be washed out by statistical background fluctuations.

(vi) *Cosmic background.*– All experiments in the vicinity of a reactor will be near-surface experiments with a high cosmic background. This may be countered by site specific overburdens (e.g. reactor building) or installation of adequate veto systems.

(vii) *Detector materials.*– The experiments have to be located in the proximity of a reactor which may limit the choice of usable materials (i.e. with respect to fire hazard) and may also limit the total mass which can be installed for the detector and shielding.

In the following paragraphs the experiments currently running or in preparation to investigate the RAA are briefly presented. The STEREO experiment will be discussed in detail in the next chapter. A summary of the most relevant experiment characteristics is given in Table 2.4.

SOX

Apart from nuclear reactors also strong isotopic β sources with PBq activities can be used for neutrino experiments. This has been successfully proven by the calibration runs of GALLEX and SAGE, see Section 2.2.1. One project of this type currently under preparation addresses Short-distance neutrino Oscillation with BoreXino (SOX) [Bel13, Cam16]. The Borexino detector at

the Laboratori Nazionali del Gran Sasso (LNGS) in Italy is an ultra low background detector originally designed for solar neutrino measurements with the capability to detect ν_e and $\bar{\nu}_e$. It is running since 2007 and is therefore a well understood system. The detector consists of several concentric spheres. The inner sphere of nylon has a radius of 4.25 m and contains about 280 t of ultra radiopure liquid scintillator. This is the target for the Borexino measurements. It is placed within a buffer volume of mineral oil doped with a light quencher. This serves as shielding against external radiation and should not scintillate itself. It is contained in a stainless steel vessel which also supports the 2212 PMTs for the light measurement. The buffer volume is subdivided into an inner and an outer volume by a nylon sphere of radius 5.5 m. One proposition for SOX is to add a scintillating liquid to the inner buffer volume to increase the target volume. The stainless steel sphere is placed in a dome of water which serves as passive shielding and muon veto. In the current target volume Borexino reaches a spatial resolution of ∼10 cm and an energy resolution of $\sigma_E/E = 5\%$ at 1 MeV. The original design of Borexino includes already a small tunnel under the outer water dome, which allows for source deployments directly under the center of the detector at a distance of 8.25 m to the detector center. This means that the target sphere (target + inner buffer sphere) covers a baseline of 4-12.5 m (2.75-13.75 m). In a first run a ^{144}Ce-^{144}Pr source will be used. ^{144}Ce has a long halflife of 296 d (Q_β =320 keV) which gives time for the source production and transport. The daughter isotope ^{144}Pr decays with $T_{1/2} = 17.3$ min and $Q_\beta = 3.0$ MeV which delivers the $\bar{\nu}_e$ of interest. In a possible second run a ^{51}Cr source, $T_{1/2} = 27.7$ d, $Q_{\mathrm{EC}} = 753$ keV, may be deployed, emitting ν_e. The source activities at this distance need to be in the order of 10 PBq. Possible analysis principles are a neutrino event rate comparison between experiment and predictions and an oscillation search throughout the detector volume, exploiting the good spatial resolution. While for SOX the detector is already available the main difficulty is the fabrication and transport of the sources. The beginning of data taking is planned for 2018.

DANSS

DANSS (Detector of the reactor AntiNeutrino based on Solid Scintillator) [Ale16] is a highly segmented plastic scintillator detector at a 3 $\mathrm{GW_{therm}}$ commercial power reactor in Kalinin, Russia. One major design goal was to avoid materials with high toxicity and flammability such as many liquid organic scintillators, to allow for usage near a power reactor. The detector is located underneath the reactor pool, viewing an extended reactor core of a height of 3.5 m and a diameter of 3.1 m from a distance of 10-12 m. The location provides a comparatively large overburden of ∼50 mwe, reducing the muon flux by about a factor of 6. The whole detector of about $1 \times 1 \times 1\,\mathrm{m}^3$ is mounted on a liftable platform and measures the neutrino flux at three heights, 10 m, 11 m and 12 m below the core. The position is changed once per day in order to reduce systematic effects from the reactor burnup. The analysis for the oscillation search is based on the ratio of the spectra of the three heights.
The detector is build up from scintillator strips of $1 \times 4 \times 100\,\mathrm{cm}^3$. These are coated with a white, reflective layer, doped with 6% Gd oxide, which amounts to $0.35\%_{\mathrm{wt}}$ of Gd with respect to the full detector. The strips are arranged in layers of alternating orientation. For light collection each strip has three grooves over the full length where optical fibres doped with wavelength shifters are installed. One of the fibres is read by an individual silicon photomultiplier, to allow for spatial event reconstruction, the other two are bundled for modules of 5×10 (width × height) parallel strips and coupled to a standard photomultiplier tube, for the energy measurement. The energy resolution is dominated by the light collection through the fibres and is given as $\sigma/E = 16\%$ at 1 MeV.
Each layer of scintillator strips is supported by a copper frame of about 5 cm thickness, which also constitutes the innermost shielding layer. The setup is enclosed in a sandwich of 8 cm borated polyethylene (BPE), 5 cm lead and 8 cm BPE. The outer BPE is supposed to stop residual neutrons from the reactor, the inner layer to stop neutrons from muon spallation in the lead. An active muon veto consisting of a sandwich of two 3 cm plastic scintillators, operated in coincidence, is added on top and on all four sides. The detector concept was tested with a prototype

detector, build with two 50-strip modules. The general functionality could be demonstrated and already a signal to background ratio of ∼1 was achieved. The high granularity of the full scale detector with 50 modules should allow for a good signal and background separation based on event topology. It was installed on site and data taking started in early 2016. Given the short baseline and high reactor power a rate of about 5000 IBD events per day is recorded.

Neutrino-4

Neutrino-4 is an experiment at the Russian SM-3 reactor [Ser13, Ser17]. This is a very compact ($35 \times 42 \times 42\,\mathrm{cm}^3$), 90 MW reactor using HEU fuel. The neutrino detector is a Gd-loaded (0.1%) liquid scintillator with a total volume of $3\,\mathrm{m}^3$, divided in 10×5 vertical sections (length × width) with a $22.5 \times 22.5\,\mathrm{cm}^2$ cross section. It is installed on a movable platform and can access baselines from 6 m to 11 m. The detector is at surface level with about 4-12 m overburden from the reactor building, depending on the direction. The liquid scintillator is not tuned to provide a pulse shape discrimination capability between weakly, e.g. IBD positron, and strongly ionising particles, e.g. recoil nuclei created by fast neutron background. Instead the target volume is segmented in order to identify positron events by the event topology of the two opposedly emitted 511 keV γ-rays from the positron annihilation. This is estimated to be applicable for $\sim 30\%$ of the expected ∼1000 neutrino signals per day. For background reduction a passive shielding of 1 cm of steel, 6 cm of lead and 16 cm of BPE with a total weight of 60 t was build around the full accessible measurement range. In addition an active muon veto was installed, consisting of three layers of 12 cm thick plastic scintillators, on top of the passive shielding and above and below the detector, inside the shielding. The main principle of operation is the measurement of the $1/r^2$ dependence of the neutrino flux over the accessible range of 6-11 m from the core and a possible deviation in case of oscillations to sterile neutrinos. In addition rate comparisons between predictions and measurements over the full length are planned. The data taking with the full size detector started in summer 2016. First results of a prototype [Ser15] and the full detector [Ser17] do not show a significant deviation from the $1/r^2$ dependence, but are at the moment limited by statistics.

PROSPECT

An experiment in preparation is the Precision Reactor Oscillation and Spectrum Experiment, PROSPECT [Ash16], located at the High Flux Isotope Reactor (HFIR) of the Oak Ridge National Laboratory (ORNL), USA. This HEU fuelled research reactor has a fuel element with a diameter of about 40 cm and a height of about 50 cm and runs at $85\,\mathrm{MW}_{\mathrm{therm}}$. The detector design is intended to minimise the hazards emanating from the detector materials to allow utilisation in a reactor environment. Extensive tests were performed and finally a low toxicity, high flashpoint liquid scintillator was developed, which could be doped with ^{6}LiCl to shorten neutron capture times while still preserving a pulse shape discrimination capability for weakly and strongly ionising particles. A detector is designed with a target volume of $120 \times 175 \times 150\,\mathrm{cm}^3$, containing about 3000 l of liquid scintillator. This volume is divided by low mass, reflective optical separators into 120 cells of $120 \times 15 \times 15\,\mathrm{cm}^3$. Each cell has a two-sided PMT readout. The separators and PMTs with special housings are fully immersed in the scintillator volume. The separation in cells allows for a good spatial resolution in two dimensions and the arrival time delay of the scintillation light at the PMTs within one cell allows for a 5 cm position resolution along the length of the cells. The reaction $^6\mathrm{Li}(n,t)^4\mathrm{He}$ produces two highly ionising particles which deposit their energy very locally and can be identified by pulse shape discrimination. The energy resolution with prototypes has been proven to reach $\sigma/E = 4.5\%$ at 1 MeV.
The 3000 l-detector will be a near detector, deployed at different positions between 7-12 m from the core and will probe the allowed parameter space of the RAA with $> 3\sigma$ significance over three years of measurements. The expected signal to background ratio is ≥ 1. The commissioning is scheduled for 2017. In addition a second detector with the same structure but three times larger is planned. It could be installed as a far detector at 15-19 m baseline and should allow

to probe the allowed parameter space at $> 5\sigma$. Its preparation and installation may depend on the results of the first detector.

SoLid

A 'Short baseline Oscillation search with a Lithium-6 Detector' is performed by the SoLid collaboration at the BR2 research reactor in Belgium [Ryd15]. The reactor has a cylindrical HEU fuel element with a diameter $< 50\,\text{cm}$ and a power of $70\,\text{MW}_{\text{therm}}$. The SoLid detector is based on a composite scintillator design. The target consists of 5 cm cubes of polyvinyl toluene (PVT), an organic scintillator. Each cube is in contact with a ^{6}LiF:ZnS(Ag) inorganic scintillator on one face and is wrapped in reflective tyvek sheets to improve the light collection. Wavelength-shifting optical fibres connect and read out the light signal of the cubes in 2D grids. The fibres have a one-sided SiPM readout and a reflective coating on the open end. Positrons from IBD events deposit their kinetic energy mostly in one PVT cube which creates a short (ns) light pulse. The two 511 keV annihilation photons leave only a small amount of additional energy in the vertex cube and can be used for positron event tagging. The neutrons are moderated in the cube and have a 50% chance to be captured on ^{6}Li, causing the reaction $^6\text{Li}(n,t)^4\text{He}$. The reaction products are highly ionising particles, causing the population of long lived ($\leq \mu$s) excited states in the ZnS(Ag), thus allowing for pulse shape discrimination. The possibilities to identify both IBD products by their signature and to use event topologies based on the high granularity of the detector allow for a good background reduction without heavy passive shielding. For the measurement position at the BR2 reactor a signal to background ratio of three is expected. A 288 kg prototype detector with 9 frames each containing 16×16 cubes was installed end of 2014. The shielding consisted only of 9 cm HDPE and plastic scintillator panels above and below the detector as active muon veto. The module was used to prove the working principle, test and develop the readout electronics and develop a software-based event identification. The installation of the full scale detector is planned in two steps. In a first phase a 1.6 t detector has been installed at 5.5-9 m from the core, which started end of 2016. The general design is the same as described above, but with two optical fibres per cube in order to improve the energy resolution, which is anticipated with $\sigma/E = 14\%$ at 1 MeV. In a second phase the detector should be upgraded to a mass of 3 t, spanning the range of 5.5-10 m.

NEOS

NEOS (Neutrino Experiment for Oscillation at Short baseline) [Ko17] is a Korean experiment, located at a $2.8\,\text{GW}_{\text{therm}}$ commercial reactor of the Hanbit power plant. The LEU-based reactor core has a diameter of 3.1 m and a height of 3.8 m. The antineutrino detector is fix centered at 23.7 m distance in a gallery below reactor walls, leading to a minimal overburden of 20 mwe. It is a cylindrical volume of 1 m diameter and a length of 120 cm with a horizontal axis. The target is a single volume of 1 t of Gd-loaded (0.5%) liquid scintillator. The light readout is done on both ends of the cylinder by 19 eight inch PMTs. The inner walls and inter-PMT spaces are layed out with white PTFE plates. The target is enclosed in 10 cm of BPE and 10 cm of lead as passive shielding, completed by 5 cm thick plastic scintillators as muon veto on top and at the sides.
The detector started data taking in early 2016 and first results are published [Ko17]. The measured IBD rate is about $2000\,\text{d}^{-1}$, with a signal to background ratio of 22 and a resolution of $\sigma/E = 5\%$ at 1 MeV. NEOS could confirm the presence of the 5 MeV excess, see Section 2.1.5, but found no evidence for oscillations towards sterile neutrinos. The sensitivity is limited by the extended core and comparatively long baseline, which can partly be compensated by high statistics. The exclusion of parameters could slightly be improved above $\Delta m^2 > 0.2$ with respect to the Bugey-3 results, which before were dominating in this parameter range.

Table 2.4: Summary of the main characteristics of the very short baseline neutrino experiments.

	Reactor Power [MW_{th}]	Core dimensions	Baseline [m]	Det. Type
Sox	Source $\mathcal{O}(10)$PBq	$d \sim h \sim 20\,\text{cm}$	4-12.5 m	LS
DANSS	3 GW (LEU)	$d \simeq 3.1\,\text{m}$, $h \simeq 3.5\,\text{m}$	10-12 m	PS & Gd-layers
Neutrino-4	90 MW (HEU)	$35{\times}42{\times}42\,\text{cm}^3$	6-11 m	LS (Gd)
Prospect	85 MW (HEU)	$d \simeq 40\,\text{cm}$, $h \simeq 50\,\text{cm}$	7-12 m	LS (Li)
Solid	70 MW (HEU)	$d \simeq 50\,\text{cm}$	5.5-9/10 m	PS & Li-layers
NEOS	2.8 GW (LEU)	$d \simeq 3.1\,\text{m}$, $h \simeq 3.8\,\text{m}$	avg.: 23.7 m	LS (Gd)
STEREO	58.3 MW (HEU)	$d \simeq 40\,\text{cm}$, $h \simeq 80\,\text{cm}$	8.9-11.1 m	LS (Gd)

LS - liquid scintillator, PS - plastic scintillator

Chapter 3

STEREO

3.1 The Site

The STEREO experiment (STErile neutrino REactor Oscillation) [Hé16, Lhu12] is located at the Institut Laue Langevin (ILL), Grenoble, France, and is dedicated to investigate the RAA. The general requirements for an experiment of this type are described in Section 2.2.6. This chapter explains how these criteria are met for STEREO. This includes the neutrino source, the experimental site in its final configuration, and the detector itself, whose design, see Sec. 3.2, is adapted to counter site specific challenges as well as to fulfill the general requirements for the investigation of the RAA in the parameter space around the best fit region.

The ILL operates a heavy water moderated research reactor with a nominal power of $58.3\,\mathrm{MW_{therm}}$, run with HEU fuel with $\geq 93\%$ enrichment. A cycle (use of one fuel element) at full reactor power lasts 45 d. The fuel element is compact, cylindric in shape with a diameter of about 40 cm and a height of about 80 cm, and thus provides a good basis for the search for neutrino oscillations with a short oscillation length. The whole reactor assembly is designed in a compact way: moderator vessel, cooling water pool and reactor wall together have a radius of less than 5 m, with the intention to provide a high flux of neutrons through beamtubes to different experiments with few transport losses. One beamtube, named H6-H7, is entirely crossing the reactor pool and hosted gamma ray spectroscopy instruments on either side (called GAMS, or synonymously PN3). One of these instruments has been decommissioned and the area been allocated for STEREO. A map of the site is shown in Fig. 3.2. This allowed to install the neutrino detector at a short baseline, with the sensitive target volume covering a distance of about 8.9-11.1 m from the fuel element. A detailed description of the detector setup is given in Section 3.2.

The area allocated for STEREO, located in the experimental hall of the reactor building, comes with a number of advantages and challenges which are described in the following sections.

3.1.1 Experimental Hall

Apart from providing the required short baseline the STEREO area has the major advantage of an overburden of a concrete channel, filled with water of a height of about 7.5 m which serves as intermediate storage place for spent fuel elements of the reactor. STEREO is not centered under this fuel element transfer channel, but located at one side, leading to an anisotropic cosmic background contribution. The transfer channel together with the reactor building itself provide a shielding of approximately 15 m.w.e. against cosmic background. At sea level (the ILL lies at about 210 m above sea level) the cosmic background is dominated by muons with a flux of about $70\,\mathrm{m^{-2}\,s^{-1}\,sr^{-1}}$ which is a factor $\mathcal{O}(10)$ higher than the hadronic and electron contributions [Pat16]. The latter are largely suppressed by the present overburden. The muon flux for different incident angles has been measured directly on site and outside of the building [Zso16]: at the STEREO site it is reduced by about a factor of 2.7, see Fig. 3.1. Most muons reach Earth's surface as minimum ionising particles with a mean energy of 4 GeV [Pat16], depositing energy

via ionisation at about 2 MeV/cm. Thus a muon crossing directly the detector can be easily identified by its large energy deposition compared to reactor anti-neutrinos ($E_\nu \lesssim 10$ MeV).

More difficult to suppress is the indirect background contribution, mainly via muon spallation, producing free hadrons by electromagnetic or neutral current interactions. The reaction cross section increases with the mass number A of the interaction medium [But01]. Thus especially lead shieldings or (structural) steels in the vicinity of the detector are possible sources. Especially the produced neutrons, having energies of a few MeV, can reach the detector and cause correlated background events in several different ways. One possibility is neutron scattering in the liquid scintillator target, producing a recoil nucleus which serves as prompt event, and subsequent moderation and capture of the neutron, thus mimicking an IBD event. The nuclear recoil of the prompt signal my by identified by pulse shape discrimination (PSD), see Sec. 3.3. In [Zso16] a study based on Geant4 simulations [Ago03] using the Cosmic-ray Shower Library (CRY) [Hag12] was performed, stating that with help of the active muon veto of STEREO, see Sec. 3.2.1, the rate of fast neutron recoil events misidentified as IBD events is reduced to $28 \pm 5\,\mathrm{d}^{-1}$. Other background caused by muon spallation are multineutron events, where several neutrons are created in the same spallation process and are captured after different moderation times within the detector. These events are not identifiable by PSD. The rate of this contribution is currently under investigation.

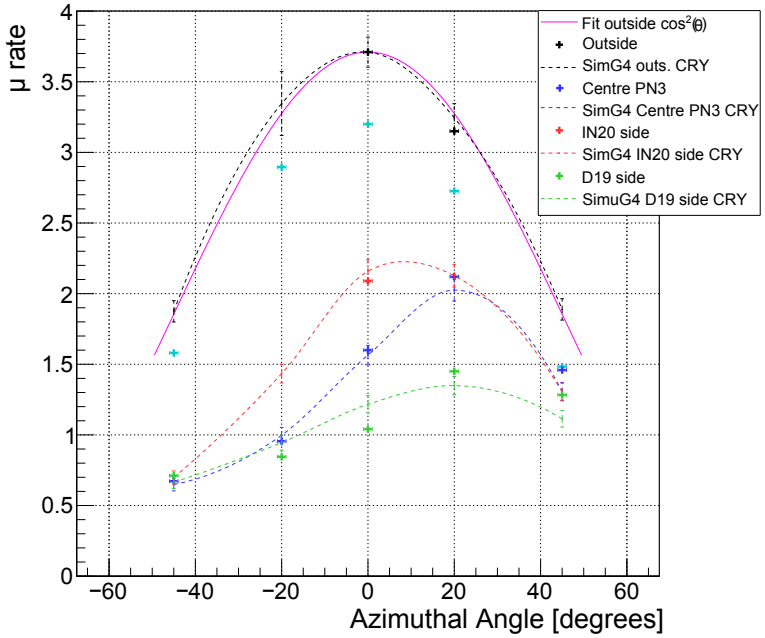

Figure 3.1: Angular dependence of the muon rate at different positions at the STEREO site (PN3) and at open air, close to the STEREO site. The rates were measured by a coincidence measurement of two plastic scintillator panels of surface $52 \times 12\,\mathrm{cm}^2$, stacked above one another with 20 cm distance. The data (points) are compared to GEANT4 simulations (lines) using the Cosmic-ray Shower Library (CRY) [Hag12]. Adapted from [Zso16].

Another positive feature of the allocated position for STEREO, apart from the overburden, is that several load-bearing walls are situated right underneath. They allow for a high floor load of $10\,\mathrm{t/m}^2$ and thus the possibility to install heavy passive shielding.

The experimental hall of the reactor building also accommodates many other instruments, mostly for neutron scattering experiments. The most important background contributions of those arise from the direct neighbour instruments, described in the next section. A more general background in the hall is created via the radioactive isotope ^{41}Ar. This is produced by neutron capture on ^{40}Ar, present in the air at about 0.93%. It decays with a halflife of $T_{1/2} = 109.6$ min [ENS17] and is thus only present during reactor cycles. The decay is in 99% associated with a

γ-ray emission of 1293.6 keV [ENS17], which is well below the energy window of the neutrino measurement (> 2 MeV), but is of interest for calibration with low energy sources, for the data acquisition rate and dead time (trigger threshold $\sim$ 250 keV), and in case the energy region should be extended. It is the dominating characteristic background at lower energies. As constituent of the air in the hall it can enter the STEREO setup through the cable feedthrough and small gaps in the shielding. Its background contribution is always visible in varying intensities during reactor cycles.

Apart from these general challenges for a neutrino experiment in a reactor environment and on Earth's surface some more particular background sources arise for STEREO. The neighbour instruments, briefly described in the next section 3.1.2, can create high γ-ray and thermal neutron backgrounds, depending on the instruments' configuration. These backgrounds were characterised in dedicated background studies and adapted shielding walls were installed around the site. The corresponding background measurement campaigns are described in Chapter 5. In addition one neighbour instrument can be equipped with strong cryomagnets, creating stray magnetic fields of up to 1.1 mT within the STEREO detector volume. To avoid any impact on the detector performance a magnetic shielding for STEREO was developed in the context of this thesis. This is described in Chapter 4. As STEREO is located at the site of a former gamma ray spectroscopy instrument the beamtube of the former experiment was still in place. In order to reduce the background for STEREO the beamtube (H7) was closed by a specially designed plug. After a first period of data taking the beamtube reached the scheduled end of its lifetime, defined by material ageing effects, and needed to be removed. In order to estimate the change in the background situation for STEREO a series of MCNP simulations was performed, which are described in Chapter 6.

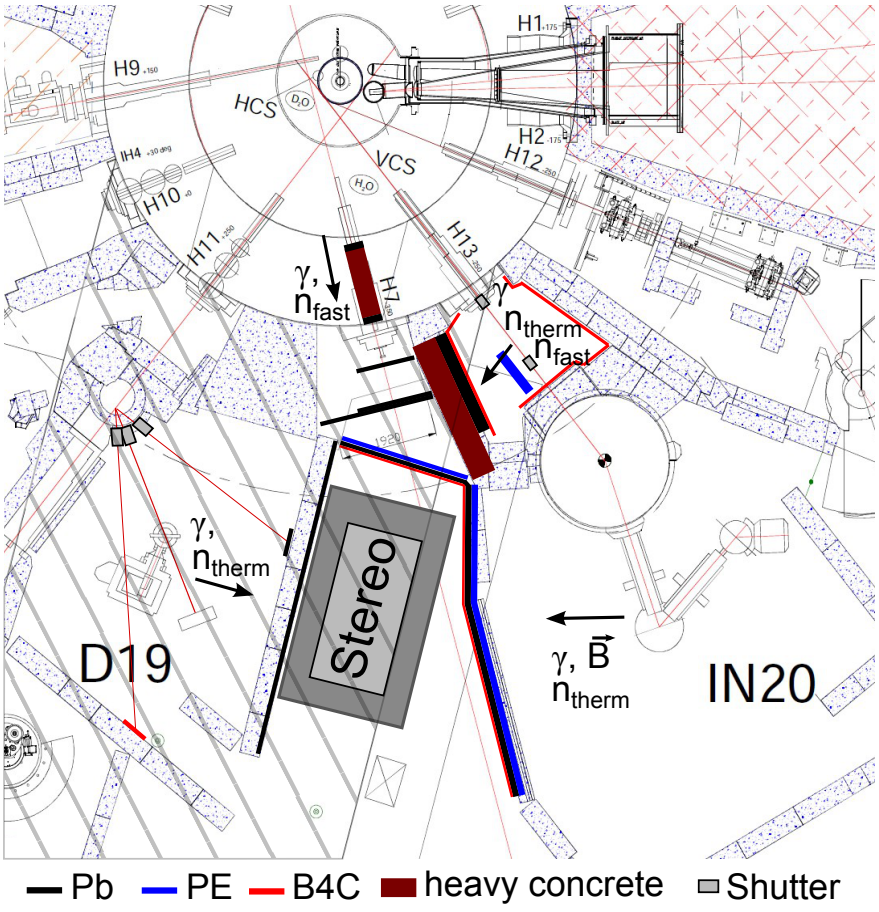

Figure 3.2: Map of STEREO's experimental zone and its surroundings. The main shielding components and background sources are indicated. The hatched area shows the coverage of the transfer channel. Shielding thicknesses not to scale.

3.1.2 Neighbour Instruments

The STEREO site is enclosed in between two neutron scattering instruments. In Fig. 3.2 on the left hand side is the diffraction instrument D19 [D19]. It is the first instrument on the shared neutron beamline H11, departing from the moderator tank. The neutron guide itself is behind a concrete wall on the opposite side of STEREO. D19 is a Laue diffraction instrument using monochromatic neutrons of different energies (wavelengths) scattered on a slowly rotating sample. The neutron beam towards the sample is produced by bringing a monochromator into the primary neutron beam and diverting some neutrons by Bragg reflection. The reflected neutron beam is collimated before entering the D19 experimental zone. The energy selection is done by choosing in between three different monochromator crystals: copper, graphite or germanium combined with three different scattering angles with respect to the primary beam. The different beam positions lead to distinctive background signatures for STEREO. Their impact is described in Section 5.1. For the 90° angle the beamstop consists of 5 cm lead, fixed at the wall in between D19 and STEREO, at the front half of STEREO. The lead is lined with a 5 mm rubber mat, containing B_4C. The ^{10}B in the B_4C has a high $^{10}B(n,\alpha)$ cross section of 3850 barn for thermal neutrons [END17] and makes it a common choice as protection against thermal neutrons. The 70° takeoff-angle beamstop is a box with 5 cm thick lead walls, open towards the impinging beam and lined with 5 mm B_4C mats. This design is supposed to reduce neutron scattering within the zone. At the 42.7° neutron beam position the beamstop is a heavy concrete block lined with B_4C in the rear wall of the D19 area. A maximum flux of $10^7 - 10^8$ n/cm^2/s at the sample position can be reached. At any time the two beam directions not in use are closed by a shutter. In case of sample or setup changes at the instrument all three shutters can be closed for varying times. The separation wall in between D19 and STEREO is a 30 cm thick concrete wall backed by a layer of B_4C and a 10 cm thick lead wall on the STEREO side. It has a height of 2.4 m, shielding the detector, but not the muon veto which is located above the wall. The remaining space above the wall and below the overlying transfer channel is shielded by a curtain of 5 mm B_4C mats and a hydrogenous fire protection foam. The main background contributions from the D19 side are thermal neutrons and γ-rays produced in neutron capture reactions.

On the other side of STEREO, right hand side in Fig. 3.2, is the three-axis spectrometer IN20 [IN20]. It has its own thermal neutron beam tube, denoted H13. Coming from the reactor the neutron beam first enters a primary casemate. This contains a primary neutron beam shutter at its entrance and two sets of collimating slits and a second beam shutter at its exit. During IN20's operation the two shutters can be opened individually which helped to identify background originating from the primary casemate H13 and background created in the IN20 experimental zone. After exiting the primary casemate the neutron beam impinges on a monochromator (first axis of the three-axis spectrometer) within a concrete bunker and is then reflected towards the sample (second axis). A three-axis spectrometer is designed for inelastic neutron scattering, which means the neutron energy on the sample is tuned to study energy and momentum transfer. This is achieved by a stepwise rotation of the sample around the monochromator allowing for different Bragg angles and thus different incident energies in the monochromatic neutron beam. An analyser can rotate around the sample to determine the scattering angles of the neutrons on the sample. The analyser (third axis) is also a crystal which finally reflects neutrons of a given wavelength into a counting neutron detector. The instrument IN20 can also provide special sample environments, where occasionally strong cryomagnets with fields up to 15 T are in use. The measuring principle of the three-axis spectrometer leads to a distinctive moving pattern. In general the sample moves away from STEREO in small steps of a few minutes duration and then moves back to the initial position in one step. This results in a sawtooth pattern which could be observed in some background studies.

The primary neutron beam from the reactor has still contributions of fast neutrons with fluxes up to 10^8 n/cm^2/s above 1 MeV (for comparison, the thermal flux at the same position in 10-50 meV is $\sim 5 \cdot 10^{10}$ n/cm^2/s) at the entrance of the casemate, calculated from [Fua15]. The fast neutrons are likely to be scattered at the collimating slits at the end of the casemate.

These are made of layers of flexible and sintered B_4C and PE to absorb thermal neutrons, but the absorption cross sections are much smaller at high energies. As a primary shielding against these scattered neutrons a 15 cm thick wall of borated polyethylene (BPE) was installed next to the collimators inside the casemate, see Fig. 3.2. An additional background source are γ-rays emitted in neutron captures on structural materials in the casemate, or even the air inside (e.g. ^{14}N emits γ-rays up to 10.8 MeV in neutron captures [Cap17]). As additional shielding a 10 cm thick lead wall inside the casemate was increased to 20 cm thickness, covering nearly the full height of the casemate, in order to reinforce the heavy concrete wall separating the H13 casemate and the STEREO zone. An additional frontal wall was installed in the STEREO zone to further reduce background from H13 and from the H7 beamtube. This consists of 10 cm of polyethylene (PE) and 10 cm of lead.

The remaining fast neutrons in the beam are diffusely scattered in the monochromator bunker. From the IN20 experimental zone the main backgrounds are γ-rays from neutron captures, thermal neutrons which can be captured on structural materials around STEREO and stray magnetic fields if the cryomagnets are in use. The wall in between STEREO and IN20 was adapted and consists of 15 cm of BPE and 15 cm of lead in a non-magnetic stainless steel support frame. The wall has a height of 2.4 m covering the main detector setup but leaving the muon veto unprotected. On top of the wall a 1 m high curtain of B_4C mats was installed to reduce the thermal neutron flux around STEREO.

3.1.3 Primary Cooling Water Circuit

The ILL reactor has two primary cooling water circuits to circulate the heavy water around the reactor core in order to dissipate the fission heat. The pumps and some lengths of both circuits are located underneath STEREO. During reactor operation fast neutrons from fissions can cause the reaction ^{16}O(n,p)^{16}N, where the latter has a halflife of 7.1 s [ENS17]. The halflife is long enough to have high activities of ^{16}N everywhere throughout the cooling water circuits. In the ^{16}N decay scheme two high energetic gamma lines are present at 7115 keV (intensity $I = 4.9\%$) and at 6129 keV ($I = 67\%$) [ENS17]. Given the location and structure of the cooling water cycles this could cause localised background contributions. Studies have been carried out on-site with high purity germanium detectors (HPGe) to measure the rate of the related gammas and verify the foreseen shielding [Zso16]. The measured rate was scaled to the size of STEREO and propagated through the detector shielding by Geant4 [Ago03] simulations. With a shielding of 20 cm of lead the number of γ-rays originating from ^{16}N and depositing energy inside the detector within the energy region of interest for the IBD neutron capture signal (5-10 MeV) is suppressed to an expected rate of 28 mHz. This was taken into account in the design of the passive shielding of the detector itself.

3.2 The Detector

3.2.1 Detector Design

Optical Signal

The design of the STEREO detector is based on known and well established technologies. The target volume (TG) consists of six identical, optically separated cells of $370\times889\times918\,\mathrm{mm}^3$, each. The separation is along the long axis of the detector. This axis is tilted by about 18° [Lhu17] against the line of propagation of the reactor neutrinos so that the detector is parallel to the aforementioned fuel element transfer channel above, see Fig. 3.2. The TG cells are filled with Gd-loaded (0.2%) liquid scintillator, its composition and characteristics are described in detail in Section 3.3. The target is surrounded by an outer crown of four cells. Two cells have about the same dimensions as the target cells and are in a row with those, one on each short

end of the detector. Two other cells are covering each long side over the full length, see Fig. 3.4. These four cells are filled with the same liquid scintillator but without the Gd-doping. They are referred to as 'Gamma Catcher' (GC) and fulfill multiple purposes: they serve as additional shield against low energetic external background, as veto against high energetic background, which might spread energy over both volumes, and for energy recovery for events which occur at the edge of the target, where photons may exit the target volume. TG and GC are contained in a double-walled stainless steel vessel.

The readout of the scintillation light follows by photomultiplier tubes (PMTs) on top of the cells, four in each TG and short GC cell and eight in the long GC cells. The PMTs are separated from the scintillator by 20 cm thick acrylic blocks, called 'buffers'. Those allow for a more homogeneous distribution of light among the PMTs even for events at the top of the scintillator volume. A side effect is that they also reduce external background, especially potential background from radioactive elements in the glass of the PMTs. The PMTs are eight inch tubes, type R5912-100 from Hamamatsu [Ham98]. In order to optically couple the bulb shaped PMTs to the buffers they are placed in small aquariums on top of the buffers, filled with mineral oil (n-dodecane).

To allow for cell-by-cell independent energy and event reconstruction the single cells are separated by specular reflective walls, covering five faces of each cell, except the top. The walls between single TG and GC cells are symmetric sandwiches of, from the outside to the inside, a 2 mm acrylic plate, an airgap, a reflective foil (VM2000) and a single central nylon net to sustain the distance between the two VM2000 foils, see Fig. 3.5. For reasons of stability the four walls separating the TG and GC volumes have the same sandwich structure but a 12 mm outer acrylic plate. VM2000 shows good specular reflection properties, namely 94% relative reflection for incident angles up to at least 80° with respect to the surface normal [Jan08]. At high incident angles the airgaps allow for total reflection on the acrylic and the VM2000. The outer walls (towards the stainless steel tank) and bottom plate have only a single reflective foil. The inside of the steel tank is coated with white, diffuse reflective Teflon, for reflection of the light transmitted through the outer optical walls.

Shielding

The shielding of the detector has been adapted to the situation at the experimental zone, described in Section 3.1. The stainless steel detector vessel is placed in a housing of borated PE-HD (BPE) with walls (floor, roof) of 15 cm (20 cm, 30 cm) thickness. This in turn is in a housing of lead with a wall (floor, roof) thickness of 10 cm (20 cm, 15 cm). The lead is in general in place to suppress the ambient γ-ray background. The thicker floor plate was included to mitigate the spatial inhomogeneous background from the ^{16}N decay in the cooling water circuits, see Sec. 3.1.3. The BPE serves as protection against fast neutrons which mainly originate from muon spallation in surrounding materials, especially the detector's lead shielding. The data of the first phase of data taking does not show indications for significant contributions of fast neutrons from the reactor.

On top of the setup an active muon veto covers most of the structure's top surface. The veto is a water Cherenkov detector of $414 \times 380 \times 26\,\mathrm{cm}^3$ filled with demineralised water. The water is doped with the wavelength shifter 4-MU (4-Methylumbelliferone) to better match the PMTs' sensitive wavelengths and to obtain a longer attenuation length for the shifted light. The walls are lined with diffuse reflective Tyvek paper. Twenty R5912-100 PMTs are deployed for the optical signal readout. While through-going muons emit Cherenkov light over the full height of the veto (26 cm) non-cosmic background, e.g. from γ-ray interactions, has lower energies and thus shorter ranges in the water, which results in less Cherenkov light. Consequently, by using the number of detected photons and topological information muons can be separated from other events. The intrinsic efficiency of the veto, tested with vertical muons identified in the detector, is 99.8% [Ber17].

Additional shielding components are a 1.5 mm thick mumetal layer, attached to the inner

surface of the BPE, and a 1 cm thick soft iron layer covering the full setup, detector and muon veto, on the outside. These two parts form a two layer magnetic shielding, based on the simulations described in Chapter 4. Finally the soft iron is covered with a layer of B_4C mats to reduce thermal neutron capture on the iron. A cross section of the detector setup is shown in Fig. 3.3.

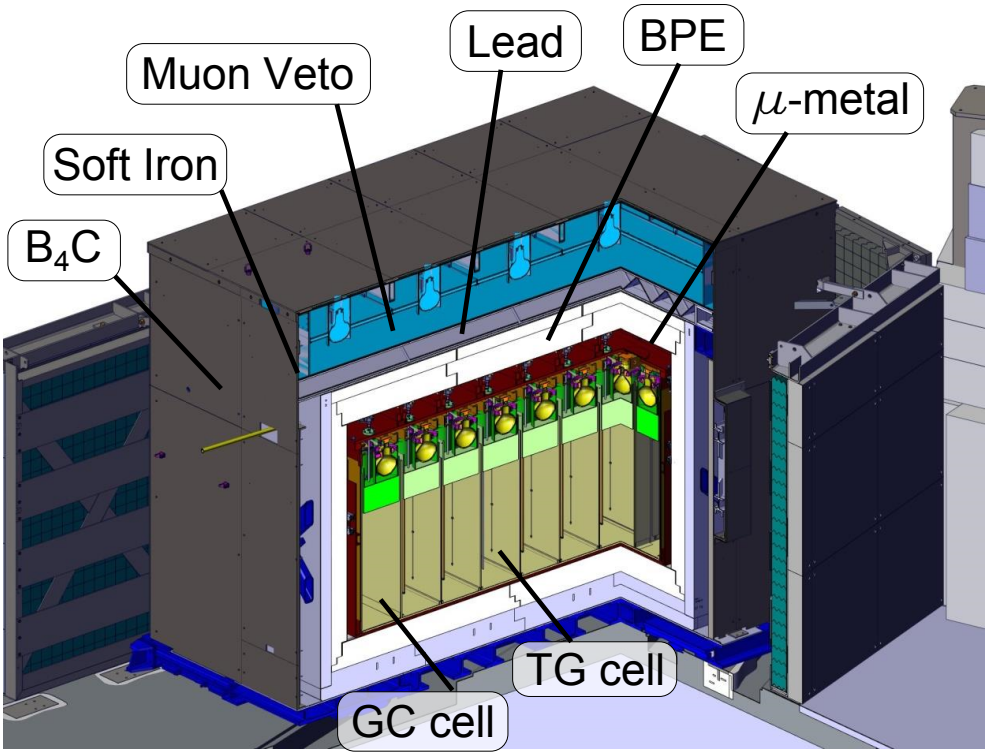

Figure 3.3: Cut view of STEREO, seen from the rear of the detector. Not shown are the calibration systems: tubes in the target cells 1, 4 and 6, an automatised, 2D movement system around the detector vessel and a rail under the detector vessel, located in a groove in the BPE shielding.

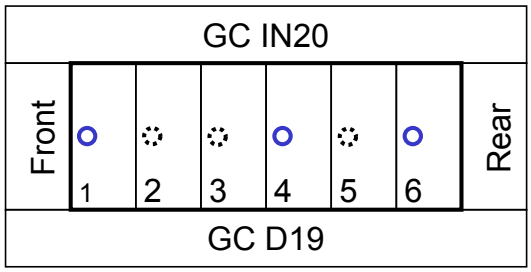

Figure 3.4: Top view and labelling of the detector cells. The calibration tubes in the cells (circles) are only connected to the outside in cells 1, 4 and 6.

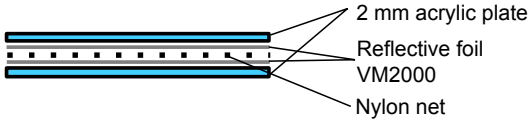

Figure 3.5: Cross section of a reflective wall separating the target cells.

Calibration Systems

In total four independent calibration systems have been integrated in the detector design, three to characterise the scintillator response with different γ-ray sources and one system of optical fibres to inject light pulses from LEDs in the cells to monitor the PMT response.

Internal Calibration

Each target cell is equipped with a single, vertical steel tube stretching from top to bottom and allowing the deployment of gamma or neutron sources at any height in the cell. For symmetry the tubes are installed in all cells, along the central axis of STEREO, but for reasons of practicability only three, in cells 1, 4 and 6, are connected by tubes to the outside of the shielding. The sources are mounted in small capsules and moved manually along the tubes with help of steel cables.

External Calibration - Pantograph

The so called 'Pantograph' is a semi-automatised system, designed to move sources around the detector vessel. Through an access door in the shielding the same sources as for the internal calibration can be inserted in a sample carrier. By software control this can be positioned at any height and at any position along the circumference of the detector. This allows a more detailed calibration of the GC cells and a more homogeneous irradiation of the TG.

External Calibration - Rail

A second semi-automatised system is installed under the detector. A source carrier can be moved along the central axis of STEREO and placed at any longitudinal position under each of the TG calls and front and rear GC cells. This gives valuable information for the intercalibration as with this system all cells can be calibrated in the same source-to-cell geometry.

LED calibration

In each detector cell (TG+GC) three optical fibres are installed in a central position at one wall, ending at three different heights (10 cm above the floor, central height ∼45 cm, 10 cm below the buffer). In the veto 12 positions are equipped at a single height. The fibres end up in diffusors, small, white teflon spheres of 1 cm diameter, resulting in a more isotropic light emission in the cells. LEDs inject light pulses at 465 nm wavelength into the fibres. This system is used to monitor the PMT response over time and can be used in three operation modes. At low LED intensity only a small number of photons arrives in a detector cell. In this mode the PMT readout electronics is set to a gain (amplification) factor of 20. In this way it is possible to measure the single (double, tripple,..) photo electron peaks and thus to determine the PMT charge per photo electron. In regular measurements, with gain 1, the measured PMT charge can then be converted in the corresponding number of detected photo-electrons (pe) per PMT. This is a first PMT intercalibration to account for differences in the PMT gains and potential gain fluctuations due to instabilities in the high voltage supply.

In the second operation mode the LEDs are operated at a higher, well defined intensity and the PMT readout electronics is set to gain one, the standard value. This calibration results in a sharp peak in the charge spectrum of the PMTs. This can be used to monitor the combined effect of the PMT signal amplification, the light collection efficiency in the cells and the light transmission of the scintillator. The three different heights give information about possible height-dependend effects. Both types of runs are also performed for the muon veto PMTs. In the detector a third possibility exists, to inject UV light from an UV-LED emitting at about 390 nm wavelength. This excites the wavelength shifter in the scintillator and thus allows to directly monitor the scintillator's performance.

A third calibration mode, also with gain one, is designed to determine the PMTs' and electronics linearity. In total three LEDs emitting at 465 nm are available to illuminate the fibres, where for each LED a different amount of photons is injected into the fibres. By combining pulses of one, two or all three LEDs at a time, different light intensities are seen by the PMTs. Comparing the signals for the combination of two or three LEDs with the signals of the single LED illumination the linearity of the PMTs can be determined. The performed measurements in the STEREO detector after commissioning show no non-linearity, from which it was concluded

that, if a non-linearity is present, it lies below 1% in the charge dynamic range 0-1500 photo-electrons per PMT, which according to simulations corresponds to the range up to a 10 MeV positron interaction directly below one PMT [Sal17].

DAQ

STEREO's data acquisition system has been custom developed at the LPSC Grenoble and is presented in detail in [Bou16]. The readout of all 68 PMTs is done fully digitally with a dedicated electronics, hosted in one single microTCA crate. The PMT signals are constantly sampled by 8-channel cards with 250 MS/s with 14 bit resolution. Two levels of triggers can be applied, a basic trigger on the sum of charges on four or eight channels of a board (4 PMT per cell), or a second level trigger, based on more complex criteria. If a valid trigger is present all channels are read out individually. For each channel a signal start is searched via a constant fraction trigger in a time window of up to 256 ns. If a start is found the following signal is integrated in two adjustable time windows, one for the full signal, and one for the signal tail which can be used for the pulse shape identification of strongly ionising particles, see Section 3.3. If no signal start point is found but a trigger is present the integration starts at the beginning of the 256 ns window. In normal acquisition mode only the two signal integrals are stored for each PMT, in debug mode also the full pulse shape can be saved. Given the overall acquisition rate during the first period of data taking of about 1-2 kHz the latter is not practicable as standard acquisition mode.

The electronics setup is in principle deadtime free. However, if the acquisition rate is too high the read/write speed on disk is too slow and the internal signal buffers on the card are not emptied fast enough. In this case no further signal is accepted until the buffers are sufficiently freed. In normal acquisition mode for neutrino runs the dead time is about 1-2% during the reactor cycles. For the most active calibration sources, listed in Chapter 7.2, Tab. 7.1, in internal calibration, dead times of up to ∼80% can be reached.

3.3 Scintillator

The STEREO detector is based on an organic, liquid scintillator. The scintillation principle of these materials is based on molecular excitations, as described for example in [Kno00]. Most organic scintillators consist of molecules with symmetric structures that lead to the formation of π bonds in between atoms. A large group are aromatic molecules with benzene ring structures. The electronic ground state is a spin 0 state. By external energy transfer the molecules can be brought into excited states, which can either be singlet states S (spin 0) or triplet states T (spin 1). For the molecules of interest the energy difference between the ground state S_0 and the first excited singlet state S_1 is 3-4 eV, and less in between higher excited states. For each electronic configuration there exists a number of vibrational states denoted by a second index S_{ij} with an energy spacing around 0.15 eV, see scheme in Fig. 3.6. After an initial excitation by energy absorption highly excited states quickly ($\mathcal{O}$(ps)) deexcite to the S_1 state via radiationless inner conversion. Vibrational states are above thermal equilibrium (0.025 eV) and quickly dissipate their energy, so that typically within less than 1 ns after the energy deposition the only excited state is the S_{10} state. If the direct deexcitation of the S_{10} state (prompt fluorescence) does not end in the lowest vibrational state of the ground state S_{00} but any vibrational state S_{0j} the emitted radiation has a too small energy to be reabsorbed in a S_{00}-S_{10} transition. In addition in thermal equilibrium the vibrational states S_{0j} are not populated, so that the emitted photons can propagate through the medium. This is the main, prompt scintillation light. After an initial build-up time to populate the S_{10} state, its intensity I decreases exponentially with time t

$$I(t) = I_0 \cdot e^{-t/\tau} \ , \tag{3.1}$$

where the decay constant τ depends on the scintillator. For a good timing resolution and high count rates a short decay time is desirable. For organic scintillators this lies usually in the range of a few nano-seconds.

The S_1 state can also populate the T_1 state via an inter-system transition. The triplet states require a spinflip for deexcitation and have significantly longer half lifes than the S_1 states, up to 10^{-3} s (slow phosphorescence). As the T_1 state is energetically lower than the S_1 state the emitted radiation has a longer wavelength. One model for a faster deexcitation is the bimolecular interaction of two molecules in a T_1 state, whereby one molecule is converted to a S_1 state, the other to a S_0 state. Thus the fluorescence occurs delayed, but has the same emission spectrum as the fast component. The signal decay time τ of the slow component lies in the range of up to a few hundred nano-seconds. This bimolecular process depends on the density of T_1 states, which is proportional to the density of excited molecules and thus depends on the specific energy loss $\mathrm{d}E/\mathrm{d}x$ of the incident particle. This allows for a pulse shape discrimination (PSD) in organic scintillators between weakly and strongly ionising particles by comparing the intensity of the fast and slow scintillation components. This effect is exploited for fast neutron detection, by identifying the heavy, strongly ionising recoil nucleus produced by scattered neutrons.

During the excitation process energy is often transferred multiple times from molecule to molecule before the final light emission, so that the initial energy deposition does not need to occur to a scintillating molecule. This allows for example to add the scintillating reagent only to a base solvent material which can be much cheaper or easier to handle. In case that the self-absorption of the scintillation light within the bulk material is too high a so called wavelength shifter can be added, which absorbs the primary scintillation light and reemits at a longer wavelength. This can also be necessary to match the emission spectrum, usually in the UV range, to the sensitivity of the PMTs.

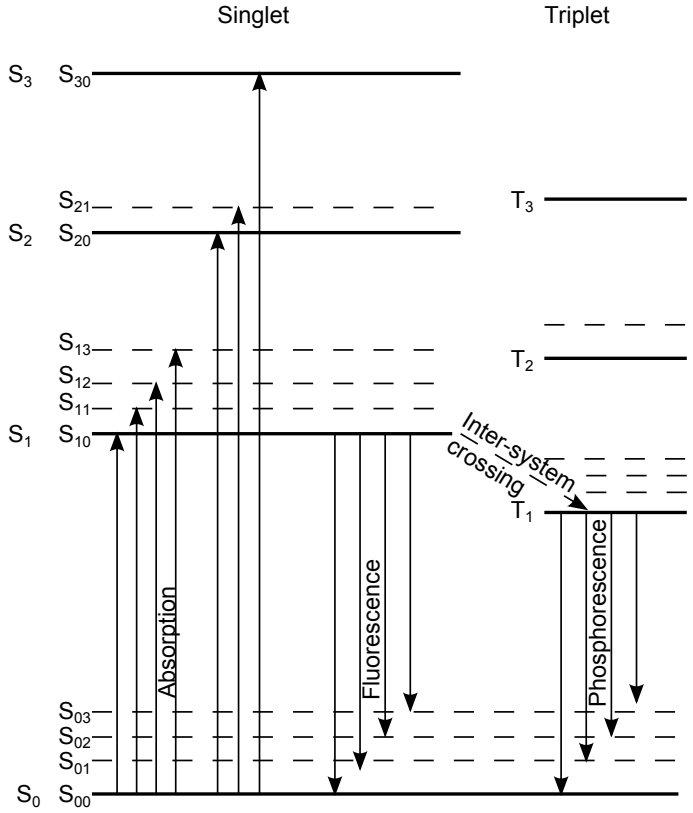

Figure 3.6: Scheme of the electron energy levels in an organic molecule with π-bond electron structure. Adapted from [Kno00], therein reprint of [Bir64].

The energy response of most organic scintillators to incident electrons is linear above about 125 keV. For heavier, charged particles the onset of a linear response occurs for much higher thresholds. This behaviour is described by the model of Birks [Bir51]. The basic assumption is that the non-linearity is caused by quenching from damaged molecules, where quenching means the dissipation of the excitation energy in any other way than radiation emission. The number

of produced excited scintillating molecules is directly proportional to the specific energy loss of the incident particle, $A \cdot \mathrm{d}E/\mathrm{d}x$. The concentration of damaged molecules along the particle track is also proportional to the specific energy loss, $B \cdot \mathrm{d}E/\mathrm{d}x$. With k as the fraction of energy transfers to damaged, relative to undamaged molecules, Birks then writes the light emission S per path length x as

$$\frac{\mathrm{d}S}{\mathrm{d}x} = \frac{A\,\mathrm{d}E/\mathrm{d}x}{1 + kB\,\mathrm{d}E/\mathrm{d}x}\ , \tag{3.2}$$

where kB is usually considered as one, adjustable parameter. For low values of $\mathrm{d}E/\mathrm{d}x$, e.g. for electrons with sufficiently high energy, Eq. (3.2) becomes $\mathrm{d}S/\mathrm{d}x \simeq A\,\mathrm{d}E/\mathrm{d}x$, which shows the observed proportionality of energy deposition and light output. For high values of $\mathrm{d}E/\mathrm{d}x$ on the other hand Eq. (3.2) results in $\mathrm{d}S/\mathrm{d}x \simeq A/kB = \text{const.}$, which means the light output saturates.

The scintillator properties, like light yield (A), emission spectrum and signal time constant are defined by the chemical reagents used. The attenuation length of the scintillation light in the scintillator itself can be increased by chemical purification of the reagents, as impurities can absorb the light without reemission. The required purity depends on the scale of the experiment. Care has to be taken in the handling of the scintillator as not only solid impurities but also gases can diffuse into liquid scintillators (LS). For example molecular oxygen dissolves in the LS. The molecules then provide additional radiationless deexcitation modes, thereby decreasing the total light output. This can be recovered by flushing the liquid with a non-solvable gas ("bubbling"), e.g. with nitrogen or argon.

The LS for STEREO has been developed and produced by the Max-Planck Institut für Kernphysik (MPIK) Heidelberg. Different mixtures have been tested, without the final Gd-doping, in order to find a liquid with a high total light yield and a good PSD capability [Pé15]. The selected composition for the target liquid is based on LAB (explanation of abbreviations see Tab. 3.1), with 75vol%. To obtain a higher light yield and introduce a PSD capability PXE is added as a second solvent, with about 20vol%. An admixture of 5vol% of DIN is added to increase the PSD performance. Small concentrations of PPO and bis-MSB serve as primary and secondary wavelength shifters. Finally a Gd-complex, Gd-β-diketone dissolved in Tetrahydrofuran, was added. This complex was developed by MPIK for the DoubleChooz experiment and fulfills the criteria of chemical stability and longtime solubility of the Gd molecules, compatibility with detector materials and good transparency [Abe12b]. The final mixture is also specified in Tab. 3.1.

The resulting scintillation light spectrum of the LS, as measured by the MPIK, is shown in Fig. 3.7. By chemical purification of all scintillator components a high attenuation length of $> 5\,\mathrm{m}$ at the reference wavelength of the maximum PMT sensitivity at 430 nm was obtained[Buc17b], see Fig. 3.8.

Table 3.1: Chemical composition of the STEREO TG liquid scintillator. The composition for the GC is the same, except for the Gd-complex.

Reagent	vol% or concentration
Linear Alkyl Benzene (LAB)	∼75%
Phenyl Xylyl Ethane (PXE)	20%
Di-isopropyl-naphtalene (DIN)	5%
Gd-β-diketone in Tetrahydrofuran (THF)	1%
2,5-Diphenyloxazole (PPO)	7 g/l
1,4-bis(2-methylstyryl)benzene (bis-MSB)	20 mg/l

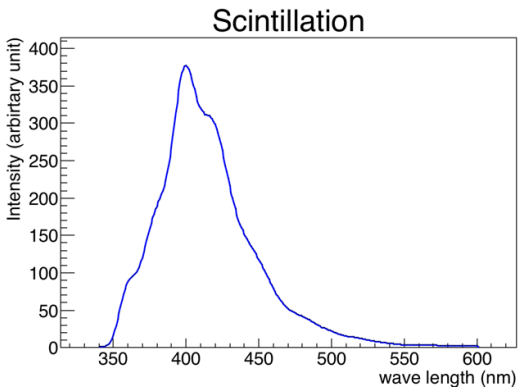

Figure 3.7: Scintillation light emission spectrum of the STEREO TG LS, as measured at the MPIK [Buc17b].

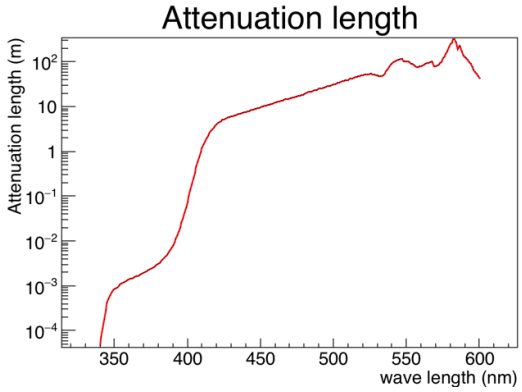

Figure 3.8: Wavelength dependent light attenuation length of the STEREO TG LS, measured at MPIK [Buc17b].

3.4 Expected Sensitivity

The IBD events are identified by the coincidence requirement for the positron and neutron, which strongly reduces the background. This, however, can still arise either from uncorrelated events, occurring randomly within the coincidence time window, or from correlated background signals, expected dominantly from fast neutron scattering and subsequent capture and multiple neutron captures, where in both cases the primary neutron source is muon spallation. The rate of random coincidences R_{rand} depends on the single background rate for the prompt-event selections R_{prompt} and delayed-event selections R_{delayed} and the coincidence time window width Δt and can be approximated as

$$R_{\text{rand}} \simeq R_{\text{prompt}} \cdot R_{\text{delayed}} \cdot \Delta t \ . \tag{3.3}$$

It can thus be reduced by optimising the coincidence time window or by reducing the single background rates, which is the reason for the installation of heavy passive shielding. The correlated background has either to be identified in data analysis, some methods are described in Sec. 7.1.2, or can be measured in between the reactor cycles and statistically subtracted from the data.

Considering the deposited energies and the anticipated background the energy ranges of interest have been defined a priori to 2-8 MeV for the prompt positron signal, in order to improve the signal to background ratio, as for lower energies the natural background increases strongly and for higher energies the neutrino signal is small, and 5-10 MeV for the neutron capture on Gd. Both energy windows may be adapted for the final analysis. The accepted prompt signal range corresponds to about 2.8-8.8 MeV neutrino energy. For 2 MeV positrons an energy resolution of $\sigma/E = 12\%$ is expected, which at this energy is dominated by the escape of 511 keV positron annihilation photons [Pé15]. For electrons at 2 MeV the resolution has been expected around 7%, which in the current state of the analysis is at 7.8% [Bla17a], see Sec. 7.1.1.

The IBD detection efficiency is dominated by the IBD-neutron detection by capture on Gd. The IBD-neutron also receives a small recoil upon creation. The detection efficiency is therefore obtained from simulations for 20 keV neutrons homogeneously distributed in the target cells and lies for central target cells at 61% with the lower energy cutoff at 5 MeV. For the border cells, 1 and 6, it is expected to be 57%, as here the spill-out, IBD-neutrons exiting the cells, has a larger impact [Pé15]. For inner cells these can still be captured on Gd in neighbour cells, which is not the case if they escape from border cells to the GC.

Under these conditions at full reactor power about 380 neutrino events per day are expected, with, at the current state of the data analysis, after subtraction of random coincidences, a signal to background ratio close to one.

STEREO measures the neutrino spectrum independently in the six target cells, at baselines between 8.9 m and 11.1 m. This allows for at least two different types of analyses. With help of Geant4 simulations the number of expected neutrino events in the whole detector or in each cell can be calculated under assumption of different oscillation hypotheses. By a statistical comparison with the experimental rates and spectra, parameters for the best agreement can be determined. Alternatively, or combined, the $\sin^2 \frac{L}{E_\nu}$ dependence of the neutrino oscillations can be exploited, which leads to distortions compared to the un-oscillated neutrino spectrum at different energies in the single cells. An analysis only based on the spectral shape among the cells would be independent of any spectra predictions. Following the envisaged performance of the detector a detailed study about the projected sensitivity of STEREO has been performed by Collin [Col14] assuming

- 300 d reactor-on data,
- signal to background ratio of 1.5,
- $2\,\text{MeV} < E_{\text{prompt}} < 8\,\text{MeV}$ (equivalent to $2.8\,\text{MeV} < E_\nu < 8.8\,\text{MeV}$),
- $5\,\text{MeV} < E_{\text{delayed}} < 10\,\text{MeV}$
- energy scale uncertainty 2% (bin-to-bin correlated, uncorrelated in between cells),
- correlated and uncorrelated normalisation uncertainties of 3.7% and 1.7%, respectively (taking into account the number of target protons, total IBD detection efficiency, solid angle coverage, reactor power, neutrino spectrum normalisation),
- an energy dependent, binwise uncorrelated uncertainty of 0.7% to 4% from the prediction of the ^{235}U antineutrino spectrum (250 keV binning).

Under these conditions STEREO will be able to explore the RAA best fit region at 95% C.L. The projected discovery potential (or exclusion area) in the $\sin^2\theta_{\text{new}}$-$\Delta m^2_{\text{new}}$-plane is shown in Fig. 3.9.

In addition the results of STEREO, measured with a basically pure ^{235}U antineutrino spectrum can be used to gain information about the origin of the 5 MeV excess in the measured neutrino spectra, as described in Section 2.1.5.

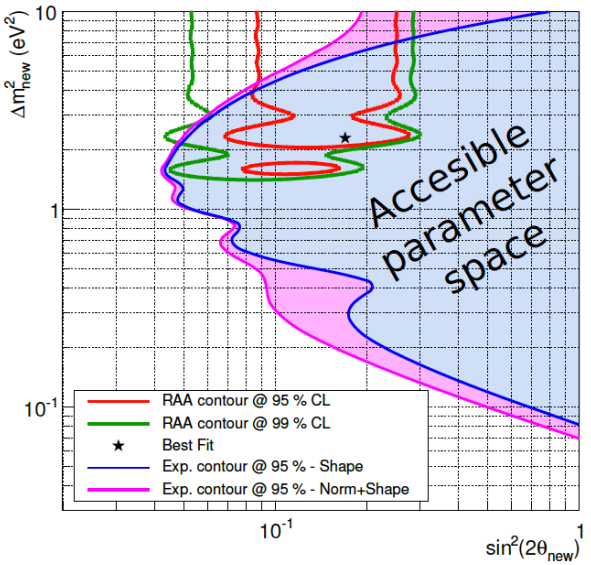

Figure 3.9: Projected sensitivity of STEREO for 300 d of data taking and the operational conditions stated in the text. The RAA best fit region is well covered at 95% C.L.

Chapter 4

Magnetic Shielding

4.1 Situation for STEREO

STEREO deploys 24 photomultiplier tubes (PMTs) in each the target and the gamma catcher and additional 20 PMTs in the muon veto. All tubes are 8-inch PMTs from Hamamatsu, model R5912-100. They have a bulb shape and a 10-stage box and line dynode structure, see Figs. 4.1 & 4.2. The photocathode is a bialkali metal coating on the inside of the bulb. The photo electrons created therein are guided by the field of focussing electrodes to the electron multiplying section, located in the straight part of the housing. Due to the large size the electrons can have comparatively long drift paths before reaching the first dynode. In external magnetic fields the Lorentz force acting on the photo electrons changes their trajectory and can prevent a certain fraction of them from reaching the first (or any subsequent) dynode. In the multiplying section this corresponds to a reduced gain and could in principle be compensated by an increased high voltage or an adapted calibration. More critical is the effect on the collection efficiency of the primary photo electrons. If they do not reach the first dynode then effectively the quantum efficiency of the tube is reduced, which not only impacts the gain but also the resolution, defined by statistical fluctuations of measured quanta ($\sigma/E \sim 1/\sqrt{\text{nb. of detected quanta}}$). The PMT's datasheet [Ham98] states a degradation of the photon sensitivity of about 10% already at a field of $20\,\mu$T. Changing magnetic fields in the vicinity of STEREO could therefore cause a temporary alteration of the amplification and resolution of some, or all the PMTs. On the other hand STEREO needs about 300 d to reach the aspired sensitivity so that a good time stability is important to reduce systematic uncertainties in the combination of all data.

The sensitivity of the R5912-100 PMTs to magnetic fields has been tested directly by the collaboration [Stu15a] in the Earth's magnetic field ($\sim 60\,\mu$T). For the tests a PMT was placed in a black box and illuminated with a LED with constant intensity. A cylinder of 1 mm of mumetal could be added as magnetic shielding. The PMT was rotated around its long axis to vary the angle between the B-field and the axis of the first dynode. For a field parallel to the unshielded PMT's symmetry axis no signal change would be expected, based on the cylindrical symmetry of the PMT. The observed variation in dependence on the orientation is less than 1%, showing the precision of the method, which is dominated by the precision of the mechanical orientation of the PMT. For a transverse field, perpendicular to the PMT's axis, the signal variation without shielding is in the range of ±30% around the average. With the mumetal cylinder it can be reduced to ±2%, see Fig. 4.3. The tests showed that a mumetal cylinder is an effective shielding against an external field of $60\,\mu$T. Consequently it was decided to install the PMTs with individual mumetal cylinders and, in order to guarantee stable run conditions of the experiment, to design an additional outer magnetic shielding with the requirement to reduce the external field below $60\,\mu$T, under all possible conditions.

Potential sources of magnetic fields are stray fields from other experiments or from nearby electrical motors. However, the most prominent sources of magnetic fields are superconducting magnets which can be deployed at the neighbour instrument IN20, see Section 3.1.2, to provide dedicated sample environments. Different magnets are available with nominal central fields of

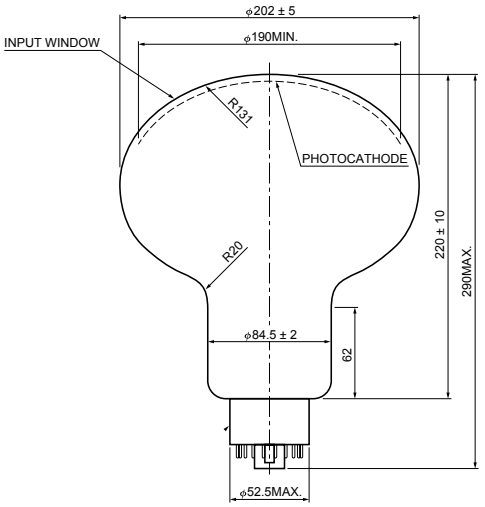

Figure 4.1: Cross-section of a Hamamatsu R5912 PMT. The photocathode is a coating directly on the inside of the glass bulb. The electron multiplying section is included in the straight part of the glass housing. From [Ham98].

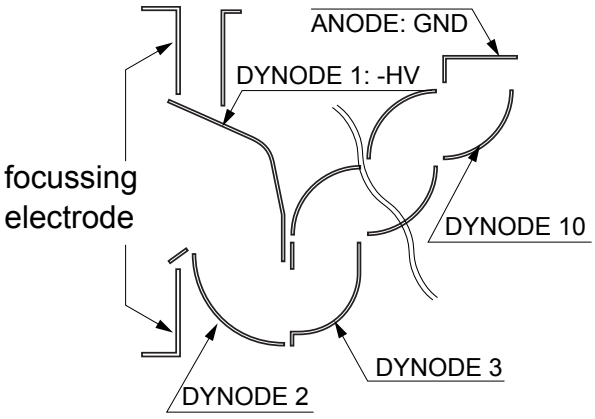

Figure 4.2: Hamamatsu's Box and Line Dynode structure as used in the R5912. If the electric field of the focussing electrode is superimposed by an external magnetic field a fraction of photo electrons may not reach the first dynode anymore. This would reduce the signal amplification and broaden the resolution. Adapted from [Ham15].

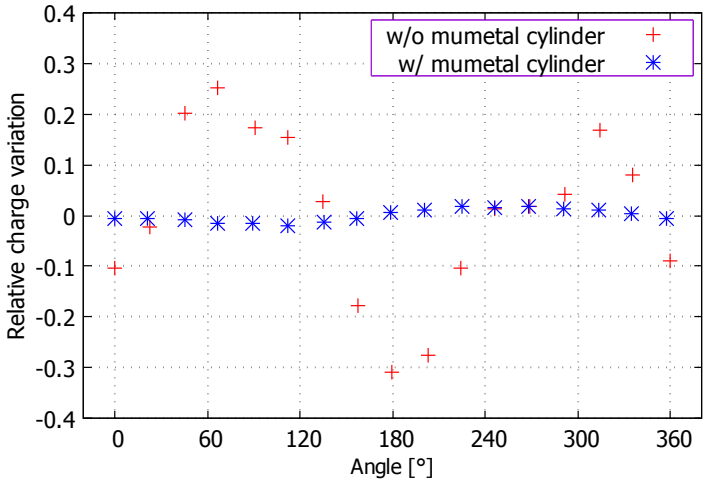

Figure 4.3: Relative signal variation of a R5912 PMT with its axis perpendicular to the Earth's magnetic field during a stepwise rotation around its symmetry axis. The size of the variation depends on the angle between the first dynode and the magnetic field vector. Measurements were performed without shielding and with a 1 mm thick mumetal cylinder around the PMT. Adapted from [Stu15a].

up to 15 T. As described previously, see Section 3.1.2, the sample position of IN20 is not fixed, but changes in the course of the measurements. The minimal possible distance to the outer shielding of STEREO is about 2.7 m, leading in absence of any shielding to simulated maximum fields of 0.83 mT (8.3 G)and 1.06 mT (10.6 G) at the position of the closest detector (GC) and veto PMTs, respectively.

4.2 Physics and concepts

The calculation of magnetic fields on a microscopic level can in principle be done by solving the corresponding Maxwell equations. However, for large and complex setups and in presence of magnetisable materials this cannot easily be done analytically. Instead the finite element method is usually used. Here the geometry of the actual problem is approximated by a grid

of polygons with adjustable precision. The underlying partial differential equations are then converted into numerically solvable systems and the quantities of interest calculated for the corner points of the polygons. Thereby a compromise has to be found between the desired precision of the calculations and the required computing power, since for each node equations with several degrees of freedom need to be solved.

To understand the underlying physical problem it is still necessary to consider the fundamental equations. For the problem at hand, a (quasi-)static magnetic field in presence of magnetisable materials, the Maxwell equations for the magnetic field and some relations for material properties are sufficient and can be found in various textbooks, e.g. [Boz03, Gre98].

The relevant equations for static magnetic problems are

$$\vec{\nabla} \cdot \vec{B} = 0 \qquad \vec{\nabla} \times \vec{B} = \mu_0 \, \vec{\nabla} \times (\vec{H} + \vec{M}) = \mu_0 \, \vec{j_0} + \mu_0 \, \vec{\nabla} \times \vec{M} \ , \tag{4.1}$$

where in the macroscopic case the magnetic flux density $\vec{B}$, the magnetic field strength $\vec{H}$ and the free current density $\vec{j_0}$ have to be understood as volume averages $\langle \vec{X}(\vec{r}) \rangle = \frac{1}{\Delta V} \int_V \vec{X}(\vec{r} - \vec{r}') \mathrm{d}V'$. In the present case the only occurring free currents, $\vec{j_0}$, are the currents inducing the field in the IN20 magnet. They fully describe the unperturbed field in absence of any shielding. The macroscopic magnetisation vector $\vec{M}$ represents the local average magnetisation of the atomic dipole moments $\vec{m}$ of a magnetisable material

$$\vec{M}(\vec{r}) = \frac{\mathrm{d}\vec{m}}{\mathrm{d}V} = \frac{1}{\Delta V} \sum_{i \in V} \vec{m}_i = n(\vec{r}) \langle \vec{m}(\vec{r}) \rangle \ , \tag{4.2}$$

where $n(\vec{r})$ is the magnetic dipole density and $\langle \vec{m}(\vec{r}) \rangle$ the mean magnetic moment. In ferromagnetic materials the atomar magnetic moments are usually clustered in domains of same orientations, which in absence of external fields are randomly oriented and their vectorial sum is zero. In presence of an external field the domains would turn parallel, leading to a high magnetisation. This requires that they can freely reorientate themselves, without being constraint by defects or stresses in the atomic lattice. The effect of the magnetisation on the B-field can be expressed in a more convenient form as

$$\vec{B} = \mu_0 (\vec{H} + \vec{M}(\vec{B})) = \mu_0 \, \mu_r(\vec{B}) \, \vec{H} \ , \tag{4.3}$$

with the relative permeability $\mu_r(\vec{B})$. Following this relation the magnetic flux density inside a paramagnetic or ferromagnetic material ($\mu_r > 1$) is increased with respect to vacuum or air ($\mu_r = 1$). At boundary surfaces of volumes with different μ_r the component of $\vec{B}$ along the surface normal is continuous. Thus, using field lines as representation of the magnetic field, a material with a higher permeability would attract the field lines in its vicinity and guide them through the material, thereby reducing the field strength in its surroundings. Only at the poles where the field enters or exits the material the outer field is increased, leading to potentially strong edge effects.

The principle of magnetic shielding is thus to enclose the source of the magnetic field or the volume to be protected from it with materials with a "sufficiently high" permeability. High permeability comes with higher costs, due to usage of special alloys and material treatments, such as thermal annealing. The latter is done to reach highest permeabilities by demagnetising the material and removing mechanical stresses which could prevent a reorientation of magnetic domains and thus reduce the maximum possible magnetisation, Eq. (4.2). An adapted study is therefore necessary for each application to find the optimum in terms of shielding layout and used materials. Here it has to be taken into account that μ_r is a function of $|\vec{B}|$, for unconstrained ferromagnetic materials. For other types it may be a function of the vector $\vec{B}$. For too high fields the magnetisation reaches a maximum and the material goes into saturation. For a further increase of the field μ_r goes to one and Eq. (4.3) reduces to $\vec{B} \simeq \mu_0 \, \vec{H}$. This should be avoided for magnetic shieldings, which restricts the usage of some materials to certain field ranges.

Chemical elements with good ferromagnetic properties are Fe, Co and Ni. A comparatively robust material, mechanically and in terms of magnetic saturation, would be pure iron, in case of

STEREO provided by AK Steel International with $> 99.8\%$ purity. According to the information provided by the manufacturer [AKS15] it reaches a $\mu_r \approx 2000$ without any special treatment, and after annealing can even gain some factor on that, see Fig. 4.4. If a higher permeability is required often nickel-alloys are used with Ni $\geq 70\%_{\mathrm{mol}}$, so-called mumetals. Those can reach a μ_r of several ten or hundred thousands, but reach saturation much faster and their magnetic properties easily deteriorate when exposed to local thermal or mechanical stress. Some examples of $\mu_r = \mu_r(|\vec{B}|)$ dependencies of mumetals are shown in Fig. 4.5.

For an easier comparison of different setups a shielding factor S can be defined as the ratio of the field without $B_{\mathrm{w/o}}$ and with shielding $B_{\mathrm{w/}}$: $S = \frac{B_{\mathrm{w/o}}}{B_{\mathrm{w/}}}$. This has the additional advantage that S will not change if the external magnetic field is different from the simulated one, as long as the resulting change of $\mu_{\mathrm{r}}(B)$ is not too large. This can be used to estimate the field inside the shielding for different external fields, without repeating the simulations.

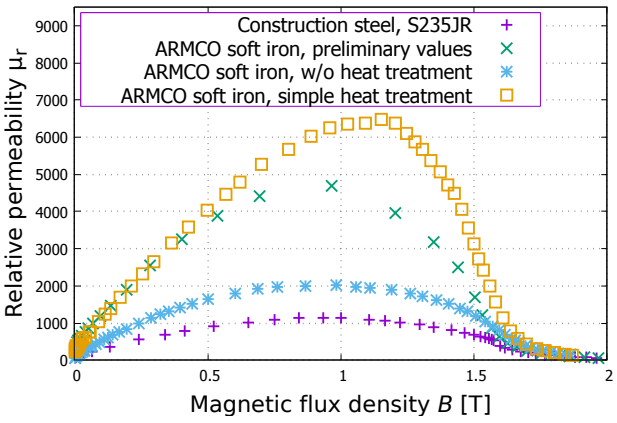

Figure 4.4: Magnetisation curves of construction steel S235JR, adapted from [Led98], and different qualities of soft iron which were considered in the simulations. Before the properties of the ARMCO pure iron ($> 99.8\%$ purity) were known, adapted from graphic in [AKS15], a preliminary curve as used for another experiment was used [Kon14] which corresponds to the values of the 700°C annealed ARMCO soft iron in the relevant field range below 0.5 T.

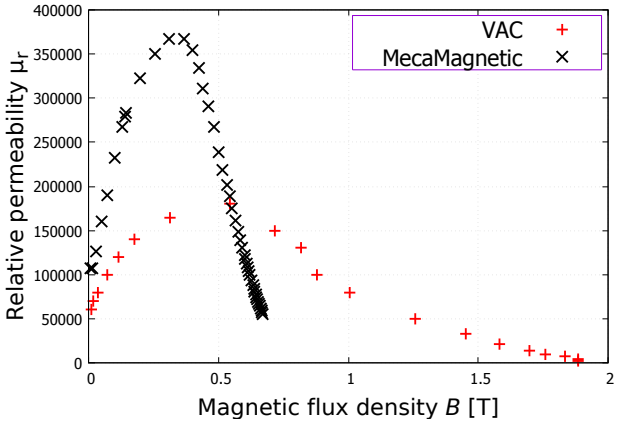

Figure 4.5: Magnetisation curves of the two simulated mumetal options: VAC mumetal, adapted from [Bol90], with moderate properties, used as preliminary option before the provider was selected, and the mumetal which finally was used, provided by MecaMagnetics [Arc04]. The mumetal from MecaMagnetics is more efficient as shielding at fields below 0.5 T but reaches saturation much faster.

Note: Magnetisation curves are measured with standard samples, either rods or a few millimeter thick plates of the tested material. In larger objects of the same material the properties can vary locally and can also differ in between single production batches. The data is provided as general information and to the "best of the knowledge and belief" of the provider [AKS15]!

For a better understanding of the shielding efficiency of different setups a few general dependencies can be considered. An analytical calculation of the shielding factor is only possible for simple geometries, e.g. for a closed cube with edge length a [Bol90]:

$$S_{\mathrm{cube}} = \frac{4}{5}\mu_{\mathrm{r}}\frac{d}{a} + 1 \ , \tag{4.4}$$

which shows a proportionality to the thickness d and the relative permeability μ_{r} of the shielding material. To obtain a high shielding factor instead of increasing the shielding thickness or using materials with a higher μ_{r} it is in general more economical to use a combination of several shielding layers. For different geometries the combined shielding factor can be approximated as

[Bol90]:

$$S = S_n \prod_{i=1}^{n-1} S_i \left(1 - \left(\frac{a_i}{a_{i+1}}\right)^k\right) + \sum_{i=1}^{n} S_i + 1 \ , \tag{4.5}$$

where n is the number of layers, S_i the shielding factors for the individual layers and a_i their side lengths (with $a_i < a_{i+1}$). The exponent k varies, depending on the field orientation, generally it is $1 \leq k \leq 2$. The combined shielding factor is highest when the a_i, the dimensions of the shielding layers, are sufficiently different. In this case the product of the individual shielding factors dominates the equation. For small differences on the other hand it is close to zero and the single shielding factors sum up, with no significant improvement compared to an increase of the thickness of a single shielding layer.

4.3 Simulations

The coordinate system used throughout this chapter is shown in Fig. 4.6. The point of origin is the center of the magnet in its closest position.

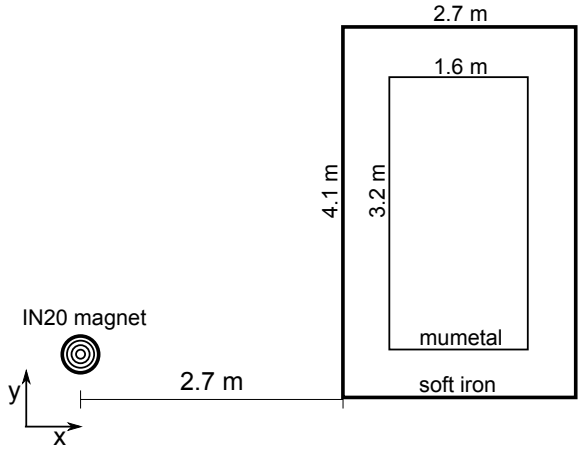

Figure 4.6: Sketch of the components relevant for the magnetic shielding simulations, with the IN20 magnet in the closest position.

For comprehension it should be mentioned that during the simulation campaign also the technical implementation of the magnetic shielding structure in the general design and the decision process on design and material choices by the collaboration took place and all processes mutually influenced each other. This had the consequence that not all studies were performed under the same assumptions. After a decision was made only the final setting was simulated again, without repeating all preceding studies. Still qualitative conclusions can be drawn with sufficient reliability from those studies. The main changes were that after the study of the PMT gain variation in the Earth's field [Stu15a] the requirement on the outer shielding was loosened from originally a maximum of $10\,\mu$T in the PMT planes to $60\,\mu$T. Furthermore the choice of the material supplier was only made during the campaign, so that the exact material properties were not known at the beginning. Also the geometrical possibilities for the magnetic shielding design changed during the campaign due to a redesign of radiation shielding components.

An additional small offset, common to all performed simulations, arose from a miscalculation of the magnetic field's source point. The magnet of IN20 can be rotated around the monochromator of the instrument, leading to a minimal horizontal distance d of about 2.7 m to the outer shielding of STEREO at a height h of 1.03 m above the floor. For the simulation only the closest position was considered. However, measurements of the distances on site, performed prior to the simulations, had been erroneous and a distance of about 3 m was obtained. This was used as input for the simulations. Later, after finishing most of the simulations, a calculation of the distance from technical drawings showed that the real, technically possible minimum is

smaller, leading to higher fields at the position of the shielding. The simulations could not all be repeated and for intercomparison they are presented with the larger original distance. The corrected, expected field can be calculated with the new initial field values and the shielding factors obtained from the simulations. They will be discussed in Section 4.3.8. Assuming a 3 m distance from the STEREO setup to the magnet the detector PMTs are at $d = 3.7\,\mathrm{m}$ and $h = 1.7\,\mathrm{m}$ and could be exposed to a maximum field of $B^{\mathrm{sim}}_{\mathrm{max.\ det}} = 0.64\,\mathrm{mT}$ and the veto PMTs at $d = 3.1\,\mathrm{m}$, $h = 3.1\,\mathrm{m}$ to $B^{\mathrm{sim}}_{\mathrm{max,\ veto}} = 0.84\,\mathrm{mT}$.

The simulations were performed with Comsol Multiphysics v4.3a. For the 15-T, vertical magnet technical drawings have been provided by the manufacturer, Oxford Instruments, to the ILL sample environment group and could be used for modelling the magnet [SAN17]. The sample environment group also measured a stray field map for the magnet which was used as basis for the simulations. The map was measured at another experimental site and does not take into account any shielding effects of structural steels around STEREO. Its purpose was to define pacemaker limit areas and the precision of the map is not known. The 15-T-magnet was adapted in the simulations in two steps. At first the magnet coil dimensions from the technical drawings were implemented in the program 'magfield2' [Glu14]. This allows to compute the magnetic field of an axially symmetric coil system for coils with a rectangular shape cross-section and in absence of materials. The field can be calculated at any point in dependence of the coil current by numerically solving the elliptic integrals of the axisymmetric problem. The calculations are performed fast and can be used as reference point for the subsequent simulations. At first the virtual coil currents were adjusted iteratively until the calculated field agreed within a few percent with the discrete field values read from the field map. Subsequently the parameters of the magnet have been adapted in Comsol. A direct comparison of magfield2 and Comsol (Fig. 4.7) shows strongly alternating deviations in the vicinity of the magnet (outer radius = 22.4 cm) which may be related to the discretisation method used in Comsol, especially for the source point distribution of the field. At a distance of about 2 m from the magnet the two programs are in good agreement, whereas Comsol calculates higher fields for larger distances. In the range of STEREO, 3.0 m to 5.8 m from the magnet, the relative deviation between the two programs is smaller than 3%. The agreement between Comsol and the field map values is in the same range in the area of STEREO. The increasing deviation over distance in Comsol could be a result of the limited simulated volume. Without the zero field point at an infinite distance an appropriate boundary condition has to be set to correctly solve the differential equations. In the present case a so called open boundary condition was chosen on the outermost surface of the simulated volume, which represents a virtual transition to infinity. The observed evolution over distance indicates that the open boundary condition may not be performing well enough. The deviation could have been reduced by increasing the simulated volume, at cost of higher demands on computing power and longer calculation times. However, this slight overestimation is acceptable considering the precision of the values read from the field map and the unknown accuracy of the map itself. In addition the actual field strength at the position of STEREO may differ from the map since this has been measured at another site. Steel components in the walls, the floor or the structure of the reactor's transfer channel above STEREO can influence the field. Due to the irregular usage of the magnet, on-site measurements could only be performed when most of the simulations were finished. The measurements are summarised and their implications for the expected field are discussed in Section 4.4.

The simulations include the structural steel parts of STEREO (without muon veto components) and the magnetic shielding structures with their respective $\mu_{\mathrm{r}}(B)$ dependences. The considered materials are construction steel (S235JRG2) for the support structure and soft iron and mumetal for the shielding. The supplier and the corresponding material properties were not known at the beginning of the simulation campaign. VAC-mumetal was considered to have average properties and was thus chosen as first default. The layout of the support structure was directly taken from a complete CAD model of STEREO [Del14], simplified by omitting fine de-

tails and imported into the simulations. The relevant components for the magnetic shielding are the groundplate, composed of several H-beams, the steel support of the lead roof, consisting of two layers of solid steel plates above the inner detector, and the vertical steel beams connecting both. Structural steel of surrounding structures (floor, transfer channel, walls) have not been included.

While most components are included in the simulations as real elements the mumetal required an adapted treatment. Given its large aspect ratio (= extent/thickness) the mumetal cannot be implemented as a real geometry in the finite element simulations, since the number of required calculation points would be too large and require an unreasonably large calculation power. Instead it is incorporated as a virtual surface property. This means that its qualities, permeability and thickness, are only considered in the calculation of the field when crossing the assigned surface but there are no quantities calculated inside the mumetal itself, i.e. the maximum field reached inside the mumetal is not directly accessible in the simulations.

The procedure of the software to calculate the material's μ_r follows an iterative method: at first the complete field is calculated for an initial value of μ_r. In the next step the actual field inside the materials due to the external field and the magnetisation of the material itself is taken into account, leading to a new, local value for μ_r given by the $\mu_\mathrm{r}(B)$ dependence. This in turn changes the field, inside and behind the single shielding components. The field strength and the permeability are then recalculated in several iterations (mostly 5-10 steps) until convergence is reached, which means that the changes per iteration are smaller than a predefined precision ($1\,\mu$T in this case).

Considering the constraints on the shielding design defined by the layout of the site and the design of the STEREO setup a few shielding options are possible:

- Single shielding walls could be installed along the existing separation walls of the experimental zones.
- An outer case could be added around the full STEREO setup. Since the ground plate of the structure is wider than the rest of the setup this would not require additional space.
- An intermediate shielding could be placed in between the lead shielding and the support structure where an air gap of 1 cm was left to allow for tolerances in the construction precision.
- An inner, thin shielding case could be placed inside the BPE shielding.
- The material for each layer can be varied.

In the following the main investigated shielding concepts are presented as well as detailed studies on special features of the final design. As for any simulation the reliability of the results is limited and the resulting numbers cannot be taken as guaranteed. In addition the exact qualities of the shielding materials may vary in between different production batches and can easily be deteriorated during production or installation, thus changing their shielding efficiency. Therefore a safety margin of a factor 2-3 to the given specifications should always be kept for this type of simulations.

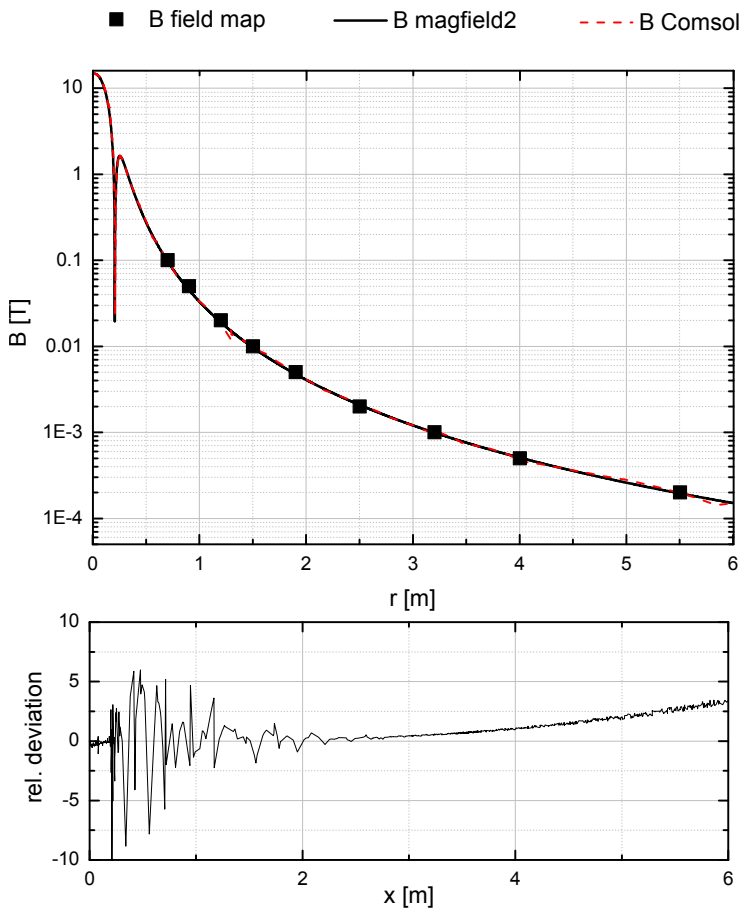

Figure 4.7: Top: Comparison of the different models of the stray field of the 15 T magnet: stray field map (unperturbed field, does not include shielding effects from structural materials), magfield2 and Comsol calculations. Bottom: Relative deviation between magfield2 and Comsol. In the range of STEREO (3 m to 5.8 m) Comsol calculates 2% to 3% higher fields.

4.3.1 First Considerations

In the absence of any magnetisable material the magnetic field reaches a maximum of 0.64 mT at the position of the detector PMTs. With the STEREO support structure alone this is reduced to 0.39 mT, which is still more than a factor of six above the specifications of 60 μT (a factor of $\sim$40 above the initial specifications of 10 μT).

By use of Eqs. (4.4) and (4.5) a first estimate of shielding efficiencies of different setups can be calculated, under simplified assumptions. As possible settings cubic shielding structures with side lengths of 3.4 m for an outer iron shielding, 2.9 m for a potential intermediate iron shielding (maximum 1 cm thickness possible) and 2.4 m for an inner mumetal shielding ($\mathcal{O}(1)$ mm thickness) and a homogeneous outer field of 500 μT over the full roof surface are considered, which corresponds to about the average of the real field, which decreases over distance. The material properties are from ARMCO soft iron with the initially available values and MecaMagnetic Mumetal, see Figs. 4.4 and 4.5. With these assumptions in an iterative process the μ_r of the material, the resulting shielding factor, the field in the inner volume of the shielding and, with the boundary condition that the overall magnetic flux $\phi = B \cdot A$ over the cross section area A of the setup is constant, the field in the shielding material itself can be calculated. For a double layer iron shielding with 2 cm and 1 cm thicknesses for the outer and intermediate shielding, respectively, a field of about 80 μT is obtained in the inner volume, including the shielding factor of the structure. This is above the required limit. The magnetic field in the soft iron reaches only a few mT, which is far from saturation. A change of the thickness would cause an about inversely proportional change in μ_r, due to the increase of the cross section area, without changing the

inner field significantly ($B = \phi/A$, $\mu_r \sim B$). In the case of an outer soft iron shielding and an inner mumetal layer the field in the inner volume would be decreased to $\sim$20 μT, which would fulfill the relaxed, final specifications.

These simplified calculations were also tested with simulations, at first it was tried to avoid the usage of mumetal by adding other shielding components. For this purpose a 2 cm thick plate was added on top of STEREO's base plate, four vertical, 1 cm thick plates in between the lead shielding and the support structure, which are in contact with the ground plate and the lead roof support, and an outer case of 3.3 m height (including the muon veto) consisting of 2 cm thick plates. The distance between the vertical walls of the cases is 23 cm, which is rather small compared to their dimensions of about 270 cm in x (short axis of STEREO) and 410 cm in y (long axis of STEREO) for the outer box. At first the case is considered that both boxes are built of soft iron, where the initial default material properties for soft iron correspond to the ARMCO iron with annealing. The field in a plane perpendicular to the x-axis at the position of the closest PMTs ($x = 3.7$ m) shows that at the level of the PMTs the field lies in-between 40 μT and 60 μT, Fig. 4.8, which is lower by a factor of $\sim$2 than the simplified calculations above. This did not fulfill the initial specification and leaves no margin to the final one. The weak point is clearly the bottom where only one closed shielding layer can be installed. In addition the magnet is at 1 m height, leading to an asymmetry in z. However, at the height of the PMTs ($z = 1.7$ m) the contribution from the high field at the bottom is not very large.

When considering only the field parallel to the x-axis through the closest detector PMT at a height of $z = 1.7$ m, Fig. 4.9 left, the two shielding layers can be clearly identified by their higher magnetisation. While the outer shielding reduces the field by nearly one order of magnitude the inner shielding reduces it only by an additional factor of two. According to Eq. (4.5) this can be understood as a consequence of the small distance in between the layers. Inside the shielding the field continues to decrease with distance.

To further improve the shielding a single shielding wall was added, following the line of the concrete walls between STEREO and IN20. This would be 2 cm thick, 4 m high and in total 6 m long. It reduces the field maximum in the simulations for the detector PMTs from about 60 μT to 40 μT, which is a rather moderate improvement compared to the required amount of material. While a single wall is an effective shielding for quasi-parallel fields, e.g. the present vertical field of the magnet, in the given setting the field lines can be easily deflected above the wall or even more through the floor below. As a consequence the wall is only effective at short distances. The comparison of the field along the same axis as before, Fig. 4.9 right, shows that in addition the magnetisation of the shielding cases is lower when the additional wall is present. This implies that their shielding efficiency is decreased, due to the $\mu_r(B)$ dependence of the materials. For these reasons, the high amount of required material and potential difficulties in the installation, e.g. a verified calculation would have been required to proof that the attractive forces between the wall and the magnet are sufficiently small not to cause damage to the magnet, the option of single shielding walls was omitted.

4.3.2 Mumetal Case

From the preceding simulations it can be concluded that a two layer shielding is necessary in order to reach a sufficiently high shielding factor. As the double soft iron case does not fulfill the specifications with a sufficient margin, materials with better shielding properties have to be considered. For this reason the inner shielding layer was replaced by 1.5 mm of mumetal and moved inside the BPE shielding. In the simulations it forms a closed box directly around the inner detector of STEREO with outer dimensions of $1.6 \times 3.2 \times 1.7\,\mathrm{m}^3$. The outer case is a 1 cm soft iron layer around the whole setup, including the muon veto. Its dimensions are $2.6 \times 4.2 \times 3.1\,\mathrm{m}^3$.

In a first comparison of possible materials for the outer case steel had turned out not to be sufficient to reach the specifications, fixed at 10 μT at that time, raised to 60 μT later. The

combination of soft iron, ARMCO, not annealed, and a closed mumetal case, MecaMagnetics, on the other hand reduces the field below 5 μT. This fulfills the original requirement and has a large margin to the new limit, thus allowing for some changes in the layout in order to obtain a feasible design. Consequently in the following studies the outer shielding is considered to be from soft iron.

The mumetal shielding was added to the general design as one of the last parts. Therefore it had to be adapted to the already planned structures. The best solution is to attach single mumetal sheets of 1.5 mm thickness to the inner surface of the polyethylene shielding. Considering the design of the BPE at the time of the first simulations it was not possible to implement the mumetal shielding as a closed box. In fact the 'roof' was detached from the walls and placed as an individual plate in between them, see option A in Fig. 4.10.

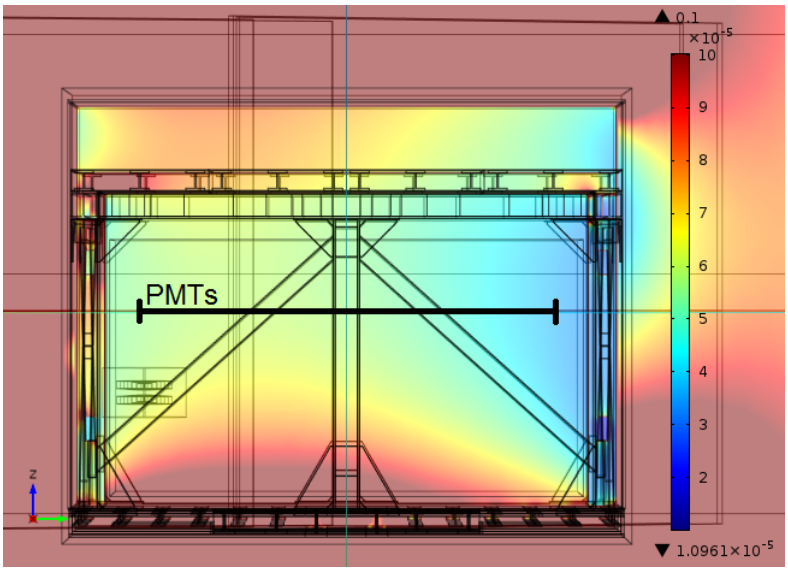

Figure 4.8: Two-dimensional cut along the length of Stereo (yz-plane) at the position of the PMTs closest to the magnet ($x = 3.7$ m). The graph shows also a projection of the IN20 magnet in the closest position. The shielding setup is a double-layer iron case (thickness outer layer: 2 cm, inner layer: 1 cm) with material properties corresponding to ARMCO iron with annealing. The magnetic field is highest at the bottom, where it is only attenuated by one shielding layer. In the area of the detector PMTs ($z = 1.7$ m, thick, black line) the field is in the range of 40-60 μT. The colour code gives the fields from $1 \cdot 10^{-5} - 10 \cdot 10^{-5}$ T.

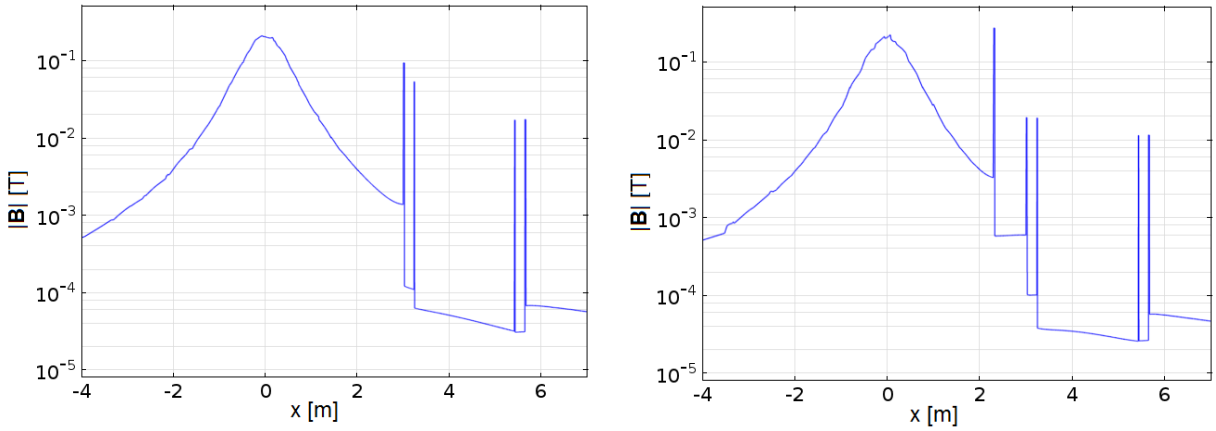

Figure 4.9: Magnetic field parallel to the x-axis through the PMT closest to the magnet ($z = 1.7$) for a double-layer iron case around Stereo (left) and with an additional single-layer iron wall between IN20 and Stereo (right).

This would cause small gaps between the roof and the walls, whose width would be in the range of 1 mm to 2 mm, given by the fabrication precision of the BPE shielding and margins needed for its installation and to compensate its thermal expansion.

Simulations of this setup, described below, showed that this configuration would cause a factor of 10 higher fields than a closed mumetal box. Considering this the BPE shielding later was redesigned so that in the final layout the mumetal forms a closed box. Horizontally bent edges are attached on top of the walls to guarantee an overlapping area with the roof. In addition gaps in between single mumetal sheets of the side walls and the roof are covered by additional stripes of mumetal, as shown in option B in Fig. 4.10. In this way the highest possible shielding efficiency is achieved.

First studies were performed for roof option A. Even so this option is not selected for the final design it gives a good indication of the importance to avoid gaps in-between single shielding plates. With 2 mm wide gaps all around the roof plate the maximum field in the plane of the detector PMTs would have been $B_{\mathrm{det}}^{\mathrm{gaps}} = 28\,\mu\mathrm{T}$, Fig. 4.11, left, leaving a safety factor of two to the specifications. The final design with a closed box on the other hand leads to a maximum field of $B_{\mathrm{det}}^{\mathrm{closed}} = 3\,\mu\mathrm{T}$ in the detector PMT plane.

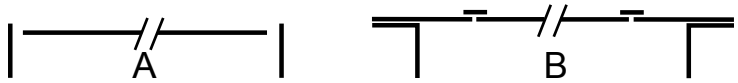

Figure 4.10: First (A) and final (B) design of the mumetal roof and the connection to the walls. Option A yields information about the impact of gaps in the shielding.

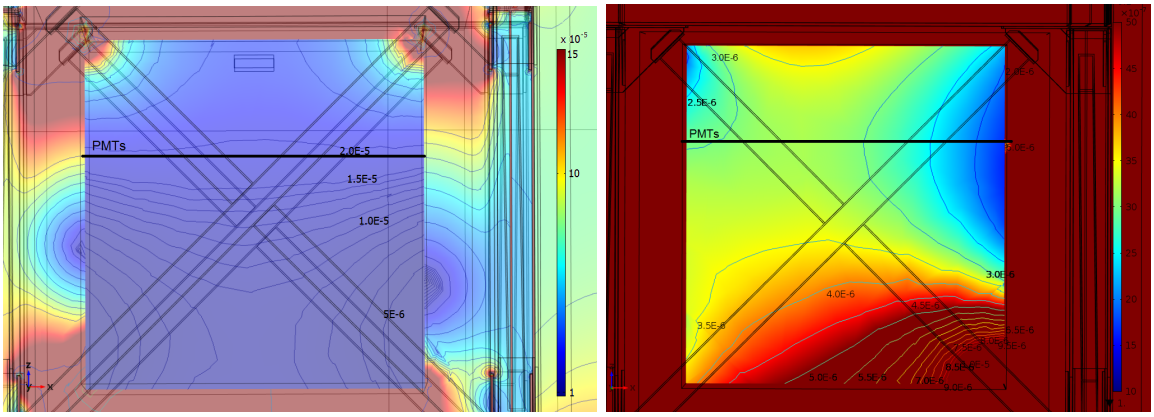

Figure 4.11: Cut in a vertical plane along the short axis of STEREO. The IN20 magnet is on the left. The PMT plane is marked by the black line. The volume shielded by mumetal is clearly identifiable by the lower fields. The shielding materials are non annealed ARMCO soft iron and MecaMagnetic mumetal. Left: roof option A (see Fig. 4.10) with 2 mm gaps around the roof plate. The resulting field in the PMT plane lies between 10-30 μT. The colour scale ranges from 10-150 μT. Right: roof option B, but with a 2 mm gap at the bottom, D19 side. The resulting fields at the PMT positions are in between 2.0-3.3 μT. The colour scale ranges from 1-5 μT. In the final design all gaps were avoided by adding additional cover panels at all junctions of single mumetal sheets, analogous to Fig. 4.10B.

Considering the strong influence of the gaps around the roof on the field in the PMT plane, the effect of gaps in other sides was investigated, too. Initially it was foreseen to place the bottom mumetal sheets on the flat BPE shielding. The sheets would be placed in contact with the walls at the IN20 side and all clearances moved to the D19 (opposite) side. To check the influence of a gap a simulation was performed where a 2 mm wide opening was included in the bottom plate along the edge towards D19. This has an impact on the field in the lower half of

the inner volume but only a small effect on the PMT plane as can be seen in Fig. 4.11, right. The increase from 3 μT to 3.2 μT is below the expected precision of the simulations and thus negligible. However, in order to avoid potential risks of gaps between mumetal sheets, especially in the side walls, grooves were cut into the PE shielding to allow to add 20 mm wide mumetal cover panels at all borders and corners of mumetal sheets, guaranteeing and overlap as shown in the sketch in Fig. 4.10B.

4.3.3 Cable Feedthrough

The instrumentation of the inner detector requires a feedthrough for cables and tubes for calibration sources in the shielding. This is included in the rear side of the setup, above the inner detector and directly underneath the roof of the mumetal shielding. It is a straight channel through all shielding layers without chicane. For the simulations an opening of 20 cm width and 6 cm height was assumed. It is located in a lateral wall and thereby parallel to the almost vertical field lines. The feedthrough leads only to a very localised increase of the field, see Fig. 4.12. Since it is situated above the PMTs, this does not alter their performance.

4.3.4 Access to the Calibration System

The calibration system of the inner detector requires mechanical access to put in place the different calibration sources. Hence a hatch had to be designed through all the shielding layers: mumetal, polyethylene, lead and soft iron. For the mumetal there are no options for the design - the opening is slightly smaller than the hatch to guarantee an overlap where the fix parts and the door come into contact. On the outside the soft iron also has to cover the rail system of the door, which is wider than the rest of the support structure. Therefore a small channel is required, where the opening can be covered in two simple ways:
A - the hatch is larger than the covered opening and is attached at the outside of the shielding. Any clearances would lead to gaps between the hatch and the fix shielding.
B - the hatch is smaller than the opening and is embedded in the small chimney. The remaining gaps in between the door and the chimney are then again in a vertical plane and parallel to the field lines of the external field, see Figs. 4.13 and 4.14.

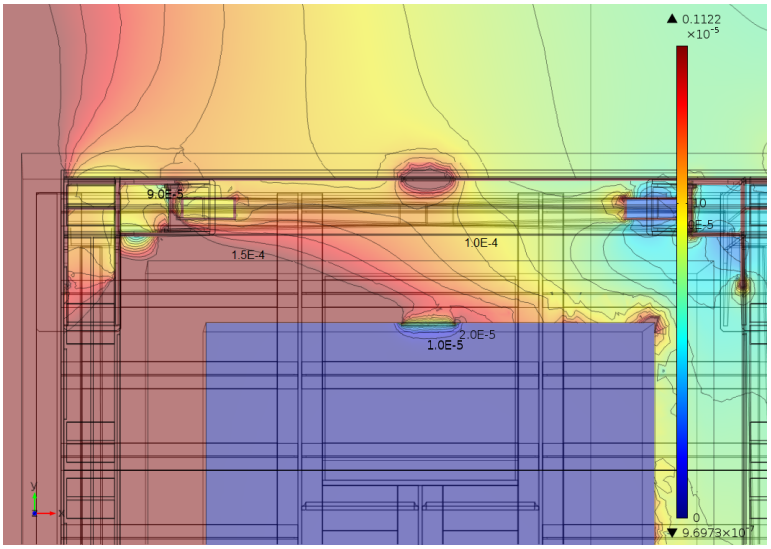

Figure 4.12: Top view of the rear end of STEREO, in a plane just below the roof of the mumetal shielding, for roof option B. The feedthroughs in the two magnetic shielding layers can be easily identified by the change in the field strength. The field inside the mumetal shielding is not significantly affected since the outer field is parallel to the openings. The given colourcode covers a range from 0 - 150 μT.

The simulations were done with gaps of 2.5 mm between the overlapping areas for option A2 and in between the hatch and the chimney for option B. The two configurations show no significant difference. In both cases there is only a small, local distortion of the field inside the soft iron shielding. There is no significant effect on the field inside the mumetal box. For an easier manufacturing it was decided later to build option A1. This was not simulated, but no significantly different behaviour is expected.

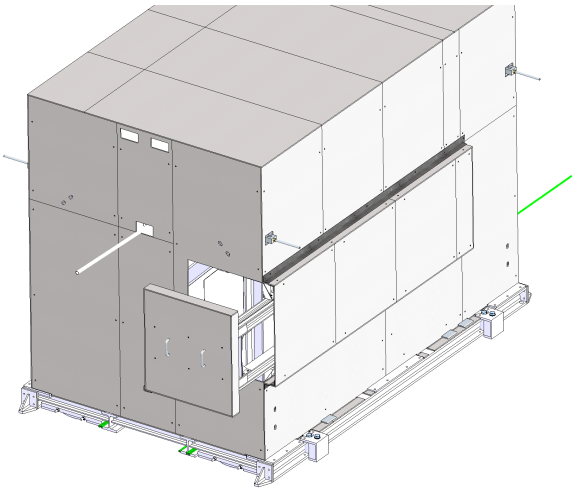

Figure 4.13: Design of the outer magnetic shielding layer around the STEREO setup. From [Fua15].

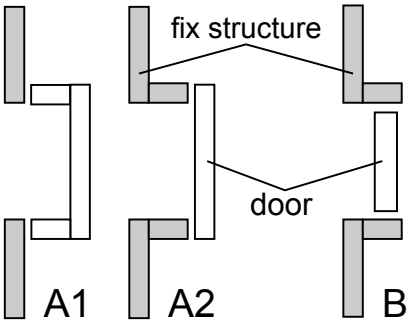

Figure 4.14: Design options for the access to the calibration system in the soft iron shielding.

4.3.5 Shielding of the Muon Veto

A change in the gain of the veto-PMTs due to magnetic fields could change the overall efficiency of the veto, which should be avoided in order to allow for a consistent data acquisition. In particular since the magnet is only used during reactor cycles, but not during the shutdown, when only the cosmic background is measured. So far in the simulations the veto was only enclosed in the soft iron shielding, resulting in a maximum field of 0.12 mT for the outermost PMTs. For an improved performance an additional mumetal box is added. In the final version of the simulations this is a closed box with the dimensions $2.57 \times 3.17 \times 0.6\,\mathrm{m}^3$ and a wall thickness of 1 mm. It has a distance of 7 mm to the lateral walls and the top plate of the soft iron and it is placed directly on the top parts of the STEREO main structure, which means that it is in contact with the upper steel plates of the lead roof support. The small distance in between the layers is unfavourable in terms of magnetic shielding, as stated in Eq. (4.5), but is a direct consequence of the aim to cover as much of STEREO's detector area as possible with the veto. The cut in the horizontal plane (x-y) in Fig. 4.15, bottom, shows the field at $z = 3.1\,\mathrm{m}$, the height of the veto-PMTs. The maximum of the field is located at the y-coordinate of the magnet and reaches a value of $19\,\mu\mathrm{T}$. This leaves a margin of a factor three to the desired $60\,\mu\mathrm{T}$. The minimum is about $10\,\mu\mathrm{T}$, giving variations of a factor two for different positions in the veto. The vertical cut along the short axis of STEREO at the position of the highest field in the veto-PMT plane, Fig. 4.15, top, shows a rather inhomogeneous field. This is caused by the local maximum corresponding to the position of the magnet and the fact that due to the small height of the veto inhomogeneities from border effects are more dominant throughout the volume.

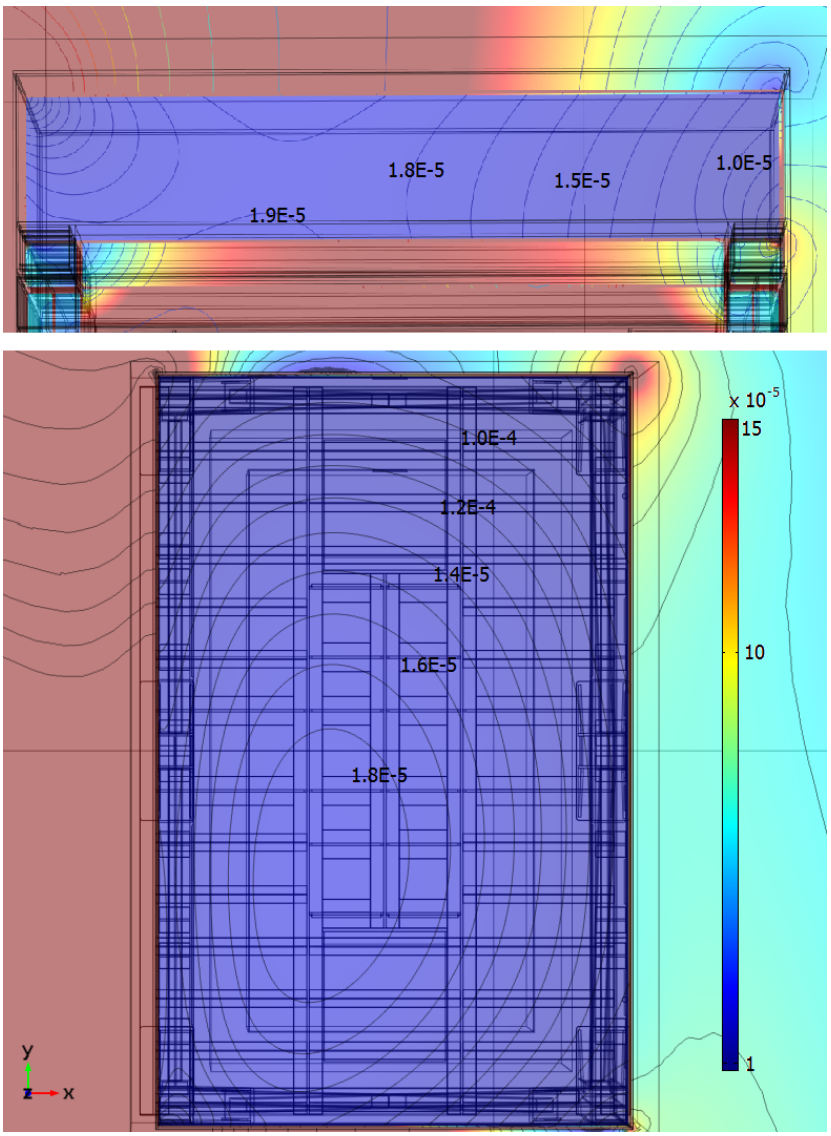

Figure 4.15: Top: vertical cut through the veto volume, at the position of the highest field. Bottom: horizontal cut in the veto volume at the height of the veto PMTs (z = 3.1 m).

The mumetal box would guide the magnetic field around the enclosed volume of the veto without any significant influence on the field strength in the main detector volume. However, considering the additional costs, difficulties in the installation when allowing for clearances and the fixation of the soft iron on the veto, it was decided not to include the mumetal box but to use double layer mumetal cylinders around the veto PMTs.

4.3.6 Field Orientation

The effect of the magnetic field on the PMTs depends on the field orientation with respect to the PMT's axis. In addition the single PMTs are protected by individual mumetal cylinders. These have not been included in the previous simulations but are studied separately in section 4.3.7. Their shielding efficiency depends strongly on the orientation of the field with respect to the cylinders' axis, where it is highest when they are perpendicular to each other and lowest when they are parallel. When installed in STEREO the cylinders will be vertical.
The field inside the closed shielding, without the veto mumetal, is shown in Fig. 4.16. While the field outside the shielding is nearly horizontal at the height of the veto, the orientation changes strongly inside the shielded volume. Inside the veto volume the field lines have an angle between 30° and 45° towards the vertical axis. In the main volume they are mainly vertical, with distortions only close to the lateral walls.

When including a veto mumetal box, as described in Section 4.3.5 the field within the veto volume turns slightly more to a vertical orientation, by about 5°. The behaviour of the field in absence of any shielding is discussed in Section 4.4.2.

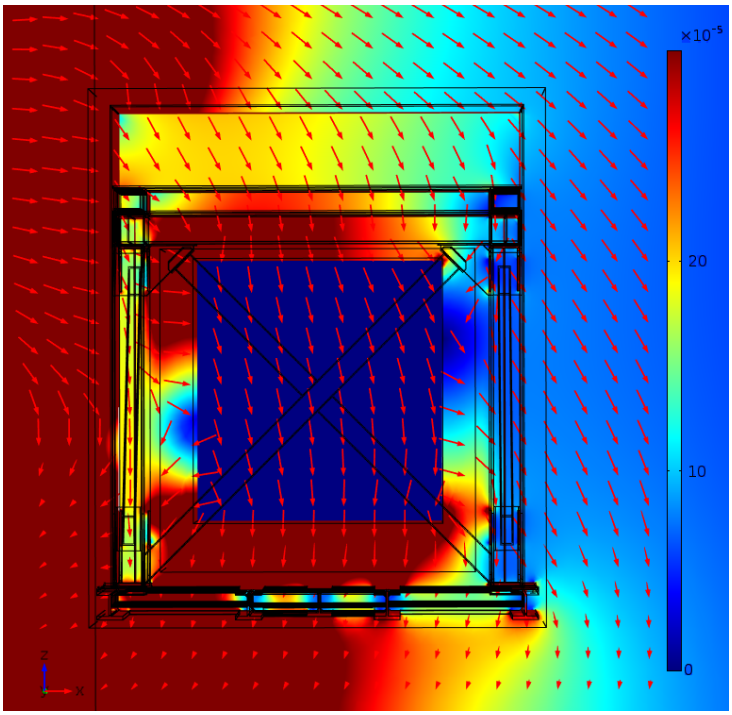

Figure 4.16: Directions of the magnetic field inside the magnetic shielding. In the veto volume the angle towards the vertical axis is between 30° and 45°. In the main volume the field is mainly vertical, with distortions only close to the lateral walls. The plotted arrows are normalised in size. The indicated direction (3D) is valid for the point of origin of each arrow.

4.3.7 Mumetal Cylinders

The mumetal cylinders which are placed around the individual PMTs have not been included in the previous simulations since their shielding effect was already included in the definition of the shielding requirements [Stu15a] and because of the otherwise much higher demands on computing power, due to their large aspect ratio. However, the shielding effects of the cylinders have been studied separately for an external field of 10 μT perpendicular or parallel to the cylinder's axis. For these simulations the same field definition as for the full simulations has been used and scaled to the required magnitude. This field has a gradient along the x-axis, perpendicular to the cylinders axis, which will also be the case in the final setup, at least for the veto where the cylinders are more important. In the final design the cylinders for the detector PMTs have an inner diameter of 217 mm, a height of 230 mm and a wall thickness of 1 mm. To allow the mechanical mounting three pairs of holes are placed at a height of 27 mm above the lower edge of the cylinders. The holes of one pair have a diameter of 5 mm and are 40 mm apart. The pairs are placed at angles of 120° to each other.

Due to an error in the manufacturing process the hole pairs have not been placed at the correct angular positions so that two additional pairs had to be drilled. To check if the additional holes have a significant influence on the shielding properties, in which case the unused holes would have to be covered, or not, simulations of the 3-hole-pair and the 5-hole-pair configuration have been performed. Due to the initial non-convergence of the simulations for a variable μ_r of the mumetal and the necessity of a quick decision about the coverage of the additional holes a constant $\mu_r = 10000$ was chosen. This led to a converging solution and largely reduced the calculation time. The chosen value seems reasonable considering the material properties provided by the supplier, Fig. 4.5.

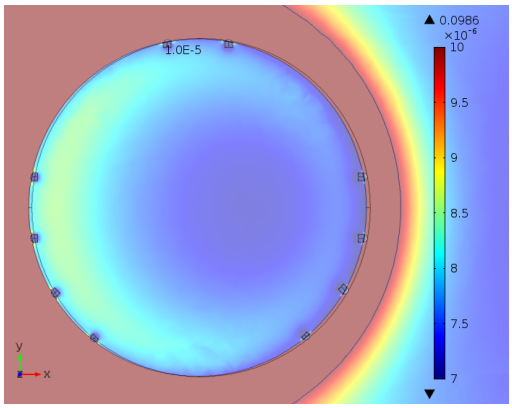

Figure 4.17: Horizontal cut through the plane of the drill holes of a mumetal cylinder in a vertical orientation, parallel to the field of 10 μT. The field has a small gradient along the x-axis. The holes have no significant effect on the field inside the cylinder.

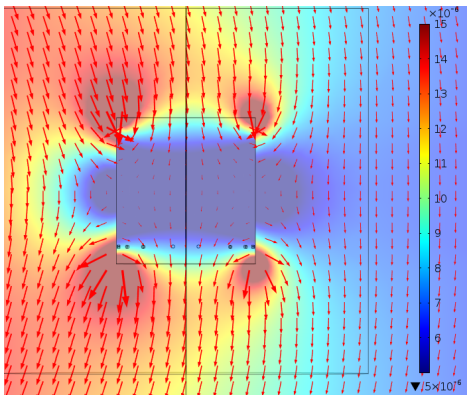

Figure 4.18: Vertical cut plane through the symmetry axis of a mumetal cylinder. The arrows indicate direction and strength of the field. The effect of the holes on the magnetic field is negligible compared to the effect of the edges of the cylinder. The external field has a small gradient perpendicular to the cylinder's axis, which will also be the case within the veto.

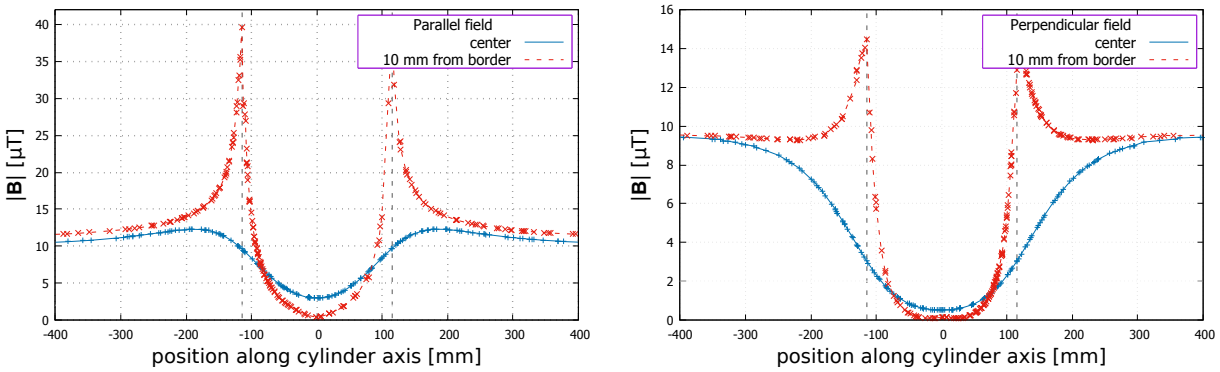

Figure 4.19: Magnetic field along the central axis and at 10 mm from the wall of a mumetal cylinder in an external field of 10 μT parallel (left) or perpendicular (right) to its axis. The cylinder is centered at zero and the vertical, dashed, black lines show its extensions. The shielding effect on the central axis is smaller due to the entering external field, but close to the wall the edge effects are more pronounced. The lateral field (right) is reduced more strongly and more homogeneously. The points correspond to nodes of the finite element simulation, the lines are interpolations for better visibility.

For both configurations of the cylinders no significant influence of the holes on the magnetic field could be seen. The resulting field for the 5-hole-pair layout, which finally has been installed, is shown in Figs. 4.17 to 4.19. For a field parallel to the cylinder's axis the field is reduced by about a factor of four on the central axis and about a factor of ten at 1 cm from the wall. On the central axis the external field reaches far into the cylinder. For a perpendicular field the suppression is about one order of magnitude in the center and nearly two orders at the side.

4.3.8 Summary of the Simulation Results

The performed simulations have shown that the field of the 15 T magnet at IN20 in the closest position can be shielded by a two layer shielding layout: a housing of non-annealed soft iron of 1 cm thickness around the whole setup combined with separate mumetal cases of 1.5 mm thickness around the inner detector and the veto. The simulated final design includes the de-

tector mumetal box option B of Fig. 4.10 and the calibration system access door option A1 of Fig. 4.14. For the veto, however, the mumetal box has not been implemented, due to the small space available between the veto and the soft iron. Instead the single PMTs are shielded by two mumetal cylinders with a 2 mm air gap in between. Without the cylinders the simulated maximum field would be $B_{\mathrm{det}} = 3\,\mu\,\mathrm{T}$ in the detector PMT plane and $B_{\mathrm{veto}} = 235\,\mu\mathrm{T}$ in the veto PMT plane, assuming a 3 m distance between the magnet and STEREO. When assuming the closest possible position at 2.7 m distance the maximum fields would be $B_{\mathrm{det}}^{\mathrm{corr}} = 4\,\mu\,\mathrm{T}$ for the detector PMTs and $B_{\mathrm{veto}}^{\mathrm{corr}} = 294\,\mu\mathrm{T}$ for the veto PMTs. The resulting shielding factors of the most relevant studied setups are listed in Table 4.1.

Table 4.1: Summary of the results for the most relevant simulated setups. The configuration which has been realised is indicated by ⊗. In addition to the outer shielding all PMTs are individually shielded by mumetal cylinders, single layered for the detector and double layered for the veto. Listed are the maximum fields in the PMT planes, obtained from the simulations for a central field of 15 T of the IN20 magnet, and the values corrected for the closest possible magnet distance as well as the shielding factors from the simulations. Considering the simulation precision and particularly possible variations of the shielding efficiencies of the considered materials a safety margin of a factor 2-3 should be taken into account.

Setup	$B_{\mathrm{max}}[\mu\mathrm{T}]$ | $B_{\mathrm{max}}^{\mathrm{corr}}[\mu\mathrm{T}]$ $z = 1.7\,\mathrm{m}$ (detector) $z = 3.1\,\mathrm{m}$ (veto)	Shielding Factor
no shielding	640 | 830	1
steel - VAC mumetal [Bol90], roof option B	10 | 13	64
steel - VAC mumetal, roof opt. A	33 | 44	19
iron, ann. - VAC mumetal, roof opt. B	5 | 6	131
iron, ann. - VAC mumetal, roof opt. A	18 | 23	36
iron, not ann. - VAC mumetal, roof opt. A	30 | 40	21
iron, not ann. - Meca mumetal [Arc04], roof opt. A	28 | 36	23
iron, not ann. - Meca mumetal, roof opt. B ⊗	3 | 4	213
veto, no shielding	840 | 1060	1
veto, iron, ann.	120 | 151	7
veto, iron, not ann. ⊗	235 | 294	3.6
veto, iron, ann. - mumetal VAC	20 | 25	42

ann. - annealed

4.4 Measurements of the Magnetic Field

4.4.1 Setup

The 15 T-magnet was installed at IN20 at the end of reactor cycle 175, from 29/07/15 to 06/08/15. During this time the setting was not constant but was changed several times. The field strength itself was set to different levels between 0 T and a maximum of 13.5 T, where the periods of constant field lasted at least several hours each time. The maximum field was chosen by the experiment responsibles, technically 15 T are possible. The magnet's position was changed in shorter intervals of only a few minutes, given by the measuring procedure of IN20. In the specific case the magnet was moved away from STEREO in small steps until a maximum distance was reached, where each intermediate position was typically kept for ≤ 10 min. Afterwards it was moved back to the initial position in one step.

For the magnetic field measurements a three-axis Hall-probe, model LakeShore 460 HSE (high sensitivity), was used. It allows the determination of the three field components inde-

pendently. The probe was mounted on a movable support on an aluminium rail, allowing to measure the field in several collinear points while guaranteeing unchanged orientations of the probe's axes. For the setup only non-magnetic materials have been used to avoid perturbations of the measured field.

All three channels of the probe have been set to the highest sensitivity setting, $\pm 3\,\mathrm{mT}$, which covers fully the expected field range. To reduce the signal noise a so called filter allows to average over an adjustable number of probe read-outs, where one value is taken every 0.25 s. The filter can be varied between 2 and 64 points with a linear averaging. It was set to 4 for all channels. In addition each position was measured three times with two seconds delay each time to obtain a more reliable result.

When switching on the probe a warm-up phase of about 30 min is recommended before the start of the measurements. After this time usually an offset in the signals of the single channels could be observed. An absolute calibration of the Hall-probe is not necessary, only the offsets of the single measuring axes have to be corrected. This can be done by setting the probe to zero when placed in a "zero gauss chamber", a small mumetal box which should reduce all external fields. However, during the preparation of the measurements it was observed that this calibration was not always sufficient, probably due to residual external fields, which caused a remaining offset in the axes. In addition a drift of the offset was observed over time, where it was not clear whether this was an intrinsic property of the probe or caused by changes in the environment. To guarantee reliable results the offsets were determined before each series of measurements (typically 12 points) by inverting the orientation of the probe in a fixed position. The shift can then be calculated by adding up the values x measured with opposite orientations:

$$B_x + \text{offset} + (-B_x) + \text{offset} = 2 \cdot \text{offset} \ . \tag{4.6}$$

By rotating the probe only two axes can be inverted at a time, leaving the third one unchanged. For reasons of practicability only one rotation was performed. For all measurements in a horizontal plane the non-inverted axis was the probe's z-axis, which showed the most stable time behaviour. For vertical measurements the x-axis was unchanged. The offset of the not inverted axis was later taken as the average offset from the measurements done in the other orientation on the same day.

In order to investigate the impact of a residual drift a long-term measurement with only the earth's magnetic field was performed. Despite the absolute drift of 0.01 mT during the 2.8 days of this measurement the average standard deviation during 5 min, which was the typical duration of one set of measurements of the magnetic field scans, is only $1\,\mu\mathrm{T}$, smaller then the envisaged accuracy.

4.4.2 Expected field

The shape of the magnetic field can be calculated with 'magfield2' [Glu14], which was already used to model the magnetic field. The program is capable of calculating the axial and radial components of the unperturbed field in cylindrical symmetry. It is preferred over Comsol for this task since the calculation times are much shorter and the field can be calculated for arbitrary points while Comsol is limited to the nodes of the finite elements geometry. The results of the two programs are in reasonable agreement, in both size (see Section 4.3) and shape.
The calculated vector field is shown in Fig. 4.20, where the length of the arrows within the STEREO area is proportional to the field strength, while in the vicinity of the magnet it is normalised, for a better visibility. The graph represents a cut through the magnet and perpendicular through the detector. In the closest magnet position this plane is at about 77 cm inside STEREO, measured from the reactor side. The field orientation differs from that inside the magnetic shielding setup described in Section 4.3.6. In the range of the muon veto (z>3 m) the field is mainly horizontal at the IN20 side and turns to 54° towards the vertical axis at the D19 side. Going to lower heights the field turns to an average angle of 30° at the inner detector's PMT plane (z =1.7 m) and is completely vertical at the height of the magnet at $z = 1.03\,\mathrm{m}$.

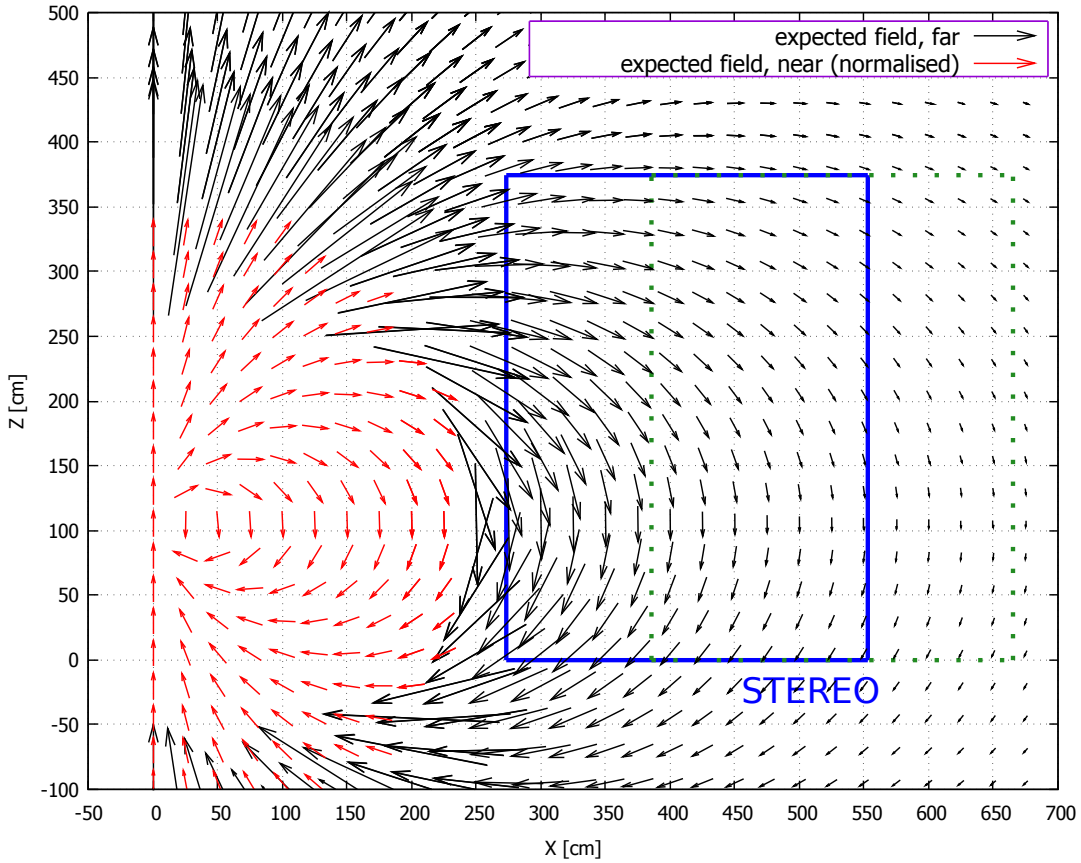

Figure 4.20: Magnetic flux density of the IN20 vertical magnet for $B_0 = 13.5\,\mathrm{T}$, calculated with magfield2 assuming an unperturbed cylindrical symmetry. Magnetic materials in the walls and the STEREO shielding are not taken into account. The graph shows the field orientation in dependence of the distance x from the magnet and the height z above the ground. The arrow length of the far field is proportional to the field strength while for the near field (red) it is normalised for a better visibility. The contours show the STEREO area in the nearest (solid line) and furthest (dashed line) magnet position.

4.4.3 Measurements

The aim of the measurements was to validate the orientation and the strength of the magnetic field within the whole unshielded STEREO volume and to detect any anomalies, either caused by additional external fields or by magnetic materials which deform the field significantly. In order to achieve a good coverage, scans were performed in three horizontal planes: the ground ($z = 6\,\mathrm{cm}$), the PMT plane of the inner detector ($z = 1.7\,\mathrm{m}$) and the PMT plane of the muon veto ($z = 3.1\,\mathrm{m}$). In each plane the field was measured along the long axis of STEREO at the outermost position on the IN20 side (approximately at the position of the outer shielding layer), in the center and at the outermost edge at the D19 side. In addition measurements were performed along the short axis of STEREO at the front, in the center and at the rear end. In order to monitor the field behaviour in between these planes, scans were also performed along vertical axes at several points along the contour of the outer shielding. The step size in between the single measured positions along these axes was always 25 cm. At some points there are deviations from the described pattern due to other setups which had been in place. In the veto plane at the front end of the IN20 side three PMTs had been placed to characterise their behaviour in the field. Two of them had mumetal cylinders as a shielding, which may have altered the measured field locally although a distance of $\sim 15\,\mathrm{cm}$ had always been kept.

The measurements were performed when the magnet was at a constant field level. Due to the field changes it was not possible to measure all positions at the maximum field of $B_{0,1}$ =13.5 T,

but some were measured at $B_{0,2} = 11\,\mathrm{T}$ instead. For comparison these values have been scaled by the factor $B_{0,1}/B_{0,2}$. The results of the measurements are shown in Fig. 4.21. The shape of the field follows the expectations in general, although the horizontal component is for all heights more dominant than predicted, i.e. the field in the veto plane is basically horizontal.

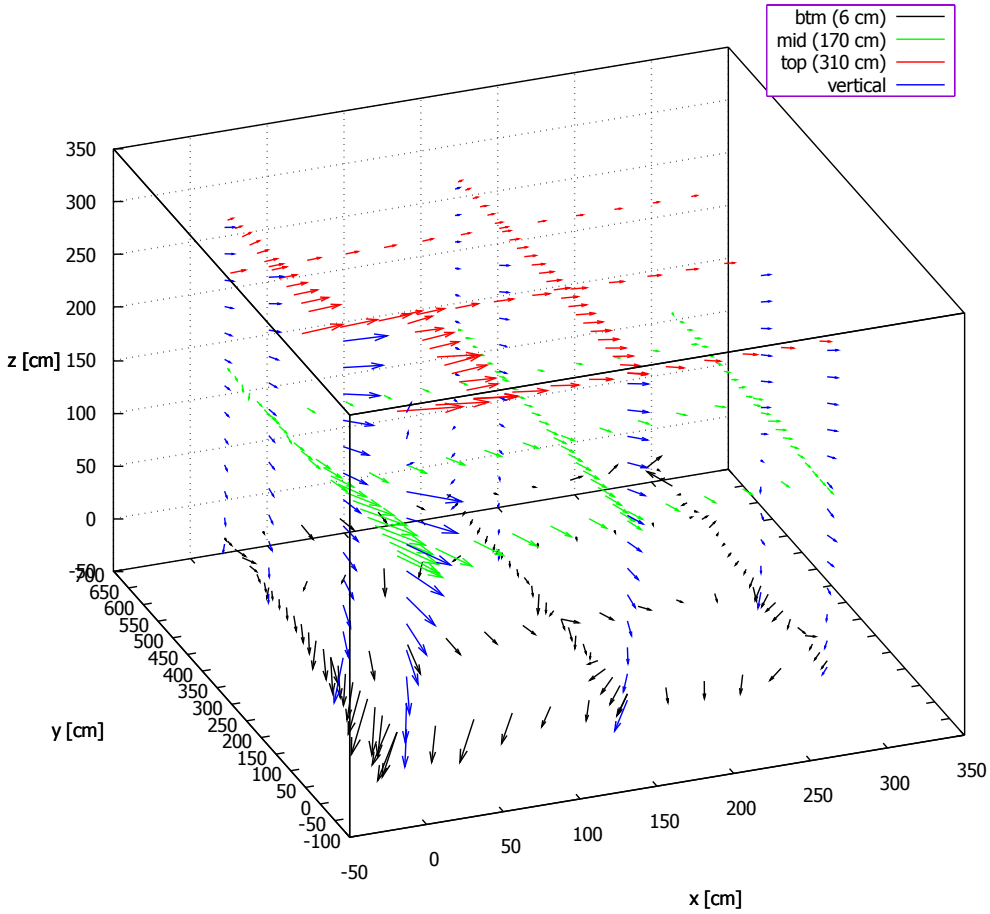

Figure 4.21: Measured field orientation at the STEREO site for a central field of 13.5 T of the IN20 magnet, as seen from the reactor side. During the measurements the magnet was located at distances between 3.5 m and 3.7 m from STEREO. The measurement positions follow the pattern described in the text. The significant differences in the field orientation at the bottom are caused by different steel structures below. The coordinates are given relative to the front-IN20 edge of STEREO's outer shielding case.

The measured orientation of the field is in general agreement with the simulated field, therefore there is no update of the simulations necessary in that respect. The field strength at the position of the outer shielding towards the IN20 side on the other hand is lower than expected from the given fieldmap when taking into account the lower maximum field of $B_0 = 13.5\,\mathrm{T}$ and the position of the magnet at the time of the measurement. The measured maxima of the field at the front end of the IN20 side are $B_{\mathrm{V,meas}} = 0.42\,\mathrm{mT}$ and $B_{\mathrm{D,meas}} = 0.41\,\mathrm{mT}$ for the veto PMT plane (V) and the detector PMT plane (D), respectively. In both cases the magnet was at a distance of about 3.7 m, where the calculated field strengths are $B_{\mathrm{V,calc}} = 0.51\,\mathrm{mT}$ and $B_{\mathrm{D,calc}} = 0.58\,\mathrm{mT}$, leading to a deficit of 18% for the veto and 30% for the detector between measurements and expectations. This is even increasing towards the rear end of STEREO, where the measured field is 30% and 50% lower than expected. The small overestimation of the field in the simulations with respect to the field map is not large enough to explain this discrepancy. Another cause could be a distance-depended shielding effect by structural steel, e.g. in the floor. This is normally arranged in a grid structure. A larger distance would therefore allow for more

parts of this grid to contribute to the field attenuation.

These observations apply to the outer shielding position at the IN20 side, which is besides the transfer channel. The lateral scans (along the short axis of STEREO) in the top plane (veto) show a sudden increase of the observed deficit from 20% to 30% - 35% at a distance of 1 m from the outer shielding position, corresponding to positions under the transfer channel. This difference in between the areas with and without overburden indicates that the structural material of the channel gives some additional shielding at the height of the veto. In the inner detector's PMT plane on the other hand this difference could not be observed. Underneath the transfer channel the deficit is constant from the IN20 side to the D19 side, but increases from the front to the rear end of the area.

The measured field is in general lower than expected. From Section 4.3.8 it is known that the expected field inside the shielding, for the corrected minimal magnet distance, is 4 μT in the detector and 0.29 mT in the muon veto. Taking into account the additional shielding effects observed in the measurements and assuming that they still would have the same impact when the STEREO setup is in place the final expected fields would be about 3 μT and 0.24 mT in the detector and the muon veto, respectively.

At the end of cycle 175 the 15-T magnet was installed for about one week. During this time the position closest to STEREO was never reached. In addition the integrated time during which the magnet was closer than 3 m was less than 10 min. This may be different for a different experiment conducted at IN20, but it is unlikely that the minimum position is kept for a long time.
A survey of previous experiments at IN20 showed that in general this magnet is used for only a few weeks per year. However, smaller magnets are used more frequently, where so far a maximum value of about 100 μT had been measured at approximately the position of the outer shielding of STEREO. This will be sufficiently attenuated by the magnetic shielding.

During the first period of data taking of STEREO, November 2016 to March 2017, only once a strong cryomagnet was active at IN20, from 07/12/2016 to 13/12/2016. During this time the central field of the magnet was varied in between $B_0 = 0$ T and $B_0 = 10$ T. For comparison only the lowest and highest fields are considered. The field inside the detector shielding is directly monitored by a three axis fluxgate, Bartington Mag–03MS1000 with a stated stability $< 1\,\mu$T, which is positioned on top of the detector, shortly below the lid of the mumetal case. With the IN20 magnet ramping from 0 T to 10 T the absolute value of the flux gate changed only from 8.7 μT to 9.9 μT. The impact on the STEREO PMTs can be monitored with the LED system, see Sec. 3.2.1, with which total-gain and single-photo-electron runs were performed every 2 h. The LED reference PMT 1, which has a smaller photocathode and is less sensitive to magnetic fields, was stable at the $< 1\%$ level. The changes are likely to be caused by the PMT, not the LED system, which is thus considered to have been stable. At the time of the magnetic field change there was neither in the Target nor in the Gamma Catcher PMTs a variation visible in the total-gain or single-PE runs which exceeded the usual $\pm 0.5\%$ fluctuations. In the muon veto PMTs, however, larger changes occurred. Most affected were the outermost PMTs on the IN20 side and the effects were visibly decreasing towards the D19 side. For example the PMTs VT10 and VT30 on the IN20 side, counted in rows and columns from the front edge (VT00 and VT20 were offline), showed a decrease of -40% and -31%, respectively, in the peak position in the total-gain runs. In the single-PE runs, performed with a higher gain in the electronics after the PMT, the mean number of detected photo electrons per light pulse, which should be stable at the 1% level in the veto, decreased by -28% and -25%, respectively. However, the overall intrinsic detection efficiency of the muon veto for vertical muons has not been affected. This is calculated by taking the ratio of muons detected by the veto and muons tagged in the detector, as described in [Ber17]. According to the online monitoring system this efficiency stayed at $>99\%$ even with the reduced gain in some PMTs.

Chapter 5

Characterisation of the Background Conditions at the STEREO Site

STEREO is installed in the experimental hall on level C of the ILL reactor. As stated earlier, see Sec. 3.1, STEREO meets challenging conditions in the research reactor environment. The main local neutron and γ-ray backgrounds originate from the neighbouring experiments D19 and IN20, and from the H7 and H13 casemates in front of STEREO. The neutrons originate initially from the beamtubes, transporting them from the moderator vessel to the experiments. At the neighbour instruments monochromators are used to select a small wavelength band at thermal energies from the primary beam and Bragg-reflect it through a collimation system towards the sample. A certain fraction of neutrons at other energies can also pass through the collimation after undergoing other scattering processes, but at a lower rate. Consequently the neutrons arriving at or around STEREO have mostly been scattered multiple times and had to pass several layers of shielding. As a result the vast majority of neutrons around STEREO are thermalised. However, a small contribution of MeV neutrons, present in the primary beams, could pass the shieldings and arrive at STEREO and, when mainly scattered on heavy nuclei still have high kinetic energies. Their rate may be small compared to the fast neutron rates from muon spallation, but they could cause reactor induced, correlated background, which cannot be measured during reactor shutdowns, and could only be identified by PSD.

The γ-ray background partially arises from natural radioactivity and activation of surrounding materials by the present ambient neutron flux and subsequent β-decays (e.g. $^{40}\mathrm{Ar}(n,\gamma)^{41}\mathrm{Ar} \xrightarrow{\beta^-} {}^{41}\mathrm{K}$). The main contribution at high energies, however, originates directly from neutron capture reactions. The most relevant nuclei, producing high energetic γ-rays in neutron captures, are listed in Table 5.1. γ-rays passing the shielding can create uncorrelated events and contribute to the random coincidence background in STEREO. The random coincidence rate R_{rand} can be approximatively calculated by the product of the background rates in the prompt-event energy window (2-8 MeV) $R^{\mathrm{rand}}_{\mathrm{prompt}}$ and delayed-event energy window (5-9 MeV)[1] $R^{\mathrm{rand}}_{\mathrm{delayed}}$ with the coincidence time window $\tau = 100\,\mu\mathrm{s}$[2]

$$R_{\mathrm{rand}} = R^{\mathrm{rand}}_{\mathrm{prompt}} \cdot R^{\mathrm{rand}}_{\mathrm{delayed}} \cdot \tau \ . \tag{5.1}$$

When assuming a neutrino signal rate of $380\,\mathrm{d}^{-1}$ and a signal to background ratio of 1.5, neglecting correlated background, the minimal goal for the suppression of random background is

$$R^{\mathrm{rand}}_{\mathrm{prompt}} \cdot R^{\mathrm{rand}}_{\mathrm{delayed}} < \frac{380\,\mathrm{d}^{-1}}{1.5 \cdot \tau} \simeq 30\,\frac{1}{\mathrm{s}^2} \ . \tag{5.2}$$

Assuming a background spectrum S_{B} which decreases as $1/E$ the ratio of the random background rates would be $R^{\mathrm{rand}}_{\mathrm{delayed}}/R^{\mathrm{rand}}_{\mathrm{prompt}} \simeq 0.04$. In order to keep some margin the maximum of $R^{\mathrm{rand}}_{\mathrm{delayed}}$

[1] This energy range for the delayed event has been used in previous γ-ray background analyses [Stu15b] and is adapted in this chapter for comparison. For the neutrino analysis, however, a range of 5-10 MeV is used, at present.

[2] This coincidence time was defined a priori, for the current neutrino analysis it is reduced to $70\,\mu\mathrm{s}$.

was fixed at 1 Hz, with a resulting limit for $R^{\text{rand}}_{\text{prompt}}$ of 25 Hz.

Several campaigns addressing the characterisation of the on-site background have been performed in preparation of the installation of STEREO. The purpose was to define the required (additional) shielding and to optimise its design with respect to required material types and quantities, and finally to validate the performance of the installed shielding. Some measurements are summarised in [Pé15] and [Zso16]. The most important measurements performed in the context of this thesis, aiming at the validation of the installed shielding, are summarised in the following sections.

Table 5.1: Neutron capture reactions which are relevant for the γ-ray background at the STEREO site during reactor operation. The most dominant contribution arises from ^{56}Fe, which is present in the largest amount in the steel structures around the site. Nickel could also be expected as constituent of some steels. Aluminium is partly used as structural material, especially around the beam tubes and ports, as it does not create long-lived activation products. Copper is used in the monochromators of the neighbouring instruments, which are exposed to primary neutron beams, and to some extent in piping around the site. Cross sections from [ENS17], γ-ray intensities from [Cap17].

Isotope	σ_n^{therm} [barn]	Abundance [%]	main γ-ray energies [keV] (intensity)
^{1}H	0.33	∼100.0	2223 (100%)
^{56}Fe	2.59	91.8	7631 (29%), 7646 (25%)
^{27}Al	0.23	100.0	7724 (27%)
^{63}Cu	4.47	69.2	7916 (33%)
^{58}Ni	4.62	68.1	8999 (51%), 8534 (24%)
^{54}Fe	2.25	5.85	9298 (unknown)

5.1 Gamma-ray Background

Two major campaigns addressing the γ-ray background have been carried out. A first campaign with the original shielding conditions: a 40 cm thick concrete wall between the STEREO area and D19, a 30 cm concrete wall towards IN20 in the front and a 10 cm lead wall on a concrete socket in the rear, and a single, 10 cm thick lead wall as shielding towards the H7 primary casemate. The data of the first campaign was analysed by Stutz [Stu15b] in parallel to the measurements, in order to gain time for the planning and installation of additional shielding. The analysis of [Stu15b] has previously been summarised in [Zso16]. Based on the conclusion of [Stu15b] the separation wall to D19 was replaced by 30 cm concrete and 10 cm of lead, the wall to IN20 by 15 cm of lead and 15 cm of BPE over the full length and an additional frontal shielding wall was constructed, connecting the two side walls, consisting of 10 cm of lead and 10 cm of PE, suppressing background from the primary casemates H7 and H13, see Fig. 5.2. Figure 5.1 shows the calculated attenuation of the γ-ray full energy intensity by different thicknesses of lead and concrete in dependence of the incident photon energy. This gives an estimate of the shielding efficiency of the walls. It holds true for the full energy γ-ray intensities measured behind the walls, but for the propagation into STEREO also the contribution of scattered photons to lower energies has to be taken into account, which is not the case in Fig. 5.1. For that reason in the analysis the attenuation factors are obtained from simulations but only for single incident energies. The curves show, however, that even by replacing the existing walls, instead of adding more material, a large factor is gained in the γ-ray attenuation at high energies.

A second γ-ray background campaign was conducted after the installation of all additional shielding walls in order to verify their shielding efficiency and estimate the resulting background for STEREO. All walls have a height of 2.4 m, shielding the detector volume but leaving the muon veto (at $\sim$ 3 m height) unprotected. As the single background sources surrounding STEREO have distinctive characteristics the measurements have been performed for each direction. In the following, after a description of the detector setup, the two campaigns will be compared for

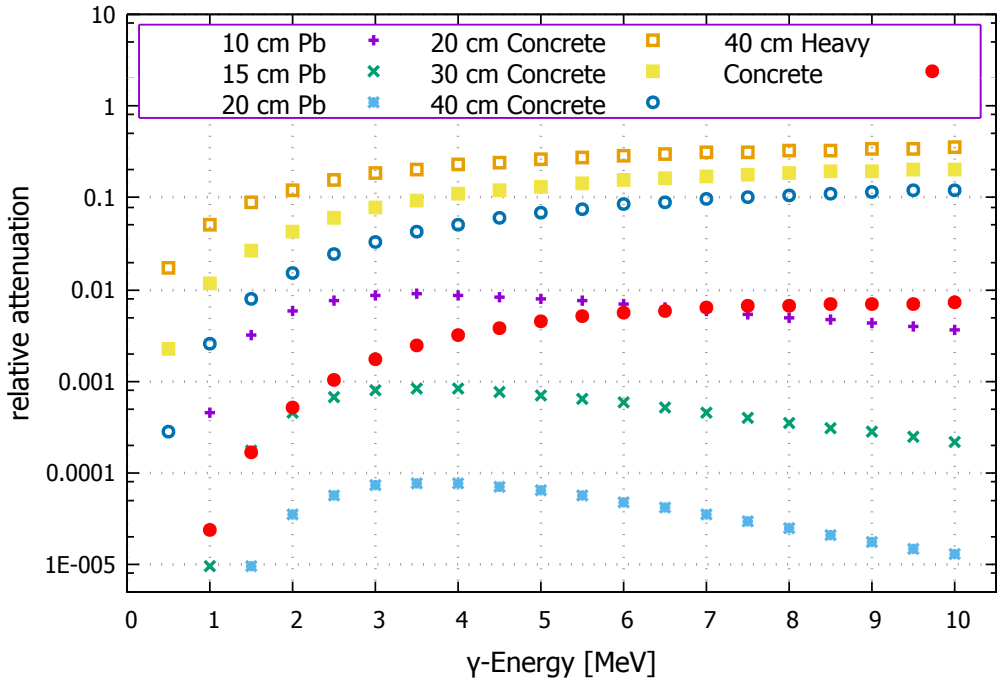

Figure 5.1: Calculated attenuation of the γ-ray full energy intensity without coherent scattering as function of the incident energy for different thicknesses of lead, concrete and heavy concrete. The build-up of lower energetic γ-rays from scattered photons is not taken into account. The chosen standard and heavy concrete compositions are listed in Appendix A. Attenuation coefficients obtained from [XCO17].

each direction. As the neutron captures, Tab. 5.1, can occur on any structural material within the experimental zones of D19, IN20 and STEREO (on detector and sample setups, pipes, structural materials, ...) the result is a diffuse and extended source and it is not possible to identify a single point of origin, but rather to estimate an average or maximum background rate.

5.1.1 Setup

Two different types of detectors have been used for the background measurements: a high purity germanium detector (HPGe), type Ortec GEM 30210, and a NaI detector, type Hawshaw 16S24/5A. The HPGe detector has a good energy resolution (FWHM/E) of 0.3% at 1.3 MeV (^{41}Ar: 1293 keV), which is useful to identify distinctive γ-lines in the background, but has a small volume ($\sim 160\,\mathrm{cm}^3$). In contrast the NaI detector has a diameter of 4 inch and a length of 6 inch ($\sim 1200\,\mathrm{cm}^3$), but a poorer energy resolution of 8% at 1.3 MeV. It can be used to measure overall background rates quicker, which allows to scan a larger total volume in between major configuration changes of neighbour instruments.

To obtain directional information the HPGe detector was enclosed in a lead shielding of a thickness of 15 cm to top and bottom, 20 cm to the sides and 10 cm to the rear side. The shielding to the rear side was not fully closed as the nitrogen dewar could not be fully covered, due to its size. As a result also the detector crystal may not have been fully shielded from the rear, upward direction. This could lead to an overestimation of the actual directional background in the analysis. Due to the heavy shielding the height of the HPGe was fixed at 30 cm above the ground. The NaI detector was installed on a liftable table in order to measure the height dependence of the background. Given the weight limit of the table the detector was shielded by 10 cm of lead in all directions, but also with an incomplete shielding to the rear top. To avoid large contributions from neutron captures on the detectors or materials in their vicinity the setups were covered with B_4C mats.

For the HPGe the γ-ray peaks in the spectra are assumed to be gaussian with a smoothed step function for the underlying Compton background. For the NaI only integrated rates were used within STEREO's prompt-event and delayed-event energy windows at 2-8 MeV and 5-9 MeV, respectively. These values are used for relative comparisons, as a signal deconvolution would be difficult, considering the Compton scattering in the detector and the concrete walls and the diffuse sources in the experimental areas. The energy response of both detectors is linear over the energy range of interest of 0.5-10 MeV. The NaI was calibrated using a ^{60}Co source, providing two γ-ray lines at 1.17 MeV and 1.33 MeV [ENS17] and their sum at 2.51 MeV. The HPGe could be calibrated using identified background peaks, namely the 511 keV positron annihilation peak and the iron capture line at 7632 keV. The stability of the energy calibration was checked regularly in between the single runs.

For the interpretation of the HPGe spectra the absolute full energy detection efficiency for the γ-ray energies of interest is required. For high energies this depends mainly on the geometry of the detector crystal. At the time of the first campaign no technical drawing was available for the detector in use but for another detector, Canberra model 7229N, which had been used in previous studies. For this MCNP simulations have been performed where initially an efficiency for γ-rays incident parallel to the detectors axis of 0.01 at 7.5 MeV [Pé14] was obtained. To determine the efficiency of the Ortec detector both detectors were placed next to each other, without any shielding, and the measured rates of the iron neutron capture lines were compared. It was found that at these energies the Ortec detector showed 2.5 times higher rates [Stu14], so that in the analysis of the first campaign [Stu15b] an efficiency of $2.5 \cdot 10^{-2}$ at 7.5 MeV was assumed. For the second campaign a detector data sheet was obtained from the manufacturer. By means of MCNP simulations the full energy detection efficiency for 7.5 MeV γ-rays incident parallel to the axis of the cylindrical detector is obtained as $\epsilon_{\parallel}^{\mathrm{Ortec}} = 3.8 \cdot 10^{-2}$. For γ-rays incident perpendicular to the detector's axis the simulations yield an efficiency of $\epsilon_{\perp}^{\mathrm{Ortec}} = 2.1 \cdot 10^{-2}$. This means the values of [Stu15b] have to be scaled by a factor $0.025/0.038 = 0.65$ in order to renormalise them to the same detector efficiency.

During the first campaign, reactor cycle 173 in November and December 2014, the reactor power was at 53 MW. For comparison the obtained background rates should be scaled to the nominal reactor power of 58.3 MW, leading to a factor of 58.3 MW/53 MW = 1.1. This scaling factor was not included in [Stu15b] but is applied here for comparison with the second campaign. During this second campaign, in reactor cycle 178 in June and July 2016, the reactor power was at 45 MW, which was adjusted to provide a longer cycle duration. The corresponding scaling factor to the nominal reactor power is 58.3 MW/45 MW = 1.3.

The general intention was to perform the measurements at meaningful positions and keep those consistent in between the two campaigns. However, both times the available space was partly limited by other setups in place and by on-site works, so that the detector positioning had to be adapted. A plan of the main positions during the second campaign is shown in Fig.5.2. Tables with measured rates for all positions can be found in Appendix A, within this section only exemplary values will be listed.

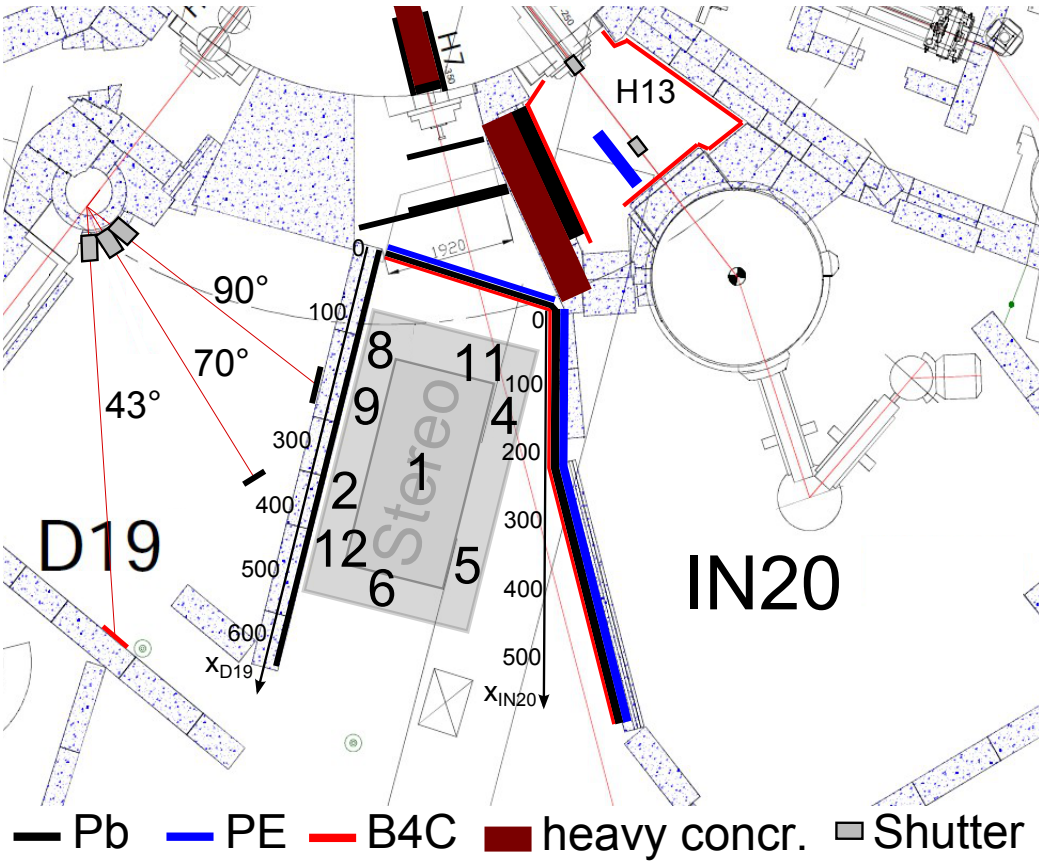

Figure 5.2: Map of the most important measuring positions during the γ-ray-background campaign of 2016. The x-coordinates of the positions refer to the distance from the lead shielding wall directly in front of STEREO, for each side (D19, IN20) independently. The positions of the second campaign have been chosen along the contour of STEREO's shielding. They are not the same as in the 2014 campaign and also differ slightly along the D19 wall for different D19 configurations due to limitations by on-site works.

5.1.2 Up- and Downward Measurements

These measurements were only performed as part of the second campaign. The HPGe was placed in a central position of the STEREO footprint, Pos1, the lead shielding closed towards the front (10 cm Pb) and opened either to the top or the bottom. In the 'upward' configuration there was no direct line of sight between the detector and the steel structures of the lateral shielding walls, but below the setup there were steel plates covering the cable channel underneath STEREO. The obtained spectra are shown in Fig. 5.3, the count rates are listed in Tab. 5.2.

The observed ^{60}Co contribution presumably originates from activation of Co-containing steels in the vicinity of the site. The 1332 keV line was observed at all positions with varying intensity. The single energy is well below STEREO's region of interest but those gammas are always emitted in coincidence with a 1173 keV gamma, leading to a possible summed energy of 2505 keV (the lower energetic line was also observed, but was not used in the analysis due to the dominating Compton continuum of the ^{41}Ar line at 1293 keV). Although the probability that both γ-rays individually pass through the detector's shielding is negligible ($1.2 \cdot 10^{-6}$·(solid angle)^2). There is also a strong contribution from the iron neutron capture lines, especially from the top. Without a direct line of sight to the steel structures of the walls the source seem to be other steel parts. Above STEREO this could be structural steel in the transfer channel or a gallery which is attached to it. For the downward direction it is most likely the steel plate covering the cable channel. Especially the gallery is unprotected against the neutron flux from IN20, at a distance of about 5 m. It is located about 1.5 m above the roof of STEREO where still thermal

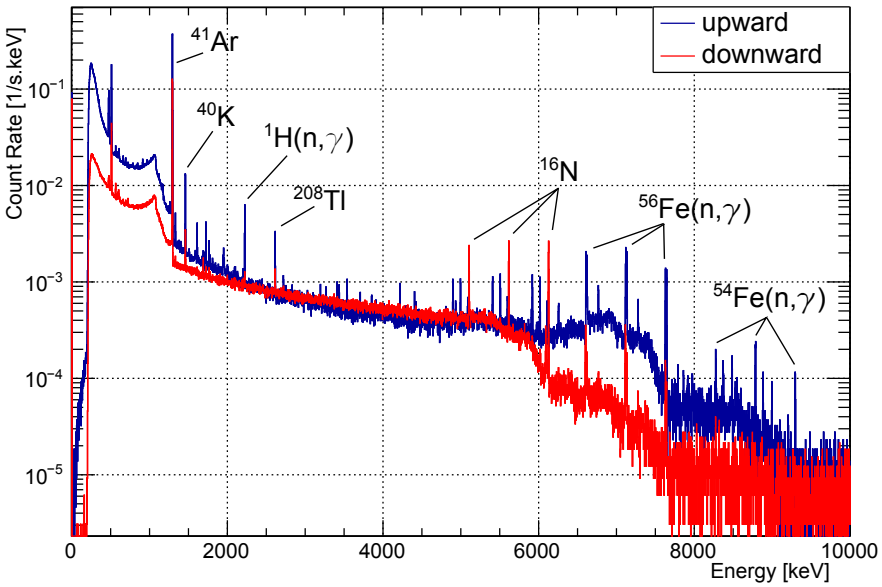

Figure 5.3: Comparison of Ge-spectra for the up-/downward configuration of the lead castle at Pos1. In the upward configuration the iron capture lines dominate the high energy spectrum, in the downward configuration the ^{16}N line, originating from the primary cooling water cycle. The most dominant γ-ray lines and their single and double escape peaks, if present, are labelled.

Table 5.2: Measured rates of the Ortec HPGe for the up-/downward configuration at a central position of the STEREO footprint, Pos1, for single gamma lines relevant for the background. The rates have to be scaled by a factor of 1.3 for the full reactor power. Only statistical uncertainties are listed.

Pos	Co-60 1332 keV [mHz]	Na-24 2754 keV [mHz]	N-16 6128 keV [mHz]	Fe-56(n,g) 7631/46 keV [mHz]	Cu-63(n,g) 7916 keV [mHz]	Ni-58(n,g) 8997 keV [mHz]	Fe-54(n,g) 9298 keV [mHz]
1-Up	12.24(36)	1.08(11)	—	18.05(43)	0.30(06)	0.32(06)	0.69(08)
1-Down	1.33(10)	—	14.90(32)	1.51(82)	—	—	—

neutron fluxes of $\mathcal{O}(10)\,\mathrm{cm}^{-2}\mathrm{s}^{-1}$ have been measured. The same flux is also expected at the position of the gallery, or an even higher one since it is less protected by the shielding wall. With STEREO in place the floor and the bottom of the transfer channel are better protected against thermal neutrons, which should strongly reduce the prompt gamma lines from neutron captures.

Following the procedure in [Stu15b] the expected background rate in STEREO can be estimated: The full energy detection efficiency of the Ortec detector, obtained from simulations, see Sec. 5.1.1, is $2.1{\cdot}10^{-2}$ for the iron capture lines for γ-rays arriving perpendicular to the detector's axis. By summing over the high energy capture lines the γ-ray rate incident on the germanium detector can be calculated (the energy dependence of the detector's efficiency is neglected since ^{56}Fe yields the main contribution to the rates)

$$R_{\mathrm{Fe,Cu,Ni}} = ((18.05 + 0.3 + 0.32 + 0.69) \cdot 10^{-3}\,\mathrm{Hz})/(2.1 \cdot 10^{-2}) = 0.93\,\mathrm{Hz}.$$

Scaling from the HPGe cross section ($\sim$36.1 cm^2) to the surface of STEREO's top lead shielding (8.32 m^2) and to the full reactor power ($\cdot$1.3) an incident rate of 2.8 kHz on the lead shielding is obtained from above.
Taking into account STEREO's shielding (15 cm Pb to the top) and response, obtained from

Geant4 simulations for 7.5 MeV γ-rays impinging perpendicularly on the shielding, the expected rate in the target volume in the delayed energy window is

$$R^{\text{top, 2016}}_{\text{delayed}} = R^{\text{scaled}}_{\text{Fe,Cu,Ni}} \cdot 1.17 \cdot 10^{-5} = 33\,\text{mHz},$$

from above. The attenuation factor includes γ-rays scattered incoherently in STEREO's shielding but still creating a signal in the 5-9 MeV window.
The same calculation for the contribution from below without (with) the ^{16}N line at 6128 keV, assuming a spatially homogeneous distribution (which in reality is not the case, see Sec. 3.1.3), taking into account the thicker lead shielding (20 cm) leads to

$$R^{\text{btm, 2016}}_{\text{delayed}} = R^{\text{scaled}}_{\text{Fe,(N}-16)} \cdot 8.75 \cdot 10^{-6} = 1.9\,\text{mHz}\ (20.7\,\text{mHz}).$$

5.1.3 Direction D19

As described earlier in Section 3.1.2 the Laue-diffraction instrument D19 has three possible beam positions within its zone, defined by their angle with respect to the primary beam. The positions are chosen according to the neutron wavelength required for each experiment and are changed when needed. As a consequence during the first γ-background campaign the positions at 43° and 90° were measured, while during the second campaign the positions 43° and 70° were in use. See Fig. 5.2 for the corresponding beamdump positions. For the 90° and 70° configurations a copper monochromator was used, for the 43° configuration both times a graphite monochromator. The D19 neutron beam is at a height of about 1.5 m above the ground.

During the first campaign it was observed that the two measured D19 beam positions cause very different background at the STEREO site. With the NaI scans along the wall were performed at heights of 65 cm, 115 cm and 155 cm of the detector center with respect to the floor. This covers about the projection of the active volume of STEREO.

For the 90° position a clear hotspot is visible at the position of the beamdump and in its surroundings, see Fig. 5.5a. Before the redesign of the walls the 5 cm lead of the beamstop were backed by a single heavy concrete block within the 40 cm thick wall. Thus the rates measured with the NaI above 5 MeV are highest just below the beamstop and this block. The high count rates at high energies are dominated by the neutron capture lines around 8 MeV. A clear identification is not possible with the NaI, given its energy resolution. For this reason an dedicated measurement was performed with a HPGe detector in a later reactor cycle, independent of the major γ-ray background campaigns. Due to the unavailability of the Ortec detector a Canberra HPGe, model 7229N, was placed on a liftable table, with only 10 cm lead shielding to the bottom, top and sides of the crystal, and B_4C against thermal neutrons. The wall to D19 was already reduced to 30 cm standard concrete, and only the hotspot was reinforced with a 5 cm lead wall. The detector was placed at 1 m height, which is about 20 cm below the hotspot's lead shielding. Measurements were performed with D19 in the 90° and 70° configurations, both times using the copper monochromator, the measured spectra are shown in Fig. 5.4. For the 90° configuration the spectrum shows a large contribution of Compton-scattered γ-rays (scattered in the wall, not the detector) which ends at the peak of the neutron capture γ-ray line of copper at 7916 keV. This contribution is not visible when D19 uses the 70° configuration, in which case the 90° direction is closed by a shutter. The shutter is designed for an effective neutron and γ-ray attenuation since with all shutters closed the zone has to be accessible. This shows that in fact the D19 monochromator causes a significant contribution to the measured rates around the hotspot. The changes at energies above 8 MeV, dominated by neutron capture γ-rays from ^{54}Fe, may be related to a reduced neutron flux impinging on the wall after the D19 position change, but could also result from a changed neutron flux and capture rate in the vicinity of the HPGe, which would rather be related to IN20, as described below.

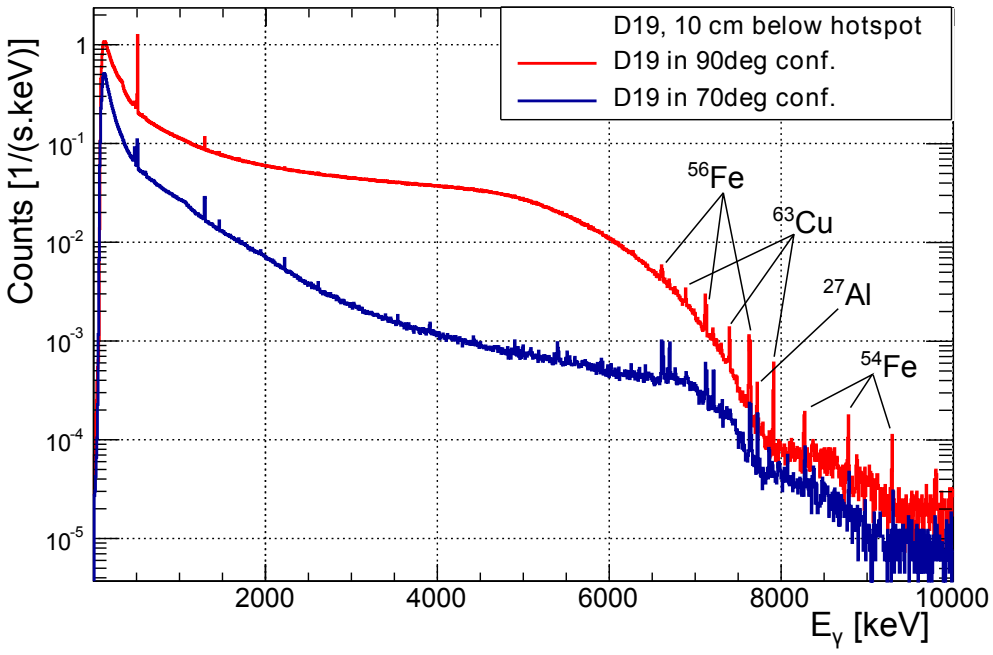

Figure 5.4: Comparison of HPGe spectra measured at the D19 wall, just below the hotspot, with D19 in the 90° (red) and 70° (blue) configuration, respectively. Both times the copper monochromator was used. In the 90° configuration a large Compton contribution is visible in the spectrum, which ends at a peak at about 7916 keV, the γ-ray energy from neutron capture on ^{63}Cu. The neutron capture related peaks and their respective single and double escape peaks are labelled.

Compared to the hotspot the rates measured with the NaI at other positions along the wall, for the 90° configuration, are lower by a factor of $\mathcal{O}(10)$, see Fig. 5.5a. With the beamstop at 43° the rates around the hotspot decrease, as the monochromator is then shielded by a shutter, but at the same x-position at the lowest and mid heights the rates increase by on average a factor of 5 and at the front and rear end of the wall by factors 2-3, compare with Fig. 5.5b. In this configuration the spectra of the NaI have all the same shape and the ratios of the rates can be used to scale the HPGe measurements from the lower position to other heights. For the HPGe detector, at 30 cm height and stronger collimated, the increase in the high energetic capture lines of Fe and Al due to the beam position change is a factor of $\mathcal{O}(10)$, depending on the position along the wall.

This increase may be due to a combination of several effects. The intensity of the monochromatic neutron beam at D19 can vary due to the selected neutron wavelength (up to a factor of 1.5 in the accessible range, assuming a Maxwell-Boltzmann energy distribution of the primary neutron beam) and due to the reflectivities of the different monochromators and scattering on different crystal planes. Another reason could be the positioning of the large D19 detector. It is always placed next to the neutron beam on that side which is away from the reactor. The detector covers a range of 120° around the sample in the horizontal plane and is in a housing of PE, only open towards the sample. Thus for the 90° configuration it is shielding all the rear part of the D19 zone from diffusely scattered neutrons. For other positions it screens less and less of the zone, exposing the wall towards STEREO and all structures in its vicinity to higher thermal neutron fluxes.

The expected rates in the target originating from side of D19 are again calculated following the same procedure as in [Stu15b], summing up the count rates in the high energy peaks, dividing by the full energy detection efficiency of the HPGe $\epsilon_{\|}^{\text{Ortec}}$, scaling to the STEREO surface and taking into account STEREO's shielding and response. The calculations for the first campaign are valid for the detector height of 30 cm and for the initial shielding walls in both D19 configurations. The rates are scaled to the full reactor power ($\cdot 1.1$). In order to achieve a conservative estimate the rates for the 43° position are scaled to the maximum rate measured

by the NaI at the higher positions

$$R_{\text{delayed}}^{\text{90deg, 2014}} = 0.19\,\text{Hz} \cdot 1.1 = 0.23\,\text{Hz} \qquad R_{\text{delayed}}^{\text{43deg, 2014}} = 4.9\,\text{Hz} \cdot 1.1 \cdot 90/51 = 9.4\,\text{Hz}\ . \tag{5.3}$$

Assuming a critical area of $1\,\text{m}^2$ around the hotspot the ten times higher rates in this area for the 90° configuration would increase $R_{\text{delayed}}^{\text{90deg, 2014}}$ to 1.4 Hz. The 43° configuration with generally higher rates leads to a much higher total background of 9.4 Hz. After the installation of 10 cm of lead along the wall the rates in the delayed energy window should be reduced to 0.09 Hz, which then lies below the specifications of 1 Hz. The main problem for the 90° configuration is that the hotspot can lead to locally, and thus inhomogeneously increased rates.

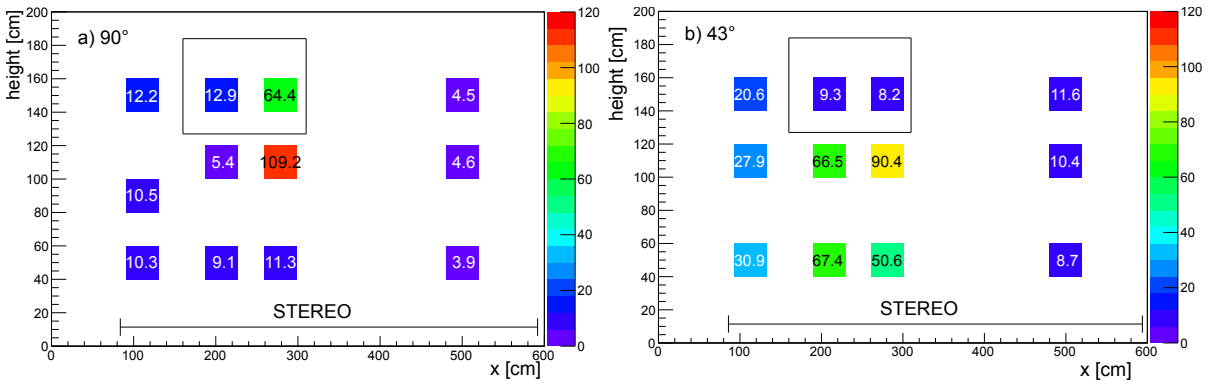

Figure 5.5: First campaign (2014): Integrated count rates of the NaI detector in Hz, between 5 and 9 MeV at different positions along the separation wall between STEREO and the D19 area, measured with the initial shielding. The black frame marks the single heavy concrete block in the originally installed wall. The D19 configuration was a) 90°, Cu-monochromator and b) 43°, C-monochromator, respectively. Rates have to be scaled by a factor of 1.1 for the nominal reactor power. (Independent analysis, following the procedure of [Stu15b].)

In the second campaign, after the installation of all additional shielding, only the 43° and 70° configurations could be measured. Although the former was only in use for a short period, the conducted measurements indicate that this configuration leads to higher rates than the 70° position, which could not be measured during the first campaign.

The few positions measured with the NaI while D19 was in the 43° configuration, see Fig. 5.6a, do not allow to draw clear conclusion, except that the rates do not seem to increase significantly from the bottom to the top (except for an unexplained high rate at $x = 355\,\text{cm}$). This is in agreement with the observations before the shielding upgrade, see Fig. 5.5b.

For the 70° configuration more positions could be investigated, see Fig. 5.6b. During all measurements with rates <4 Hz H13 was OFF (the primary shutter closed). This shows that despite the detector's shielding H13 and IN20 still have a major impact on the measured rates on the D19 side. Taking this into account the observed scaling factor from 'bottom' to 'top' rates at the position of the hotspot would be larger than the observed factor of three.

For both D19 configurations all HPGe spectra have the same general shape, see Fig. 5.7. Above the dominating peak of ^{41}Ar at 1293 keV the spectra decrease smoothly with only a few characteristic lines, e.g. of ^{208}Tl and neutron capture lines of ^{1}H and ^{56}Fe. Above 9 MeV the spectra turn flat. Most spectra are even comparable in magnitude, where the rates are always highest close to the hotspot around the beamdump of the 90° configuration of D19, even so this position was not in use (compare Pos2 & 3 to Pos8 (70°) and Pos12 & 10 to Pos9 (43°) in Fig. 5.7). The comparatively low count rate during a long measurement with H13 and IN20 OFF but D19 ON (38.5 h @ Pos9) shows that despite the heavy shielding of the detector a significant fraction of the measured rate has been caused by IN20, either due to an unshielded area at the rear top of the detector or due to the fact that the main part of the on-site thermal neutron background ($\sim$ 70% [Hé15]) originates from IN20. This measurement is the only one towards D19 where despite the long integration time no neutron capture lines can be identified for the HPGe (but in the NaI with its larger crystal and larger acceptance angle of the collimation).

This indicates that a non-negligible fraction of these lines observed at other positions is not produced in the D19 area but on the STEREO site, either by neutron captures on the D19 wall structure or correlated to the strong contribution from the top direction described in Section 5.1.2, whereto the detector's lead shielding is incomplete.
The neutron capture lines of iron at 7631 keV and 7646 keV are the only high energetic gamma lines which could be identified at other positions. The highest rates have been observed in the center of STEREO, for the 43° configuration of D19, also at Pos9, see Tab. 5.3. A similar position has also been measured in the first campaign. Then a rate of 30.8 mHz · 1.1 = 33.9 mHz has been measured for the iron capture lines, which is now at 0.77 mHz · 1.3 = 1 mHz. This gives a reduction factor of 34 with the new shielding wall, where a factor of 100 would have been expected from the attenuation factors in Fig. 5.1. Although some settings may have changed in between the two campaigns no big effect is expected from that, which means that there is a factor 2-3 discrepancy between the expected and observed attenuation. The most probable explanation is that at this position 50-67% of the measured rate of the iron capture lines is not produced in the D19 area. At distances closer to the reactor wall about a factor of two higher rates have been measured in 2014, but the position has not been accessible in 2016 due to on-site works.

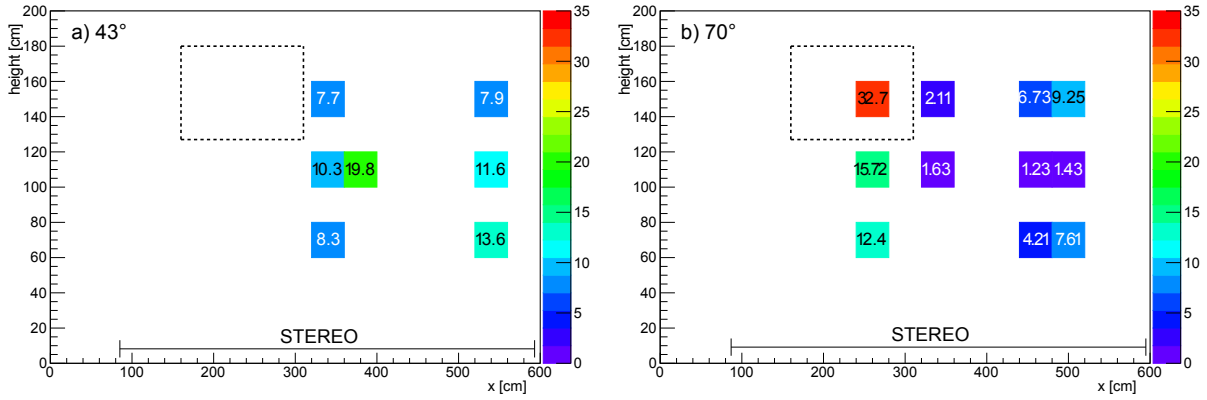

Figure 5.6: Second campaign (2016): Integrated NaI count rates in Hz in the high energy window 5-9 MeV, after the installation of all external shielding. For comparison the dashed, black frame marks the position of the former heavy concrete block, which is not in place anymore. For rates below 4 Hz H13 was OFF. The D19 configuration was a) 43°, C monochromator and b) 70°, Cu monochromator, respectively. The rates have to be scaled by a factor of 1.3 for the nominal reactor power.

Table 5.3: HPGe-rates measured from the D19 side in the 2016 campaign (new shielding). Listed are rates of single γ-rays relevant for the background. The rates have to be scaled by a factor of 1.3 for the full reactor power.

Pos	Fe-56(n,g) [mHz]	Al-27(n,g) [mHz]	Fe-56(n,g) [mHz]
	D19 @ 43°		D19 @ 70°
2-HPGe	0.302(27)	—	0.184(32)
8-HPGe	—	—	0.308(33)
9-HPGe	0.765(95)	0.182(46)	—

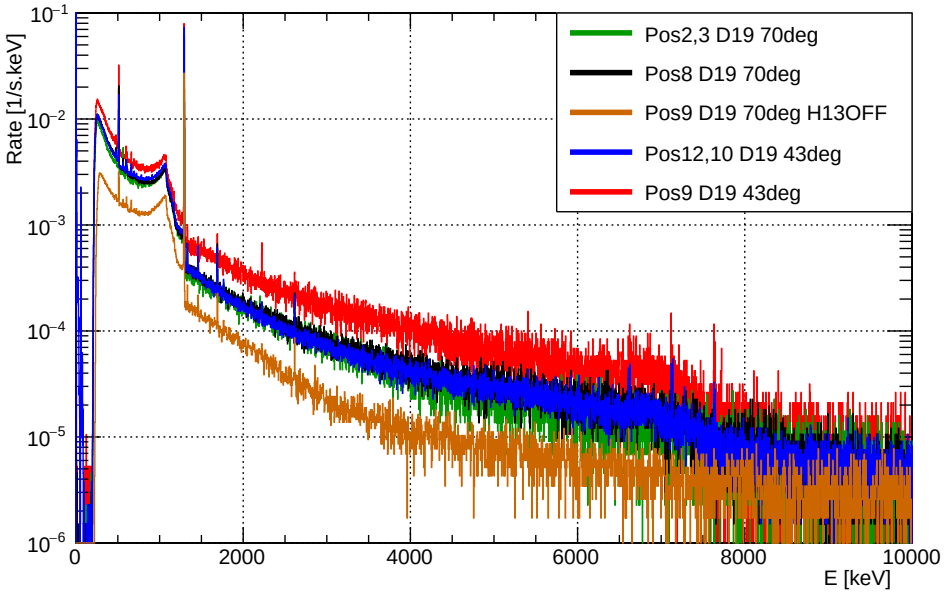

Figure 5.7: Second campaign (2016): Ge-spectra for different positions along the D19 wall for both D19 configurations with the new shielding. The spectrum at Pos9 with H13 OFF, where no iron capture lines are visible, indicates that a certain amount of these gammas is produced on-site by neutron capture and rather correlated with IN20 than with D19.

Considering the highest measured rates, at Pos9, originating from capture on iron and aluminium (0.765 mHz + 0.182 mHz) and following the procedure as above, a maximum rate of

$$R_{\text{delayed}}^{\text{43deg, 2016}} = 75\,\text{mHz}$$

is expected in the delayed energy window of the STEREO target with the new shielding. This is slightly lower than the previously estimated rate of 90 mHz. However, the former estimate was calculated for the highest flux measured with the NaI at 1.15 m height, which was not available in the second campaign at the same x-position. In general the precision of both estimates is limited by the fact that the rates are measured in a small, collimated detector volume and are thus sensitive to local sources (e.g. steel structures) and that a significant fraction of the observed rates seem to have been produced on-site by neutron capture. This contribution may have changed in between the campaigns, e.g. by the installation of the steel support frame of the lead wall which increased the local steel content, or by a different IN20 beam intensity. Considering these effects the estimated rates are in good agreement.

Considering the Ge-rate of the iron lines at the x-coordinate of the hotspot (Pos8, 0.308 mHz) for the 70° configuration, assuming a scaling factor of 4 from the height of the germanium detector (30 cm) to the hotspot, a critical area of 1 m^2 and a shielding factor of STEREO of 10^{-3} (from [Stu15b]) an additional event rate in STEREO's target, close to the hotspot is obtained:

$$R_{\text{delayed,hotspot}} = 16\,\text{mHz}.$$

5.1.4 Direction IN20

In a similar way scans have been performed along the IN20 wall. The IN20 sample position and direction of the monochromated beam change frequently in small steps, leading to frequent changes in the background intensity. The background measurements take the time average over these changes. In addition the collimation of the neutron beam can be changed, which also has

a direct impact on the measured background rates. The collimation is normally opened to allow a maximum beam intensity, but can be adjusted for single experiments. It is then stable over a period of days. The IN20 neutron beam is at about 1 m height.

In the scan with the NaI during the first campaign the measured rates were about a factor of 2.5 higher than at the D19 side (except the D19 hotspot), see Fig. 5.8. The top part of the original rear wall consisted already of 10 cm of lead, which was installed to protect the detectors of the former instrument at this position. The lead part clearly leads to reduced rates, compared to its 30 cm thick base made of concrete. The relative rate changes with the x-coordinate along the rear part of the wall ($x \gtrsim 200$) are much smaller at the top (maximal factor 1.6) than at the bottom (maximal factor 3.9) which shows that also for these measurements a certain offset of the countrates originates from other sources, likely from above. Subtracting an offset of about 4.5 Hz would lead to similar relative changes. This offset is small compared to the rates measured at $x = 1.45$ m and can be neglected for this position. The measured height dependence at $x = 1.45$ m is less pronounced than at the D19 side, with about 20% increase from the bottom to the top.

The rates at the bottom seem to be higher in the center ($x = 3.8$ m) of the wall than towards the front. This was also observed with the HPGe at slightly different positions. Highest rates are observed at 2.8 m from the front, which is also the measurement position closest to the IN20 sample position. The IN20 sample region is exposed to the highest neutron flux among the structures within the area, besides the monochromator which is located in a heavy concrete bunker. The sample and surrounding structures are good candidates for being the main sources of neutron capture related γ-rays. Some components of the wall, like supporting aluminium beams, may also cause local effects. Summing over all γ-ray lines of Fe, Al, Cu and Ni and propagating these to the STEREO detector as before, and scaling to the full reactor power and to the maximum rate observed at 1.55 m height a total rate in the delayed-event energy window of

$$R_{\text{delayed}}^{\text{IN20, 2014}} = 16.2\,\text{Hz} \cdot 1.1 \cdot R_{\text{NaI}}^{\text{top}} / R_{\text{NaI}}^{\text{bottom}} = 21.7\,\text{Hz} \tag{5.4}$$

is expected, extrapolated from the rate measured behind the front, concrete part of the IN20 wall. Even with 10 cm of additional lead this would result in 0.22 Hz in the delayed energy window, which leaves little margin to the envisaged 1 Hz. Thus finally the complete wall was replaced by a wall of 15 cm of lead and 15 cm of PE over the full height, starting from the floor, which should reduce the rate to 0.05 Hz. At positions further to the front (rear) on the other hand the estimated total rates in the delayed-event energy window of 9.7 Hz·1.1 (0.6 Hz·1.1) would be attenuated to 0.025 Hz (0.002 Hz). The estimate for the central position can therefore be considered as being conservative.

During the second campaign the measurements did not follow the outline of the walls between the experimental zones, but the contour of STEREO. Measurements have been performed at a front and a rear position of the STEREO contour (Positions 4 and 5 in Fig. 5.2), with the detectors oriented perpendicular to STEREO's side. Only the top and bottom position have been measured with the NaI detector. The results are summarised in Tab. 5.4.

At Pos4 the Ge-detector inside the lead castle is within 1 m of the lateral shielding wall, consisting of lead and a stainless steel support frame. To investigate the amount of neutron capture γ-rays originating from the wall itself the area of the wall which has a direct line of sight to the detector was covered with B_4C sheets (Pos4+B_4C). Without significant changes in the IN20 setting the count rate in the iron capture lines at 7631 keV and 7646 keV alone decreased from 1.26(7) mHz to 0.65(10) mHz. This shows that with the new shielding walls a significant amount of the remaining high energy γ-ray background is produced on the STEREO site.

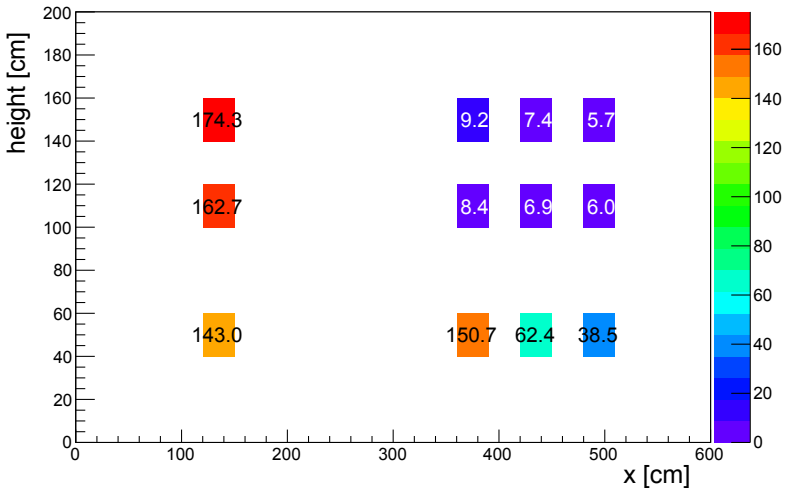

Figure 5.8: First campaign (2014): NaI rates between 5-9 MeV in Hz along the IN20 wall. Rates have to be scaled by 1.1 for the nominal reactor power. (Independent analysis, following the procedure of [Stu15b].)

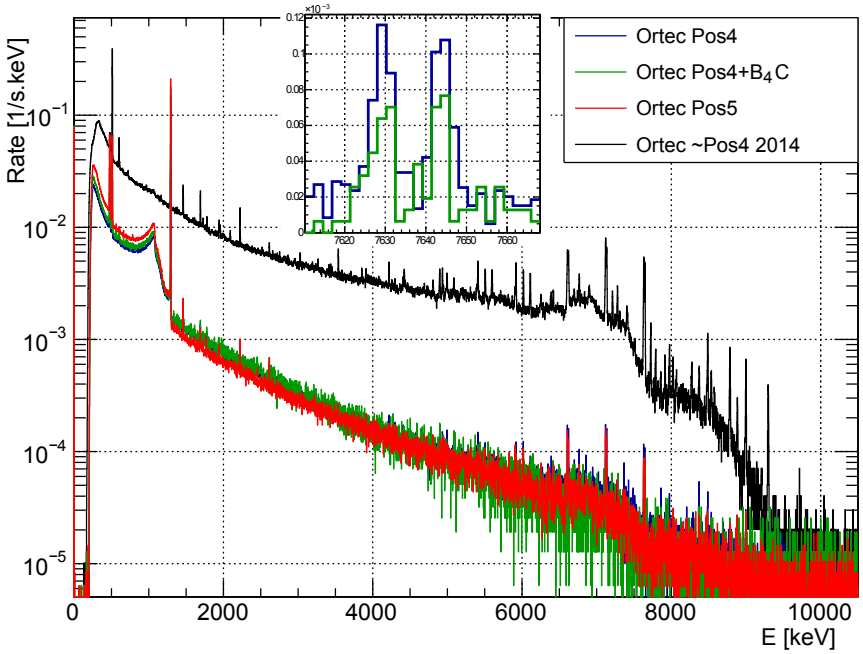

Figure 5.9: HPGe-spectra measured during the second campaign in direction of IN20 compared to one spectrum measured at a comparable position in the first campaign. The inset shows a zoom on the iron neutron capture lines around 7640 keV for Pos4 and Pos4+B_4C (in linear scale).

Table 5.4: Second campaign: Ge and NaI rates in direction of IN20, Pos4 and Pos5, integrated over the energy range of interest (top) and for single gamma lines relevant for the background (bottom). The rates have to be scaled by a factor of 1.3 for the full reactor power.

Pos	2-8 MeV (Hz)	5-9 MeV (Hz)
4-Ge	1.138(2)	0.193(1)
4-NaI btm	27.08(2)	7.6(1)
4-NaI top	42.43(4)	11.25(2)

Pos	2-8 MeV (Hz)	5-9 MeV (Hz)
5-Ge	0.999(2)	0.163(1)
5-NaI btm	23.57(2)	7.43(1)
5-NaI top	35.96(3)	11.69(1)

Pos	Ar-41 1293 keV [mHz]	Co-60 1332 keV [mHz]	H-1(n,g) 2223 keV [mHz]	Tl-208 2614 keV [mHz]	Fe-56(n,g) 7631/46 keV [mHz]	Ni-58(n,g) 8997 keV [mHz]
4-Ge	784.9(18)	1.12(7)	1.22(07)	0.986(64)	1.260(73)	0.193(28)
4+B_4C-Ge	791.5(18)	1.36(14)	0.86(11)	1.00(12)	0.65(10)	—
5-Ge	1103.4(24)	—	1.92(10)	1.650(92)	1.092(23)	0.105(23)

The positions in the first campaign have not been exactly the same but there was one measurement close to Pos4 with the only difference that the detector was oriented perpendicular to the IN20 wall in 2014 and perpendicular to the STEREO side in 2016 (rotation by about 20°). In 2014 the HPGe-rates above 2 MeV and 5 MeV scaled to the full reactor power have been 20.7 Hz and 6.7 Hz, respectively, which changed to 1.48 Hz and 0.25 Hz, corresponding to reduction factors of 14 and 27 in the respective energy ranges. In the setting with B_4C covering the wall the reduction factors are 16 and 39, respectively. It is clearly visible that the shape of the spectrum has changed in that now the high energetic capture lines and the correlated Compton continua are less pronounced, i.e. mainly iron capture lines remain, see Fig. 5.9. These are reduced from 100.3 mHz to 1.64 mHz without B_4C on the wall and 0.85 mHz with B_4C (scaled to nominal reactor power). This corresponds to reduction factors of 61 and 118, respectively. The previously observed capture peaks of aluminium and copper are not present anymore.

Using the Ge-rates at Pos4 without (with) B_4C at the wall and taking into account a possible scaling factor of 1.5 from comparison of the NaI rates at the lower and the upper position, the propagation to the STEREO target yields in the delayed-event energy window an expected rate of

$$R_{\text{delayed}}^{\text{IN20, 2016}} = 0.18\,\text{Hz}\ (0.08\,\text{Hz}).$$

This shows that care has to be taken concerning the thermal neutron flux at the STEREO area. To reduce the neutron capture in the steel support structure of the lead walls they have been covered with B_4C mats on the side of STEREO. An additional 1 m high curtain of B_4C mats was installed on top of the IN20 wall in order to reduce the neutron flux on the bottom of the transfer channel and the top of STEREO and to reduce the number of neutrons "leaking" over the wall. The rate of 0.08 Hz is still higher than what was expected from the 2014 campaign (0.05 Hz). This could be due to the generally increased iron content in the vicinity in form of the support structures of all lead walls. The front part of the previous wall consisted only of concrete.

5.1.5 Front Direction

The measurement was performed at the front center of the STEREO footprint, Pos11 in Fig, 5.2, with the collimation pointing towards the reactor, parallel to STEREO's long axis. In the first campaign a high rate of iron capture lines was observed (166 mHz·1.1 = 183 mHz), 90% of which was correlated with the opening of the H13 main beam shutter. Propagating this rate to STEREO, this would result in a rate of 5 Hz. Using the attenuation factor from [Stu15b] the additional frontwall of 10 cm of lead should reduce this to 0.05 Hz.

In the second campaign two measurements have been performed in the front direction, one with the H13 main shutter closed and a second one with the shutter open, but over a comparatively short time, as the space was needed for preparing works for the installation of STEREO. In none of these two measurements any high energetic gamma lines could be identified. A comparison of the NaI rates with H13 on and off shows that still, with the new wall, the integrated rate in the 5-9 MeV window is about a factor of 9 higher with H13 in operation, see Tab. 5.5.

Table 5.5: Second campaign: NaI-rates in the front direction measured at Pos11, integrated over the 2-8 MeV and over the 5-9 MeV window. The rates have to be scaled by a factor of 1.3 for the nominal reactor power.

Pos	2-8 MeV (Hz) H13 ON	5-9 MeV (Hz) H13 ON	2-8 MeV (Hz) H13 OFF	5-9 MeV (Hz) H13 OFF
11-NaI btm	20.84(4)	5.71(2)	—	—
11-NaI top	29.55(5)	8.94(2)	4.620(8)	1.079(4)

5.1.6 Rear Direction

During the first campaign no dedicated measurement was performed in the rear direction. The measurement of the second campaign in the rear direction shows several characteristic, high energetic gamma lines at a high intensity, see Fig. 5.10 and Tab. 5.6. The ^{60}Co activity is the highest one observed in this campaign and except for Pos1-Up (see Fig. 5.2) this also holds true for the neutron capture rates on hydrogen and iron. The high capture rates are expected considering the amount of material in the field of view of the collimated detector, which in most other positions was limited by the proximity of the walls. At Pos6 the detectors face the cabin of the D19 instrument control room and next to it a wide open area. An important source may be the steel plates covering the cable channel. If the steel contains cobalt they are presumably a significant source of the observed ^{60}Co activity. They experienced a longer activation time than the steel of the lateral walls and could have accumulated ^{60}Co ($T_{1/2} = 5.3$ a) over the previous cycles.
The ^{24}Na ($T_{1/2} = 15$ h, $E_\gamma = 1368.6\,\text{keV}, 2754.0\,\text{keV}$) has two production channels: thermal activation of ^{23}Na and fast neutron (n,α) reactions on ^{27}Al. The latter occurs for example in the fuel element and leads to a high ^{24}Na activity in the water of the primary cooling circuit. The primary cooling circuit also contains ^{16}N ($T_{1/2} = 7.1$ s, $E_\gamma = 6128.6$ keV) which is not visible in the Ge-spectrum. This leads to the conclusion that the observed ^{24}Na is not related to the cooling water but originates from thermal activation on site. A possible source could be concrete which can contain 0-2 wt% of sodium, depending on the exact type.

Table 5.6: Second campaign: Ge- and NaI-rates in the rear direction at Pos6, integrated over the energy range of interest (top) and for single gamma lines relevant for the background (bottom). The rates have to be scaled by a factor of 1.3 for the nominal reactor power.

Pos	2-8 MeV (Hz)	5-9 MeV (Hz)
6-NaI btm	27.63(2)	9.48(1)
6-NaI top	30.83(2)	10.77(1)

Pos	Ar-41 1293 keV [mHz]	Co-60 1332 keV [mHz]	H-1(n,g) 2223 keV [mHz]	Tl-208 2614 keV [mHz]	Na-24 2754 keV [mHz]	Fe-56(n,g) 7631/46 keV [mHz]
6-Ge	1482.93(84)	238.02(88)	14.07(21)	5.72(14)	67.37(49)	2.54(9)

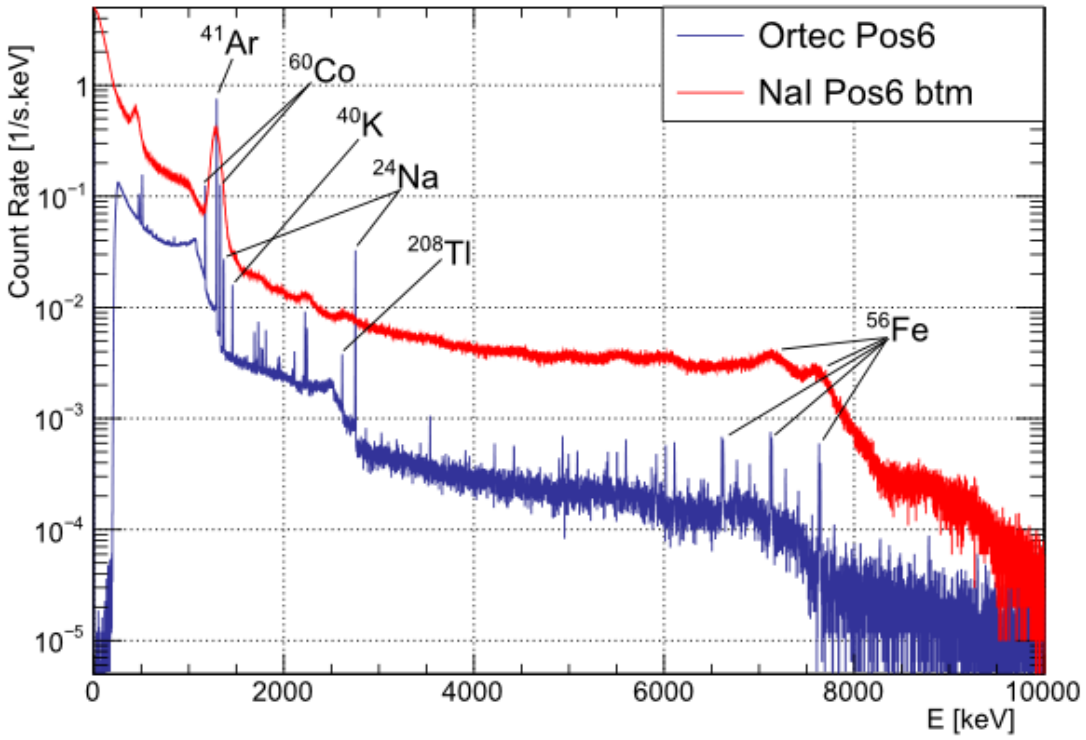

Figure 5.10: Second campaign: Ge- and NaI spectra in the rear direction. The Ge-spectrum shows several characteristic and high energetic gamma lines with a high intensity, such as ^{60}Co, ^{24}Na and the neutron capture lines of iron isotopes, which cannot be resolved with the NaI. The HPGe was at a height of about 30 cm above the floor, the NaI at about 65 cm.

Following the same procedure as before, with a surface of STEREO's rear shielding of 5.3 m^2 and an attenuation factor of $6.67 \cdot 10^{-4}$ the estimated background rate in the delayed-event energy window in STEREO, originating from the rear direction amounts to

$$R_{\text{delayed}}^{\text{Rear, 2016}} = 0.12\,\text{Hz},$$

at nominal reactor power.

5.1.7 Conclusions of the γ-background Measurement Campaigns

The contribution of the external gamma background to the signals in the delayed-event energy window of the target volume has been approximatively calculated with a resulting total rate of

(Top + Btm (w/o ^{16}N) + D19 + hotspot+ IN20 (w/o B_4C) + Front + Rear) = w/(w/o) B_4C
(0.03 + 0.02 (0.002) + 0.08 + 0.02 + 0.08 (0.18) + 0.0 + 0.12) Hz = 0.35 (0.45) Hz.

All rates have been scaled to the nominal reactor power of 58.3 MW. For the calculations the highest measured rates have been used for each direction. Changes in the maximum rates could be expected due to changes in IN20's operational parameters (sample position, beam intensity) and a D19 configuration change to the 90° position. As observed during the first campaign this reduces the overall background from this side, but increases the rates locally around the beamstop.

An unknown but presumably substantial fraction of the background seems to be produced by neutron captures on the STEREO site. At Pos4 (IN20, front) a reduction of the intensity of the iron capture lines of nearly 50% was observed when parts of the wall have been covered with B_4C on STEREO's side. A similar observation was made at Pos9 (D19, center) where the iron lines could always be identified in the HPGe as long as H13 was ON, but have not been visible

anymore when H13 switched OFF. This indicates that the on-site thermal neutron background, which was found to be produced to 70% by IN20 [Hé15], has a significant impact on the γ-ray background.

Throughout the measurements contributions from activation products, i.e. ^{60}Co and ^{24}Na have been observed. The sources are not clearly identified. In the previous campaign [Stu15b] ^{60}Co was only observed towards D19, with higher rates than now: $\mathcal{O}(10)$ mHz in 2014, $\mathcal{O}(1)$ mHz in 2016. This reduction is by far less than the expected reduction of a factor of ~ 500 for 10 cm of lead. The constant measured rate around 1.1 mHz of the 1332 keV line could also be related to an activation of the detector setup or dewar itself in a previous experiment, which cannot be excluded. In this case only the contributions from the top (12.2 mHz) and rear directions (238 mHz) are significant. Possible candidates for sources are the structural steel in the transfer channel, the gallery next to it and the steel plates covering the cable channel below STEREO.

It is not clear how much of the total background is produced on-site and might be reduced when STEREO with its outer B_4C shielding is in place - screening also surrounding structural materials from thermal neutrons, i.e. the D19 wall, partly the front wall and also the transfer channel. To further reduce the contribution of on-site produced background the structural steel parts of the IN20 wall and the front wall have been covered with B_4C mats. An additional curtain of 1 m height of B_4C mats on top of the IN20 wall should further reduce the thermal neutron flux at the STEREO site.

5.1.8 Situation for the STEREO Detector

After the commissioning of STEREO some periods with different IN20 beam intensities have been observed. During the period with the highest background rates, around December 19, 2016, a rate of about 2.9 Hz was measured in the STEREO target in the energy window 5-9 MeV. At the same time in the energy window 2-8 MeV a rate of 21.1 Hz was measured. Muon events and events 100 μs after a muon have been excluded. During the following reactor shutdown the rates stabilised around 1.6 Hz in 5-9 MeV and 9.8 Hz in 2-8 MeV, see Fig. 5.11, which is purely caused by cosmic and other natural background. Scaling the rates during the cycle to the nominal reactor power by 58.3 MW/56 MW = 1.04 and taking the difference in both windows, reactor related rates of 1.4 Hz in the delayed-event energy window and 12.2 Hz in the prompt-event energy window are obtained. Among the cells the background rates decrease slightly from the front to the rear of the detector during the cycle and during the shutdown from the border cells to the center cells.

The rate in the high energy window is a factor of 4.1 above the final predictions of Sec. 5.1.7. Although it was tried to keep the estimates conservative for each direction there are some potential sources of uncertainties in the procedure.

Uncertainties in the calculations themselves arise from the fact that the full energy efficiency of the HPGe is purely obtained from simulations, since it is difficult to have a adequate calibration source at 7-8 MeV γ-ray energy, and the attenuation factors for the propagation into STEREO, which have been simulated with 2-3% statistical precision, but depend also on the accuracy of the simulation and the exact implementation of the layout.

However, the procedure itself yields more significant uncertainties. While γ-rays which are incoherently scattered in the HPGe and thus do not deposit their full energy are taken into account in the full energy detection efficiency of the detector, γ-rays which undergo incoherent scattering within the shielding walls towards D19 or IN20 also do not show up in the full energy peak of the HPGe, but can still have energies above 5 MeV. This contribution has been neglected in the estimations. The impact is difficult to estimate without simulations since it depends on the positions and extensions of source, shielding and detector.

A simplified estimation can be done, in order to estimate the order of magnitude of this effect: About 33% of the γ-rays of 7.5 MeV energy which interact in lead (mean free path $\sim$ 1.9 cm, [XCO17]) undergo incoherent scattering (67% electron-positron pair production), whereof, according to the Klein-Nishina formula (see e.g. [Kno00]), about 25% are scattered at

maximum at 15°, leaving them with 5 MeV energy. If they interact further their energy falls below the region of interest. Another reduction arises from the solid angle coverage of STEREO with respect to the shielding, and the γ-rays scattered therein. In case of the D19 side, where STEREO covers about the full angular range of the 15° scattered γ-rays, calculating the incident γ-ray rate on the wall from the D19 side from the attenuation factors in Fig. 5.1, considering only γ-rays interacting within the last 2 cm of the wall, and an attenuation factor for the propagation into STEREO as before but increased by a factor of 1.5 for the decreased energy of scattered γ-rays, yields a contribution of 0.014 Hz, which, for this simplified calculation, is in the same order of magnitude as the full energy γ-ray contribution (0.08 Hz). Similar effects from the front and IN20 side may explain some fraction of the underestimation.

An additional uncertainty arises from the fact that the γ-ray rates have been measured only punctually with collimated detectors at low heights, and then have been extrapolated to the full STEREO volume. Local sources or strong rate changes in certain areas may not have been identified. Furthermore STEREO itself changes the steel inventory at the site significantly. Although it is shielded against thermal neutrons with B_4C mats on the outside this may not be fully sufficient, especially against neutrons above thermal energies, which can penetrate the B_4C and are moderated and captured within the structure.

The count rates in STEREO measured at the end of the reactor cycle in December 2016 together with a coincidence time window of $\tau = 70\,\mu$s which is currently foreseen for the final analysis (instead of $\tau = 100\,\mu$s as proposed beforehand) lead to a random coincidence rate of

$$R_{\text{rand}}^{\text{cycle}} = 2.9\,\text{Hz} \cdot 1.04 \cdot 21.1\,\text{Hz} \cdot 1.04 \cdot 7 \cdot 10^{-5} = 400\,\text{d}^{-1}\ , \tag{5.5}$$

compared to a expected neutrino rate of 380 d^{-1}. This rate can, however, easily be reduced by additional cuts. For example from simulations it is known that IBD events spread basically only over neighbouring cells [Bon17b]. The probability that two random, uncorrelated events fulfill this condition within the six target cells lies at about 44%. The remaining contribution can be determined with high statistics and subtracted as is described in Section 7.1.2.

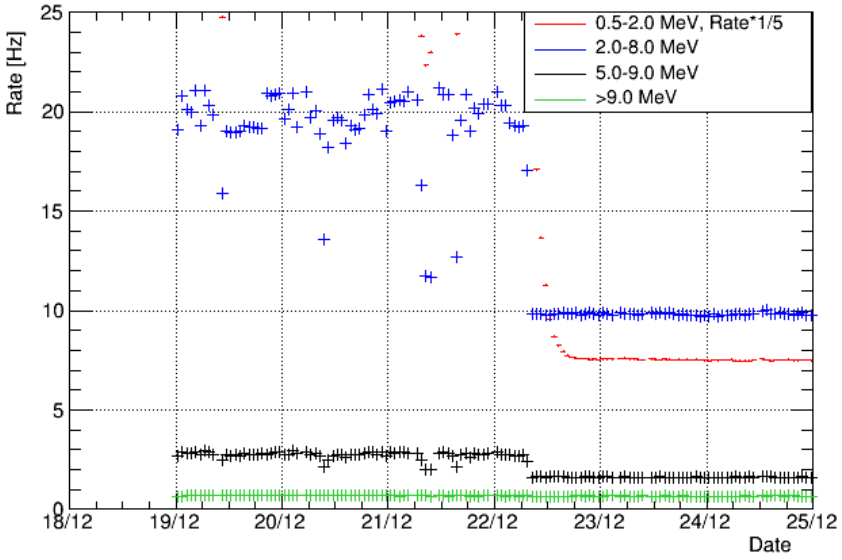

Figure 5.11: Evolution of the count rates in the STEREO target volume in different energy intervals at the end of reactor cycle 179 in December 2016. For the rate calculation only energy depositions in the target are taken into account. A muon veto of 100 μs is applied and the rates are corrected for deadtime.

The overall spectrum measured in STEREO's target is shown in Fig. 5.12, with the selection criteria for the prompt event. Selections are based on asymmetry of the collected light in one

cell, described in Sec. 7.1.2, and the vertex multiplicity. The dominating background above 2 MeV is muon induced, which can be suppressed by tagging muons with help of the muon veto and large energy deposits in the detector. At lower energies the dominant contribution during reactor cycles arises from the neutron activation product ^{41}Ar which is present in the air, see Sec. 3.1.1. Large rate changes in the argon contribution have been observed, up to a factor of ∼5. Due to its short halflife (∼110 min) this depends on the production rate but likely also on the air convection within the experimental hall and especially around, and inside STEREO. The shoulder in the spectrum around 2.5 MeV is always present, also during reactor shutdowns. It includes different contributions, such as neutron capture on hydrogen at 2.2 MeV, where the neutrons can originate from muon spallation, ^{60}Co (2.5 MeV) which is present in the detector's steel vessel, and ^{208}Tl (2.6 MeV), from natural background.

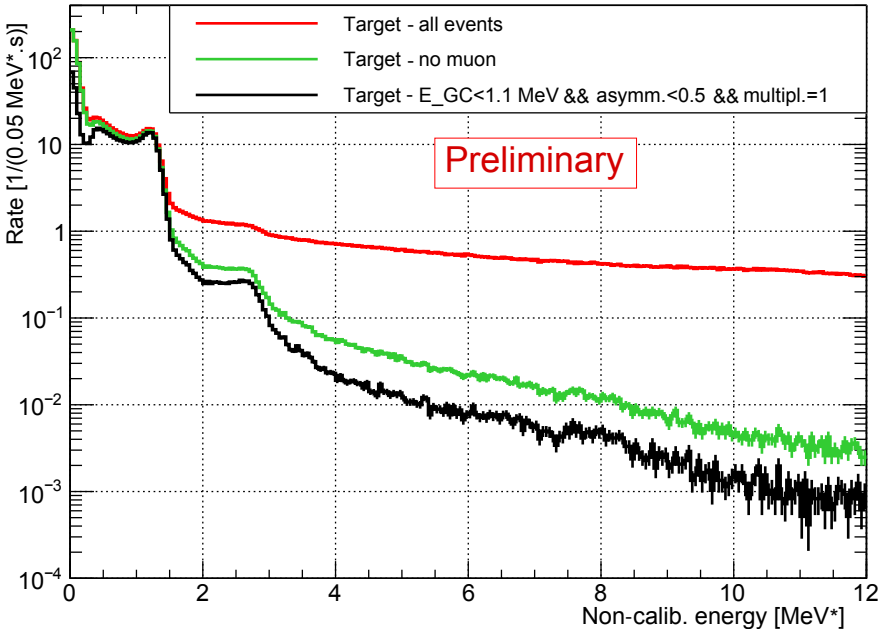

Figure 5.12: Spectra measured in the STREO target during a reactor cycle with different cuts, corresponding to a preliminary prompt-event selection (described in more detail in Sec. 7.1.2). The energy corresponds to a preliminary calibration, not taking into account quenching effects. The dominating contribution arises from muon induced background. The characteristic features after the muon cut are the ^{41}Ar peak around 1.3 MeV, a shoulder from ^{1}H(n,γ), ^{60}Co and ^{208}Tl around 2.5 MeV and the signal from neutron capture on Gd around 8 MeV.

Chapter 6

MCNP Simulations of the H7 Beamtube

The ILL operates one beamtube which is entirely crossing the reactor pool, including light and heavy water tank and passing by the fuel element at a minimal distance of about 55 cm. This tube, named H6-H7, served several generations of the GAMS instrument (GAMma ray Spectrometer [GAM17, Koc80]) located at both exits of the tube. In order to install STEREO, one of the GAMS instruments was dismounted and the corresponding beam port, H7, closed. This chapter describes simulations of the radiation level at the exit of the tube for different configurations of the beam tube and port.

The beam tube has a sample irradiation position in the center, close to the fuel element. The samples brought there are exposed to a high, largely thermalised neutron flux and serve as intense γ-ray sources for the GAMS instruments. A small carrier with a cylindrical zircalloy housing with graphite insets as sample container is in place to move probes to and from the irradiation position. For safety reasons the tube is kept under ^{4}He atmosphere. Given that the tube is not pointing towards the fuel element but only passing by, the radially emitted neutrons from the core are less likely to follow the tube directly. Due to the neutron's random walk during thermalisation and their scattering off the sample carrier, the ^{4}He or the tube itself there is still a high neutron flux at the end of the tube, at about 4.7 m from the center. Neutron capture on the GAMS sample and the tube results in an additional high gamma ray flux. Gamma rays from fission products have only a small contribution since the direct line of sight from the fuel element to the end of the tube is at least shielded by the water tank and partly by the heavy concrete reactor wall, see Fig. 6.1.

In order to protect STEREO from this elevated background an adapted plug was designed to close the H7 tube from the STEREO side. A series of MCNPX [Pel11] simulations has been performed by Pequignot [Pé15] to find a design which effectively reduces the neutron and gamma background for STEREO without introducing background for the GAMS6 experiment, still operating on the opposite side (H6) of the tube. In the final design this plug consists of, as seen from the direction of the reactor, 2 cm Boral (boron aluminium alloy, 4.5 wt% boron, 95% enriched in ^{10}B), 8 cm lead, 1 m of heavy concrete and again 8 cm of lead. This is enclosed in a shell of 3 mm of stainless steel and in order to allow mechanical movement a gap of 3 mm to the tube is kept all around. The plug ends at the outer side with a 2 cm stainless steel disk ("endcap") with a 8 mm thick boral inset facing the circular gap.

Neutron reactions in the beamtube's material (Al alloy), mainly neutron captures, and subsequent beta decays slowly change the material's structure on the scale of the atomic lattice, causing its mechanical stability to degrade over the years. For this reason beamtubes need to be exchanged after several years of operation. In case of the H6-H7 tube the maximum lifetime was reached after the end of ILL's reactor cycle 181 in March 2017. Due to problems in the manufacturing no new beamtube could be provided at this time. As a consequence the old tube could only be removed, without direct replacement. A remaining shroud of the tube in the light water tank and all the way to the end of the former tube is filled with heavy water. Without the

tube also the adapted plug cannot be deployed anymore. Instead a 42.5 cm thick stainless steel cap closes the tube towards STEREO. A new series of MCNPX simulations has been performed in the context of this thesis in order to evaluate how this change of the setup would affect the background conditions for STEREO and, if necessary, to design an adapted additional shielding. One major concern was that, given that deuterium is a good neutron moderator but has a moderate capture cross section of $\sigma_{\mathrm{D}}^{\mathrm{therm}} = 0.5\,\mathrm{mbarn}$ [END17], the newly established heavy water column connecting the core and the H7 beamport might cause a high thermal neutron flux on the proposed stainless steel endcap. This in return would result in a high rate of neutron captures and related γ-rays.

In addition the simulations with the beamtube and plug present have been repeated to crosscheck the results of both campaigns where different variance reduction methods of MCNP have been employed. In the following at first the methods which have been used and which are important for the interpretation of the simulations will be presented and finally the results of the simulation campaigns. Although in this work the setup without the beamtube had been considered first and in more detail the two setups will be presented in chronological order, where at first the beamtube is present.

6.1 MCNP methods

MCNP is a Monte-Carlo particle transport code. Particles are created in a source, transported through a predefined problem geometry via a random walk, taking into account possible physical interactions and are finally counted in a so called 'tally'. In the standard MCNP procedure the particles get assigned a given weight upon creation, usually 1 if created in the primary source or for secondary particles the current weight of the primary particle. In interactions the occurring process is chosen among all possibilities by its probability of occurrence in the given situation and the particle's weight is decreased to the probability of the process which takes place. Any produced secondary particles are stacked and treated subsequently in the same way before a new source particle is started. Only if particles, primary or secondary, reach a tally before their weight falls under a defined threshold their weight is registered, which is the measurement performed by the tally. In a well adjusted simulation the weights of tallied particles scatter around a central value and according to the central limit theorem the mean value of this distribution should converge to the true value for a high number of particles. This corresponds then to the probability for the simulated scenario that for any source particle a particle with the predefined tally characteristics (particle type, energy, ...) arrives in the tallied region. MCNP calculates also an uncertainty for each tally bin as the standard deviation of the mean of the distribution. Following the MCNP nomenclature [X-503] a tally bin with <10% relative uncertainty is considered as generally reliable, between 10% and 20% as questionable, between 20% and 50% as possibly off by a factor of a few and above 50% as not meaningful. Several so called variance reduction methods are provided whose aim is to optimise the use of computing time and reach a faster convergence of the tallied distributions by biasing the particle flux towards the tally in a controlled and well defined manner. Each method has its own advantages and disadvantages which have to be understood before choosing a suitable method for a given problem.

A common method is that of geometry splitting [X-503]. For this procedure an importance value I is assigned to each volume i, reflecting the interest of the particle transport in the respective volume. If a particle n with an assigned weight w moves from volume i to volume j two cases can occur. If $I_i<I_j$ the particle is split into I_j/I_i particles, where each of them carries the weight $I_i/I_j \cdot w$. Each daughter particle is then tracked individually which allows to have better statistics in the region of interest and to 'investigate' more possible trajectories without the need to get more particles directly from the source to this part of the geometry. If $I_i>I_j$ only the fraction I_j/I_i of particles is tracked any further, the others are stopped and deleted (called "Russian roulette" in MCNP). The weight of the surviving particles is increased to $I_i/I_j \cdot w$. In this way the overall particle weight is kept constant. The importance values are assigned to user

defined volume elements (cells) which means that the geometry of the problem has to be split into small subvolumes along the desired path of the particles. For the importance sampling it is vital that the volumes are not larger than a few free path lengths of the considered particles. If the attenuation within one volume element is too large some information will be lost (e.g. about the exact energy distribution) and cannot be regained by particle splitting. In general this method allows to investigate only certain parts of a larger geometry with more detail while the calculation time used for the major part of the volume is kept as small as possible. For large and complex geometries the calculation time can still be considerable. Problems can arise if neighbouring cells have large differences of importance values which would cause a sudden creation of many particles, which can slow down the simulation or cause the calculation to abort.

Another method is the deterministic transport, called 'DXTRAN'. Here at first a sphere is defined around a region of interest, containing a tally. Then from each interaction point anywhere in the geometry a virtual particle is transported to that sphere, where the particle's weight is calculated deterministically from the probability of being scattered in this direction and the attenuation along the path. Within the DXTRAN sphere particles are transported normally (=probabilistically). The total weight is balanced by deleting all particles reaching the DXTRAN sphere in a classical way, since they have already been accounted for. One big advantage of this method is that it can strongly increase the statistics of sampled particles in a volume far from the source. The problem is that the virtual particle is transported without interactions along the path which prevents the creation of secondary particles, multiple scattering and lateral diffusion which might be important especially for thermal neutrons.

To obtain the final result MCNP provides several tally types, which measure different quantities. The tallies used in the current simulations are the 'F1' and 'F4' tallies. Detailed descriptions of those and others can for example be found in the MCNP5 manual [X-503]. The surface current tally F1 counts the weight w of particles crossing a surface. In terms of particle transport theory, considering the angular flux Ψ as function of the particle's position $\vec{r}$, direction vector $\vec{\Omega}$, energy E and the time t, the number of particles crossing a surface A (with surface normal $\hat{\mathrm{n}}$) is

$$\int_{E_i} \mathrm{d}E \int_{\vec{\Omega}_j} \mathrm{d}\Omega \int_{t_k} \mathrm{d}t \int \mathrm{d}A \, |\vec{\Omega}\hat{\mathrm{n}}| \, \Psi(\vec{r}, \vec{\Omega}, E, t) \ , \tag{6.1}$$

in energy bin i, directional bin j and time bin k. The integration ranges in E, t and angle towards the tally surface are user-defined. The tally output, the number (weight) of particles, is useful if the simulation is to be continued in another, independent simulation, but to obtain the physically correct particle flux also the incident angle of the particles with respect to the surface has to be taken into account. This can be achieved with the F4 tally. Writing the angular flux as product of velocity v and particle density $n(\vec{r}, \vec{\Omega}, E, t)$ the scalar particle flux ϕ averaged over a volume V is

$$\begin{aligned} \bar{\phi}_V &= \frac{1}{V} \int \mathrm{d}E \int \mathrm{d}V \int \mathrm{d}t \int \mathrm{d}\vec{\Omega} \, \Psi(\vec{r}, \vec{\Omega}, E, t) \\ &= \frac{1}{V} \int \mathrm{d}E \int \mathrm{d}V \int \mathrm{d}t \int \mathrm{d}\vec{\Omega} \; vn(\vec{r}, \vec{\Omega}, E, t) \\ &=: \frac{1}{V} \int \mathrm{d}E \int \mathrm{d}V \int \mathrm{d}t \, vN(\vec{r}, E, t) \end{aligned} \tag{6.2}$$

where N is the particle density at a given point and time. Defining a differential track length $\mathrm{d}s = v\mathrm{d}t$ (6.2) becomes

$$\bar{\phi}_V = \frac{1}{V} \int \mathrm{d}E \int \mathrm{d}V \int \mathrm{d}s \; N(\vec{r}, E, t) \ . \tag{6.3}$$

The expression $\mathrm{d}s \; N(\vec{r}, E, t)$ can now be considered as a track length density in V. Thus, to estimate the average flux in a given volume the F4 tally counts $w \cdot T_l/V$ where T_l is the track length of the particle in V. The tally output is the flux in units of particles/cm^2. By default all tallies are normalised to the number of source particles. By renormalising to the actual rate

of source events, based on external information, the flux in terms of particles/($\mathrm{cm}^2\,\mathrm{s}$) can be obtained.

6.2 Normalisation of the MCNP results

The geometry used for the simulations was adapted from a preexisting model of the reactor, thankfully provided by Fuard [Fua15], including all major elements in the reactor assembly: fuel element, control rod, heavy water moderator tank and vessel, light water pool, air gap between the pool and the concrete enclosure, the heavy concrete reactor wall and all beamtubes and hot/cold neutron sources in a simplified description.

The sufficiently detailed description of the fuel element allowed to set up the simulations as 'criticality problems' in MCNP in order to obtain a correct initial source point and neutron/γ-ray energy distribution. This simulation mode is designed to obtain the k_{eff} factor of critical systems, which in reactor theory is the ratio of the number of neutrons in subsequent generations of fissions ($k_{\mathrm{eff}} = 1$ in self-sustaining chain reactions). To initialise the simulation neutrons are started from a defined source point distribution and transported through the surrounding volume by the standard random walk process. If a fissile material is present the neutrons can be absorbed in a fission process. This is not immediately simulated but the coordinates are stored and serve as source points for the fission neutrons which are started as source particles in subsequent events. For the neutrons prompt and delayed emission is considered with the corresponding energy distributions. For γ-rays on the other hand only the prompt emission from the deexcitation of the primary fission fragments is included. The contribution from delayed γ-rays, from subsequent beta decays of the fission products, has to be determined separately. Since the particles are transported by random walk they can also leave the fuel element. Those are the particles of interest for the final result and the variance reduction methods described above can be deployed to focus the simulations on particles transported towards the region of interest.

At the beginning of a calculation a number of so-called inactive generations of source particles can be defined for which no photons are produced and no quantities are tallied. This serves to guarantee that the fission source point distribution reaches an equilibrium condition in the fissile material. Subsequently the full simulations are started. During the simulations not all neutrons cause a fission process, but can leave the fuel element or be captured at any material, without causing fission. After finishing the 'inactive' simulations MCNP creates a particle balance table where the fraction of neutrons causing fissions is accounted as loss-to-fission (l.t.f.). This number can be used to renormalise the tally output, which is by default normalised to be per source particle (fission neutron), to tally events per fission. For practical problems it is useful to give quantities per unit of time. The rate of fissions N_{f} can be calculated from the reactor power P as

$$N_{\mathrm{f}} = \frac{P}{E_{\mathrm{f}}} \,, \tag{6.4}$$

where E_f is the average energy absorbed per fission in the reactor. According to Kopeikin *et al.* [Kop04] the latter is the sum of four contributions

$$E_{\mathrm{f}} = E_{\mathrm{tot}} - \langle E_\nu \rangle - \Delta E_{\beta\gamma} + E_{\mathrm{nc}} \,. \tag{6.5}$$

E_{tot} is the total released energy from the beginning of the fission process until all fission products have fully decayed to stable isotopes. It can be most precisely determined from the mass difference of the initial (fissile nucleus + neutron) and final state (stable fission products according to their total yields + number of fission neutrons) of the fission process. $\langle E_\nu \rangle$ is the average energy carried away by the neutrinos from the β-decays ($\sim 6\,\bar{\nu}_e$/fiss.). Given that in a real reactor not all fission products reach equilibrium a small correction $\Delta E_{\beta\gamma}$ is introduced, which accounts for the fact that at a given time not all fission products have reached β-stable isotopes, thus the kinetic energy of β particles and γ rays which have not yet been

emitted have to be subtracted from the total energy. The correction obtained from the midpoint of a standard 1.5 a PWR cycle for ^{235}U is given as (0.35 ± 0.02) MeV/fiss [Kop04]. In the same reference also an empirical dependence of $\Delta E_{\beta\gamma}$ on the irradiation time is given: $\Delta E_{\beta\gamma}^{\text{U-235}} = 8.8\,\text{MeV} \cdot \exp(-2.15 \cdot t[\text{d}]^{0.108}) + 0.185\,\text{MeV}$, which for the midpoint of an ILL reactor cycle (total length ~ 50 d) would amount to $\Delta E_{\beta\gamma} = 0.6$ MeV/fiss. Since this difference of the corrections is less than 1% of E_f and smaller than the stated uncertainty of E_f this difference is negligible for the current considerations. The last contribution to E_f results from energy release in neutron captures, other than fission, which mostly ($> 80\%$) occur in the fuel and fission products. Thus this contribution does not depend much on details of the reactor layout but on the fuel element composition. The values lie between 8.6 MeV/fiss. for ^{235}U and 11.6 MeV/fiss. for ^{241}Pu at the midpoint of a PWR cycle [Kop04].
In [Ma13] Ma *et al.* revised these calculations and used updated libraries for the calculation of E_tot and a more detailed calculation of $\langle E_\nu \rangle$, while $\Delta E_{\beta\gamma}$ and E_nc were adapted from [Kop04]. The values for ^{235}U are listed in Table 6.1. The resulting average absorbed energy in a reactor per fission of ^{235}U is (202.36 ± 0.26) MeV. Scaling to the nominal nuclear power of the ILL of 57.8 MW[1] [DRe17] the fission rate is

$$N_\text{f}^\text{ILL}(57.8\,\text{MW}) = 1.7830(23)\,10^{18}\,\frac{1}{\text{s}}\ . \tag{6.6}$$

Thus the physical flux at the nominal reactor power can be obtained from the MCNP simulations by using the F4 tally:

$$\phi = \frac{\text{F4-tally}}{\text{l.t.f.}} \cdot N_\text{f}^\text{ILL}\ . \tag{6.7}$$

Table 6.1: Contributions to the energy release per fission of ^{235}U in a nuclear reactor as stated in Eq. (6.5). Values from [Ma13].

E_tot [MeV]	$\langle E_\nu \rangle$ [MeV]	$\Delta E_{\beta\gamma}$ [MeV]	E_nc [MeV]
203.19 ± 0.06	9.06 ± 0.13	0.35 ± 0.02	8.57 ± 0.22

6.3 Simulations with the Beamtube present

6.3.1 Previous Simulations

First simulations of the H7 tube with the heavy concrete plug in place have been performed by Pequignot [Pé15, Pé13]. The general concept in these studies was to use geometry splitting within the heavy water moderator vessel to transport a high number of neutrons and photons from the fuel element to the beamtube. There they could be scattered on the tube materials or the GAMS sample carrier and follow the line of the tube. Different designs of the H7 beamtube plug were tested so that a short calculation time was desirable. For this reason the DXTRAN method was deployed to create contributions from each particle interaction around the moderator vessel to the tallies at the end of the beamtube. The tallies have either been placed behind the plug or behind the circular gap surrounding it. The resulting energy integrated fluxes are summarised in Table 6.2. The integrated neutron and γ-ray fluxes are attenuated by 10 and 6 orders of magnitude, respectively, behind the plug compared to the gap.

[1] The nominal thermal power of the ILL reactor is 58.3 MW, where about 0.5 MW are contributed by the cooling water pumps.

Table 6.2: Energy integrated neutron and photon fluxes at the end of the installed H7 beamtube, behind the plug and the circular gap, respectively. Simulations were performed with MCNPX using the DXTRAN method (columns 2 and 4), from [Pé15] - no uncertainties stated therein. The corresponding total rate is calculated from these values for a diameter of the plug of 21.4 cm and a surrounding 3 mm gap (columns 3 and 5).

	Neutrons		γ-rays	
	$[1/cm^2/s]$	$[1/s]$	$[1/cm^2/s]$	$[1/s]$
behind plug	$1.2 \cdot 10^{-4}$	$4.32 \cdot 10^{-2}$	$1.3 \cdot 10^{1}$	$4.68 \cdot 10^{3}$
behind gap	$5.0 \cdot 10^{6}$	$1.02 \cdot 10^{8}$	$1.6 \cdot 10^{7}$	$3.27 \cdot 10^{8}$

6.3.2 New Simulation Setup

In the new series of simulations the intention was to avoid the usage of the DXTRAN method. The deterministic particle transport without intermediate interactions may not be suitable for penetration problems where processes like multiple scattering or production of secondary particles can occur. Thus DXTRAN should not be used for the simulations after the beamtube removal, instead the particle transport is fully performed with geometry splitting. To have a consistent set of simulations also the setup with the H7 tube present was simulated in this way.

For the simulations the preexisting model of the reactor was modified. Especially the description of the H7 tube was extended in more detail to include also aluminium and steel sleeves around the actual beamtube, see Fig. 6.1, which may be important for the generation of secondary γ-rays. Subsequently the importance value assignment was prepared.

In a first step concentric ellipsoids have been introduced in the heavy water volume between the H7 tube and the fuel element. Their purpose is to guide neutrons and γ-rays from the fuel element preferentially towards the center of the tube and the H7 side, the H6 side was left unchanged. Subsequently the H7 tube, its inner volume, its outer sleeve and a surrounding ring of 5 cm thickness passing through the light water pool and the reactor's concrete wall have been split into slices of 5 cm thickness to implement a continuous increase of the cell importance towards the exit of H7.

In order to include a larger volume around the tube five concentric cylinders parallel to the tube's axis have been introduced, with their radii increasing in steps of 12 cm and with offsets of their central axes in steps of 4 cm towards the fuel element in a horizontal plane. In this way the outermost cylinder had a minimal distance of 45 cm from all components of the H7 tube, see Fig. 6.1. They are subdivided in slices of 15 cm along their axes. These additional cylinders around the central tube allow to completely switch off the largest part of the light water volume and the reactor wall while still maintaining important effects:

1. backscattering of neutrons exiting the tube back towards the tube,
2. a direct line of sight from the fuel element to the H7 exit, necessary to allow a direct contribution of fission-related γ-rays,
3. a large acceptance angle for (fast) neutrons entering the H7 tube at a larger distance from the fuel element.

Inside the moderator vessel the importance values increase from one ellipsoid to the next from the fuel element towards the H7 tube. Along the tube and the coaxial cylinders the importance values increase from slice to slice along the tube's axis and for each slice decrease from the central tube towards the outermost cylinder. For the simulations only the moderator vessel and all structures therein, a 30 cm thick layer of light water around the moderator tank, the aforementioned cylinders around the H7 tube and the simplified beamtubes H13 and H10, crossing those cylinders, have been activated. This means particles entering any other volume were stopped and not tracked any further. This restriction of the geometry was necessary to reduce the computing time and to guarantee a stable performance. It was observed in preceding

tests that the simulations often stopped with memory allocation errors when the full geometry was activated. The reason was not clearly identified but it seems likely to be related to large differences between importance values I of e.g. the main light water tank (I=1) and the H7 tube and its surrounding cylinders with exponentially increasing importance values. If a particle (e.g. a neutron coming from another beamtube) reaches the H7 tube far from the moderator vessel it would have been split immediately into a huge number of particles, corresponding to the ratio of the importance values of the cells. This could cause memory allocation faults or extremely long calculation times for this particular source event.
To further reduce the calculation time only photons above 100 keV have been considered. Photons of lower energy can easily be shielded in the steel cap at the end of the tube or by external shielding. The photonuclear effect has been taken into account.

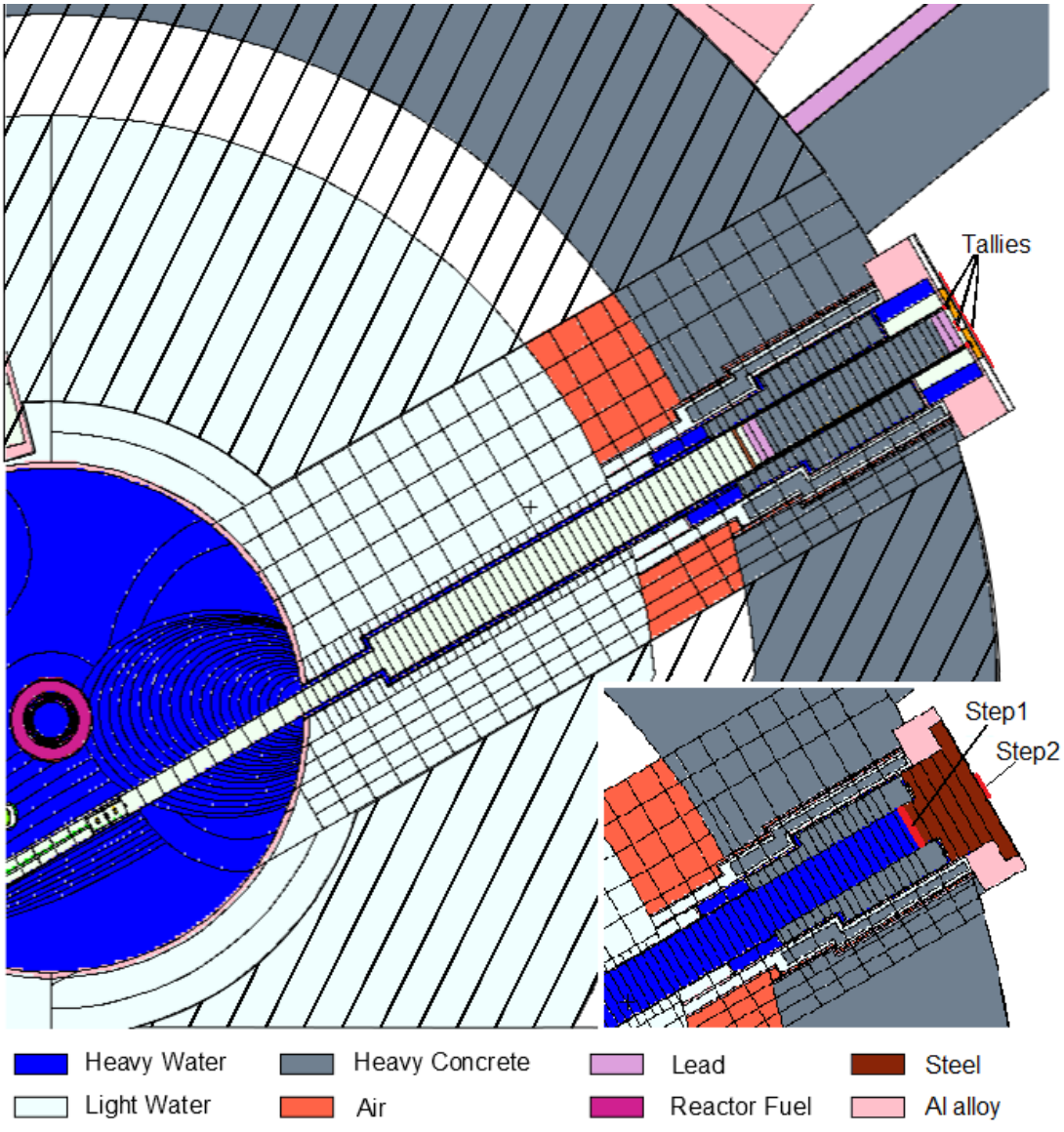

Figure 6.1: Cross section of the MCNP model of the reactor pool on the H7-side with beamtube and plug present (large) and removed (inlay), respectively. The cylindric fuel element is in the center of the heavy water moderator tank. Ellipsoidal volumes in the heavy water allow to preferentially guide particles towards the H6-H7 beamtube. The tube and elements in its vicinity are divided in slices of 5 cm for the importance value assignment (see text), the surrounding coaxial cylinders in slices of 15 cm. The hatched areas in the light water, the heavy concrete wall and the intermediate airgap are deactivated during the simulations.

This setup only based on geometry splitting has the advantage that all secondary particles and scattering processes are taken into account and all parts of the beamtube can be explored at the same time. On the other hand the restriction of the geometry may introduce some bias if the active volume is not sufficiently large. Another problem is that the computing time is large, with calculation times around three weeks per setup to reach a meaningful precision in the tallies located at the end of the beamtube, even with parallel processing on 24 processors with a utilisation efficiency of about 50%. This was partly caused by long calculation times for single batches of source particles, or likely even by single events where particles cross adjacent volumes with largely different importance values. This problem may have been limited by further optimisation of the cell importance parameters.

6.3.3 Simulation Results

A first point of reference for the simulations is the GAMS sample irradiation position. There the nominal thermal neutron flux is $5.5 \cdot 10^{14}\,\mathrm{cm^{-2}\,s^{-1}}$ [Koc80]. Although it is not specifically stated it is presumed that the flux was determined by gold foil activation measurements and the quoted flux should be understood as a 'capture neutron flux'. This refers to the simplified flux calculation from the measured gold foil activity with an averaged, energy independent cross-section value under assumption of a fully thermalised neutron spectrum. This method is usually used for flux measurements at the instruments, at the end of a beamtube. The flux of a warmer in-pile spectrum is thus slightly overestimated since an additional activation by epithermal neutrons is attributed to the thermal flux, especially relevant due to a large capture cross-section resonance of ^{197}Au around 5 eV neutron energy [END17]. From the simulations an energy-integrated flux of $(5.92 \pm 0.01) \cdot 10^{14}\ \mathrm{cm^{-2}\,s^{-1}}$ is obtained, which is about 8% higher than the quoted flux. This is a reasonable agreement when considering experimental uncertainties and the expected precision for the simulation of absolute values.

For comparison with the results of the previous simulations tallies have been added behind the plug and the circular gap, but before the stainless steel endcap of the plug, which has not been included in the previous simulations of Ref. [Pé15]. The relative uncertainties per bin for the neutron and gamma F4-tally centered behind the plug lie mostly between 10% and 20% which is acceptable. For the tallies behind the gap they mostly are significantly above 20%, due to the smaller tallied volume. Except for a few single bins they do not exceed 50%, which is sufficient for the estimation of the correct order of magnitude of the flux. Comparing the current results, Tab. 6.3, with the previous ones, Tab. 6.2, the neutron and γ-ray fluxes behind the gap are in good agreement in both methods, $5.0 \cdot 10^6 \frac{\mathrm{n}}{\mathrm{cm^2 s}}$ with DXTRAN compared to $2.3 \cdot 10^6 \frac{\mathrm{n}}{\mathrm{cm^2 s}}$ with geometry splitting and $1.6 \cdot 10^7 \frac{\gamma}{\mathrm{cm^2 s}}$ compared to $1.9 \cdot 10^7 \frac{\gamma}{\mathrm{cm^2 s}}$, respectively. For the values behind the plug on the other hand large differences are obtained. For the new simulation setup with transport via geometry splitting the neutron flux obtained is nearly eight orders of magnitude higher, the γ-ray flux three orders of magnitude. This shows the inherent problem of the DXTRAN method for penetration problems. The particles arriving behind the plug experience the full, deterministic attenuation from the entire plug (1 m heavy concrete + 16 cm Pb). In the split geometry on the other hand all particles undergo a random walk, so that particles originally propagating along the gap can be scattered later and travel only through a small part of the plug. For the γ-ray flux also the neutron capture in the iron of the heavy concrete of the plug or in its housing may play an important role. It should be noted that the total fluxes behind the gap are dominating by at least one order of magnitude, so that the new results behind the plug do not significantly change the total background estimation.

Table 6.3: Energy-integrated neutron and γ-ray fluxes at the end of the installed H7 beamtube, behind the plug and the circular gap, respectively, before the stainless steel endcap (first two lines). Simulations were performed with MCNPX using the geometry splitting method (columns 2 and 4). The corresponding total rates are calculated from these values for a diameter of the plug of 21.4 cm and a surrounding 3 mm gap (columns 3 and 5). The particle fluxes and total rates behind the endcap (last line) are averaged over a circular area with diameter of 55.5 cm. The listed uncertainties include only statistical uncertainties of MCNP.

	Neutrons		γ-rays	
	$[1/\mathrm{cm}^2/\mathrm{s}]$	$[1/\mathrm{s}]$	$[1/\mathrm{cm}^2/\mathrm{s}]$	$[1/\mathrm{s}]$
behind plug	$(8.18 \pm 1.88) \cdot 10^3$	$(2.94 \pm 0.68) \cdot 10^6$	$(3.02 \pm 0.26) \cdot 10^4$	$(1.09 \pm 0.09) \cdot 10^7$
behind gap	$(2.27 \pm 0.38) \cdot 10^6$	$(4.64 \pm 0.78) \cdot 10^7$	$(1.88 \pm 0.72) \cdot 10^7$	$(3.85 \pm 1.47) \cdot 10^8$
behind endcap	$(3.60 \pm 0.45) \cdot 10^3$	$(8.71 \pm 1.09) \cdot 10^6$	$(5.23 \pm 0.55) \cdot 10^5$	$(1.27 \pm 0.13) \cdot 10^9$

Another set of tallies measures the final neutron and γ-ray fluxes obtained at the outside of the endcap of the plug. The dominating contribution originates from the gap, with an outer radius of 11 cm. The final tallies have a disk shape with an outer radius of 27.75 cm, to obtain an average flux at the outside by including all particles which arrived through the gap and are scattered in the steel endcap. The energy-integrated fluxes of these tallies are also listed in Tab. 6.3, the spectra are compared to the spectra after beamtube removal in Fig. 6.4 in the next section.

6.4 Simulations without the Beamtube

After removal of the H7 beamtube no structures remain inside the moderator tank, all the newly available volume will be filled with heavy water. In the light water tank and all the way to the H7 exit flange an outer manchette of the beamtube will remain in place. This will also be completely filled with heavy water. These changes have been adapted in the simulations, otherwise the layout is the same as before. As now the attenuation along the former beamtube is much larger the simulation has been split in two steps. In a first step neutrons and γ-rays are propagated from the fuel element to the end of the heavy water column. In a second step they are propagated through the 42.5 cm thick stainless steel endcap, see inlay in Fig. 6.1. This separation also allows to test different endcap designs without repeating the time-consuming first step.

6.4.1 Propagation from the Fuel Element to the End of H7

In the first iteration of step 1 the outer coaxial cylinders around the beamtube had not been included, but only the innermost 5 cm. Considering a mean free path of only about 2 mm of thermal neutrons in water it was expected that this would allow for sufficient neutron backscattering for a flux estimation. One deficit of this setup was the lack of a direct line of sight from the fuel element to the end of the tube, which could be relevant for the γ-ray flux. With this first step it was shown that the simulations could be performed in an acceptable time.

Hence, in a second iteration the active volume of the geometry has been extended to the setup described earlier, see Fig. 6.1. The neutron and γ-ray spectra obtained from the two versions at the end of the beamtube are shown in Fig. 6.2 and 6.3, respectively. The neutron spectrum shows the expected shape of a moderated fission spectrum with a strong contribution of thermal neutrons with a maximum between 25 meV and 30 meV and a strong, monotonous decrease towards higher energies up to the MeV range. Above 5 MeV the spectrum decreases sharply by several orders of magnitude. The extended geometry (v2) leads to a total neutron flux which is higher by about a factor of 20 compared to the first geometry (v1). The increase is associated

with the changed equilibrium condition in the beamtube. While in the first geometry particles have been deleted at five centimeter distance from the beamtube, corresponding to a strong sink for the flux, there is in the second version a minimum distance of 45 cm between beamtube and inactive volume. This is especially relevant for neutron energies above the thermal range. In all coaxial cylinders around the beamtube there are neutrons present which shows that the extension of the volume was necessary and also that it might not have been completely sufficient, although the number of neutrons decreases fast with radial distance from the tube. Thus a further increase of the active volume might again increase the flux slightly, but the additional effect is expected to be much less pronounced. A further increase of the volume might have the additional effect of allowing for "lateral diffusion" of neutrons from other beamtubes. This might especially be important in the 50 cm wide air gap between the light water pool and the heavy concrete wall. In this range the other beamtubes (e.g. the neighbouring tubes H13 and H10) still have fluxes in the order of 10^{11} n/cm2/s. Although they are surrounded by about 10 cm of water a high number of neutrons could exit the tubes. Within the airgap the attenuation is not very strong and dominated by geometrical effects so that still a large number of neutrons could arrive at the H7 tube. These effects of lateral diffusion are not included in the simulations (except close to the moderator tank where the neighbouring tubes are within the coaxial cylinders).

The γ-ray spectrum, Fig. 6.3, is increased by about a factor of 10 in the second version. It is virtually flat between 2 MeV and 7.5 MeV, which indicates a strong contribution of Compton scattered γ-rays. The most characteristic signature is a high peak in the energy bin 7.7-7.8 MeV. This is associated with neutron capture on ^{27}Al ($E_\gamma = 7724$ keV), which is the structural material for the fuel element, the moderator vessel and the manchette of the beamtube. At even higher energies the spectrum decreases quickly up to 10.5 MeV.

The γ-rays originating from β-decays of fission products are not included in the standard MCNP simulations. In order to estimate their contribution the fact was used that the energy and intensity of the β-delayed γ-radiation are smaller than for the prompt radiation [Reu08]. Thus another, simplified MCNP simulation was started where the neutron transport was limited to the fuel element and its vicinity and neutron capture was deactivated outside the fuel element. The photon transport on the other hand was kept the same as before throughout the full reactor volume. In this way only γ-rays produced in the fuel element itself are transported to the end of the heavy water column in the H7 tube, where they were tallied. In only a few energy bins does the γ-ray flux obtained in this way exceed a fraction of 6% compared to the flux obtained for version 2 of step 1 of the simulations. Taking into account that this corresponds to the prompt γ-ray flux and thus represents an upper boundary of the β-delayed flux, the latter would not cause a significant additional contribution and is therefore neglected in the following studies.

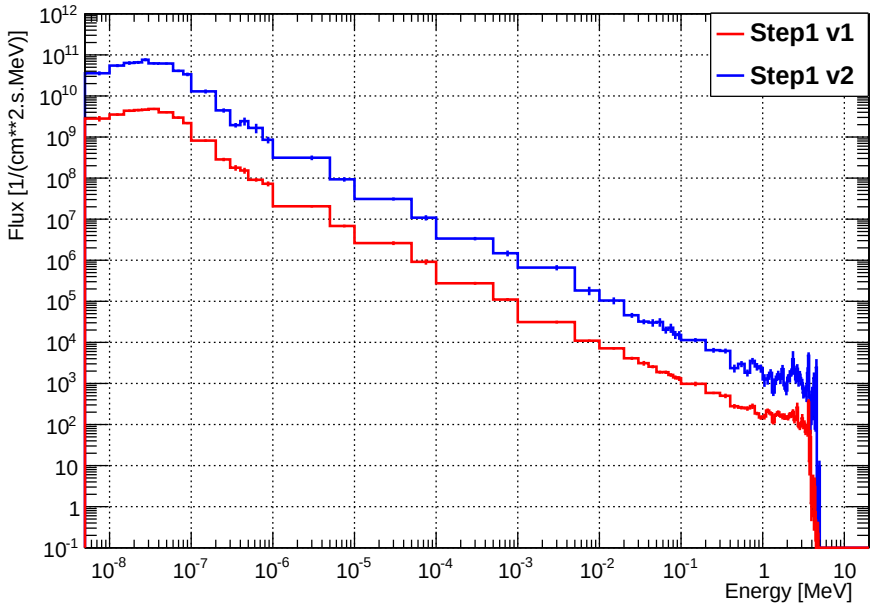

Figure 6.2: Simulated neutron flux at the end of the heavy water filled tube of H7 after the beamtube removal (simulation step 1). The red (lower) curve corresponds to the first version of the geometry (v1). This appeared to be too limited and a larger volume was included around the beamtube and in between the fuel element and the H7 exit (v2). This second geometry leads to a flux which is higher by about a factor of 20 (blue/upper line).

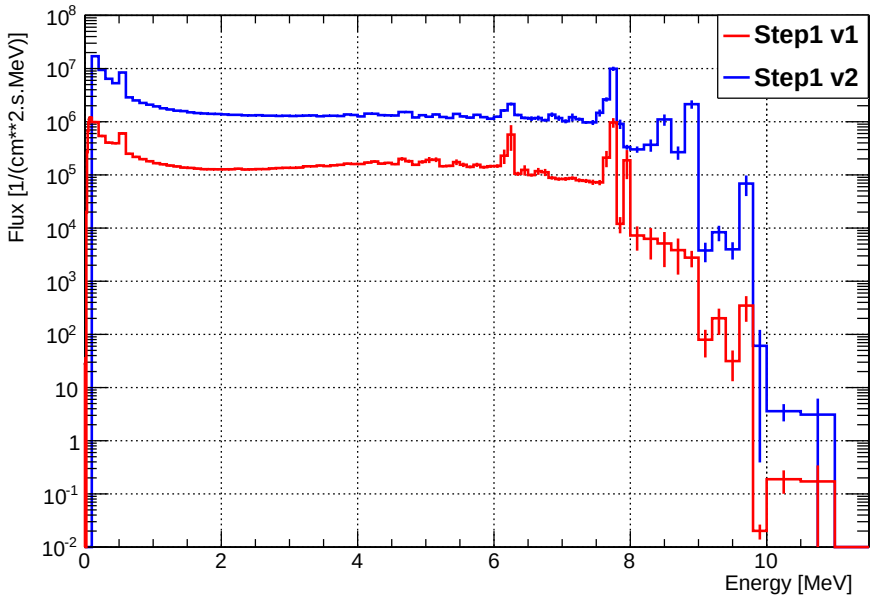

Figure 6.3: Simulated photon flux at the end of the heavy water filled tube of H7. The comparison of the first (v1, red/lower line) and second (v2, blue/upper line) version of the geometry (description see text) shows an about one order of magnitude higher flux for the extended geometry. The spectrum in the high energy range is dominated by characteristic lines from neutron captures in the structural materials. This is correlated with the increased neutron flux and proportionally increased neutron capture rates.

6.4.2 Propagation through the Endcap and Conclusion

Subsequently the propagation through the new beamtube endcap was simulated. This consists of six individual steel disks with stepwise increasing diameters and a total thickness of 42.5 cm. The first two disks contain 10 mm thick boral insets under a 3 mm steel cover under those surfaces which are in direct contact with the heavy water column. In the 2nd step of the simulations all particles are started homogeneously distributed over the terminating surface of the heavy water column in the beamtube. Neutrons and low energetic γ-rays ($< 3\,\mathrm{MeV}$) are started with a cosine angular distribution, while for higher energetic γ-rays a more forward peaked distribution was chosen, to account for the source-to-tally geometry and the collimation effect of the heavy concrete reactor wall. This corresponds approximately to the angular distributions of the particles incident on the endcap as determined from step 1 of the simulations. In the new configuration, without the plug, the tube volume contains homogeneously heavy water. Thus within the tube the attenuation is everywhere the same, but it is higher in the surrounding materials. Consequently the flux at the end of the tube is expected to be highest on the tube's axis and to decrease with increasing radial distance. After propagation through the 42.5 cm steel endcap the flux around the tube's axis should be more homogeneous, but still decrease slowly for increasing radii. To guarantee a conservative result for the final estimate the tally behind the endcap averages the flux over a circular area around the tube's axis with a radius of 7.7 cm, which slightly overestimates the average flux over the complete outer surface of the endcap.

The final spectra behind the new beamtube cap are shown in Fig. 6.4 for neutrons and γ-rays. The rates of both simulation steps are given in Tab. 6.4. The beamtube endcap reduces the overall neutron flux by more than three orders of magnitude. The relative reduction is strongest for thermal neutrons, where it reaches $\mathcal{O}(10^5)$, due to absorption and (back-)scattering in the steel. Also the neutron flux above 1 MeV is strongly suppressed, by a factor of $\mathcal{O}(10^2)$, but due to the poor moderation quality of heavy nuclei (the maximum neutron energy transfer in elastic scattering on ^{56}Fe is $\sim 7\%$) the fast neutrons are not thermalised and contribute to the intermediate energy range, so that the overall neutron attenuation is about a factor of $\mathcal{O}(10^3)$, with a flux maximum behind the endcap at about 1 eV.

By traversing the endcap the γ-ray flux is on average attenuated by a factor of $\mathcal{O}(10^5)$. The shape of the spectrum changes slightly as high energetic γ-rays are strongly attenuated, but partly by incoherent scattering and thus contribute to the low energy part of the final spectrum. As a consequence the γ-ray flux outside the endcap now decreases smoothly by one order of magnitude between 1 MeV and 8 MeV. The most characteristic feature is still the peak from γ-rays of the neutron capture on ^{27}Al at 7724 keV.

In order to make a decision about the installation of additional shielding the final fluxes of both H7 configurations obtained at the beam port behind the endcaps have to be compared:
The integrated neutron flux in the new configuration is lower by a factor of $\mathcal{O}(10)$ with reduced thermal (factor $\mathcal{O}(10^5)$) and fast neutron contributions ($\mathcal{O}(10)$), see Fig. 6.4. Especially the suppression of MeV neutrons is positive since those could penetrate further through the subsequent shielding and contribute to the background in the STEREO detector. The γ-ray flux outside the new, adapted endcap is lower than outside the previously present plug by a factor of $\mathcal{O}(10^2)$. While in the configuration with the beamtube and plug present it was strongly dominated by the flux through the gap around the plug it is now more homogeneously distributed over the surface.

With both background components reduced in the new configuration, according to the performed simulations, the new endcap as proposed by the ILL, consisting of 42.5 cm of steel with boral insets towards the reactor, is sufficient as shielding and no further adaption of the endcap or installation of additional shielding is required. An experimental confirmation whether a difference is visible in STEREO will not be possible before the next reactor cycle, early in 2018.

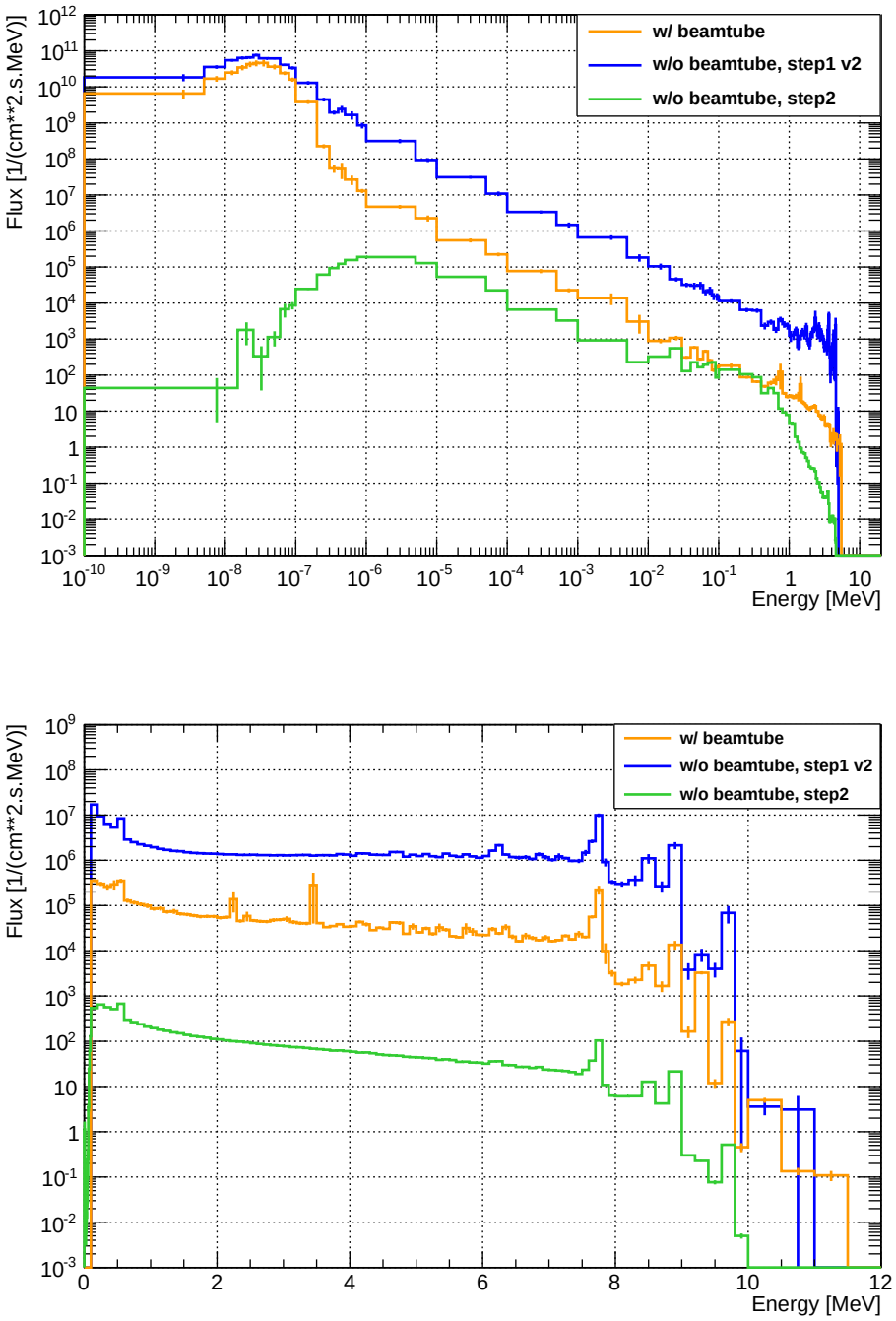

Figure 6.4: Simulated neutron flux, top plot, and γ-ray flux, bottom plot, at the H7 beamport for the configuration after removal of the H6-H7 beamtube and installation of the new stainless steel endcap (green, lower curve) compared to the flux impinging on the frontal surface of the endcap, facing the reactor (blue, upper curve) and the situation with the beamtube and heavy concrete plug present (orange, central curve).

Table 6.4: Simulated neutron and γ-ray fluxes after removal of the beamtube, impinging on the new endcap and behind the new endcap in the configuration of 42.5 cm of stainless steel with boral insets towards the reactor (column 2). The fluxes on the outer surface have been averaged over a central circular area with a diameter of 15.4 cm to guarantee a conservative estimate. The total rates before the endcap are calculated for the diameter of the heavy water column (24.8 cm), the rates outside are scaled to a disk of 55.5 cm diameter, for comparison with Tab. 6.3. The simulations were performed in two subsequent steps, the uncertainties of the first step are propagated and listed separately for the second step. Only statistical uncertainties of MCNP are given.

	Neutrons	
	$[1/\mathrm{cm}^2/\mathrm{s}]$	$[1/\mathrm{s}]$
impinging on endcap (step 1)	$(2.88 \pm 0.12) \cdot 10^4$	$(1.39 \pm 0.06) \cdot 10^7$
behind endcap	$(8.40 \pm 0.35\|_{\text{step 1}} \pm 0.01) \cdot 10^1$	$(2.032 \pm 0.088\|_{\text{step 1}} \pm 0.002) \cdot 10^5$
	γ-rays	
	$[1/\mathrm{cm}^2/\mathrm{s}]$	$[1/\mathrm{s}]$
impinging on endcap (step 1)	$(1.67 \pm 0.03) \cdot 10^7$	$(8.07 \pm 0.14) \cdot 10^9$
behind endcap	$(8.73 \pm 0.16\|_{\text{step 1}} \pm 0.02) \cdot 10^2$	$(2.112 \pm 0.037\|_{\text{step 1}} \pm 0.005) \cdot 10^6$

Chapter 7

Data Analysis

The first run period of the STEREO experiment took place from November 2016 to March 2017. After an initial commissioning phase data was taken during about 70 d with the operating reactor and during about 28 d of reactor shutdown. In this chapter at first an overview is given over the performance of the detector and the status of the analysis methods developed by the collaboration, as of summer 2017. The described methods and parameters are not finally fixed and may be subject to changes in the future. Consequently for some procedures only qualitative descriptions are given. The second part of the chapter, Sec. 7.2, describes the calibration procedure for the in-situ quenching determination, developed in the context of this thesis, and the results obtained for the quenching analysis of STEREO's liquid scintillators.

7.1 Status of the STEREO Experiment

7.1.1 Detector Performance

The STEREO detector was operational and started data taking on November 10, 2016. The first weeks were reserved for commissioning, which was necessary to optimise the operational parameters (trigger thresholds, signal integration windows) and for the scintillator to settle. During the filling bubbles may have been created in the liquid which needed to surface to avoid an impact on the performance. In addition the scintillator's temperature only slowly adapted from the lower temperature in the storage area to the temperature in the reactor hall. Small changes in the scintillator's light yield are expected from that. During the commissioning time two mechanical defects of components were observed. The first one concerned two of the optical buffer volumes hosting the PMTs which were leaking the buffer liquid (n-dodecane) into the cells underneath. This happened in the cells GC-Front and TG4. As the buffer liquid is chemically compatible with both scintillator liquids no impact is expected on the overall performance of the scintillators. However, a small impact could arise by an effective reduction of the Gd concentration at the top of cell TG4, although no indication for this effect could be found, yet. More prominent is the loss of the optical contact between the PMTs and the acrylic buffers. The n-dodecane has a similar refractive index n as the acrylic ($n \sim 1.5$) while that of air ($n \simeq 1$) is lower, resulting in total reflection at the optical boundary. As a result in both cells the light collection decreased by about 50%.

A second effect was the slow increase of the optical cross talk between cells. They are separated by sandwiches of acrylic plates and VM2000-foils with intermediate airgaps, see Fig. 3.5.

The ratio of detected scintillation photons in a cell next to the actual interaction and the vertex cell, due to light transmission through the VM2000 or propagation through corner parts where the VM2000 coverage is not complete, was expected around $Q_{\text{neighbour}}/Q_{\text{vertex}} \sim 5\%$, for TG and short GC cells, and about 1.3% for central cells to the long GC cells. As it turned out the glue between the acrylic sandwich plates became porous in most of the optical separation walls, despite previous successful tests for chemical compatibility with the scintillator, and the optical separation walls were slowly filling with scintillator. Thus the total reflection for small grazing angles was lost and the fraction of light detected in the non-vertex cells, named 'light

leaks' (LL), increased to about 12-15% between central cells and about 2-3% towards the long GC cells, respectively.

The light leaks can be described quantitatively by parameters LL_{ij} defined as the fraction of light detected in non-vertex cell j relative to the vertex cell i. These parameters can be obtained directly from data of neutrino runs by plotting Q_j versus Q_i where i and j run over all cells, and subsequently determining the average slope of $Q_j(Q_i)$[Rea16]. This gives the LL parameter for events homogeneously distributed over the cell volumes. The parameters can also be obtained from source calibrations. The emitted γ-rays have a limited interaction radius around the source, dependent on the energy, which allows to measure the height dependence of the LL. This depends also on the central ($\sim$ mid-height) value and varies from about $5 \pm 1\%$ to about $10 \pm 2\%$ [Min17]. The values obtained from the neutrino runs are in agreement with the source values slightly below mid-height.

During a long reactor shutdown in 2017 the STEREO detector had to be moved from its measuring position to allow for reactor maintenance works. This time period was also used to repair the defects of the buffers and optical separation walls. Restart of data taking is scheduled for October 2017.

The readout of the scintillation light in STEREO is done with PMTs on top of the cells, as described in Sec. 3.2.1. Each PMT has its own characteristics and the measured electronic signals need to be calibrated for each PMT individually. For this purpose single photo-electron calibrations are performed every 1-2 h with the LED system, see Sec. 3.2.1. As a first intercalibration of all PMTs the measured electronic signals are normalised to the number of detected photo electrons (pe), which is the common unit of measured charges used within the collaboration and will also be used throughout this chapter.

For a correct energy reconstruction in the measurements also the optical cross talk between the cells needs to be taken into account. Many different options have been discussed in the collaboration, such as summing over the charge of the full detector and using the cells only to tag the vertex, or summing over subsets of the detector. The preferred option so far is the more straightforward option of reconstructing the energy cell-wise and taking the light leaks into account explicitly. This facilitates the treatment of cell-dependent effects, as for example the cell TG4 has the same scintillator light yield as the other target cells, but a reduced light collection efficiency, whereas the GC scintillator has a different light yield than the target.

A procedure was developed by collaborators to correct explicitly for the optical crosstalk [Lhu16, Bla17b]. For each energy deposition E^{dep} in the detector, cell i detects the charge

$$Q_i = \sum_{\forall j} E_j^{\text{dep}} \cdot \text{LY}_j \cdot \mathcal{L}_{ji} \cdot \alpha_i \ , \tag{7.1}$$

where the index j runs over all six TG cells and four GC cells. The detected charge in cell i is composed of the scintillation light produced in cell i, which is the product of the energy deposited in the cell E_i^{dep} and the light yield of the cell LY_i (LY is different for TG and GC but is assumed to be the same among all cells in each sub-volume), and the fraction $\mathcal{L}_{ji}$ of the light created by energy deposition E_j in the other cells j. α_i describes the total light collection efficiency of the cell. For convenience the parameter LL_{ii} from above, which is the light detected in a cell relative to the vertex cell, is defined to be one, which means the parameters $\mathcal{L}$ in Eq. (7.1) are normalised to $\mathcal{L}_{ii}$, the fraction of the light produced in cell i that is detected in the cell i itself.

The parameters required for Eq. (7.1) can then be obtained from calibrations with γ-ray sources, where only the light detected in one cell is considered, the light leaking out of the cell is ignored. This results in the calibration coefficients $\text{CC}_i = \text{LY}_i \cdot \mathcal{L}_{ii} \cdot \alpha_i$. Their values slowly changed over time as the light leaks increased. The parameters LL_{ij} are obtained as described above by determining the slope of $Q_j(Q_{\text{vertex}})$, which corresponds in this notation, for cases without energy leaks ($E_j = 0$), to

$$\text{LL}_{ij} = \frac{Q_j}{Q_i^{\text{vertex}}} = \frac{E_i \cdot \text{LY}_i \cdot \mathcal{L}_{ij} \cdot \alpha_j}{E_i \cdot \text{LY}_i \cdot \mathcal{L}_{ii} \cdot \alpha_i} \tag{7.2}$$

Thus Eq. (7.1) can shortly be written as a single sum over all ten detector cells

$$Q_i = \sum_{j=\text{cells}} E_j^{\text{dep}} \text{CC}_j \text{LL}_{ji} \ , \tag{7.3}$$

or alternatively in matrix form by summarising the ten cells in a vector

$$Q = \mathbf{M} \cdot E \qquad E = \mathbf{M}^{-1} \cdot Q \ , \tag{7.4}$$

where $\mathbf{M}$ is a 10×10 matrix, combining the parameters CC_i and LL_{ij}. By inverting $\mathbf{M}$ the deposited energy can be obtained from the measured charges in the cells.

The LL values are calculated from each neutrino run ($\sim$ every hour) and the CC were measured with a ^{54}Mn source three times per week and can be interpolated in between if necessary. This allows to compensate the time evolution of the cell's response due to the light leaks. One verification of the algorithm is done by using it to monitor the hydrogen neutron capture line ($E_\gamma = 2.2\,\text{MeV}$), present in the background (e.g. due to neutrons from muon spallation). While some parts of the procedure are still under refinement the peak position is stable within statistics, see Fig. 7.1. The resolution in the reconstructed energy is about 7.8% (σ/E) at 2.2 MeV, or for comparison, assuming a $\sigma \propto \sqrt{E}$ dependence, 11.6% at 1 MeV.

This resolution corresponds to events homogeneously distributed over the cell volume. For more localised sources, as calibration sources, a height dependence of the charge peak position, resulting from the position-dependence of the light collection efficiencies, can be resolved. This lies in the expected range around 6% between top and bottom, see Fig. 7.3.

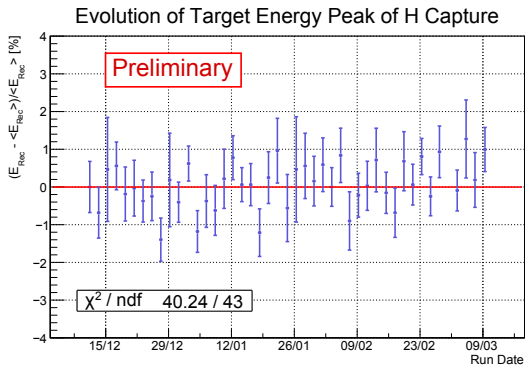

Figure 7.1: Relative variation of the position of the hydrogen neutron capture peak at $E_\gamma = 2.2\,\text{MeV}$, after application of the energy reconstruction algorithm [Bla17a]. The slow evolution of the light leaks (optical crosstalk) is compensated and no systematic drift is observed within the available statistics.

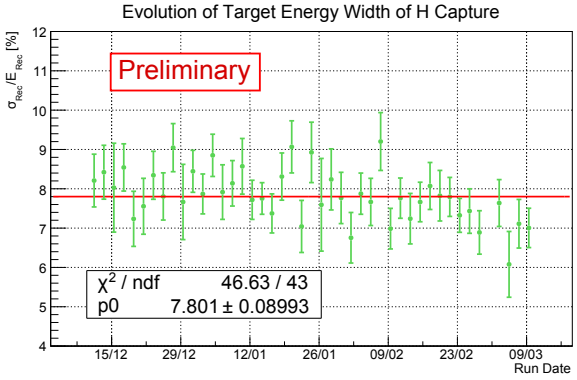

Figure 7.2: The width of the hydrogen neutron capture peak at $E_\gamma = 2.2\,\text{MeV}$ in the reconstructed energy spectrum is stable within statistics and has a resolution (σ/E) of 7.8% [Bla17a].

The doping of the scintillator with Gd not only allows to detect the neutron via the γ-rays emitted in the capture, it also strongly reduces the diffusion time of the neutron in the scintillator due to the high capture cross section of Gd, see Tab. 2.3. This allows to set a shorter coincidence time window for IBD events and thus to reduce the contribution of random coincidences compared to an undoped scintillator. The time constant of the neutron capture can be obtained from the time correlation of IBD candidate pairs, where the positron serves as prompt trigger and the neutron capture event is detected in delayed coincidence. As crosscheck the time constant can be determined from calibrations with an isotopic neutron source, e.g. an Am-Be source. In most cases the neutrons emitted from this source are in coincidence with a 4.4 MeV γ-ray, which can be used as prompt trigger. The capture time constants determined in both methods are in good agreement, see Fig. 7.4.

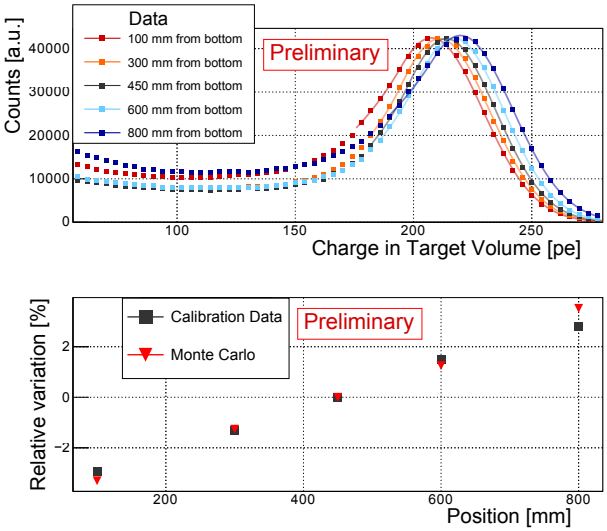

Figure 7.3: Height dependence of the total charge measured in the target for different positions of a ^{54}Mn source in cell TG6. From [Bon17c].

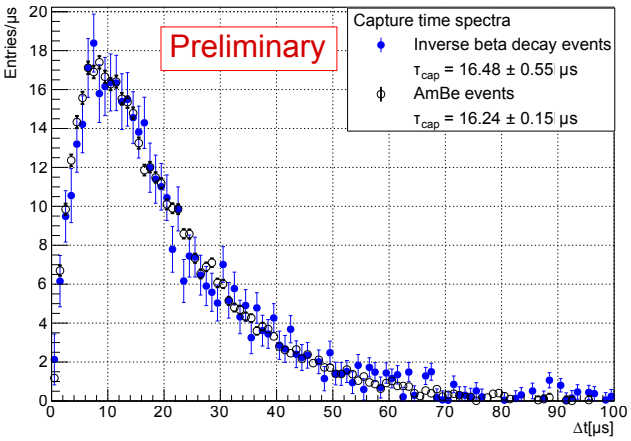

Figure 7.4: Distribution of the time delay of the neutron capture signal after a prompt trigger, compared for IBD events and Am-Be source calibrations. The increase between 0 and $\sim 10\,\mu$s is due to improving moderation. From [Alm17].

7.1.2 Status of the Neutrino Analysis

The search for IBD events is based on the delayed time coincidence of the positron (prompt event) and neutron (delayed event) detection. As prompt event qualifies any energy deposition in the window [2-8] MeV. This is set to exclude background at lower and higher energies. From the neutron capture on Gd about four γ-rays with a total energy of 8 MeV are expected. To allow for one of them to escape from the detector undetected, which is likely at the borders, the energy window is set to [5-10] MeV for the delayed event. These windows have been set a priori, but an increase would reduce the signal to background ratio without increasing the sensitivity significantly, due to a larger accessible energy range [Bon17d]. The time coincidence window τ is set to $70\,\mu$s.

Possible background can either be random coincidences or correlated events. The rate and spectrum of random coincidences can be determined statistically by opening a coincidence time window of the same width at later times, where no correlated delayed events occur (e.g. 1 ms after the prompt) and recording the coincidences obtained therein. By use of multiple shifted time windows the accidental background can be measured with high statistical precision. At the current stage of the analysis cuts the accidental background is nearly one order of magnitude lower than the correlated rates, see Fig. 7.5. The latter are composed of neutrino events, during the reactor cycles, and, dominating in number, cosmic background. This can for example be scattering and subsequent capture of fast neutrons or multiple neutrons produced in muon spallation and being captured with some delay. Fast neutrons could in principle also originate from the reactor, but so far no indication for such events could be found. In order to reduce the contribution of cosmic background the muon veto on top of the detector setup is used. This has an intrinsic efficiency for vertical muons of $> 99\%$, as mentioned before in Sec. 3.2.1. If a muon is detected a veto of $100\,\mu$s is applied, off-line, on subsequent events. Remaining background mainly originates from muons passing next to the veto, but still hitting the shielding or materials close to the detector and causing spallations. Another class of background events are muons stopping inside the detector and their subsequent decay. If this occurs within a short range from the border of the scintillator only little energy may be deposited inside the scintillator, thus fulfilling the energy selection criteria. If this occurs close to the top of a cell the scintillation light is distributed very inhomogeneously over the cell's PMTs, which can be used for distinction

from IBD events which show a more homogeneous light distribution, due to the larger interaction radii of the γ-rays produced in positron annihilation and neutron capture. This cut has a high selectivity on muon events [Bon17a].

Further background reduction methods are developed and under refinement, such as exploiting the PSD capability of the scintillator to identify fast neutron scattering or using the prompt-delayed-event distance or topology, leading to a major reduction of correlated background rates, see Fig. 7.6. The event selections are not yet fully optimised and a further improvement is expected. The remaining background can be measured during reactor shutdowns and subtracted statistically. The cosmic background has a slight dependence on the atmospheric pressure. This is taken into account by determining the pressure dependence in the correlated rates and renormalising all rates to a reference pressure. In Fig. 7.6 the pressure-corrected rates for the full detector are shown. With the currently best cuts a neutrino rate of about 300 per day in the full detector is obtained. In the final analysis the neutrino spectra will be reconstructed per TG cell.

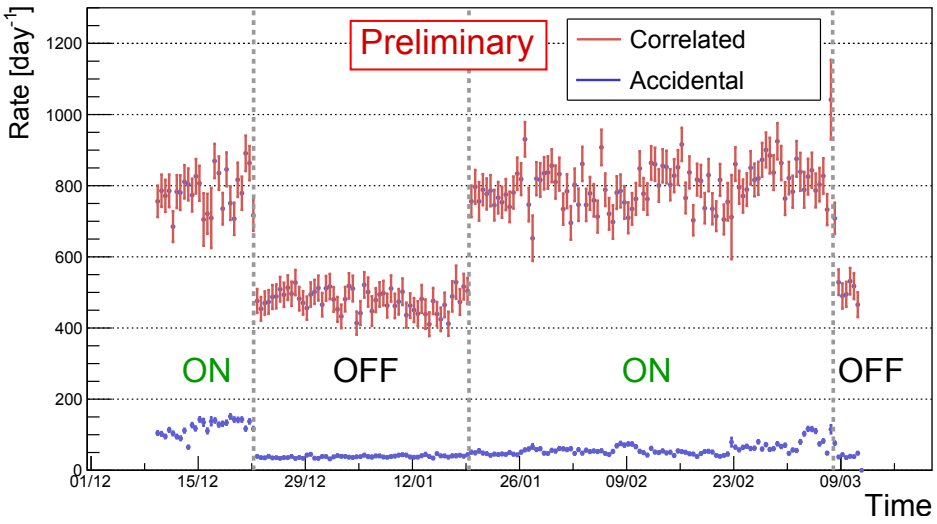

Figure 7.5: Evolution of random and correlated coincidence rates in the full STEREO detector, corrected for variations of the atmospheric pressure. The periods with the reactor 'on' and 'off' are labelled accordingly. All current event selection criteria are applied, compare Fig. 7.6. From [Bon17c].

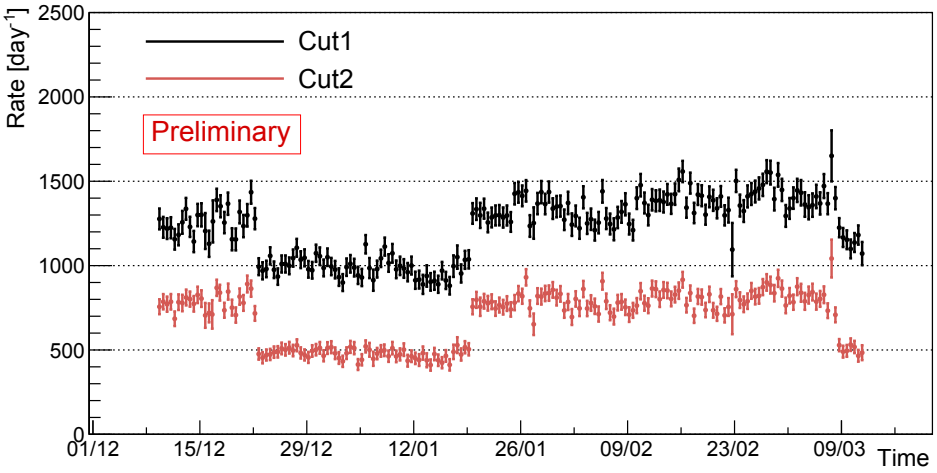

Figure 7.6: Evolution of the correlated event rates in the full STEREO detector, corrected for variations of the athmospheric pressure. Comparison of the initial proposal cuts (Cut1) and additional cuts, currently under development (Cut2). Cut1: prompt and delayed event energy windows, PSD cut, coincidence time $\leq 70\,\mu$s, $100\,\mu$s veto after identified muon crossing. Cut2: Cut1 and event asymmetry, prompt-delayed interaction distance, prompt event topology. From [Bon17c].

7.2 Determination of the Quenching Curves of the STEREO Scintillator Liquids

The properties of liquid scintillators in general and the STEREO scintillator in particular have been described in Section 3.3. One important property is the quenching behaviour of the liquid, which causes a non-linear relation between the incident energy and the light output and needs to be known for a correct energy reconstruction. This section describes a study on the in situ determination of the quenching properties of the STEREO scintillator.

In general the quenching of the energy deposited via ionisation in a scintillator increases with the specific energy loss $\mathrm{d}E/\mathrm{d}x$ of the particles. From the IBD two particles need to be measured, the positron, depositing energy first directly by ionisation and subsequently via the two annihilation γ-rays, and the neutron, which is detected by capture on Gd (or H), where γ-rays are emitted. Proton recoil of the IBD neutron is negligible and is not considered here. The scintillator's response to electrons is linear above about 125 keV [Kno00]. Considering the low atomic number of its main constituents carbon and hydrogen, the dominating interaction process for γ-rays between 40 keV and 10 MeV is Compton scattering, see Fig. 7.7. Thus especially from low energetic γ-rays also a large number of low energetic electrons is created. The fraction of Compton-electrons created into the linear region (>125 keV) increases with the γ-ray energy which causes also an overall non-linear response to γ-rays. This response approaches a nearly linear regime when the relative changes in the fractions of electrons created above 125 keV becomes small with increasing γ-ray energy, above approximately 2 MeV. Difficulties arise in the mixed energy deposition of the positron (high energetic positron plus two low energetic γ-rays), which causes a different total quenching than for γ-rays of the same energy.

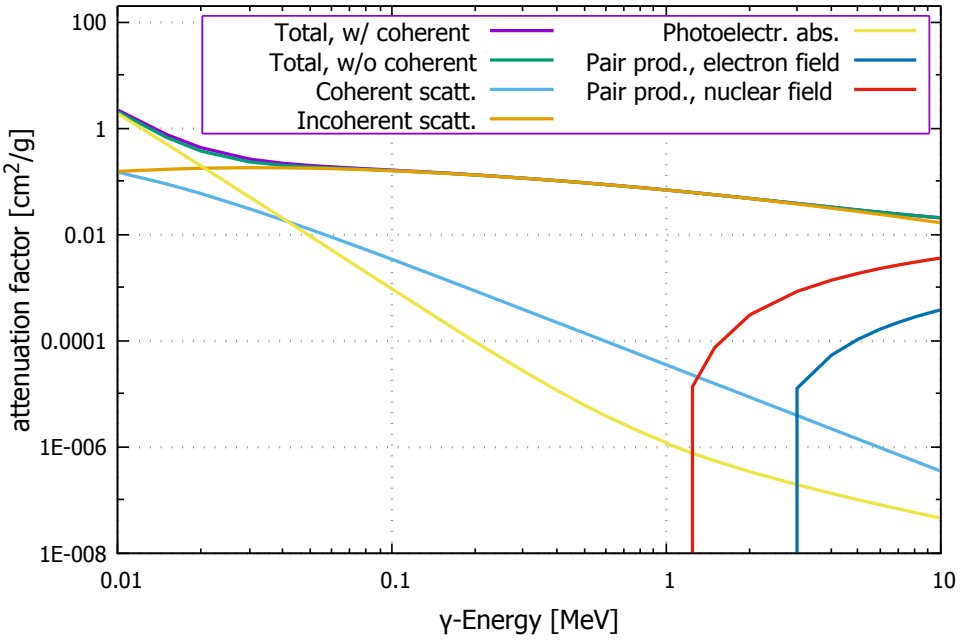

Figure 7.7: Photon attenuation coefficients for a liquid scintillator with a hydrogen/carbon ratio of 1.2. For energies above $\sim 40\,\mathrm{keV}$ incoherent (Compton) scattering is the dominating interaction process. Data from [XCO17].

In order to correctly take into account all individual interaction steps a Monte-Carlo simulation (MC) can be used. For STEREO a Geant4-based [Ago03] simulation was developed by the collaboration, including the real geometry of the detector and the PMTs, the creation of scintillation light in each particle interaction step in the scintillator and the transport of the scintillation photons. The scintillator model also includes the quenching effect by applying the quenching factor to the deposited energy E_{dep} of each interaction step:

$$E_{\mathrm{quenched}} = \frac{E_{\mathrm{dep}}}{1 + k_{\mathrm{B}}^{\mathrm{MC}} \left.\frac{\mathrm{d}E}{\mathrm{d}x}\right|_{\mathrm{MC}}} \,. \tag{7.5}$$

Birks' parameters for both liquids (TG and GC) in the simulation $k_{\mathrm{B}}^{\mathrm{MC}}$ are those of the Double Chooz experiment as first estimates and need to be adjusted.

The photon energy deposition at the energies considered will always occur via electron interactions. Thus, in order to calibrate the fundamental quenching behaviour, it would be natural to use (quasi) mono-energetic electron sources, as for example conversion electrons. Given the short range of electrons in matter an in-situ calibration would require to dissolve a source material in the scintillator. This could potentially alter the optical properties and a test of this kind could rather be done at the end of the experimental campaign.

The best way to non-invasively access STEREO's inner volume is with γ-ray sources, for which several calibration mechanisms have been implemented, see Section 3.2.1. The calibrations considered here are performed by source deployment in the calibration tubes. As the quenching is a property only of the liquid and not of the geometry, only calibration runs at one central height, at about 45 cm above the cell floor are used, where border effects from escaping γ-rays towards the top or bottom are smallest. The height dependence of the measured charge, see Fig. 7.3, should average out and only cause a slightly increased width of the charge peaks.

Some difficulties arise for the calibrations. For internal source calibrations STEREO basically resembles a full-absorption γ-ray detector. With Compton scattering as dominating interaction process γ-rays will deposit their energy in several interactions. The mean free path of γ-rays in a typical scintillator liquid ($n_{\mathrm{H}}/n_{\mathrm{C}} \sim$1.2, $\rho \sim 0.9\,\mathrm{g/cm^3}$) is about 23 cm at 2 MeV. Considering a cell width of about 37 cm a substantial fraction of events will distribute their energy over at least two cells. For the determination of the scintillator's response it is necessary to have quasi

monoenergetic energy deposits, i.e. the full energy deposition within one cell. In order to select these events cuts have to be applied to suppress events which deposit energy outside the cell of interest (named 'Compton events'). As mentioned before an optical cross-talk is observed between the cells, even for full energy deposits within one cell. This effect of scintillation light leaks overlaps with the energy leaks and limits the efficiency of possible Compton suppressing cuts.

A set of γ-ray sources is available, covering the energy range from 511 keV, from positron annihilation, to 4.4 MeV, emitted from an Am-Be source. The sources and some relevant properties are listed in Table 7.1. While most have been purchased some additional, short-lived sources have been produced in-house at the ILL by neutron activation of suitable materials. Some of the sources emit only, or dominantly, one gamma line, others emit two or more, partly in coincidence, which has to be taken into account for the calibration as nearly all emitted γ-rays will deposit energy within the detector.

In the following the general calibration procedure will be explained on the example of ^{137}Cs, for all other sources only characteristic features will be explained and the results presented. In all cases the calibrations with the source deployment in TG1 will be discussed. The full set of calibration was also performed in TG6 to determine the quenching of the GC liquid. These runs will only be described where they show different characteristics. All considered runs have been performed on the same day, February 22, 2017, so that no changes in the detector performance are expected between the runs. Finally the quenching dependencies will be presented for both scintillators (TG and GC) for the current state of the simulations and the analysis.

Table 7.1: Sources available for the determination of the quenching behaviour of STEREO's scintillator liquids. The date is the reference date for the activity.

Source	Activity	Date (if stated)	Main γ-ray energy [keV]
^{68}Ge (^{68}Ga)	90 kBq	01/10/16	2×511 keV (coincident)
^{137}Cs	37 kBq		662 keV
^{54}Mn	90 kBq	01/10/16	835 keV
^{65}Zn	2.8 kBq	15/12/16	1116 keV
^{124}Sb	1.6 kBq	15/12/16	603 keV, 1691 keV (coinc.)
^{24}Na	5.9 kBq	22/02/17 18:00	1368 keV, 2754 keV (coinc.)
Am-Be	250 MBq (^{241}Am)		59.5 keV (^{241}Am)
	$\sim$ 10-20 kBq (neutrons)		4438 keV

7.2.1 General Considerations for the Calibration Procedure

The quenching is a property of the scintillator liquid and not of the cell geometry. Thus it is sufficient to perform the quenching analysis in one TG and one GC cell, only. The major problems the calibration procedure has to address are

(i) Applicability for both volumes (TG and GC),

(ii) Applicability for all sources (single- and multi-γ-ray sources),

(iii) Suppression of the Compton background,

(iv) Evaluation of the mean deposited energy (given the detector design and resolution, a complete Compton suppression cannot be achieved),

(v) Consistency over the full energy range,

(vi) Minimal systematic uncertainties.

Point (i) is already constraint by the detector design. Tubes for internal calibration are only connected in cells TG1, TG4 and TG6, denoted 'source cells' (S) in the following. The

tubes are centered with respect to the width of the cells (y-axis) but shifted towards the front along the length of a cell (x-axis), see Fig 7.8. If also the GC should be calibrated in the same source-to-cell geometry as the TG, in order to share the same systematics, then the calibration has to be done in a cell next to a source cell. An additional constraint results from the reduced light collection efficiency and resolution in the cells with empty buffers, GC-Front and TG4. It is preferable to avoid these cells for the quenching analysis. The long GC volumes at the sides of STEREO have a different geometry than all other cells which leaves the GC-Rear as best option for the GC calibration. This requires the cell used for the calibration ('calibration cell' C) to be the downstream neighbour of the source cell.

For multi-γ sources, point (ii), the sum peak of several γ-rays cannot be used for calibration. As the quenching decreases with increasing initial γ-ray energy it would be less pronounced for a single γ-ray of a given energy than for the coincidence of two γ-rays which would sum up to the same total energy. The sources in use have a maximum of two high-intensity γ-rays emitted in coincidence. To make use of the single γ-rays emitted in a cascade the individual photons need to be separated. This can be achieved by requiring their detection in different cells. For this reason the cell upstream of the source cell is used as a 'gate cell' (G), to allow for a coincidence condition between gate and calibration cell. Two of the sources, ^{24}Na and ^{124}Sb, emit a low and a high energetic γ-ray. The low energetic one, with a shorter range, will be used as trigger in the gate cell, which is at a shorter distance to the calibration tube, and the high energetic one, which is in a region not accessible with the single-γ sources and therefore of larger interest, is detected in the calibration cell. A scheme of the cells and their labelling is shown in Fig. 7.8. This configuration has the advantages that still Compton suppressing cuts can be applied on the source cell and that the optical cross-talk from the gate cell to its next-next neighbour, the calibration cell, is smaller than for direct neighbours. In addition, by having both γ-rays confined the cross-talk can be taken into account explicitly by determining the leakage coefficient between the cells from another, single-γ-ray source with comparable energy and correcting the signal in the calibration cell for it.

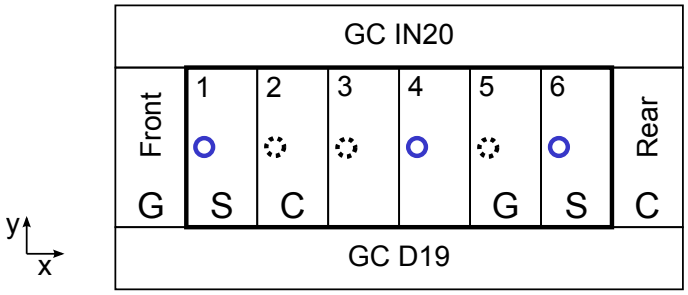

Figure 7.8: Top view of the detector cells with the labelling used for the quenching analysis of the TG liquid (left) and the GC liquid (right): G - gate cell, S - source cell, C - calibration cell. The calibration tubes (circles), for reasons of homogeneity present in all cells, are only accessible in three cells: TG1, TG4 and TG6 (solid, blue circles). For the quenching analysis calibration runs in cells TG1 and TG6 at a central height (45 cm) have been considered.

(Remark: During the maintenance period in 2017 not only the buffer leaks in cells GC-Front and TG4 and the leaks in the optical separation walls have been repaired, but also the tubes in cells TG2 and TG5 were connected to the outside. This provides two additional calibration tubes, next to the three previous ones. In principle this allows for future calibration runs to perform the TG quenching calibration for other sets of Gate-Source-Calibration cells.)

Points (iii) to (vi) will be explained on basis of the calibration example in the next section. In general the steps of the calibration procedure are:

1. Definition of a region of interest.
2. In situ determination of light leaks (LL).
3. Definition of Compton suppression cuts based on the LL.
4. Calculation of the calibration coefficients.
5. Determination of systematic uncertainties resulting from the cut parameters.

7.2.2 Calibration Procedure Explained on the Example of Cs-137

^{137}Cs undergoes β^--decay with a halflife of 30.1 a to ^{137}Ba, with about 95% branching ratio to $^{137\mathrm{m}}$Ba which has a halflife of 2.5 min. The latter deexcites via emission of a single γ-ray of 661.7 keV (with an internal conversion coefficient of about 15%), which is used for the calibration (all values from [ENS17]).

With the setting as defined above, the first step in the calibration procedure is the definition of an energy region of interest (ROI). For single-γ sources this is a range around the peak in the calibration cell, for multi-γ sources around the peaks in the calibration and the gate cells, for which the coincidence condition is established. The other purpose of the ROI is to limit the energy range for the subsequent determination of the light leaks from the calibration cell to other cells, since with only small fractions of the full energy detected in the calibration cell the energy sharing by Compton scattering to neighbour cells would dominate over the light leaks.

For ^{137}Cs with a comparatively low γ-energy of 662 keV only a small fraction of the emitted γ-rays reaches the calibration cell without an initial interaction in the source cell. Due to the large Compton background and the small separation in energy of Compton-scattered and full energy events, compared to the detector resolution, the full energy is only visible as a shoulder in the spectrum if no event selection is applied, see Fig. 7.9. With the source in TG1 the height of the shoulder in TG2 is about 25 times smaller than the peak in TG1, which shows the inherent disadvantage of this method, that a high statistics is required. On the other hand for ^{137}Cs only one minute of measuring time was used as default. The region of interest for the in-situ determination of the light leaks was chosen to include the full energy peak area and a tail to lower energies, see Fig 7.9.

In the second step the LL parameters and the Compton suppressing cuts are defined. The former are also used as correction in multi-γ sources and are determined in-situ for each (single-γ) source as described below. This guarantees that the LL parameters are determined for the same source point and interaction point geometry as is used for the calibration. This is relevant since also the LL parameters show a small height dependence [Min17] (about 1-2 percent points for central values of 5-10%) and γ-rays of different energies have different interaction radii within the detector.

The average fraction of leaking light from calibration cell C to any other cell i, $\mathrm{LL}_{\mathrm{C}i}$, can be determined by recording event by event the ratio of charges Q_i/Q_C, $\forall i \neq$C. This results per cell in a distribution with an approximately gaussian peak at low charge ratios, corresponding to the mean light leak fraction, with an underlying contribution from Compton scattered events, as exemplarily shown with simulated data in Fig. 7.10. The magnitude of the Compton contribution varies from cell to cell, dependent on the position with respect to the source and calibration cell. In general it slowly decreases from low to high charge ratios. The light leak peak dominates at low values and the Compton contribution is suppressed, see the different curves in Fig. 7.10. $\mathrm{LL}_{\mathrm{C}i}$ is then determined by fitting the peak with a gaussian function, which is done in an asymmetric range of $[\mu - 1.5\sigma | \mu + 1\sigma]$, assuming no background from the Compton contribution. This in fact causes a small shift of the mean value to higher charge ratios, which overestimates the centroid position by about 2-3% ($< 0.1 \cdot \sigma$ for all sources). This offset has no impact on the

calibration, as will be shown later in the studies of systematic uncertainties in Sec. 7.2.3. From the fit the mean light leak value $\mathrm{LL}_{\mathrm{C}i}$ and the standard deviation of the distribution $\sigma_{\mathrm{LL},i}$ are obtained.

A γ-ray which is Compton-scattered in the source cell and subsequently detected in the calibration cell causes scintillation light emission in both cells, which is detected in the cell's PMTs. Without optical cross-talk the scintillation light would only be collected in the cell where it was created and an event selection could be performed by requesting no light signal outside the calibration (and for multi-γ sources also the gate) cell. With the light leaks a minimum of light is detected in other cells even if the energy was completely deposited in the calibration cell.

The cut for Compton suppression is now based on the charge ratios of the considered cells. Here at least the mean light leak value and fluctuations to lower and higher values have to be accepted, since otherwise the cut could be selective on certain interaction positions. As can be seen from Fig. 7.10 this means that a certain fraction of Compton scattered events is accepted as well. The selection condition has been defined as

$$Q_i < (\mathrm{LL}_{\mathrm{C}i} + k/2 \cdot \sigma_{\mathrm{LL,C}i}) \cdot Q_{\mathrm{C}} \ , \tag{7.6}$$

where $k = 7$ is chosen for all sources, as this causes the smallest systematic uncertainties, see Section 7.2.3. This corresponds to $\mathrm{LL}_{\mathrm{C}i} + 3.5 \cdot \sigma_{\mathrm{LL,C}i}$ and includes the full light leak peak in Figs. 7.10 and 7.11. For single-γ sources condition (7.6) is applied to all direct neighbour cells of the calibration cell, for multi-γ sources it is only applied on the downstream neighbour. For the source cell and long GC cells also the light leaks from the gate cell G have to be taken into account and (7.6) is extended to

$$Q_i < (\mathrm{LL}_{\mathrm{C}i} + k/2 \cdot \sigma_{\mathrm{LL,C}i}) \cdot Q_{\mathrm{C}} + (\mathrm{LL}_{\mathrm{G}i} + k/2 \cdot \sigma_{\mathrm{LL,G}i}) \cdot Q_{\mathrm{G}} \ . \tag{7.7}$$

In this case the parameters $\mathrm{LL}_{\mathrm{C,G}i}$ and $\sigma_{\mathrm{C,G}i}$ are determined from the single-γ sources with energies closest to the gate and calibration γ-rays.

Since Compton scattered events cannot be fully suppressed and with a detector resolution of about 7.8% at 2.2 MeV, see Fig. 7.2, the average energy of the events contributing to the peak in the charge spectrum is below the nominal γ-ray energy. To determine this difference the simulation of the STEREO detector is used. Although at the time of this analysis the fine-tuning of the simulations was not finished the most relevant effects of scintillation light production and transport are included, namely quenching with predefined parameters (see above), increased optical cross-talk between the cells and empty buffer volumes in GC-Front and TG4.

The simulation output provides a charge spectrum, to which the same procedure is applied as to the measured data. The procedure is followed until the end and calibration coefficients for the MC are calculated, in order to obtain quantities which can be compared to the experimental data. In the simulations for each event also the deposited energy per cell is stored. By selecting only events passing the conditions for the charges (7.6) or (7.7) the distribution of the corresponding deposited energy is obtained.

For the determination of the quenching parameters the specific photo-electron yield as a function of deposited energy is required ('calibration coefficient' - CC). This corresponds to the ratio of the experimentally determined charge Q and the actual deposited energy E_{dep}, obtained from simulations,

$$\mathrm{CC}_{\mathrm{source}} = \frac{\langle Q \rangle}{\langle E_{\mathrm{dep}} \rangle} \ , \tag{7.8}$$

where the average refers to all events fulfilling condition (7.6) (and (7.7) for multi-γ sources). The remaining task is to determine these quantities in a way which is consistent over all energies and introduces minimal systematic uncertainties.

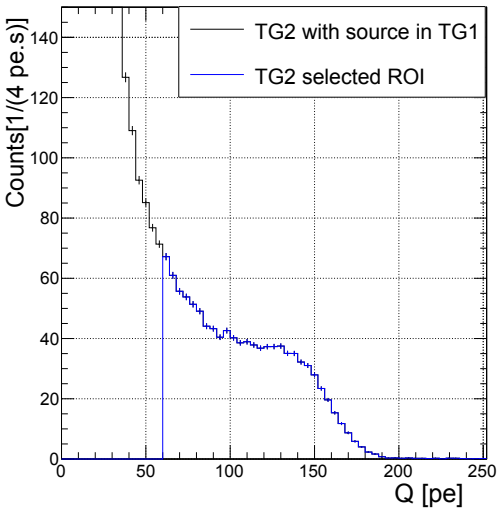

Figure 7.9: Step 1 - selection of the ROI. In the ^{137}Cs spectrum, here measured data, the peak in the calibration cell is not well separated from the Compton contribution. The ROI is defined to include the full energy region and a tail to lower energies.

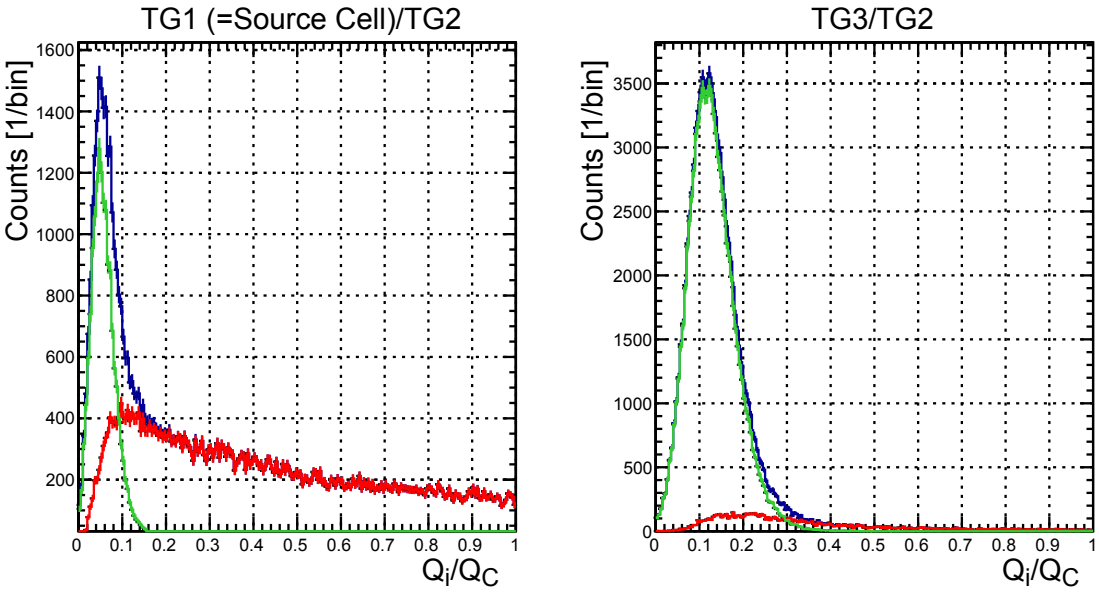

Figure 7.10: Charge ratio distributions of the calibration cell (TG2) and its upstream (left) and downstream (right) neighbours, obtained from simulations of a ^{137}Cs source at 45 cm height in the calibration tube in TG1. At low values the light leak contribution (green) dominates, at higher values only the Compton contribution (red) is present. In the experimental data only the sum of both distributions (dark blue) is accessible. The mean value of the light leak peak depends on the overall reflection efficiency of the optical separation walls between the cells.

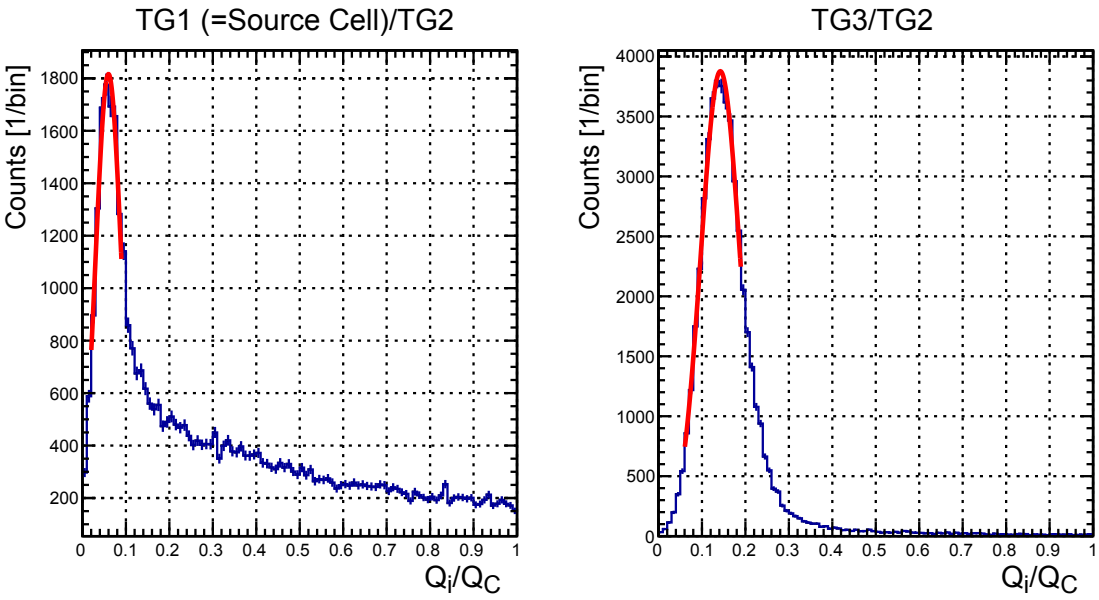

Figure 7.11: Step 2 - in-situ determination of the light leaks. Measured charge ratios of neighbour cells relative to the calibration cell for the events selected in the ROI in Fig. 7.9. The mean and the width of the light leak fraction are obtained from a gaussian fit to the peak.

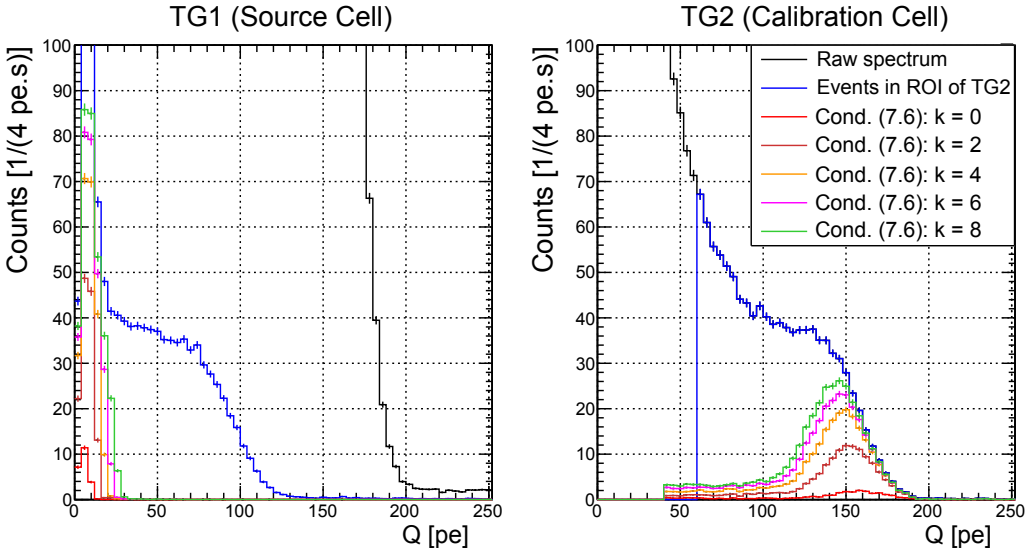

Figure 7.12: Step 3 - Compton suppressing cuts. Condition (7.6) is applied to the spectrum of ^{137}Cs from Fig. 7.9, for different k values (the legend applies to both plots) and with the parameters obtained from the fit of the LL contribution, see Fig. 7.11.

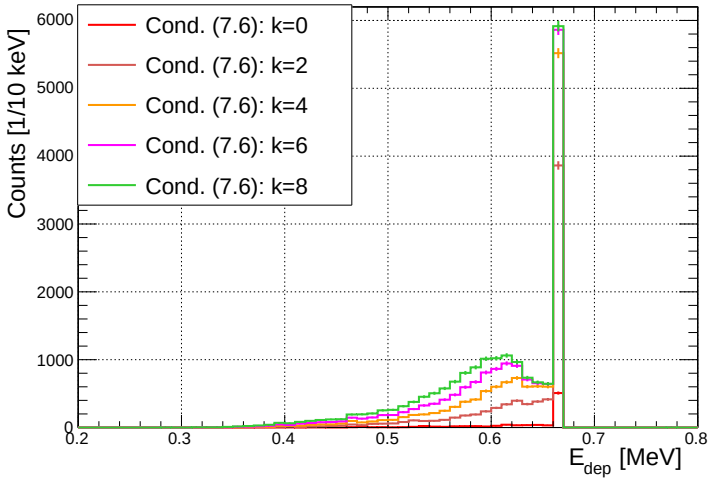

Figure 7.13: Simulated distribution of the energy deposited in the calibration cell for the events which passed the charge selection criteria. The events correspond to those selected in Fig. 7.12, right, within a range around the respective peak of $[\mu - 2.5\sigma|\mu + 4\sigma]$.

For an ideal detector with a linear energy response each energy deposit with the same total energy causes the same corresponding signal, whose only uncertainty is based on the statistical nature of the signal creation and thus, for a sufficiently large number of secondary particles (in each step along the signal conversion chain), follows a normal distribution around a central value. Due to the non-linear behaviour of the scintillator the response depends on the single interaction steps. This means that the signal created by a γ-ray depends not only on the total deposited energy but also on the distribution of the energy over the single secondary electrons, and is thus different between single γ-rays. This makes a correct, analytical modelling of the response function difficult. Thus the calibration parameters cannot be obtained from fitting the convolution of the simulated energy with the γ-ray response function to the experimental charge distribution. For incident mono-energetic electrons, e.g. conversion electrons, the overall energy dependence of the signal would still be non-linear, but electrons with the same energy would all experience the same effects (within statistics) and lead to the same signal, so that a direct convolution of the deposited energy would be possible.

For γ-rays another approach is chosen. Given the shape of the E_{dep} spectrum the mean deposited energy is calculated as the arithmetic mean of the distribution. As the distribution is gained from the event-by-event correspondence of charge and energy in the simulations, the event selection by charge is sufficient and no further cuts need to be applied on the energy. Consequently all entries in the E_{dep} distribution have to be taken into account for the averaging.

The charge spectrum shows a gaussian-like peak with a tail to lower energies, since the quenching varies slightly event by event and the detector resolution causes an overlap of full energy events and Compton events. The asymmetry may vary with energy, due to the decreasing quenching contribution, and with the efficiency of the Compton suppression cuts. The mean value is again obtained as the arithmetic mean value of the distribution of all events that fulfill the selection criteria. A fit with a gaussian-like function is not adequate since it would not weight events at the edges of the distribution in the same way and return the mode rather than the mean of the distribution.

The calibration should determine the response at a certain energy and should therefore mainly make use of full energy events. The high energy tail in the charge distribution is dominated by the convoluted full energy events. Thus a symmetric range around the mode of the distribution may exclude a part of the full energy events. To avoid losing them the range can be set asymmetric, with the upper bound set large enough not to exclude the high energy tail of the peak, but low enough to reduce the influence of possible background. In a similar way the lower boundary should include as much of the peak as possible, while excluding as much

of the Compton continuum as possible, since the quenching is energy dependent. To define the boundaries of the averaging range the peak in the charge spectrum can be used as reference. As can be seen in Fig. 7.12 the peak position and width slightly change with cut parameter k. To account for this the boundaries are not fixed but adapted to always include the same fraction of the peak.

To achieve this for each k the peak in Fig. 7.12 is fitted iteratively with an asymmetric gaussian, to avoid the low energy tail from the Compton contribution. The upper averaging boundary is set to $\mu + 4\sigma$ of the gaussian fit, the lower bound was varied by $\mu - l \cdot \sigma$, $l = \{0.5, 1.0, 1.5, 2.0, 2.5, 3.0, 4.0\}$, see Sec. 7.2.3, and finally set to $l = 2.5$.

For the averaging procedure itself two options are possible. As the energy and charge information is available event by event the true values E_i for each of the N events can directly be used for calculating the arithmetic mean and its uncertainty. For the measured charge on the other hand it can be relevant to subtract background events. This is done statistically and requires some binning in bins j with N_j events ($\sum_j N_j = N$) and central values Q_j for each bin. The averages of the distributions are then obtained as

$$\langle E \rangle^{\text{unbinned}} = \frac{\sum_i E_i}{N} \qquad \langle Q \rangle^{\text{binned}} = \frac{\sum_j Q_j \cdot N_j}{\sum_j N_j} \ . \tag{7.9}$$

The statistical uncertainty of the mean values are calculated for unbinned data from the variance of the distribution, for the binned data as propagation of statistical uncertainties from the individual bins:

$$\left(\sigma^{\text{unbinned}}_{\langle E \rangle,\,\text{stat}}\right)^2 = \frac{1}{N(N-1)} \sum_i \left(E_i - \langle E \rangle\right)^2 \qquad \left(\sigma^{\text{binned}}_{\langle Q \rangle,\,\text{stat}}\right)^2 = \sum_j \left(\frac{Q_j N - \sum_m Q_m N_m}{N^2}\right)^2 \cdot N_j \tag{7.10}$$

The binning introduces some additional uncertainties, especially for the energy distribution. The full energy deposition has a very small width, compared to typical bin widths. In dependence of how the binning is defined the bin centroid of the full energy bin will deviate from the true value. To avoid this uncertainty the energy is averaged without binning. The charge distribution is not dominated by a single bin and the bin entries change smoothly between neighbour bins, thus the binning dependent effect is less significant. This is discussed in Sec. 7.2.3. In both cases all cuts are applied to unbinned data.

7.2.3 Cut Stability and Systematic Uncertainties

The parameters of the cuts described above are chosen in a way to minimise systematic uncertainties. This means small changes of a parameter should not change the final value of CC (Eq. (7.8)) significantly.

In the described method mainly two parameters can be varied to determine the CC per source of Eq. (7.8). These are the strength of the Compton suppression cuts k, Eq. (7.6), and the parameter l of the averaging range for the charge, $\mu - l \cdot \sigma, \mu + 4\sigma$. The parameter k is varied in the range [0;9], the parameter l in $\{0.5, 1.0, 1.5, 2.0, 2.5, 3.0, 4.0\}$. Both parameters are varied for data and simulation simultaneously. For $k \leq 6$ ($\leq 3\sigma$) a change of k mainly changes the acceptance of light leaks, for $k > 6$ almost all light leak events are included and the variation changes the acceptance of Compton events. Those should be varied consistently in experimental data and MC, requiring the same absolute step size. For this reason σ_{LL} of condition (7.6) is always obtained from data, but also applied to simulated spectra. The dependence of $\text{CC}_{\text{Cs-137}}$ of the parameter k is shown in Fig. 7.14 for different lower bounds l. For small values of k CC decreases and stabilises for $k \gtrsim 6$. This can be explained as follows: A small k means that a large fraction of pure light leak events is excluded, which are mainly full energy events. Consequently, increasing k decreases $\langle Q \rangle$, whereas in the energy distribution at first also the full energy peak gets more populated and consequently $\langle E \rangle$ decreases much more slowly. When the cut includes most of the light leak events ($k = 6 \mathrel{\hat{=}} 3\sigma_{\text{LL},i}$) both averages decrease since only Compton events

are added. Since light leaks are not perfectly well-described in the simulations, a cut in the light leak distribution may work differently for experimental data and MC. Therefore $k \geq 6$ is chosen, accepting most of the pure light leak events. The description of the Compton process in the simulations is much better than of the LL, so that the k-dependence should be more similar in data and simulation. On the other hand a high Compton acceptance should be avoided, as the quenching is an energy dependent effect, so that the value of k should stay close to 6.

Figure 7.15 shows $\mathrm{CC}_{\text{Cs-137}}$ calculated only from the difference of the spectra of subsequent k values. Above $k = 5$ $\mathrm{CC}_{\text{Cs-137}}$ increases again because $\langle E \rangle$ starts to decrease slightly faster. However, the change of $\mathrm{CC}_{\text{Cs-137}}$ of the difference spectra around $k = 7$ is smaller than the statistical uncertainties. In addition the number of added events with each unit above $k = 5$ is small ($< 10\%$ of the total events), so that this shift has only a small weight. As can be seen in Fig. 7.14 $\mathrm{CC}_{\text{Cs-137}}$ calculated from the full spectra remain stable within statistical uncertainties in $5 < k < 9$. As k can vary by one unit without changing $\mathrm{CC}_{\text{Cs-137}}$ any uncertainty in the determination of LL_{Ci} and $\sigma_{\mathrm{LL},i}$ ($< 0.1 \cdot \sigma$ for all investigated runs) which is smaller than $0.5 \cdot \sigma_{\mathrm{LL},i}$ has no impact on the result. Based on these conclusions $k = 7$ is chosen.

Around $k = 7$ $\mathrm{CC}_{\text{Cs-137}}$ is also stable with respect to the lower bound of the averaging range around $l = 2 - 3$. The general requirements for this selection are the same, to include as much of the full energy peak as possible, which means the range should cover at least the width of the detector resolution around the full energy. In addition the quenching is not yet well-modelled in the simulations, so that the distribution of full energy events over the peak may differ in experimental data and MC, which requires to include most of the peak to determine the correct $\langle E \rangle$. But again Compton events should be avoided as much as possible. Thus a value of $l = 2.5$ (corresponding to 2.5σ) is chosen.

The stability with respect to k and l varies in between the sources, and differences in the CC for neighbouring k or l values can be in the range of or even exceed the statistical uncertainty. To account for this the maximum of the deviations between neighbouring values around $k = 7$ and $l = 2.5$ is included as systematic uncertainty:

$$\begin{aligned} \Delta_{k,\,\mathrm{sys}} &= \max(\ |\mathrm{CC}(k-1,l) - \mathrm{CC}(k,l)|\ ,\ |\mathrm{CC}(k,l) - \mathrm{CC}(k+1,l)|\ ) \\ \Delta_{l,\,\mathrm{sys}} &= \max(\ |\mathrm{CC}(k,l-1) - \mathrm{CC}(k,l)|\ ,\ |\mathrm{CC}(k,l) - \mathrm{CC}(k,l+1)|\ ) \\ &(k = 7,\ l = 2.5) \end{aligned} \tag{7.11}$$

Apart from the choice of l there is also an uncertainty resulting from the determination of the absolute value for the cut position, defined by μ. This is determined from a fit on the charge peak with a gaussian function, in a range asymmetric to higher energies. This is treated independently in simulations and measured data. The uncertainty on the fit values μ and σ for $k = 7$ is typically below 1 pe. To account for uncertainties from this fit the lower boundaries of the averaging range are varied independently in data and simulation.

For a simultaneous variation of the boundary around $\mu - 2.5 \cdot \sigma \pm 2\,\mathrm{pe}$ with opposite signs in data and MC, $\mathrm{CC}_{\text{Cs-137}}$ changes by $\pm 1.0\,\mathrm{pe/MeV}$ in data and MC. This is added as systematic uncertainty. The same value is also adapted for ^{68}Ge and ^{54}Mn. The impact of this variation decreases with increasing energy and for ^{65}Zn the resulting uncertainty on $\mathrm{CC}_{\text{Zn-65}}$ is only $\pm 0.6\,\mathrm{pe/MeV}$ ($\pm 0.5\,\mathrm{pe/MeV}$) in data (MC). This value is also used for ^{124}Sb, ^{24}Na and Am-Be.

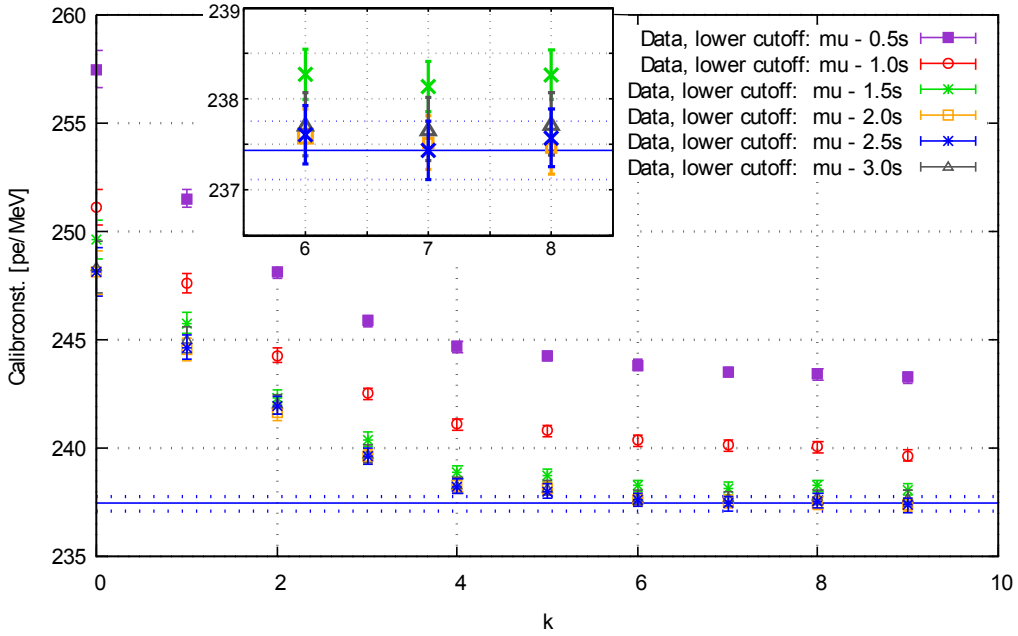

Figure 7.14: Variation of $CC_{Cs\text{-}137}$ (Eq. (7.8)) for cell TG2 with change of the cut parameter k of the Compton suppression cuts (Eq. (7.6)). The different colours represent different lower bounds l of the averaging range. Stable conditions are reached for the selected parameters $k = 7$ and $l = 2.5$. The blue horizontal lines correspond to the CC value for these cuts (solid) and the range of the corresponding total uncertainty (dashed).

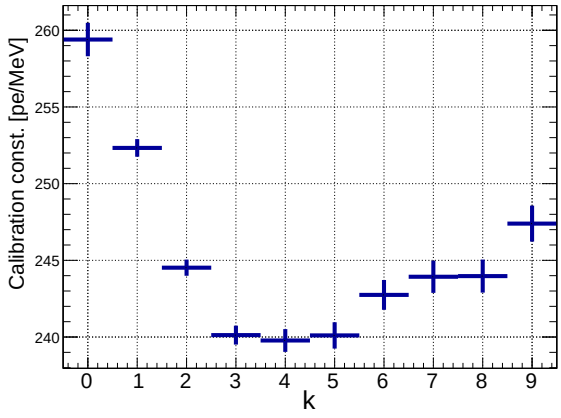

Figure 7.15: CC_{Cs137} (Eq. (7.8)) for cell TG2 calculated for the difference of simulated charge and energy spectra of subsequent k values ($S(Q, k = n + 1) - S(Q, k = n)$).

When averaging over binned data the size of the bins may play a role, as, depending on the shape of the distribution, the bin center and the centroid of the unbinned data may deviate from each other. The size of the deviation depends on the shape of the distribution and the width of the bins. As discussed before this is especially relevant for the energy distribution, where the full energy bin has the largest number of entries. As a measure for the binning effect the deviation of the binned mean value to the unbinned mean value is used, see Eq. (7.9). With a coarse binning, as the 10 keV used for the graphical representation in Fig. 7.13, a shift in $CC_{Cs\text{-}137}$ of about 0.5 pe/MeV was observed, almost twice the size of the statistical uncertainty (∼0.32 pe/MeV). The effect expectedly decreases with finer binning. However, as the deposited energy obtained from the simulation requires no binning it was decided to use the unbinned data, in order to avoid this effect. For the charge however binning is necessary for a statistical

subtraction of background spectra for some of the sources. For ^{137}Cs the deviation between unbinned and binned calculation for a 4 pe binwidth is smaller than the statistical uncertainty by one order of magnitude. A shift of the bin boundaries by half a bin width (2 pe) has only an effect for small averaging ranges, but is smaller than the effect of the binning itself for $l = 2.5$. For higher energetic sources (^{124}Sb, ^{24}Na, Am-Be) a binning of 8 pe is used. Also for these sources the shift in $\mathrm{CC}_{\mathrm{source}}$ by the binning effect is a factor of 10 lower than the statistical uncertainty. Therefore no additional uncertainty due to the binning needs to be added.

Following this procedure the calibration coefficient obtained for ^{137}Cs for cell TG2 is

$$\mathrm{CC}_{\mathrm{Cs137}} = (237.43 \pm 0.32|_{\mathrm{stat}} \pm 1.04|_{\mathrm{sys}})\,\mathrm{pe/MeV}\ , \tag{7.12}$$

where the systematic uncertainty is largely dominated by the uncertainty of the lower averaging boundary.

7.2.4 Results for the Calibration Coefficients

This section gives a short overview over the individual sources and some specific treatments where necessary. Tables with the single calibration coefficients are given at the end of the section, the analysis of the quenching behaviour in the next section, for TG and GC scintillator in data and simulations. In general in the calibration of cell GC-Rear the charge peaks show larger tails to lower energies. This is a consequence of the fact that for this cell no downstream neighbour exists, so that Compton scattering in this direction cannot be vetoed.

^{68}Ge

^{68}Ge decays with a halflife of 271 d to ^{68}Ga purely via electron capture without radiation emission but low energetic x-rays and Auger electrons. ^{68}Ga in return has a $\sim 89\%$ branching ratio for β^+ decay. With its halflife of 68 min it is in equilibrium with the ^{68}Ge activity. From the positron annihilation two 511 keV γ-rays are obtained, emitted back-to-back. This allows to set a coincidence condition for the gate and calibration cell, otherwise the calibration procedure is followed as described before. The mean values of charge and energy obtained in TG2 are $\langle Q\rangle_{\text{Ge-68, TG2}} = 101.67\,\mathrm{pe}$ and $\langle E_{\mathrm{dep}}\rangle_{\text{Ge-68, TG2}} = 439.23\,\mathrm{keV}$. At the same time in the gate cell a mean charge of $\langle Q\rangle_{\text{Ge-68, GC-Front}} = 71.82\,\mathrm{pe}$ is measured, averaged over the peak. The light yield is larger in the GC, but due to the missing buffer liquid in GC-Front the detected charges are lower than in other cells, see Sec. 7.1.1. From the ^{137}Cs source ($E_\gamma = 662\,\mathrm{keV}$) a light leak coefficient from GC-Front to TG2 of 2.8% is calculated, which leads to an average shift of the charge in TG2 of +2.01 pe. This 2% shift is corrected for before calculating the calibration coefficient. The charge in the gate cell and the light leak coefficient can be calculated with relative uncertainties on the percent level, so that this correction does not introduce significant uncertainties for $\mathrm{CC}_{\text{Ge-68, TG2}}$. This correction is calculated for all multi-γ sources.

^{54}Mn

^{54}Mn undergoes a pure electron capture decay to ^{54}Cr, with a halflife of 312 d. ^{54}Cr is produced in an excited state and deexcites via emission of a single 834.8 keV γ-ray (99.98%) with a small conversion coefficient ($< 1\%$). The γ-ray energy is similar to ^{137}Cs and the source is treated analogously. The mean deposited energy and resulting calibration coefficients for this and the following sources are given in Table 7.2.

^{65}Zn

^{65}Zn has been produced by thermal neutron activation of natural zinc. Its halflife of 244 d is much longer than those of the other activation products $^{69\mathrm{m}}$Zn (14 h) and ^{71}Zn (4 h) so that from about 4 d after the irradiation a pure source is available. It decays via EC, with a 1.4% branching for β^+ decay associated with positron annihilation photons. A 1116 keV γ-ray is

emitted in 50% of the EC decays. The source activity is one order of magnitude lower than for the sources discussed before. Due to this the background from ^{41}Ar (E_γ = 1294 keV) plays a significant role, see Fig. 7.16, especially since it is close in energy. Between the inner detector and the shielding there is an airgap of about 10 cm width, where the Pantograph calibration system circulates, see Fig. 3.3. The argon, as constituent of the air, can enter this gap through small gaps in the shielding, the calibration system access door and a cable feedthrough in the rear top of the setup. Consequently the γ-rays reach the detector from the sides and from the top and thus interact mainly in the GC. At several occasions large fluctuations in the count rate in the ^{41}Ar peak have been measured, even over short periods. During the day of calibration changes of several 10 Hz integrated over the full detector have been observed, which requires that the background is determined close in time to the calibration run. No dedicated background runs have been performed during the calibration campaign. For this reason the background for source runs in TG1 (TG6) is determined from calibration runs with a source at the opposite end of the detector, in cell TG6 (TG1). The same Compton suppression cuts as for the source run are applied to the background spectrum before subtraction. The impact of this background on the calibration of TG2 is not very large, see Fig. 7.16 left, since it is a central cell. For calibrations in GC-Rear, an outer cell, the subtraction is essential as otherwise the peak centroid would be shifted to higher energies by about 10%, see Fig. 7.16 right.

In GC-Rear a large variation of $CC_{\text{Zn-65, GC-R}}$ with k is observed. The reason for this is not yet fully understood, but is likely related to the large background.

^{124}Sb

^{124}Sb was also produced by thermal neutron activation at the ILL, with a sample of natural antimony. The only byproduct is ^{122}Sb which is produced in a higher amount but has a halflife of only 2.7 d. Consequently about three weeks should be waited after the activation before using the source. ^{124}Sb has a halflife of 60 d. It decays via β^--decay to ^{124}Te. Several γ-ray cascades can occur in its deexcitation. The highest intensity results from a coincidence of a 1691 keV γ-ray followed by a 603 keV γ-ray. The latter is used as trigger in the gate cell. Other coincidences with this γ-line and lines at 632 keV, 646 keV or 662 keV are possible [ENS17], although with a lower intensity. This requires to set a rather narrow selection of the energy ROI on the gate γ-ray. An irreducible background results from the cascades of 2091 keV+603 keV and 1368 keV+700 keV+603 keV with emission intensities relative to the 1691 keV γ-ray of 11.5% and 4.8%, respectively. The latter would require a triple coincidence, which has a much smaller probability. In the simulations of the source so far only the two γ-rays of interest are simulated, considering their relative weight. This may introduce some bias which is not yet investigated. For the correction of light transmission from the gate to the calibration cell also the light leak coefficient calculated with ^{137}Cs is used.

^{24}Na

^{24}Na decays with a halflife of only 15 h and was produced by neutron activation of NaCl the day before the utilisation. The only other relevant activation product, ^{38}Cl decays with a halflife of 37 min and it could be waited for its decay within a few hours. About 99.9% of the ^{24}Na decays occur via the same decay branch, associated with only two γ-rays in coincidence, at 2754 keV and 1369 keV. Again the lower energetic γ-ray is used as trigger in the gate cell. The light leak coefficient from gate cell to calibration cell was determined with the ^{65}Zn source and is 2.2% from GC-Front to TG2. This is slightly smaller than the value obtained with the lower energetic ^{137}Cs. The same effect was observed for the light leaks from TG5 to GC-Rear. One explanation is that with the higher energy the interactions are further distributed throughout the cell volume, while for ^{137}Cs they mostly occur closer to the separation wall. This would imply that the cell average of the light leaks to the next-next neighbour cell is lower than for events close to the wall.

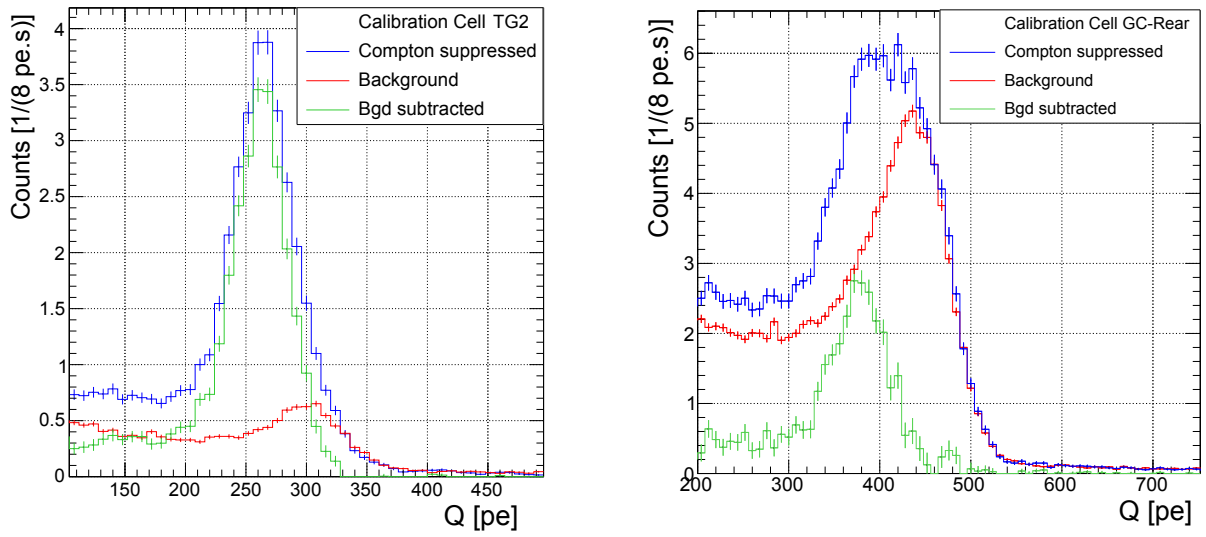

Figure 7.16: Charge spectrum (blue) obtained in TG2 with the ^{65}Zn source deployed in TG1, left, and in GC-Rear with the source in TG6, right. Due to the comparatively low source activity (2.8 kBq) the background (red) plays a more important role than for other sources, especially in the border cell GC7, and needs to be subtracted for the analysis (green).

Am-Be

^{241}Am is an α-emitter with 433 a halflife. In the reaction ^{9}Be(α,n)^{12}C$^{(*)}$ fast neutrons with energies up to about 11 MeV are produced. In most reactions the ^{12}C nucleus is produced in an excited state which limits the corresponding maximum neutron energy to about 6.6 MeV. The ^{12}C* deexcites under emission of a 4.4 MeV γ-ray before the nucleus is at rest, causing a doppler broadening of about 90 keV [Jan80]. Due to the short lifetime of the excited state the γ-ray is always emitted in coincidence with the fast neutron.

The general approach for this source is the same as for multi-γ sources. The detection of the neutron is required in the gate cell and that of the γ-ray in the calibration cell. The difficulty is that the energy deposition of the neutron recoil is not at a well defined energy, but in the case of scattering on hydrogen can range from zero up to the full neutron energy. The quenching for the recoil protons is higher than for electrons and in detail depends on the scintillator, but in general for a few MeV of proton energy the light yield is about half of that of electrons. Thus the gate energy window has to be set wide, which allows for coincidences with other events. When simply applying the coincidence condition of gate and calibration cell and the Compton suppression cuts of Eq. (7.7), with the light leak parameters defined from ^{65}Zn (mono-γ source with the highest energy) still a large background is obtained around the full energy peak, see Fig. 7.18. The background reaches even to higher energies than the γ-ray full energy. Given the generally low rate of external background this cannot be explained by random coincidences with background in the gate cell or pile-up in the calibration cell, which implies that rather a summing effect of the two source particles occurs. In the PSD distributions of both, the gate and the calibration cell, low PSD (electronic signal) and high PSD (nuclear recoil) values are present. One explanation is that for some events one of the two particles reaches directly the calibration cell while the other is first scattered in the gate cell, depositing enough energy to exceed the gate cell energy threshold, and propagates then to the calibration cell, without depositing much energy in the source cell, which lies in between and on which Compton suppression cuts are applied. To improve the event selection the PSD capability of the scintillator can be exploited. By selecting only high PSD events in the gate cell (> 0.42 in case of GC-Front, see Fig. 7.17) the signal to background ratio in the calibration cell can be improved, see Fig. 7.18. For the calibration of GC-Rear the PSD condition in the gate cell alone was not sufficient (set to PSD > 0.56 in TG5 - the TG and GC PSDs are different) so that also a PSD selection on the calibration cell was

applied (PSD < 0.36). Still a small summing contribution remains. This different behaviour might be due to the missing downstream neighbour cell and a lack of Compton suppressing cuts in this direction.

However, the scintillator's pulse shape is not modeled in sufficient detail in the simulations to apply the same selection. So far the spectrum obtained in the simulations renders it difficult to apply the same procedure as above to determine $\langle Q_{\mathrm{MC}} \rangle$ and $\langle E_{\mathrm{dep}} \rangle$.

From the data which was stored from the simulations until now it is not possible to track the neutron specifically in the mixed neutron and γ-ray event. This may be changed for further simulations by explicitly including secondary particles of the neutron (recoil protons or nuclei) in the stored tracking list, so that the interaction coordinates could be used instead of a PSD selection.

As a temporary solution the $\langle E_{\mathrm{dep}} \rangle$ for the Am-Be source is determined empirically. The difference between $\langle E_{\mathrm{dep}} \rangle$ and E_{source} results from the overlap of full energy and Compton events. It is thus related to the detector resolution and the fraction of events scattered into the energy range within one resolution width below the full energy peak. Considering the decrease of the relative resolution with energy the relative difference of $\langle E_{\mathrm{dep}} \rangle$ and E_{source} is also expected to be smaller at higher energies. Fig. 7.19 shows the ratios of $\langle E_{\mathrm{dep}} \rangle$ to E_{source} for all sources except Am-Be. This ratio increases with energy and approaches some saturation. It can therefore be assumed that for Am-Be the same ratio would be at least as large as the preceding point (^{24}Na, $E_\gamma = 2754\,\mathrm{keV}$)), and would increase slower than a linear dependency, which is defined by a linear fit of the last three points of ^{65}Zn, ^{124}Sb and ^{24}Na. These two extreme cases are considered as lower and upper limit. The ratio for Am-Be is then taken as the average of these limits at the corresponding energy of 4438 keV, with an uncertainty of half the difference of the limiting values.

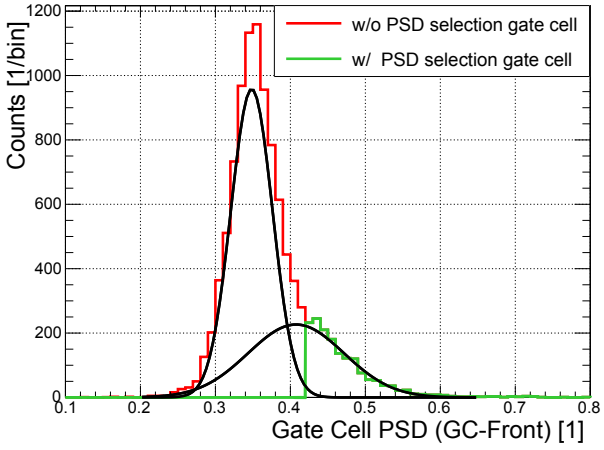

Figure 7.17: Measured PSD value distribution in GC-Front with the Am-Be source deployed in TG1. By selecting only high PSD events (green) it can be assured that the neutron interacted in the gate cell. The impact on the charge spectra in the calibration cell is shown in Fig. 7.18.

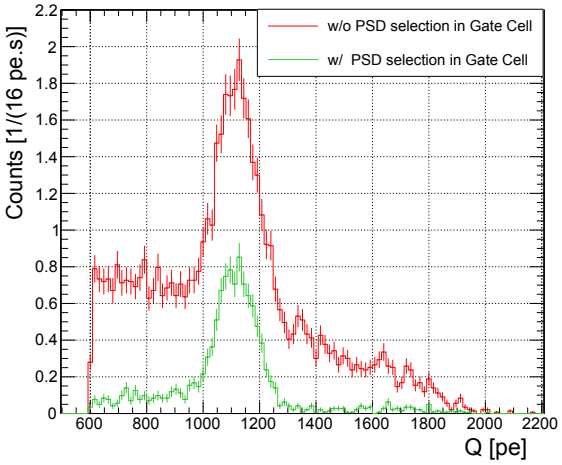

Figure 7.18: Measured charge spectra in the calibration cell TG2 with the Am-Be source deployed in TG1. Without PSD selection in the gate cell (red) summation of the neutron and γ-ray occurs, leading to a non-negligible background. When the neutron is localised in the gate cell by a PSD selection (green) only the γ-ray is detected.

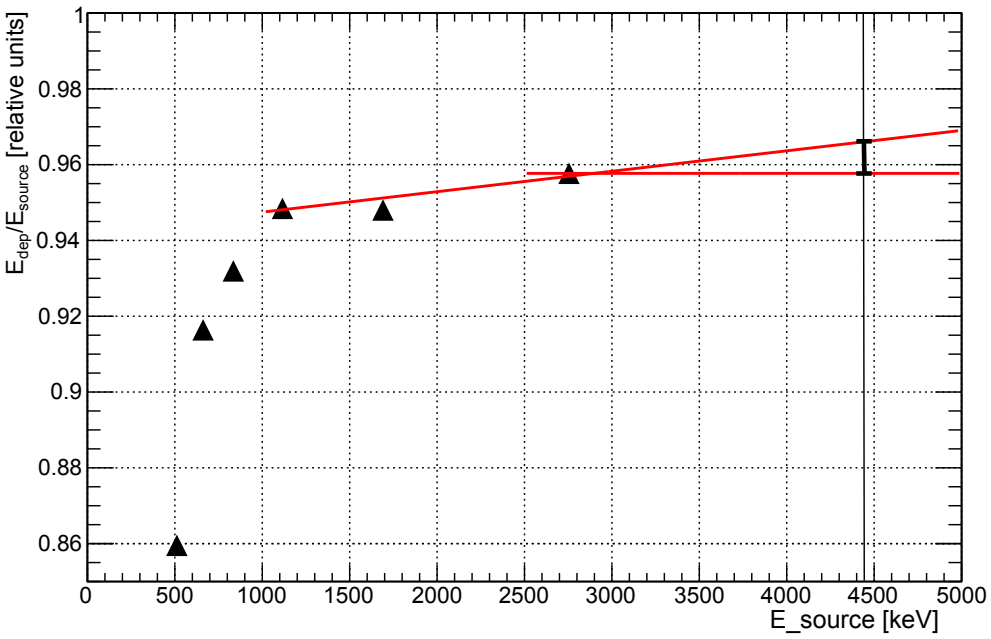

Figure 7.19: The ratio of the mean deposited energy and the nominal source energy increases with energy and approaches saturation. This is exploited for the extrapolation of the same ratio for the Am-Be source, as described in the text.

The calibration coefficients obtained in the calibration runs are listed in Table 7.2. In general the $\langle E_{\text{dep}} \rangle$ values are lower in GC-Rear than in TG2, which is expected since without a downstream neighbour cell in the GC Compton events in this direction cannot be suppressed and thus decrease the average deposited energy. The only exception is the Am-Be source for which $\langle E_{\text{dep}} \rangle$ was extrapolated, but within uncertainties the same trend would be possible. The calibration coefficients in GC-Rear show larger systematic uncertainties, resulting mainly from the larger uncertainty from the variation of the lower averaging boundary, i.e. values of 1.4 pe/MeV and 1.2 pe/MeV for energies below 1 MeV are obtained in data and simulation, respectively, and 0.9 pe/MeV and 0.7 pe/MeV for energies above 1 MeV, whereas the corresponding values in TG2 are 1.0 pe/MeV below 1 MeV for both, data and simulation, and 0.6 pe/MeV and 0.5 pe/MeV, respectively, above 1 MeV. Also the uncertainties from the variation of k and l are generally larger in the GC than in the TG, which is likely caused by the larger acceptance of Compton events, due to one lacking vetoing neighbour cell.

7.2.5 Considerations on the Calibration Sources

Considering the calibration runs themselves the measurements with the purchased sources ^{68}Ge, ^{137}Cs and ^{54}Mn, which have high activities ($\mathcal{O}(10)$ kBq) appear to be sufficient with the run duration of 1 min. Given the high source activity the background is negligible. For the Am-Be source the coincidence condition and the strong PSD cuts significantly decrease the statistics and about 1000 events (for $k = 7$, $l = 2.5$) are counted in the peak region of the calibration cell. Although this is sufficient to reduce the statistical uncertainty of the mean value below 1% this impacts the identification of the charge peak and thus the determination of the averaging boundaries, leading to an about 1% uncertainty from the k and l variation. For the measuring positions considered here (TG1 and TG6 at 45 cm height) it may be worthwhile to increase the measuring time from 5 min to 10 min for a better peak identification.

Table 7.2: Calibration coefficients and $\langle E_{\mathrm{dep}} \rangle$ values obtained for the calibration runs in TG2 (top) and GC-Rear (bottom) for the calibration campaign on February 22, 2017, and the STEREO simulation software revision 1333.

Source	E_γ [keV]	$\langle E_{\mathrm{dep}} \rangle$ [keV]	$\mathrm{CC}_{\mathrm{TG,\ Data}}$ [pe/MeV]	$\mathrm{CC}_{\mathrm{TG,\ MC}}$ [pe/MeV]
^{68}Ge	511	439.2 ± 1.3	$226.85 \pm 0.84\vert_{\mathrm{stat}} \pm 1.46\vert_{\mathrm{sys}}$	$241.0 \pm 1.1\vert_{\mathrm{stat}} \pm 1.24\vert_{\mathrm{sys}}$
^{137}Cs	662	606.4 ± 0.5	$237.43 \pm 0.32\vert_{\mathrm{stat}} \pm 1.04\vert_{\mathrm{sys}}$	$244.76 \pm 0.31\vert_{\mathrm{stat}} \pm 1.09\vert_{\mathrm{sys}}$
^{54}Mn	835	778.0 ± 0.6	$240.42 \pm 0.28\vert_{\mathrm{stat}} \pm 1.10\vert_{\mathrm{sys}}$	$249.56 \pm 0.30\vert_{\mathrm{stat}} \pm 1.09\vert_{\mathrm{sys}}$
^{65}Zn	1116	1058.0 ± 0.6	$246.49 \pm 0.32\vert_{\mathrm{stat}} \pm 0.81\vert_{\mathrm{sys}}$	$257.12 \pm 0.50\vert_{\mathrm{stat}} \pm 0.60\vert_{\mathrm{sys}}$
^{124}Sb	1691	1603.1 ± 2.0	$255.36 \pm 0.88\vert_{\mathrm{stat}} \pm 1.08\vert_{\mathrm{sys}}$	$266.46 \pm 0.56\vert_{\mathrm{stat}} \pm 0.69\vert_{\mathrm{sys}}$
^{24}Na	2754	2637.6 ± 2.8	$256.68 \pm 0.30\vert_{\mathrm{stat}} \pm 0.88\vert_{\mathrm{sys}}$	$273.04 \pm 0.48\vert_{\mathrm{stat}} \pm 0.60\vert_{\mathrm{sys}}$
Am-Be	4438	4269 ± 18	$260.30 \pm 0.49\vert_{\mathrm{stat}} \pm 2.00\vert_{\mathrm{sys}}$	—

Source	E_γ [keV]	$\langle E_{\mathrm{dep}} \rangle$ [keV]	$\mathrm{CC}_{\mathrm{GC,\ Data}}$ [pe/MeV]	$\mathrm{CC}_{\mathrm{GC,\ MC}}$ [pe/MeV]
^{68}Ge	511	421.7 ± 1.1	$334.45 \pm 1.07\vert_{\mathrm{stat}} \pm 2.40\vert_{\mathrm{sys}}$	$438.79 \pm 1.62\vert_{\mathrm{stat}} \pm 1.88\vert_{\mathrm{sys}}$
^{137}Cs	662	572.6 ± 0.7	$353.49 \pm 0.57\vert_{\mathrm{stat}} \pm 1.83\vert_{\mathrm{sys}}$	$457.08 \pm 0.75\vert_{\mathrm{stat}} \pm 1.49\vert_{\mathrm{sys}}$
^{54}Mn	835	733.6 ± 0.6	$359.23 \pm 0.42\vert_{\mathrm{stat}} \pm 1.29\vert_{\mathrm{sys}}$	$471.97 \pm 0.54\vert_{\mathrm{stat}} \pm 1.53\vert_{\mathrm{sys}}$
^{65}Zn	1116	1009.0 ± 0.3	$365.13 \pm 0.55\vert_{\mathrm{stat}} \pm 7.05\vert_{\mathrm{sys}}$	$489.01 \pm 0.33\vert_{\mathrm{stat}} \pm 0.89\vert_{\mathrm{sys}}$
^{124}Sb	1691	1570.7 ± 1.7	$375.93 \pm 1.11\vert_{\mathrm{stat}} \pm 1.54\vert_{\mathrm{sys}}$	$508.32 \pm 0.81\vert_{\mathrm{stat}} \pm 0.85\vert_{\mathrm{sys}}$
^{24}Na	2754	2594.7 ± 2.5	$377.58 \pm 0.41\vert_{\mathrm{stat}} \pm 1.02\vert_{\mathrm{sys}}$	$521.45 \pm 0.74\vert_{\mathrm{stat}} \pm 0.78\vert_{\mathrm{sys}}$
Am-Be	4438	4278 ± 97	$389.98 \pm 1.03\vert_{\mathrm{stat}} \pm 9.51\vert_{\mathrm{sys}}$	—

For the sources produced at the ILL by neutron activation it was intended to obtain sources with lower activities in order to keep the electronics deadtime small. For the produced ^{65}Zn source the background resulting from ^{41}Ar is comparable to the source activity, in case of cell GC-Rear even dominating, see Fig. 7.16. For calibrations in cells TG1 and TG6 the background can be determined from calibration runs performed in the cell at the other end of the detector without performing dedicated background runs. This is also possible if the procedure should be applied to inner cells, e.g. with the new calibration tubes, as long as the energy and light leaks to the calibration cells are negligible. Otherwise dedicated background runs are required. In general a problem remains that the ^{41}Ar activity can change over short times so that calibration and corresponding background determination need to be close in time. One option to counter this would be to produce a source with a higher activity, which increases the signal over background and reduces the required measuring time and thus limits possible changes in the ^{41}Ar rate. At the day of calibration the source had an activity of about 2.3 kBq, with 50% γ-ray intensity and was measured for 6 min at mid-height. The rate measured in the calibration cell GC-Rear was about a factor of two lower than the background from ^{41}Ar, which means that an at least three times higher source activity (~ 7 kBq) would be desirable.

For the ^{124}Sb and ^{24}Na sources the applied coincidence condition strongly reduces the impact of background. On the other hand with an activity of about 0.7 kBq for ^{124}Sb at the time of the measurement a measuring time of 30 min was required (20 min were defined a priori for ^{24}Na (5.8 kBq), which was largely sufficient). A higher activity would reduce the time proportionally. One additional problem of the ^{124}Sb source is the irreducible background from competing γ-ray cascades with the same gating γ-ray energy, see Sec. 7.2.4. These need to be included in the simulations, where currently only the two γ-rays of interest are simulated, in order to check if these cause a systematic shift to higher calibration coefficients. In TG and GC the point of ^{124}Sb lies above the fit of the quenching curve for measured data, see Figs. 7.20 and 7.22 below, which gives no evidence for but would be consistent with a small upward shift. If this is correctly reproduced in the simulations, and the shift is small or negligible, since calibrations should be done monoenergetically, this point can safely be used.

Alternatively a single-γ-ray source with a similar energy may be produced from potassium. Potassium has three natural abundant isotopes: ^{39}K (93.3%), ^{40}K (0.01%) and ^{41}K (6.7%). ^{40}K is instable with a halflife of $1.2 \cdot 10^9$ y [ENS17]. In $\mathcal{O}(10)$ mg of KCl the activity of ^{40}K is

$\mathcal{O}(0.1)$ Bq. By neutron activation of 20 mg KCl in a cold neutron beam with a neutron capture flux of $\phi = 2 \cdot 10^{10}$ and 30 min irradiation time (same parameters as used for the ^{24}Na source production), the ^{40}K activity will not increase significantly, due to its long halflife, but by $^{41}\mathrm{K}(n,\gamma)$ reactions ^{42}K is produced with an activity of about 5 kBq. This decays with a halflife of 12.4 h via pure β^- decay. The main γ-ray associated with the decay is at $E_\gamma = 1524.6$ keV, intensity = 18.1%, which is mostly emitted as single γ-ray and only in about 2.4% of the cases in coincidence with other γ-rays [ENS17]. The γ-ray energy is well above the ^{41}Ar background. ^{42}K has a halflife comparable to ^{24}Na (^{42}K 12.4 h, ^{24}Na 15 h) and reaches comparable activities during the activation, assuming the same sample mass. Given the lower γ-ray intensity of 18.1%, compared to ^{24}Na (99.9%) a higher sample mass may be used. Thus it can be produced along with the ^{24}Na source on the day of usage, or the day before, and it has to be waited the same cooldown time of a few hours for the decay of the activated chlorine.

Another point of interest may be to add calibration points at the lower and higher end of the sources' energy range as those have a large impact on the curvature of the quenching curve. The high energy range would be of larger interest, as this is the energy region for neutrino measurements, but no suitable isotopic source could be identified. One possibility for a low energy source may be ^{113}Sn. It has a halflife of 115.1 d and can be produced by neutron activation of natural tin. In this case it would be necessary to wait for the decay of ^{125}Sn ($T_{1/2} = 9$ d) which is also produced. ^{113}Sn decays purely via electron capture, emitting a 391.7 keV γ-ray, in 3.2% of the cases in coincidence with a 255.2 keV γ-ray. Due to the low energy the γ-rays do not have a large mean free path in the scintillator, so that only a comparatively small fraction reaches the calibration cell without prior interaction. With the current simulations (including light leaks) the full energy events and Compton background overlap more strongly than for other sources. This may improve with the repair of the optical separation walls, which will reduce the light leaks and thus allows for a stronger Compton event suppression. In this way a single-γ low energy calibration point could be added.

7.2.6 Quenching Behaviour of the Scintillators

As described earlier the quenching occurs on the level of single secondary electrons produced in γ-ray interactions. At higher energies also the fraction of Cherenkov light produced by electrons in the scintillator increases and the relation of visible charge and deposited energy could be described, as for example in the Daya Bay experiment [An17b], by

$$\frac{Q_{\mathrm{vis}}}{E_{\mathrm{dep}}} = \mathrm{const} \cdot \left[f_{\mathrm{q}}(E_{\mathrm{dep}}, k_{\mathrm{B}}) + k_{\mathrm{c}} f_{\mathrm{c}}(E_{\mathrm{dep}}) \right] . \tag{7.13}$$

In this relation f_{q} accounts for the ionisation quenching, described by Birks' parameter k_{B}, and f_{c} describes the influence of the contribution of Cherenkov light, with a scaling factor for the fraction of Cherenkov light at 1 MeV k_{c}. The functions f_{q} and f_{c} can be linked to the fundamental interactions of the secondary electrons via simulations.

In general also a possible non-linearity resulting from the PMTs and electronics has to be taken into account. However, for STEREO this contribution was studied with LED pulses in a dynamic range equivalent to up to 10 MeV deposited energy, but no effect was measurable, which means it would lie below 1%, as described earlier, see Sec. 3.2.1.

Instead of the description based on fundamental processes as in Eq. (7.13) the scintillator's non-linearity can also be described by an empirical model. This was already proposed and used for preliminary Monte-Carlo studies for STEREO in [Man16]:

$$\mathrm{CC} = \frac{\mathrm{p}_2 + \mathrm{p}_3 \cdot E_{\mathrm{dep}}}{1 - \mathrm{p}_0 e^{-\mathrm{p}_1 E_{\mathrm{dep}}}} . \tag{7.14}$$

This can be fitted to the data and MC separately to obtain the different energy dependencies. The quenching curve obtained with γ-rays and fitted with Eq. (7.14) does not give direct access to the liquid parameters k_{B} and the light yield (LY, corresponding to the factor A in Birks formulation, see Eq. (3.2)), but may be used as reference for an iterative adjustment of the

parameters in the simulations. This may be necessary in any case, since, as it was pointed out in [Abe12b], the best value of k_B to match the data may not be the physical value, but also depends on parameters of the simulations. If for example the minimal allowed stepwidth (in space) is decreased, which allows for the creation of secondary particles with shorter ranges and thus lower energies, also k_B needs to be reduced. This can be understood as the quenching effect increases for lower energetic electrons.

If the general simulation parameters are not to be changed only the two liquid parameters need to be adjusted. The Birks parameter k_B defines the quenching and thus mainly the curvature of the function. The absolute light yield, as number of scintillation photons emitted per energy deposited, effectively shifts the curve parallel to the ordinate axis. As secondary effects a lower or higher quenching would also allow for a slightly higher or lower total amount of scintillation photons, and the LY changes the effective fraction of Cherenkov light with respect to the total light produced and thus slightly alters the behaviour especially at high energies.

The fit of Eq. (7.14) to the data points obtained in the calibration campaign is shown in Figs. 7.20 and 7.22 for the TG and GC scintillators, respectively. For the fit all uncertainties were added in quadrature, the parameter p_3 of Eq. (7.14) was limited to values > 0, all other parameters were left free.

The fits to the measured data, according to their reduced χ^2 values, have probabilities of about 6% and 20% in the TG and GC, respectively, which is rather low in the TG. One critical point is the calibration coefficient of the Am-Be source, which was determined differently than the others, but has a large impact on the high energy slope of the curve. In the simulations the values of $\langle Q \rangle$ and $\langle E_{\text{dep}} \rangle$ for each source are obtained from the exactly same set of events, which are selected by their charge, which means after the simulation of all statistical transport processes. Consequently no fluctuations would be expected. The fit could rather be used as a consistency check of the procedure in the considered energy range. For the GC calibration, see Fig. 7.22, the reduced χ^2 of 0.05 shows that with the procedure described above consistent results can be obtained, including the corrections of multi-γ sources for the light leaks from gate to calibration cell. For the TG calibration, Fig. 7.20, a larger χ^2 is obtained for the simulations. When comparing with the relative calibration coefficients, see Fig. 7.21, it can be seen that mainly the point at lowest energy, from ^{68}Ge, deviates from the general trend of higher quenching in the simulations and is primarily responsible for the higher χ^2 (by excluding this point from the fit a $\chi^2 = 0.6$ is obtained). Considering the event-by-event charge and energy correspondence this deviation cannot result from the calculation of the calibration coefficient (Eq. (7.8)) itself, but rather from the correction of the light leak contribution from the gate to the calibration cell, which seems to be underestimated.

In general the curves show that the simulations overestimate the LY and k_B values in both liquids. For the latter this is better visible in a normalised representation, see Figs. 7.21 and 7.23. Since the quenching effect decreases with energy the highest point available in all data sets, ^{24}Na ($E_\gamma = 2754\,\text{keV}$), is used as reference. In the simulations the calibration coefficients at lower energies are suppressed more strongly than in the experimental data, due to a higher quenching.

For the adjustment of the scintillator parameters in the simulations a first estimate for the LY can be obtained from the ratio of the CC of ^{24}Na for data and MC, which corresponds to a deposited energy of about 2.6 MeV, where the quenching is less pronounced. This means that for the TG the LY should be reduced to $\text{CC}_{\text{Na-24, Data}}/\text{CC}_{\text{Na-24, MC}} = 96\%$, and for the GC, where the LY was known to be largely overestimated, to 72% of the value used in STEREO's simulation software revision 1333. The effect of k_B on the quenching measured with γ-rays is difficult to predict. To have a first measure for the strength of the quenching the ratios of the calibration coefficients for a high and a low energy can be compared. For the TG the ratio $R = \text{CC}_{\text{Cs-137}}/\text{CC}_{\text{Na-24}}$ yields values of $R_{\text{TG, Data}} = 92.5\%$ and $R_{\text{TG, MC}} = 89.6\%$ in experimental data and MC respectively, for the GC the ratios are $R_{\text{GC, Data}} = 93.6\%$ and $R_{\text{GC, MC}} = 87.7\%$. For the iterative adaption of k_B^{MC} at first these two fix-points (^{137}Cs and ^{24}Na) can be used and once a reasonable agreement is achieved all other sources should be included.

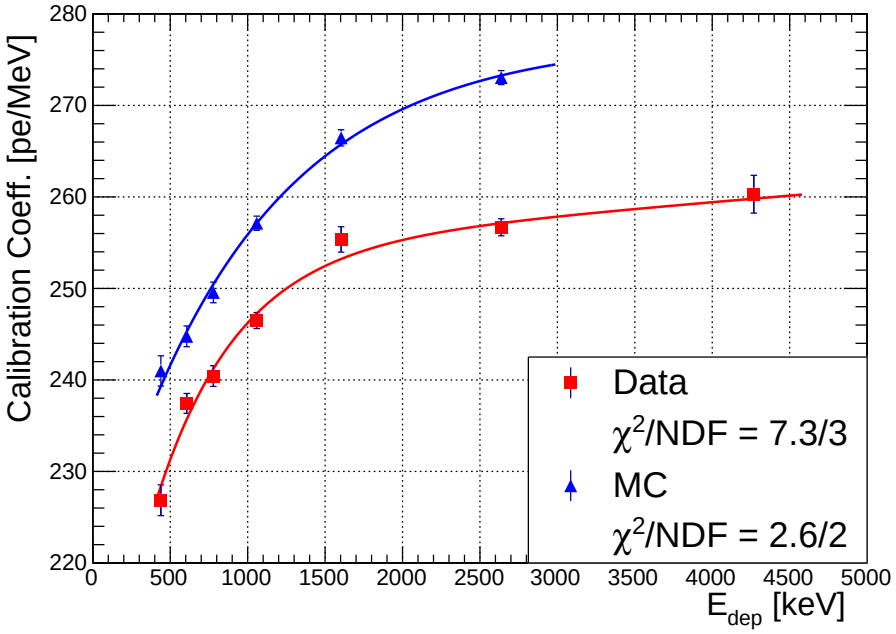

Figure 7.20: Quenching curve of STEREO's TG scintillator for experimental data and MC for TG2, obtained from the calibration data of February 22, 2017 and STEREO's simulation software, revision 1333. The fit function is given in Eq. (7.14), the fit parameter in Tab. 7.3.

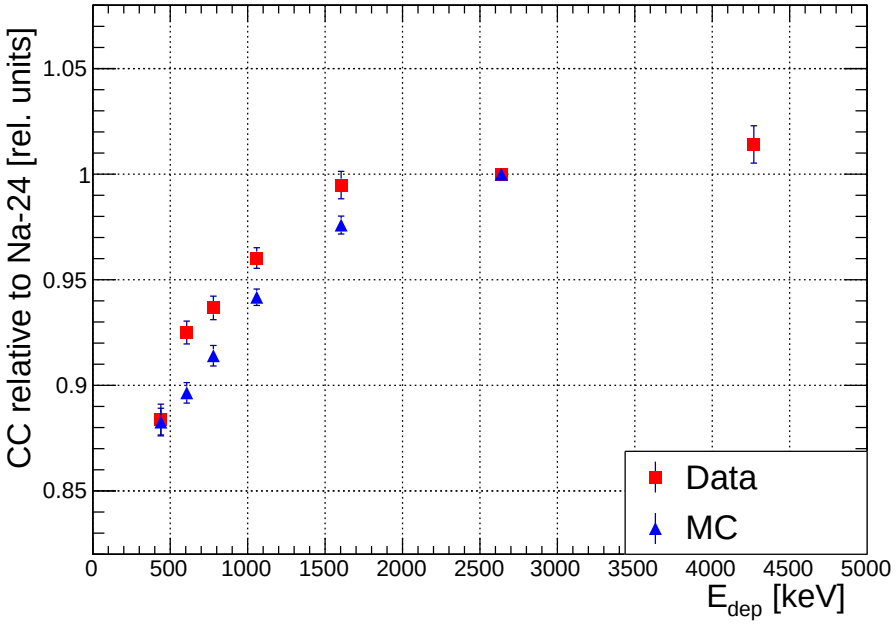

Figure 7.21: Calibration coefficients of the TG scintillator normalised to the value of ^{24}Na, the point with highest energy available in all data sets. At lower energies the calibration coefficients are suppressed more strongly in the simulations than in experimental data.

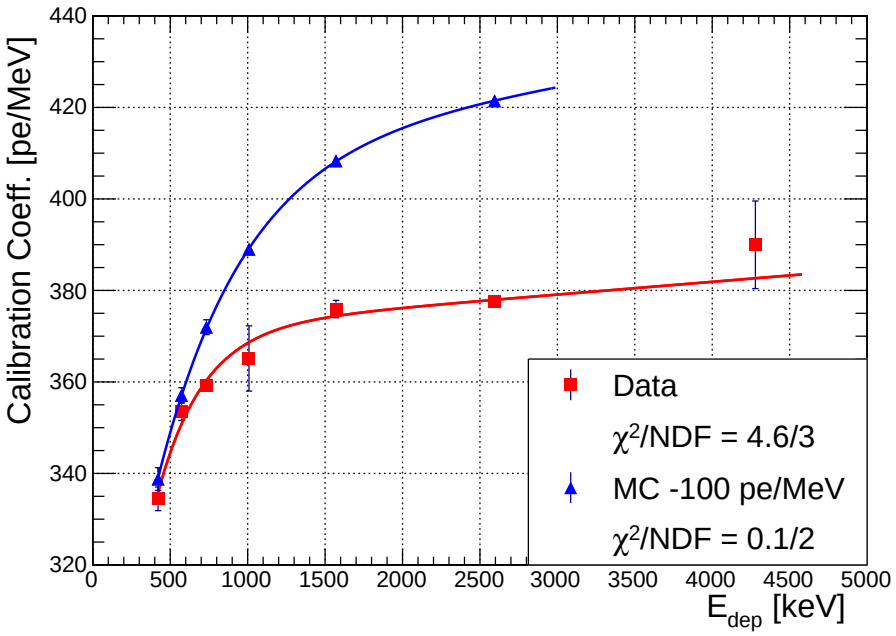

Figure 7.22: Quenching curve of STEREO's GC scintillator for experimental data and MC for GC-Rear, obtained from the calibration data of February 22, 2017 and STEREO's simulation software revision 1333. The fit function is given in Eq. (7.14), the fit parameter in Tab. 7.3. The MC values have been shifted by -100 pe/MeV for better visibility.

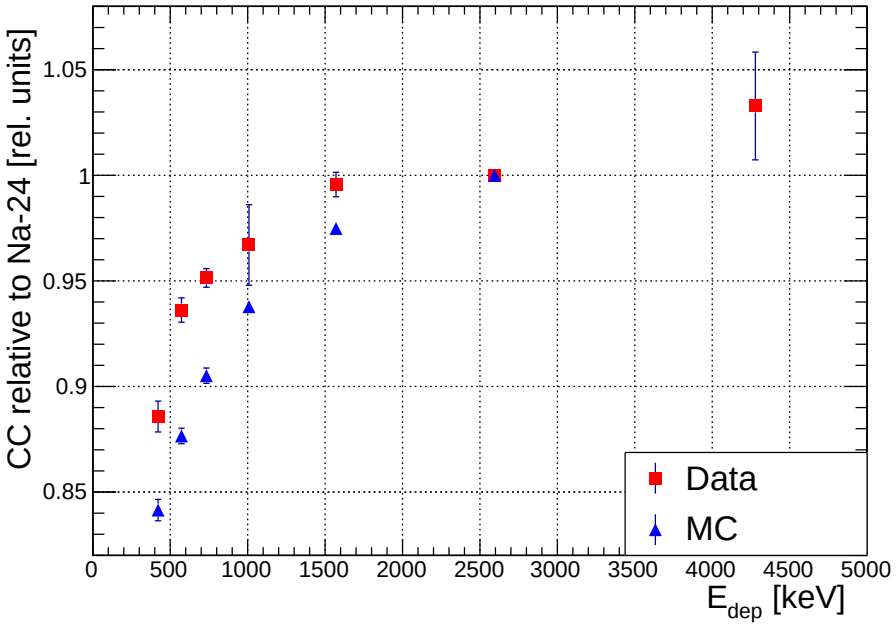

Figure 7.23: Calibration coefficients of the GC scintillator normalised to the value of ^{24}Na. Also for this liquid the quenching is overestimated in the simulations.

Table 7.3: Fit parameter of the fits of Eq. (7.14) to the calibration coefficients determined in experimental data and simulations for the TG and GC scintillator's, as shown in Figs. 7.20 and 7.22.

Parameter of Eq. (7.14)	TG, Data	TG, MC	GC, Data	GC, MC
p_0	0.236 ± 0.033	0.215 ± 0.011	0.41 ± 0.12	0.376 ± 0.025
p_1	1.90 ± 0.44	1.02 ± 0.12	3.41 ± 0.84	1.81 ± 0.38
p_2	253.8 ± 4.5	277.3 ± 1.7	370.8 ± 6.1	409 ± 13
p_3	1.4 ± 1.4	~ 0 (at limit)	2.8 ± 2.4	5.4 ± 4.9

In summary a procedure was proposed for the in-situ determination of the quenching behaviour of both scintillator liquids used in the STEREO experiment. A study on systematic uncertainties was performed and it was discussed and demonstrated how those can be determined. In general the systematic uncertainties obtained are below 1%. The procedure shows in general consistent results in the simulated data over the energy range 511 keV to 2754 keV incident γ-ray energy. With an adaption of the simulations to include a PSD selection, or an equivalent option for neutron tagging, this may also be extended to the γ-ray of the Am-Be source at 4438 keV. From the measured experimental data an empirical quenching description was obtained with reasonable precision, which can be used as reference for an iterative tuning of the Monte-Carlo parameters of the scintillator: the total light yield and Birks' parameter k_B. The experimental quenching curve depends on the simulations via the calculation of $\langle E_\mathrm{dep} \rangle$ so that changes in the simulations will also change at least the absolute values of the experimental calibration coefficients, so that a recalculation will be necessary.

Conclusion

In the context of this thesis finite element simulations for the design of the magnetic shielding of STEREO's PMTs have been performed. Based on these simulations the collaboration chose a shielding design which consists of a 1 cm soft iron layer around the full setup (detector and muon veto), a 1.5 mm mumetal layer around the detector (TG and GC) and single-layer and double-layer mumetal cylinders around the detector and muon veto PMTs, respectively. The shielding has been installed and has so far proven to be sufficient to limit the PMT gain variations in the detector due to magnetic field changes, if present, below a measurable level. However, since the installation of STEREO the main source of magnetic fields, the cryomagnets at IN20, reached a maximum field of only 10 T, although 15 T are technically possible. It remains to be seen whether the shielding performs well enough also for the highest field, which according to the simulations should be the case. In the muon veto a higher field is expected since it is not enclosed in an additional mumetal layer. This visibly altered the performance of single PMTs temporarily, but without affecting the overall intrinsic efficiency for the detection of vertical muons, according to the current method of analysis. The subject of the magnetic shielding is completed and no further changes of the setup in this respect are necessary.

The γ-ray background measurement campaigns which have been performed provided data for the definition of the required on-site, passive shielding, and served for its validation after the installation. Although the final background in STEREO was underestimated by a factor of four, partly due to the negligence of γ-rays Compton-scattered in the shielding walls and the strong extrapolation from small detectors to the full STEREO volume, at the current state of the analysis the random coincidences are a minor background contribution and can be determined with high statistical precision. Further improvements of the shielding are possible. For example in the muon veto, which is not covered by the shielding walls and where non-cosmic background causes signals with a small number of detected photons, a possible background of epithermal neutrons from the reactor side was identified, by moving thin layers of absorbers around the veto and comparing the count rates in near PMTs. Since this may, to a smaller extent, also affect the full setup a wall of 40 cm thick water containers is planned to be installed in front of STEREO, covering the full height. Other local background sources may be identified with the help of STEREO itself.

The MCNP simulations of the H7 beamtube were required to assess whether after removal of the tube and the dedicated beamtube plug in front of STEREO additional shielding would be needed, in order to suppress the background at least to the same level as in the previous configuration, with the tube and plug present. Considering the strong attenuation of the particle fluxes from the reactor core to the exit of the H7 tube the simulations are not expected to deliver exact results, but nevertheless to yield about the correct order of magnitude. In a direct comparison of both configurations the smallest flux reduction in the new configuration, of about a factor of 10, appears for epithermal neutrons. This "safety factor" compared to the previous configuration should be sufficient, and is even larger for other energy ranges and for γ-rays. Thus after removal of the tube and the installation of the new, reinforced endcap, as proposed by the ILL, the integrated neutron and γ-ray fluxes are expected to be reduced, compared to the previous configuration. This however could not be verified yet by measurements, as the first restart of the reactor after the beamtube removal is scheduled for early 2018.

The definition of a calibration procedure for the quenching behaviour of the scintillator liquids and the determination of associated uncertainties is required for a precise reconstruction of the energy scale. This is important for an oscillation analysis based only on ratios of spectra in the individual cells (shape analysis), where the oscillation pattern is searched for by the L/E dependence and which would be independent of model predictions. Also in an analysis which compares predicted and measured rates a precise modelling of the detector response

in the simulations is necessary for simulation-based rate predictions. The fine tuning of the simulations, in this case in terms of the quenching parameters, has also an impact on the precise simulation of detector efficiencies and correction factors for border effects (spill-in, spill-out). Another method is developed independently by collaborators of the Laboratoire d'Annecy de Physique des Particules, which allows for crosschecks of obtained results.

With the proposed procedure the simulation parameters can be adapted iteratively, which yet needs to be done. The calibration will be repeated after the reinstallation of STEREO after the current maintenance phase to check the stability of the scintillator's performance. Optimizations of the production of the short lived sources, including additional sources, and of the calibration run sequence have been proposed, which will help to improve the precision of the results.

Appendix A

Measured Count Rates in Gamma-Ray Background Studies

Table A.1: Measuring positions during the 2016 γ-ray background campaign: x - distance from the front wall, y - distance from the D19 wall.

Det.	Pos 1	Pos 2	Pos 3	Pos 4	Pos 5	Pos 6
Ge x	235	390	390	195	440	535
Ge y	145	20	20	280	280	145
NaI x	—	460	485	275	515	535
NaI y	—	20	20	280	280	65

Det.	Pos 7	Pos 8	Pos 9	Pos 12	Pos 10	Pos 11
Ge x	105	190	260	485	485	120
Ge y	120	20	20	20	20	110
NaI x	110	265	350	555	330	120
NaI y	40	20	20	20	20	185

Campaign 2016 - Germanium Detector

Table A.2: 2016 campaign: count rates of the Ortec Ge-detector for single gamma lines relevant for the background. The rates have to be scaled by a factor of 1.3 for the full reactor power. Only statistical uncertainties are listed. Some data of similar positions have been combined to increase the statistics.

Pos	Co-60 1332 keV [mHz]	H-1(n,g) 2223 keV [mHz]	Tl-205 2614 keV [mHz]	Na-24 2754 keV [mHz]	Fe-56(n,g) 7631/46 keV [mHz]	Al, Cu, Ni, Fe-54 >7700 keV [mHz]
1-Up	12.24(36)	22.37(45)	12.28(36)	1.08(11)	18.05(43)	0.131(12)
1-Down	1.33(10)	1.41(10)	3.22(15)	—	1.51(82)	—
D19@43°						
2 & 10	1.404(58)	0.211(22)	0.564(36)	—	0.302(27)	—
9	1.543(13)	1.67(14)	0.573(82)	—	0.765(95)	0.182(46)
D19@70°						
2 & 3	0.975(74)	—	0.461(51)	—	0.184(32)	—
8	1.378(72)	—	0.756(53)	—	0.308(33)	—
9	0.896(80)	—	0.465(58)	—	—	—
IN20						
4	1.12(7)	1.22(07)	0.986(64)	—	1.260(73)	0.193(28)
4b	1.36(14)	0.86(11)	1.00(12)	—	0.65(10)	—
5		1.92(10)	1.650(92)	—	1.092(23)	0.105(23)
Front - Canberra detector						
11	0.389(56)	0.632(71)	0.706(75)	0.384(55)	—	—
Rear						
6	238.02(88)	14.07(21)	5.72(14)	67.37(49)	2.54(9)	—

Table A.3: Ordinary concrete and heavy concrete compositions chosen for the calculation of the γ-ray attenuation factors with [XCO17] in Fig. 5.1. Compositions taken from [McC11].

Concrete, Ordinary (NIST) density: 2.3 g/cm^3		Concrete, Iron-limonite density: 4.4 g/cm^3	
Element	wt%	Element	wt%
H	2.21	H	0.0500
C	0.2484	O	17.9910
O	57.4930	Mg	0.1999
Na	1.5208	Al	0.4998
Mg	0.1266	Si	1.3993
Al	1.9953	S	0.1000
Si	30.4627	Ca	6.0970
K	1.0045	Mn	5.1992
Ca	4.2951	Fe	72.0640
Fe	0.6435		

Appendix B

Résumé en français

B.1 Chapitre 1 - Les principes de la physique des neutrinos

Au début du XXe siècle il existait un grand interêt dans la physique autour de la recherche sur la radioactivité. Un enjeu important durant de nombreuses années a été la compréhension de la désintégration beta. En ne considérant que les particules détectables produites lors de la désintégration, le noyau d'origine, le noyau produit et un particule beta (electron), ni l'énergie ni le spin ne seraient conservés dans cette réaction. Pour résoudre ces contradictions Pauli a postulé l'existence d'une troisième particule produite dans cette reaction avec de l'énergie et un spin et qui interagirait très faiblement [Pau91]. Basé sur cette hypothèse Fermi a dérivé une théorie quantique de la désintégration beta qui permit de calculer le spectre de l'énergie des électrons beta. Il a donné le nom de "neutrino" à cette troisième particule [Fer34].

La première détection des neutrinos (de saveur) électronique a été faite par Cowan, Jr and Reines en 1956 [Cow56] utilisant pour cela un réacteur nucléaire comme source de neutrinos. En 1962 Lederman *et coll.* ont réussi à détecter aussi un neutrino muonique [Dan62] et en 2001 la collaboration DONUT a mesuré les neutrinos du tau [DON01]. Ces sont les trois types des neutrinos connu aujourd'hui dans le modèle standard de la physique des particules.

Actuellement ce modèle se compose de trois groupes de jauge: $\mathrm{SU}(3)_c \otimes \mathrm{SU}(2)_\mathrm{L} \otimes \mathrm{U}(1)_y$. Le groupe $\mathrm{SU}(3)_c$ décrit l'interaction forte entre les quarks, caractérisée par une propriété nommée "couleur" c, qui ne va pas être discuter dans cette section. Les interactions faibles et électromagnétiques sont décrites par la partie $\mathrm{SU}(2)_\mathrm{L} \otimes \mathrm{U}(1)_y$, où L dénote que que seules les particules avec une chiralité gauche (angl. "left") participent et y est l'hypercharge. Une particularité de l'interaction faible est qu'elle viole la parité, une symétrie qui décrit une reflexion des coordonnées d'espace par rapport à l'origine. Cet effet a été mesuré la première fois par Wu *et coll.* [Wu57] dans l'asymétrie de l'émission des électrons dans la désintégration beta de noyaux polarisés. Ceci'implique que les autres particules qui sont emises dans la désintégration, les neutrinos, ont une chiralité préférentielle. Cela a été mesuré explicitement par Goldhaber *et coll.* [Gol58], qui ont trouvé des résultats compatible avec 100% de chiralité gauche pour les neutrinos. En consequence le modèle standard actuel inclut seulement des neutrinos de chiralité gauche. Les fermions élémentaires (quarks et leptons) sont regroupés dans les doublets de chiralité gauche et des singulets de chiralité droite (Éq. (1.11)).

Pour obtenir des termes de masse invariante sous des transformations de jauge le formalisme de Higgs est utilisé. Ce formalisme permet des transformations covariantes, et avec une brisure de symmetrie de l'état fondamental permet aussi de créer des masses différentes de zéro.

Dans le cadre du modèle standard les neutrinos n'ont pas de masse. Toutefois ce n'est pas le cas dans la nature, comme l'ont montré l'observation des oscillations entre saveurs de neutrinos, les premières fois par les expériences Super-Kamiokande et Sudbury-Neutrino-Observatory. L'origine de cet phénomène est que les états propres des masses et de l'interaction faible ne sont pas les mêmes. Ils sont connectées par une matrice unitaire 3×3, qui peut être parametrisée par trois angles de mélange θ_i et trois différences de masses au carré Δm_i^2 des états de masse, qui décrivent l'amplitude et la fréquence de l'oscillation. Vu que les oscillations dépendent que

des Δm_i^2 des masses absolues, la hiérarchie des états de masse est inconnue. Les meilleures valeurs actuelles des paramètres d'oscillation sont indiqués dans Éq. 1.32. Des neutrinos stériles pourraient être inclus en élargissant la matrice de mélange à 4×4 et en introduisant de nouveaux couplages des paramètres d'oscillation.

B.2 Chapitre 2 - Les neutrinos emit par les réacteurs nucléaires

Les réacteurs nucléaires sont les sources de neutrinos artificiels les plus puissantes. Les produits de fission sont instables et riches en neutrons et décroissent via la désintégration beta. Au total $10^{17}\,\bar{\nu}_e(\mathrm{s{\cdot}MW_{therm}})$ sont émis. Les produits de fission des quatre isotopes ^{235}U, ^{238}U, ^{239}Pu et ^{241}Pu génèrent plus que 99% du flux total de neutrinos, dont ^{238}U et ^{241}Pu produisent environ 10%. On distingue les réacteurs avec des éléments de combustibles hautement enrichis, $>90\%$ ^{235}U, qui sont uniquement des réacteurs de recherche comme celui de l'ILL et qui produisent effectivement un spectre des neutrinos de ^{235}U pur, de ceux avec des éléments combustible faiblement enrichis, $<20\%$ ^{235}U, et qui sont des réacteurs utilisée pour la production de puissance. Ceux-ci fonctionnent en cycles d'environ une année. Pendant les cycles des isotopes de Pu sont produits et le spectre des neutrinos se compose de tout les quatre contributions et change lentement au cours des cycles.

Pour faire des prédictions du spectre des neutrinos il existe deux méthodes. L'un est de mesurer le spectre cumulatif des électrons emis dans les désintégrations beta et de les convertir en spectre de neutrinos. Pour ce faire les mesures des spectres cumulatifs des electrons de ^{235}U, ^{239}Pu et ^{241}Pu ont été réalisées par Schreckenbach *et coll.* [Sch81, vF82, Sch85, Hah89] à l'ILL à Grenoble, France, ceux du spectre de ^{238}U par Haag *et coll.* [Haa14] à FRM II à Munich, Allemagne. Pour la conversion des spectre ils sont partitionnés en intervalles en énergie. Puis chaque intervalle, l'un après l'autre en commençant à l'energie maximum, est décrit par une fonction d'un spectre beta et ensuite soustrait du spectre total. Le spectre extrait de chaque intervalle est converti en un spectre des neutrinos et puis ceux-ci sont additionnés.

L'autre méthode, un calcul ab-initio, calcule le spectre des électrons et des neutrinos pour chaque produit de fission à partir d'une base des donnés et après ceux-ci sont additionnés. Pour faire cela on a besoin des données d'environ 800 isotopes par isotope fissile et d'environ 10000 branches des désintégrations beta différentes. Avec cette méthode et les données existant aujourd'hui on peut reproduire les résultat de la conversion avec une précision d'environ 10%, qui est moins precise que ceux de la conversion.

En 2011 les calculs des spectres de neutrinos, faits par Schreckenbach *et coll.* ont été réévalués par deux groupesindépendantes, en utilisant les mêmes données des spectres d'électrons de Schreckenbach *et coll.* Le premier groupe de Mueller *et coll.* [Mue11] a utilisé la méthode ab-initio pour toutes les isotopes connus avec assez de précision et après ils ont utilisé la méthode de conversion pour le spectre résiduel. Huber [Hub11] a fait une conversion pure, comme Schreckenbach *et coll.*, mais il a utilisé une description de la désintégration beta avec plus de détails. Les deux groupes ont trouvé un flux des neutrinos plus élevé d'environ 3% par rapport à Schreckenbach *et coll.*, Fig. 2.4. La raison est dans chaque cas une description plus détaillée des paramètres du spectre beta. Avec une section efficace de la désintégration beta inverse, la réaction utilisée pour la détection des neutrinos des réacteurs, augmentée d'environ 2% au cours des années passées, le résultat est un deficit d'environ 5% entre le taux des neutrinos mesuré dans les expériences et le taux calculé. Ce deficit est connu comme l'anomalie des neutrinos des réacteurs (RAA).

Les prédictions sont fait indépendamment pour chacun des quatre isotopes fissiles. Pour avoir une prédiction du flux des neutrinos précise pour chaque expérience il faut que l'on connaisse les proportions de fission pour chaque isotope. De plus il y a des corrections à appliquer dependant du type du réacteur. Après le démarrage du réacteur, chaque produit de fission prend un temps pour trouver l'équilibre entre production et désintégration, qui est fonction de son temps de vie. A cause de plusieurs isotopes qui ont un temps de vie long, le spectre des neutrinos ne se stabilise à un niveau de 1% pour toutes énergies qu'après environ 100 d, mais les spectres de référence des

électrons de Schreckenbach *et coll.* et de Haag *et coll.* avaient été mesurés qu'après environ 1 d'irradiation. L'évolution des spectre peut ensuite être calculée grâce à la méthode ab-initio. De plus les captures des neutron par les produits de fission peut changer l'inventaire nucléaire en fonction quadratique du flux des neutrons dans le coeur du réacteur (probabilité de fission × probabilité de capture). Une autre source de neutrinos peut être les éléments combustibles usés, qui sont stockés près du réacteur pour un certain temps. Les désintégrations beta qui continuent dans cette zone produisent un flux d'un niveau d'environ 0.3% de l'élément combustible actif.

Une autre possibilité pour obtenir un spectre des neutrinos de référence est d'utiliser le spectre mesuré par l'expérience Daya Bay [An16a], qui est la mesure le plus précise à ce jour. Le spectre est mesuré à une distance d'environ 500 m de six réacteurs nucléaires et il est publié pour corriger pour l'oscillation θ_{13} et tous les effets du détecteur. Ces résultats confirment le déficit du taux des neutrino mesuré par rapport au modèle Huber-Mueller [Hub11, Mue11] mais il trouve une autre anomalie cette fois dans dans la forme du spectre. Lorsqu'il est corrigé du déficit global le spectre de Daya Bay révèle un excès d'environ 10% aux energies des neutrinos dans le domaine d'énergie 5-7 MeV. Cette observation est confirmée par les expériences Double Chooz [Abe14, Abe15] et RENO [Cho16]. L'origine de cette anomalie est aussi inconnue, mais elle n'est pas nécessairement corrélée avec l'anomalie du flux global.

Une possibilité d'examiner l'anomalie de la forme du spectre est de comparer des spectres mesurés auprès de réacteurs fonctionnant avec des proportions de noyaux de fission différentes. Par exemple la recherche de l'anomalie des neutrinos des réacteurs a initié des expériences à très courtes distances des réacteurs, dont des réacteurs de recherche avec des éléments combustibles enrichis en ^{235}U, qui émettent effectivement un flux de neutrinos de ^{235}U pur. Le rapport de ce spectre avec des spectres des éléments combustibles faiblement enrichis va permettre de mettre des contraintes sur les isotopes fissiles responsables pour cette anomalie, voir par example Fig. 2.6 et Fig. 2.7.

L'anomalie des neutrinos des réacteurs (angl.: reactor antineutrino anomaly (RAA)) a été étudiée en plus détail par Mention *et coll.* [Men11]. Plusieurs explications pour l'anomalie peuvent être trouvées: des erreurs dans les spectres de référence des électrons, des effets systématiques dans toutes les expériences des neutrinos auprès de réacteurs, mais aussi l'existence des neutrinos stériles, qui seraient responsables d'oscillations aux très courtes distances. Par example celles-ci ne peuvent pas être résolues aux distances supérieure à 20 m et résultent en un déficit global. Une anomalie comparable a été trouvé dans les expériences GALLEX et SAGE qui ont mesuré les neutrinos solaires dans la réaction $^{71}\mathrm{Ga}(\nu_e, e^-)^{71}\mathrm{Ge}$. Pour faire des calibrations de leurs détecteurs ils ont utilisé des sources isotopiques de haute intensité (∼PBq) à courtes distances. Dans ces calibrations le taux des neutrinos mesuré a été inférieur à celui calculé, avec une proportion d'environ 87% [Kae10]. Pour étudier la possibilité de la participation des neutrinos stériles aux oscillations, Mention *et coll.* ont pris en compte 19 expériences aux courtes distances auprès des réacteurs et les résultats des calibrations des expériences avec du Ga. Avec les deux anomalies ils ont trouvé des limites des paramètres d'oscillation de $\Delta m^2 > 1.45\,\mathrm{eV}^2$ et $0.05 < \sin^2(2\theta) < 0.22$ en excluant l'hypothèse de l'inexistence des oscillations des neutrinos stériles avec 99.7% C.L. Les paramètres de oscillation possibles sont montrés dans Fig. 2.8.

Une autre explication pour la RAA à part celle des oscillations, est une surévaluation du flux des neutrinos escomptés. Des indications pour ce scénario ont été trouvées par l'expérience Daya Bay. Avec six réacteurs de puissance comme source et quatre détecteurs de neutrinos à courtes distances (~ 550 m) ils a collecté environ $2.2 \cdot 10^6$ événements neutrinos pendant quelques cycles de chaque réacteur. Ca permet d'étudier le flux des neutrinos en fonction de la proportion de fission de ^{239}Pu, F_{239}, (ou de ^{235}U) qui changent le plus pendant un cycle. Celles-ces de ^{238}U et ^{241}Pu restent presque constants. Car les spectres des neutrinos sont différentes pour chaque isotope fissile le flux des neutrinos et la forme du spectre changent pendant un cycle. En considérant le flux provenant de ^{238}U et ^{241}Pu comme constant, le changement du flux avec F_{239} permet de calculer explicitement le flux causé par ^{239}Pu et celui de ^{235}U. Dans cette analyse il s'est trouvé que le flux venant de ^{239}Pu est en accord entre l'expérience et les calculs, mais pour ^{235}U le taux des événements IBD est trop haut dans les calculs par environ 8%, voir Fig. 2.9.

Ceci peut expliquer une grande partie, voir tout, de la RAA. Pour confirmer ce résultat, les expériences auprès réacteurs avec des combustibles hautement enrichis ($F_{235} \sim 1$) sont importantes. Mais pour exclure des oscillations à courtes distances définitivement des mesures du flux des neutrinos aux courtes distances différentes sont nécessaires. En ce moment plusieurs expériences aux courtes distances des réacteurs hautement et faiblement enrichis sont en preparation ou ont déjà commencé de prendre des données (voir Tab. 2.4). Parmi ellesSTEREO, qui va être présentée en plus de détail dans la section suivante.

B.3 Chapitre 3 - L'expérience STEREO

L'expérience STEREO est localisée à l'institut Laue-Langevin, Grenoble, France. L'institut gère un réacteur de recherche avec une puissance maximum de 58.3 $\mathrm{MW_{therm}}$. L'élément combustible est dans une géométrie très compacte (cylindrique, hauteur $\simeq$ 80 cm, diamètre $\simeq$ 40 cm) et hautement enrichi en ^{235}U, ce qui en général est très favorable pour une recherche d'oscillations des neutrinos aux courtes distances. Le détecteur STEREO est positionné dans la halle expérimentale du réacteur à une distance de 8.9-11.1 m d'éléments combustibles. Un plan du site est montré dans Fig. 3.2. Le détecteur est localisé effectivement en surface de la terre et en conséquence il est exposé à un bruit de fond cosmique élevé. Par contre le bâtiment du réacteur et un canal utilisé pour transférer des éléments combustibles rempli avec de l'eau qui est situé directement au dessus de STEREO, atténuent le flux des muons cosmiques par un facteur 2,7, Fig. 3.1, [Zso16]. Néanmoins, le bruit de fond causé par les muons, notamment par les spallations dans des éléments lourds qui créent des neutrons rapides ou des multi-neutrons, qui peuvent créer des signaux corrélés dans STEREO, constitue le bruit de fond dominant pour l'expérience. Cette contribution peut être mesurée pendant les arrêts du réacteur. D'autres sources de bruit de fond sont corrélées avec le fonctionnement du réacteur. A basse énergie la source dominante est l'^{41}Ar, qui est instable, avec un temps de vie de $T_{1/2} = 109.6$ min [ENS17]. Il est produit par les captures des neutrons dans ^{40}Ar dans l'air. Après sa désintégration un rayon gamma de l'énergie 1293.6 keV [ENS17] est emis, toujours visible dans les spectres de STEREO pendant des cycles du réacteur, mais avec une énergie inférieure au seuil d'analyse des neutrinos. D'autres sources de bruit de fond viennent des instruments voisins, d'un doigt de gant dans la piscine du réacteur directement avant STEREO, nommé H7, qui a délivré des rayons gammas pour une ancienne expérience, et les circuits de refroidissement du réacteur, situés dans le sous-sol, dessous STEREO. Dans l'eau de refroidissement il y a le noyau ^{16}N, produit proche de l'élément combustible dans la réaction $^{16}\mathrm{O}(n,p)^{16}\mathrm{N}$. Dans sa désintégration beta, des rayons gammas de l'énergie 7115 keV (intensité $I = 4.9\%$) et de 6129 keV ($I = 67\%$) [ENS17] sont émis. Cette composante du bruit de fond a été étudiée dans [Zso16] et en consequence la structure de STEREO contient un sol de 20 cm du plomb pour atténuer ces gammas. Aux côtés de STEREO il y a deux instruments pour la diffusion des neutrons. L'un, D19, est un instrument de diffraction Laue pour étudier les structures des cristaux. L'instrument a trois configurations principales, qui produisent du bruit de fond caractéristique et différentes pour STEREO. De l'autre côté il y a l'instrument IN20, qui utilise la diffusion inélastiques des neutrons. Pour avoir des énergies des neutrons incidentes variables, l'échantillon est placé aux angles différentes autour du monochromateur de l'instrument. En fonction de la position d'échantillon le bruit de fond pour STEREO change légèrement. Le bruit de fond venant de ces deux instruments voisins sont des neutrons thermiques, qui après sont capturés dans les matériaux autour de Stereo, qui génèrent des rayon gammas de haute énergie. L'étude de ce bruit de fond sur le site de STEREO est décrit dans le chapitre 5. En plus IN20 peut être utilisé avec des aimants supraconducteurs qui causent des champs magnétiques au niveau de la position de STEREO et qui altèrent le fonctionnement des photomultiplicateurs utilisés par STEREO. Pour éviter une détérioration de la performance du détecteur pendant l'utilisation des aimants un blindage magnétique a été construit pour protéger STEREO. Les simulations des éléments finit qui forment la base pour la choix du design du blindage sont décrits dans le chapitre 4.

Après une première phase de fonctionnement de STEREO, le doigt de gant H7 était arrivé

à sa fin de vie prévue. Le doigt de gant a été enlevé sans remplacement direct. Cela a empêché la réinstallation d'un bouchon protégeait STEREO dans cette direction, et étudié dans [Pé15]. Une solution de blindage alternative a été proposé par l'ILL. Pour étudier le changement du bruit de fond pour STEREO et pour decider si ce nouveau blindage suffisait des simulations MCNP ont été effectuées. Celles-ci sont décrites dans le chapitre 6.

Le détecteur est conçu pour faire face aux enjeux de bruit de fond du site, tout en restant simple dans le design et en utilisant des technologies bien connues. Le volume cible du détecteur est constitué de six cellules de $370\times889\times918\,\mathrm{mm}^3$ (TG, angl. target - cible). Elles contiennent du scintillateur liquide, dopé avec du gadolinium. Les six cellules sont disposées le long de la ligne de propagation des neutrinos, mais avec un angle d'environ 18°, pour rester parallèle au canal d'eau situé au dessus de STEREO. Les neutrinos sont détectés dans une réaction de désintégration beta inverse (IBD, engl. inverse beta decay) avec des noyaux d'hydrogène ($\bar{\nu} + \mathrm{H}^+ \rightarrow e^+ + n$) contenus dans le TG. Les positrons déposent alors leur énergie directement dans le scintillateur et les neutrons sont détectés par ses captures sur les noyaux de gadolinium, après lesquelles des rayons gammas sont émis. Autour du volume cible il y a quatre cellules qui contiennent du scintillateur non-dopé, nommé "gamma catcher" (GC), voir Fig. 3.4. Ils servent comme blindage, mais aussi pour récupèrent les rayon gamma qui sortent de la cible et pour identifier des événements selon la topologie de leur distribution d'énergie. Les cellules sont séparées par des parois réflectives spéculaires, construites comme des sandwiches de plaques de verre acrylique, des films réfléchissants (VM2000) et des couches de l'air entre eux, pour permettre de la réflexion interne totale, voir Fig. 3.5. Au dessus des cellules, des bloc de verre acrylique séparent le scintillateur et les photomultiplicateurs (PM), qui vont collecter les photons de scintillation et générer les signaux. Cette distance minimum permet d'avoir une distribution de la lumière plus homogène entre les PM, et ceci même pour les événements en haute des cellules.

Autour de tout le TG et le GC il y a des blindages de polyéthylène boré (BPE) et de plomb. Au dessus de la structure il y a un veto à muon, un volume d'eau déminéralisée avec des PM pour detecter la radiation Cherenkov, emit par les muons qui traversent le veto. Le blindage est complété par une couche de mu-métal à l'intérieur du BPE et une couche de fer doux autour de toute la structure, incluant aussi le veto. Ces deux couches forment le blindage magnétique, décrit en plus en détails dans le chapitre suivant. A l'extérieur, une couche de matériau contenant du B_4C pour réduire le nombre des captures des neutrons dans le fer. Voir Fig. 3.3 pour une vue schématique du détecteur.

Quatre systèmes de calibration sont intégrées dans la structure du détecteur. Trois systèmes permettent de positionner des sources de rayons gammas et de neutrons dans les cellules et aux autre de les faire circuler autour du TG et GC, pour faire des calibrations de l'échelle d'énergie et de l'efficacité du détecteur. Il y a aussi un système de LEDs pour calibrer et suivre la réponse des PMs. Les LEDs peuvent aussi être utilisées pour mesurer la linéarité des PMs et de l'électronique. Aucune non-linéarité n'a pas pu être vue, ce que signifie que si une non-linéarité est potentiellement présente elle est inférieure à 1% sur tout le domaine en energies utilisé pour l'analyse des spectres des neutrinos [Sal17].

Comme indiqué auparavant, la cible de STEREO consiste en un scintillateur organique liquide. Cette type de détecteur a les advantages de pouvoir être produit en grande quantité, d'être comparativement moins cher et d'être flexible dans sa forme. En plus quelques scintillateurs ont la propriété de pouvoir différencier des particules selon leurs dépôt d'énergie le long du trajet. Ces scintillateurs ont deux composantes de scintillation, une rapide et une lente. La proportion de la composante lente est plus importante pour les particules fortement ionisantes, par example les noyaux de recul produit par les neutrons rapides. Le scintillateur de STEREO est adapté pour différencier les interactions électromagnétiques (électrons/positrons, rayons gamma) des interactions des neutrons rapides. Il a été développé et produit par le Max-Planck-Institut für Kernphysik Heidelberg (MPIK). Sa composition est donnée dans Tab. 3.1.

Pour faire l'analyse d'oscillation il est important de déterminer les spectres des neutrinos dans chaque cellule. Dans la réaction IBD le positron récupère effectivement tout l'énergie

cinétique du neutrino, moins la masse du positron et l'énergie pour convertir le proton dans un neutron. Le positron va déposer tout cette énergie plus l'énergie de l'annihilation avec un électron dans le scintillateur. En consequence il y a une relation fixe entre l'énergie du neutrino et l'énergie déposée par le positron: $E_{e^+} \simeq E_{n\bar{\nu}u} - 782\,\text{keV}$, ce qui permet de mesurer le spectre des neutrinos. Le neutron du IBD va être modéré dans le scintillateur avant d'être capturé par un noyau de gadolinium (ou hydrogène). Grâce à cela il y a deux signaux en coincidence retardé qui proviennent de l'IBD. Ça permet de fortement réduire le bruit de fond. Cela peut encore venir des coïncidences fausses, par les événements non-corrélées, ou des coïncidences corrélées, par example des multi-neutrons produit par la spallation des muons. Les deux types de bruit de fond doivent être pris en compte et être rejetés dans l'analyse des données, si possible. Une possibilité simple est d'introduire des coupures en énergie. Par exemple dans le cas de STEREO le dépôt d'énergie du positron doit être entre 2-8 MeV et celle du neutron entre 5-10 MeV, avec un temps de corrélation inférieur à 70 μs.

Pour faire l'analyse des oscillation des neutrinos pour STEREO, la forme des spectre entre les six cellules va être comparée en fonction de l'énergie et de la distance au cour du réacteur. Cela permet de faire une analyse indépendante des modèles des spectres des neutrinos. Avec des paramètres de prise de donnée prévus pour STEREO, listé dans chapitre 3.4 STEREO va être capable de couvrir la plupart de l'espace des paramètres possibles pour les oscillations des neutrinos stériles, voir Fig. 3.9.

B.4 Chapitre 4 - Le blindage magnétique

Pour détecter les signaux optiques, produits dans le scintillateur, STEREO utilise des photo-multiplicateurs (PMT), au total 68 dans le TG, le GC et le veto à muons. Tous les PMTs sont des R5912-100 de Hamamatsu [Ham98], avec un diamètre de 8 pouces ($\simeq$20 cm). À cause de ces grandes dimensions ils sont sensibles aux champs magnétiques, qui dévient les photo-électrons dans le PMT par la force Lorentz. Cela diminue l'amplification des signaux dans les PMTs et leur gain mais aussi dégrade leur resolution, qui est fonction du nombre des photo-électrons collectés. La variation des signaux des PMTs a été mesurée par la collaboration STEREO dans le champ magnétique terrestre ($\sim$60 μT) [Stu15a]. En tournant un PMT dans ce champ la variation de l'amplitude de ses signaux peut être $\pm$30% autour de la valeur moyenne. Avec un cylindre de mu-métal d'une épaisseur de 1 mm autour du PMT, la variation peut être réduite à $\pm$2%, voir Fig.4.3. Pour avoir des conditions stables pour les PMTs pendant toute la durée de l'expérience, la collaboration a décidé d'installer les PMTs entourés individuellement de cylindres de mu-métal et d'y ajouter un blindage magnétique qui doit atténuer tous les champs magnétiques externes, qui peuvent être présents au niveau du détecteur de STEREO, jusqu'à un maximum de 60 μT. Les sources les plus importantes de champs magnétiques sont des aimants supraconducteurs installés dans l'instrument IN20, localisé à une distance minimale de 2.7 m de STEREO. L'aimant le plus fort, avec un champ central de 15 T, génère, selon des simulations, des champs maximum de 0.83 mT dans le détecteur (GC) et de 1.06 mT dans le veto à muons.

Pour réaliser le design d'un blindage efficace il est nécessaire d'en faire des simulations. Le calcul des champs magnétiques nécessite de résoudre les équations différentielles du problème fundamental. Comme cela n'est pas réellement possible pour de grands volumes en présence de matériaux aimantables, des simulations des éléments finis sont utilisées. Dans ce type des simulations le volume d'interêt est divisé en polygones avec une précision ajustable. Pour les coins des polygones les équation différentielles sont résolues numériquement. Le principe d'un blindage magnétique est d'entourer le volume à protéger (ou la source) avec des matériaux magnétisables. Comme cela le champ est guidé dans ce matériau et le champ effectif dans le volume est réduit. Des matériaux avec de bonnes propriétés magnétiques sont le fer doux ou le mu-métal (un alliage avec une grande proportion de nickel), qui ont une haute perméabilité magnétique relative μ_r. Pour augmenter l'efficacité d'un blindage on peut augmenter l'épaisseur des matériaux, prendre des matériaux avec un μ_r plus haute ou, plus efficacement, utiliser des couches multiples de blindage. Il est important de noter qu'en pratique dans les matériaux la

perméabilité magnétique est une fonction du champ magnétique $\mu_r = \mu_r(\vec{B})$.

Les simulations ont été effectuées avec Comsol Multiphysics v4.3a. en parallèle de cette série de simulations, les composants du blindage ont été adaptés pour être compatibles avec le dessin général du détecteur et la collaboration a pu ainsi faire les choix entre les options du design et des matériaux utilisés. Tous ces processus s'influencent les uns les autres, et en conséquence les configurations considérées dans les simulations ont changé plusieurs fois, sans toujours répéter toutes les simulations précédentes. Néanmoins, avec des changements suffisamment faibles les résultats sont comparables. Pour modéliser l'aimant de 15 T dans les simulations, des dessin techniques de l'aimant et une carte du champ magnétique, mesuré sur autre site, ont été fournis par le groupe d'instrumentation (SANE) de l'ILL [SAN17]. Dans les simulations la conception général du blindage et des détails importants ont été étudiés comme la qualité nécessaire des matériaux utilisés, le passage des cables dans le blindage, une porte d'accès pour le système de calibration interne, l'orientation du champ magnétique à l'intérieur du blindage et la performance des cylindres de mu-métal autour des PMTs. Le design final comprend une couche de fer doux de 1 cm, couvrant tout la structure (veto inclus), une couche de mu-métal de 1.5 mm autour du détecteur (TG et GC) et des cylindres du mu-métal (une couche autour des PMTs du détecteur et deux couches autour des PMTs du veto). Les champs maximals dans les plans des PMTs obtenus pour cette configuration sont de $B_{\mathrm{det}} = 4\,\mu$T dans le GC et de $B_{\mathrm{veto}} = 294\,\mu$T dans le veto. Pour autres configurations les résultats sont listés dans Tab. 4.1.

Le champ magnétique n'a pu être mesuré qu'après que le plupart des simulations ait été finies. Pour les mesures une sonde de Hall de trois axes a été utilisée. Le champ a été mesuré dans trois plans dans le volume de STEREO : le sol, le plan des PMTs du détecteur et le plan des PMTs du veto, voir Fig. 4.20. Le champ résiduel a été mesuré pour un champ externe maximum de 13.5 T. Après avoir corrigé ce résultat prendre en compte le champ théoriquement possible de 15 T, le champ mesuré reste encore plus faible d'environ 20-30% que prévu, et une orientation plus horizontale dans le plan du veto. L'origine de cet écart est probablement dû à l'acier structurel de Stereo dans le sol, des murs et du canal au dessus de STEREO. Si cette réduction du champ magnétique résiduel reste inchangée en présence de STEREO, la valeur du champ maximum à l'intérieur du blindage doit être revu à $3\,\mu$T pour les PMTs du détecteur et 0.24 mT pour les PMTs du veto.

Après la mise en exploitation de STEREO un aimant a été utilisé à IN20 en décembre 2016, avec un champ central maximale de 10 T. Aucun effet n'a été observé pour les PMTs du TG et du GC. Pour le veto à muons quelques PMTs ont vu leur gain efficacité de collection des photo-électrons et leur gain être réduit de quelques % amplification absolue, sans que cela n'affecte l'efficacité de detection du veto pour les muons verticaux, qui est restée $> 99\%$ telle que calculée par [Ber17].

B.5 Chapitre 5 - Le bruit de fond gamma

Le bruit de fond des rayonnements gamma sur le site de STEREO comporte trois composantes: la radioactivité naturelle, les isotopes des activations neutroniques et les rayons gammas produits lors des processus liés aux captures de neutrons. Ces dernières représentent la contribution dominante. Les neutrons sont générés dans des doigts de gant qui les transportent du coeur du réacteur aux instruments. Après la diffusion un certain nombre de neutrons sont émis dans le hall expérimental où ils sont capturés par les matériaux présents. Autour de STEREO en particulier les pieces métalliques produisent des rayons gamma de haute énergie après ces captures. Les isotopes les plus importants sont listés dans Tab. 5.1. Deux campagnes majeures de mesures du bruit de fond du rayonnement gamma ont été effectuées sur site dans le contexte de cette thèse. Une première quand la zone et les murs autour étaient dans les configurations initiales. Les données de cette campagne ont été analysées par Stutz [Stu15b] pour déterminer le blindage supplémentaire nécessaire pour diminuer le bruit de fond à un niveau qui permet un bon fonctionnement de STEREO. Le résultat a conduit à remplacer le mur entre STEREO et D19 par 30 cm de béton et 10 cm de plomb, et le mur vers IN20 par 15 cm du plomb et 15 cm

du BPE et enfin un mur supplémentaire de 10 cm du plomb et 10 cm du PE a été construit vers l'avant. Voir Fig. 5.2 pour un plan du site avec ces éléments de blindage. Après que tous ces éléments du blindage aient été construits, une deuxième campagne des mesures a été effectuée pour verifier leur efficacité. Pour les deux campagnes un détecteurs germanium (HPGe) et un détecteur NaI ont été utilisés. Le HPGe a une bonne résolution en énergie, mais un petit volume ($\sim 160\,\mathrm{cm}^3$) tandis que le NaI a une moins bonne résolution mais un volume plus grand ($\sim 1200\,\mathrm{cm}^3$) permettant des mesures plus rapides, qui permet de scanner une surface plus grande avant des changements de configurations par les instruments voisines. Le HPGe a été placé à une hauteur d'environ 30 cm avec une collimation forte avec 10-20 cm du plomb dans cinq directions, incomplet seulement vers le haut dans sa partie arrière. Le NaI a été placé sur une table réglable en hauteur avec une collimation de 10 cm du plomb dans cinq directions, aussi incomplet en arrière, dans sa partie haute. Grâce à la collimation des détecteurs la dépendance directionnelle du bruit de fond a pu être étudiée. Pour chaque côté les taux de comptage dans le HPGe pour les rayons gammas caractéristiques sont mesurés. Ils sont calculés pour toute la surface de STEREO et après sont propagés à l'intérieur de STEREO à l'aide des simulations Geant4 [Ago03]. Dans la suite les observations les plus caractéristiques pour chaque côté sont résumées, avant de discuter la situation globale pour STEREO.

Au début la collimation du HPGe a été ouverte vers le haut et par la suite vers le bas. Par le haut, une contribution forte des gammas venant du fer a été observée, voir Fig. 5.3 et Tab. 5.2. La source est très probablement une galerie en acier, installée à côté du canal au dessus de STEREO. La galerie est exposée sans protection au flux des neutrons thermiques diffusés par IN20. Pour ce qui est du bas, la contribution dominante est issue du ^{16}N contenu dans le circuit de refroidissement. Cette contribution a été mesurée en [Zso16] et elle est déjà prise en compte dans le blindage de STEREO.

L'instrument D19 a trois configurations avec des positions du faisceau de neutrons différentes. Dans chaque configuration différents monochromateurs peut être utilisés, du carbone, du germanium ou du cuivre. Le bruit de fond total venant de D19 a été trouvé être maximal dans la configuration à 43° (angle du faisceau d'instrument relatif au angle du faisceau principale), voir Figs. 5.5 et 5.6. Cependant dans la configuration à 90°, où le faisceau est arrêté par le mur entre D19 et STEREO, il existe un 'hotspot' à l'arrière de l'arrêt du faisceau, voir Fig. 5.5. Avec un détecteur HPGe positionné à cette position, des rayons gammas, diffusés dans le mur, ont été mesurés, et qui arrivent jusqu'à l'énergie de captures des neutrons par le cuivre à 7916 keV, voir Fig. 5.4. Ceci montre que le 'hotspot' est, au moins partiellement, causé par le monochromateur de l'instrument.

Le bruit de fond venant de IN20 est généralement plus haut que cela du D19. En plus nous avons trouvé qu'environ 70% du flux des neutrons thermiques sur le site de STEREO venaient de IN20 [Hé15]. Ceux-ci créent de nouveau des rayons gammas dans ses captures. Des mesures proches du mur vers IN20, qui comporte du plomb avec une structure de support d'acier, montrent que les rayons gammas de la capture des neutrons dans fer peuvent être réduits fortement si les composants métalliques autour de STEREO sont couverts par le B_4C, voir Fig. 5.9.

Les mesures vers l'avant ne montrent pas de caractéristiques spéciales, sauf que le bruit de fond directionnel augmente presque d'un facteur 10 quand H13 et IN20 sont actifs, comparé à l'état inactif de ces deux dispositifs. Vers l'arrière beaucoup de gammas de captures des neutrons ont été mesurés, mais aussi des produits d'activation neutronique, comme ^{60}Co et ^{24}Na, qui sont créés dans les matériaux structurels.

En général nous avons observé que non seulement les rayons gammas venant des instruments voisins sont importants, mais aussi ceux-ci produits par les captures de neutrons dans la zone de STEREO. Les murs de blindage installées ont prouvés être suffisants, et au total un taux de comptage de 0.35 Hz a été estimé pour le fenêtre d'énergie des neutrons IBD (avec une specification de $\leq$1 Hz).

Après l'installation et la mise en service de STEREO, un taux de comptage de 1.4 Hz a été mesuré, ce qui veut dire que ce taux a été sous-estimé par un facteur quatre. Les raisons peuvent

être que les gammas diffusés dans le HPGe ont été pris en compte, mais pas ceux diffusés dans les murs avant d'arriver dans le détecteur. En plus les taux ont été mesurés avec des détecteurs qui ont des surfaces de quelques centimètres carrés et après ont été extrapolés à la surface de STEREO de quelques mètres carrés. En conséquence, les sources locales peuvent ne pas avoir été remarquées.

Si l'on prend en compte seulement les taux de comptages dans les intervalles d'énergie de l'IBD-positron et le IBD-neutron (2-8 MeV et 5-9 MeV) et un temps de corrélation de 70 μs, les fausses coïncidences sont de l'ordre de $400\,\mathrm{d}^{-1}$, ce qui doit être comparé avec le taux des neutrinos d'environ $380\,\mathrm{d}^{-1}$. Toutefois le nombre de ces fausses coïncidences peut être réduit fortement par les coupures par exemple sur la topologie des événements. Les composantes restantes peuvent être déterminées avec précision dans les fenêtres de temps non-corrélées et être soustraites statistiquement.

Le spectre total obtenu avec STEREO est dominé par les signaux créés par des particules cosmiques, notamment des muons, voir Fig. 5.12. Après avoir appliquer un rejet à l'aide d'un veto a muons les sources dominantes des signaux sont le ^{41}Ar à basse énergie et la radioactivité ambiante et naturelle. Le bruit de fond externe des rayons gammas n'est pas dominant.

B.6 Chapitre 6 - Simulations MCNP du bruit de fond venant d'un faisceau de neutrons près de STEREO

L'ILL possède un doigt de gant qui traverse tout la piscine du réacteur et passe près de l'élément combustible à une distance d'environ 55 cm. Ce tube, nommé H6-H7, a été utilisé pour positionner des cibles près du cœur du réacteur pour créer un faisceau des rayons gammas d'haute intensité, utilisé par les instruments GAMS (GAMma ray Spectrometer [GAM17, Koc80]), dans le passé situés à chaque extrémité de ce tube. Un de ces instruments, GAMS5, a été décommissionné pour libérer l'espace pour l'installation de STEREO, mais à l'autre côté GAMS6 est resté en fonction. Pour protéger STEREO contre le faisceau des gammas et contre les neutrons qui se propagent dans le tube, un bouchon dédié a été construit pour fermer le tube dans la direction de STEREO. Le design de ce bouchon a été étudié par Pequignot [Pé15, Pé13] et il est conçu pour être efficace pour STEREO sans créer du bruit de fond pour GAMS6, opérationnel de l'autre côté du tube. L'élément central du bouchon est une partie d'un mètre de béton lourd, renforcé par 8 cm de plomb au début et à la fin et du boral (alliage d'aluminium borée) vers le faisceau. Un interstice de 3 mm tout autour du bouchon permet son insertion. À la fin du cycle du réacteur en mars 2017, le doigt de gant est arrivé à sa fin de vie et a dû être retiré. Le bouchon n'a pas pu être réinstallé à la suite l'enlèvement du doigt de gant et un nouveau blindage a été proposé par l'ILL, qui consiste de 42.5 cm d'acier, aussi avec du boral vers le faisceau. Une série de simulations neutroniques et photoniques (MCNP) a été effectuée pour étudier l'effet de ce changement sur le bruit de fond autour de STEREO et pour décider si le blindage proposé est suffisant. Les deux scénarios avant et après l'enlèvement ont été simulés et comparés entre eux et avec les simulations de [Pé15].

Pour les simulation le mode de calcul des criticités a été utilisé, lequel prend en compte les fissions, l'emission des neutrons et des gammas prompts. Un modèle préexistant du réacteur [Fua15] a été remanié avec plus de détails du doigt de gant H7 et adapté pour les deux configurations. Un schéma des composants inclus est montré dans Fig. 6.1. Pour les simulations avec le tube H7 et le bouchon actuels le flux des neutrons et le flux des gammas ont directement été calculé à la sortie du tube et du bouchon. Les résultats sont listé dans Tab. 6.3.

Après l'enlèvement deH6-H7 tout le volume du tube est rempli avec de l'eau lourde. Pour avoir la possibilité de tester des blindages différentes les simulations ont été réparties en deux étapes, la première d'élément combustibles jusqu'à la surface du blindage et la deuxième traversant le blindage. Les résultats des deux étapes sont montrés dans Fig. 6.4 et listés dans Tab. 6.4. Dans la nouveau configuration, sans doigt de gant, le flux des neutrons intégré sur toutes les énergies est réduit par un facteur $\mathcal{O}(10)$ en comparaison de la configuration avec le tube. Le flux intégré des gammas est réduit par un facteur $\mathcal{O}(10^2)$. Pour les neutrons la réduction est

plus forte pour les neutrons thermiques et les neutrons rapides, qui seraient plus dangereux pour l'expérience car ils ont une probabilité plus grande de traverser le blindage suivant. Pour les rayons gammas la réduction est plus homogène pour toutes les énergies. En général la situation du bruit de fond est espérée être d'améliorée, mais la preuve expérimentale ne peut pas être faite avant le prochain démarrage du réacteur au printemps 2018.

B.7 Chapitre 7 - Analyse des données de STEREO

Le détecteur STEREO était mis en service en Novembre 2016. Aprés il a collecté des donnes pendant environ 70 jours des cycles du réacteur et 28 jours d'arrêts. En été 2017 l'analyse des donnés a été sous développement. Quelques méthodes et algorithmes pour la différenciation des classes des événements, pour l'analyse des spectres des neutrinos et pour la réconstruction d'énergie des événements ont déjà été en place, sans être finalisé. Néanmoins, la reconstruction d'énergie a été consideré d'être stable en temps, voir Fig. 7.1. Dans ce chapitre une méthode est proposé pour aussi faire la calibration d'echelle d'énergie, qui dans le cas de STEREO (cas des scintillateurs liquides) n'est pas linéaire. La non-linéarité est un résultat du 'quenching' des signaux pour les particules fortement ionisant [Bir51].

Les calibrations ont été fait avec des sources gammas dans les tubes de calibration dans les cellules TG1 et TG6. Les sources utilisées sont listé dans Tab. 7.1. Une procédure de calibration doit satisfaire plusieurs conditions:

(i) Applicabilité pour les deux volumes du détecteur (TG et GC),

(ii) Applicabilité pour toutes les sources (emission des rayons-γ seul ou double),

(iii) Suppression du bruit de fond des événements Compton,

(iv) Calculation de la moyenne de l'énergie déposé (prendre en compte la résolution du détecteur une suppression complète des evennements Compton n'est pas possible),

(v) Cohérence pour toutes les énergies,

(vi) Incertitudes systematiques minimales.

Un plan schématique de la procédure proposé est montré dans Fig. 7.8. Les sources sont placé dans la cellule 'source' (S). Pour aussi faire une calibration du GC, où on n'a pas des tubes de calibration, la cellule de calibration (C) est une cellule voisine de la cellule S. Quelques sources emittent deux rayons gammas en coïncidence. Pour éviter une superposition des dépositions de l'énergie de ces deux gammas il est demandé que un gamma dépose s'énergie dans l'autre cellule voisine de S, nommé 'gate' G. Dans ce contexte la calibration est fait comme suivant:

1. Définition d'un interval d'énergie d'intérêt.

   C'est utilisé pour avoir une première suppression des événements Compton dans cellule C et pour établir la coïncidence entre les cellules G et C dand le cas de deux gammas. L'example pour ^{137}Cs est montré dans Fig. 7.9.

2. Détermination 'in-situ' de la fuite de lumière entre cellule C et ses voisines.

   La separation optique entre les cellules n'est pas parfait. Pour chaque événement quelques photons de scintillation peuvent arriver aux cellules voisines de l'interaction. Cette fuite peut être calculé en utilisant la proportion des signaux mesurés des cellules voisines par rapport à la cellule d'interaction, voir Figs. 7.10 et 7.11. La fuite moyenne correspond à la valeur maximale dans les graphes.

3. Suppression des événements Compton.

   Les événements d'intérêt pour la calibration sont ceux-ci qui déposent tout l'énergie dans la cellule C. Pour les sélectionner on n'accepte que les événements où la proportion des signaux entre les cellules voisines et la cellule C correspond à la fuite de lumière déterminé avant. Ça permet de separé les événements, voir Fig. 7.12.

4. Calcul des coefficients de calibration.

   Les coefficients de calibration sont calculés comme $\langle Q \rangle / \langle E_{\mathrm{dep}} \rangle$. Car la suppression des événements Compton n'est pas parfait, l'énergie déposée moyenne $\langle E_{\mathrm{dep}} \rangle$ est inferieur à l'énergie des rayons-gammas incidentes. Dans la simulation du détecteur tous les processus de la scintillation sont inclus. Ça permet d'appliquer les mêmes coupures comme décrit avant. En plus l'énergie deposée est connu exactement dans les simulations, permettrant de calculer $\langle E_{\mathrm{dep}} \rangle$, voir Fig. 7.13.

5. Calcul des incertitudes systematiques.

   Celles-ci viennent pour la plupart de la définition exacte des coupures des événements Compton et peuvent être determiné par la variation des parametres de coupure.

Les coefficients de calibration (CC) calculés pour la calibration du 22/02/2017, obtenu selon cette procédure sont listé dans Tab. 7.2. Le but de ces calibrations est d'adapter les parametres de la scintillation et du 'quenching' des scintillateurs dans les simulations. Pour faire ça les courbes de calibration sont comparé pour les donnés (Data) et la simulation (MC). Les courbes sont obtenu selon la fonction (7.14). Ils sont montré dans les Figs. 7.20 à 7.23, les paramètres dans Tab. 7.3. En comparant les courbes on peut voir que dans les simulation l'efficacité de la scintillation et le paramètre du 'quenching' sont surestimé. La tâche restante est d'iterativement adapté les deux paramèters dans les simulation pour avoir une bonne déscription du détecteur réel. Cette tâche n'est pas addressé dans le contexte de cette thèse.

Bibliography

[AA13] A. A. Aguilar-Arevalo, B. C. Brown, L. Bugel, et al., *Improved Search for $\overline{\nu}_\mu \to \overline{\nu}_e$ Oscillations in the MiniBooNE Experiment*, Phys. Rev. Lett. **110** (2013), 161801.

[Aar16] M. G. Aartsen, K. Abraham, M. Ackermann, et al., *Searches for Sterile Neutrinos with the IceCube Detector*, Phys. Rev. Lett. **117** (2016), 071801.

[Abd99] J.N. Abdurashitov, V.N. Gavrin, S.V. Girin, et al., *Measurement of the response of a gallium metal solar neutrino experiment to neutrinos from a ^{51}Cr source*, Phys. Rev. C **59** (1999), 2246–2263.

[Abd06] J.N. Abdurashitov, V.N. Gavrin, S.V. Girin, et al., *Measurement of the response of a Ga solar neutrino experiment to neutrinos from a ^{37}Ar source*, Phys. Rev. C **73** (2006), 045805.

[Abd09] J.N. Abdurashitov, V.N. Gavrin, V.V. Gorbachev, et al., *Measurement of the solar neutrino capture rate with gallium metal. III. Results for the 2002–2007 data-taking period*, Phys. Rev. C **80** (2009), 015807.

[Abe12a] Y. Abe, C. Aberle, T. Akiri, et al., *Indication of Reactor $\overline{\nu}_e$ Disappearance in the Double Chooz Experiment*, Phys. Rev. Lett. **108** (2012), 131801.

[Abe12b] C. Aberle, C. Buck, B. Gramlich, et al., *Large scale Gd-beta-diketonate based organic liquid scintillator production for antineutrino detection*, JINST **7** (2012), no. 06, P06008.

[Abe14] Y. Abe, J. C. dos Anjos, J. C. Barriere, et al., *Improved measurements of the neutrino mixing angle θ 13 with the Double Chooz detector*, JHEP **2014** (2014), no. 10, 86.

[Abe15] Y. Abe, J. C. dos Anjos, J. C. Barriere, et al., *Erratum to: Improved measurements of the neutrino mixing angle θ 13 with the Double Chooz detector*, JHEP. **2015** (2015), no. 2, 74.

[Ach95] B. Achkar, R. Aleksan, M. Avenier, et al., *Search for neutrino oscillations at 15, 40 and 95 meters from a nuclear power reactor at Bugey*, Nucl. Phys. B **434** (1995), no. 3, 503 – 532.

[Ada16] P. Adamson, I. Anghel, A. Aurisano, et al., *Search for Sterile Neutrinos Mixing with Muon Neutrinos in MINOS*, Phys. Rev. Lett. **117** (2016), 151803.

[Ago03] S. Agostinelli, J. Allison, K. Amako, et al., *Geant4 — a simulation toolkit*, Nucl. Instr. Meth. A **506** (2003), no. 3, 250 – 303, Geant4 website: http://geant4.cern.ch/.

[Agu01] A. Aguilar, L. B. Auerbach, R. L. Burman, et al., *Evidence for neutrino oscillations from the observation of $\overline{\nu}_e$ appearance in a $\overline{\nu}_\mu$ beam*, Phys. Rev. D **64** (2001), 112007.

[Ahm02] Q.R. Ahmad, R.C. Allen, T.C. Andersen, et al., *Direct Evidence for Neutrino Flavor Transformation from Neutral-Current Interactions in the Sudbury Neutrino Observatory*, Phys. Rev. Lett. **89** (2002), 011301.

[Ahn10] J.K. Ahn, S.R. Baek, S. Choi, et al., *RENO: An Experiment for Neutrino Oscillation Parameter θ13 Using Reactor Neutrinos at Yonggwang*, arXiv:1003.1391 [hep-ex] (2010).

[Ahn12] J.K. Ahn, S. Chebotaryov, J.H. Choi, et al., *Observation of Reactor Electron Antineutrinos Disappearance in the RENO Experiment*, Phys. Rev. Lett. **108** (2012), 191802.

[AKS15] AK Steel International, *Fer Pur Armco*, 2015, Brochure received from provider AK Steel.

[ALE06] ALEPH Collaboration, DELPHI Collaboration, L3 Collaboration, et al., *Precision electroweak measurements on the Z resonance*, Physics Reports **427** (2006), no. 5, 257 – 454.

[Ale16] I. Alekseev, V. Belov, V. Brudanin, et al., *DANSS: Detector of the reactor AntiNeutrino based on Solid Scintillator*, JINST **11** (2016), no. 11, P11011.

[Alg10] A. Algora, D. Jordan, J. L. Taín, et al., *Reactor Decay Heat in ^{239}Pu: Solving the γ Discrepancy in the 4–3000-s Cooling Period*, Phys. Rev. Lett. **105** (2010), 202501.

[Alm17] H. Almazan, *Neutron efficiency studies*, STEREO collaboration, internal note (2017), stereo–doc–352–v3.

[An12] F.P. An, J.Z. Bai, A.B. Balantekin, et al., *Observation of Electron-Antineutrino Disappearance at Daya Bay*, Phys. Rev. Lett. **108** (2012), 171803.

[An16a] F. P. An, A. B. Balantekin, H. R. Band, et al., *Measurement of the Reactor Antineutrino Flux and Spectrum at Daya Bay*, Phys. Rev. Lett. **116** (2016), 061801.

[An16b] F. P. An, A. B. Balantekin, H. R. Band, et al., *Improved search for a light sterile neutrino with the full configuration of the daya bay experiment*, Phys. Rev. Lett. **117** (2016), 151802.

[An16c] F.P. An, J.Z. Bai, A.B. Balantekin, et al., *The detector system of the Daya Bay reactor neutrino experiment*, Nucl. Instr. Meth. A **811** (2016), 133–161.

[An17a] F.P. An, A.B. Balantekin, H.R. Band, et al., *Improved measurement of the reactor antineutrino flux and spectrum at Daya Bay*, Chin. Phys. C **41** (2017), no. 1, 013002.

[An17b] F.P. An, A.B. Balantekin, H.R. Band, et al., *Measurement of electron antineutrino oscillation based on 1230 days of operation of the Daya Bay experiment*, Phys. Rev. D **95** (2017), 072006.

[An17c] F.P. An, A.B. Balantekin, H.R. Band, et al., *Evolution of the Reactor Antineutrino Flux and Spectrum at Daya Bay*, Phys. Rev. Lett. **118** (2017), 251801.

[Apo03] M. Apollonio, A. Baldini, C. Bemporad, et al., *Search for neutrino oscillations on a long base-line at the CHOOZ nuclear power station*, Eur. Phys. J. C **27** (2003), no. 3, 331–374.

[Arc04] Groupe Arcelor Imphy Alloys, *Mumetal - Permimphy - Supermimphy -Alliages Magnetiques Doux FeNi* , 2004, Brochure received from provider MecaMagnetics.

[Ash16] J. Ashenfelter, A.B. Balantekin, H.R. Band, et al., *The PROSPECT physics program*, J. Phys. G **43** (2016), no. 11, 113001.

[Bah97] J.N. Bahcall, *Gallium solar neutrino experiments: Absorption cross sections, neutrino spectra, and predicted event rates*, Phys. Rev. C **56** (1997), 3391–3409.

[Bel13] G. Bellini, D. Bick, G. Bonfini, et al., *SOX: Short distance neutrino Oscillations with BoreXino*, JHEP **2013** (2013), no. 8, 38.

[Ber17] L. Bernard, *Muon Veto efficiency and rates*, STEREO collaboration, internal note (2017), stereo–doc–256–v1.

[Bir51] J.B. Birks, *Scintillations from Organic Crystals : Specific Fluorescence and Relative Response to Different Radiations*, Proc. Phys. Soc. A **64** (1951), 874.

[Bir64] J.B. Birks, *The Theory and Practice of Scintillation Counting*, Pergamon Press, Ltd., 1964.

[Bjo64] J.D. Bjorken and S.D. Drell, *Relativistic Quantum Mechanics*, McGraw-Hill, New York, 1964.

[Bla17a] A. Blanchet, *Validation of Calibration via Energy Reconstruction*, STEREO collaboration, internal note (2017), stereo–doc–349–v1.

[Bla17b] A. Blanchet and D. Lhuillier, *Energy reconstruction*, STEREO collaboration, internal note (2017), stereo–doc–198–v2.

[Bol90] R. Boll, *Weichmagnetische Werkstoffe: Einführung in den Magnetismus. VAC-Werkstoffe und ihre Anwendung*, 4th ed., Publicis Corporate Publishing, 1990.

[Bon17a] A. Bonhomme, *Pair candidates: main background sources and rejection cuts*, STEREO collaboration, internal note (2017), stereo–doc–242–v1.

[Bon17b] A. Bonhomme, *Updates on correlated background rejection*, STEREO collaboration, internal note (2017), stereo–doc–293–v1.

[Bon17c] A. Bonhomme and C. Roca, et al., *Blessed plots*, STEREO collaboration, internal note (2017), stereo–doc–332–v16.

[Bon17d] A. Bonhomme and T. Salagnac, *Pair search update*, STEREO collaboration, internal note (2017), stereo–doc–355–v2.

[Bou16] O. Bourrion, J.L. Bouly, J. Bouvier, et al., *Trigger and readout electronics for the STEREO experiment*, JINST **11** (2016), no. 02, C02078.

[Boz03] R.M. Bozorth, *Ferromagnetism*, John Wiley & Sons, Inc, 2003.

[Buc17a] C. Buck, A.P. Collin, J. Haser, and M. Lindner, *Investigating the spectral anomaly with different reactor antineutrino experiments*, Phys. Lett. B **765** (2017), 159–162.

[Buc17b] C. Buck, MPIK, *private communication*, 2017.

[But01] A.V. Butkevich and S.P. Mikheyev, *The cross-section of muon-nuclear inelastic interaction*, arXiv:hep-ph/0109060 (2001).

[Cam16] A. Caminata, et. al, *Search for sterile neutrinos with the SOX experiment*, Nuovo Cim. **C39** (2016), no. 1, 236.

[Cap17] Capgam database, based on ENSDF and XUNDL libraries, part of the National Nuclear Data Center, *http://www.nndc.bnl.gov/capgam/*, June 2017.

[Cap17] F. Capozzi, E. Lisi, and A. Marrone, *Probing the neutrino mass ordering with KM3NeT-ORCA: Analysis and perspectives*, arXiv:1708.03022 (2017).

[Cha32] J. Chadwick, *The existence of a neutron*, Proc. of the Royal Society A **136** (1932), 692–708.

[Cho16] J.H. Choi, W.Q. Choi, Y. Choi, et al., *Observation of Energy and Baseline Dependent Reactor Antineutrino Disappearance in the RENO Experiment*, Phys. Rev. Lett. **116** (2016), 211801.

[Col14] A. Collin, *Etude des antineutrinos de réacteurs : mesure de l'angle de mélange leptonique θ et recherche d'éventuels neutrinos stériles*, 2014, PhD Thesis, Université Paris Sud.

[Col16] G. H. Collin, C. A. Argüelles, J. M. Conrad, and M. H. Shaevitz, *First Constraints on the Complete Neutrino Mixing Matrix with a Sterile Neutrino*, Phys. Rev. Lett. **117** (2016), 221801.

[Cow56] C.L. Cowan, Jr., F. Reines, F.B. Harrison, H.W. Kruse, and A.D. McGuire, *Detection of the Free Neutrino: a Confirmation*, Science **124** (1956), 103–104.

[D19] ILL website D19 instrument description, *https://www.ill.eu/instruments-support/instruments-groups/instruments/d19/description/instrument-layout/?l=0*, May 2017.

[Dan62] G. Danby, J.-M. Gaillard, K. Goulianos, et al., *Observation of high-energy neutrino reactions and the existence of two kinds of neutrinos*, Phys. Rev. Lett. **9** (1962), 36–44.

[Del14] G. Deléglise, LAPP, *private communication*, 2014.

[dG09] A. de Gouvêa and T. Wytock, *Light Sterile Neutrino Effects at θ_{13}-driven Reactor Neutrino Experiments*, Phys. Rev. D **79** (2009), 073005.

[DON01] DONUT Collaboration, *Observation of tau neutrino interactions*, Phys. Lett. B **504** (2001), 218–224.

[DRe17] ILL Intranet, internal note, restricted access, *https://intranet.ill.eu/divisions/reactor-dre/accueil-dre/ : A few words on the reactor's power*, August 2017.

[Dwy15] D.A. Dwyer and T.J. Langford, *Spectral Structure of Electron Antineutrinos from Nuclear Reactors*, Phys. Rev. Lett. **114** (2015), 012502.

[Ell27] C.D. Ellis and W.A. Wooster, *The Average Energy of Disintegration of Radium E*, Proc. Roy. Soc. A **117** (1927), no. 776, 109–123.

[END17] Online data base of the Evaluated Nuclear Data File, B-VII.1 , part of the National Nuclear Data Center, *http://www.nndc.bnl.gov/endf/b7.1/*, July 2017.

[Eng64] F. Englert and R. Brout, *Broken Symmetry and the Mass of Gauge Vector Mesons*, Phys. Rev. Lett. **13** (1964), 321–323.

[ENS17] Online data base of the Evaluated Nuclear Structure Data File, part of the National Nuclear Data Center, *http://www.nndc.bnl.gov/ensdf/*, 2017.

[Fal12] M. Fallot, S. Cormon, M. Estienne, et al., *New Antineutrino Energy Spectra Predictions from the Summation of Beta Decay Branches of the Fission Products*, Phys. Rev. Lett. **109** (2012), 202504.

[Fer34] E. Fermi, *Versuch einer Theorie der β-Strahlen 1*, Z. Phys. **88** (1934), 161–177.

[Fua15] S. Fuard, ILL, *private communication*, 2015.

[Fuk98] Y. Fukuda, T. Hayakawa, E. Ichihara, et al., *Evidence for Oscillation of Atmospheric Neutrinos*, Phys. Rev. Lett. **81** (1998), 1562–1567.

[GAM17] ILL website: Presentation of the GAMS instrument, *https://www.ill.eu/instruments-support/instruments-groups/instruments/pn3/description/instrument-layout/?l=0*, June 2017.

[Gan11] A. Gando, Y. Gando, K. Ichimura, et al., *Constraints on θ_{13} from a three-flavor oscillation analysis of reactor antineutrinos at KamLAND*, Phys. Rev. D **83** (2011), 052002.

[Giu07] C. Giunti and C.W. Kim, *Fundamentals of Neutrino Physics and Astrophysics*, Oxford University Press, 2007.

[Giu12] C. Giunti, M. Laveder, Y. F. Li, Q. Y. Liu, and H. W. Long, *Update of short-baseline electron neutrino and antineutrino disappearance*, Phys. Rev. D **86** (2012), 113014.

[Gla61] S.L. Glashow, *Partial-symmetries of weak interactions*, Nuclear Physics **22** (1961), no. 4, 579 – 588.

[Glu14] Glueck, F., *The axisymmetric magnetic field calculation program package magfield2*, received 2014.

[Gol58] M. Goldhaber, L. Grodzins, and A.W. Sunyar, *Helicity of Neutrinos*, Phys. Rev. **109** (1958), 1015–1017.

[Gre92] R.C. Greenwood, R.G. Helmer, M.A. Lee, et al., *Total absorption gamma-ray spectrometer for measurement of beta-decay intensity distributions for fission product radionuclides*, Nucl. Instr. Meth. A **314** (1992), no. 3, 514 – 540.

[Gre98] W. Greiner, *Classical Electrodynamics*, Springer-Verlag New York, 1998.

[Hé15] V. Hélaine, et al., *2014 November and December ILL neutron background measurements*, STEREO collaboration, internal note (2015), stereo–doc–94–v1.

[Hé16] V. Hélaine, *Sterile neutrino search at the ILL nuclear reactor: the STEREO experiment*, arXiv:1604.08877v2 [physics.ins-det] (2016).

[Haa14] N. Haag, A. Gütlein, M. Hofmann, et al., *Experimental Determination of the Antineutrino Spectrum of the Fission Products of ^{238}U*, Phys. Rev. Lett. **112** (2014), 122501.

[Hag12] C. Hagmann, D. Lange, J. Verbeke, and D. Wright, *Cosmic-ray Shower Library (CRY)*, UCRL-TM-22945, 2012.

[Hah89] A.A. Hahn, K. Schreckenbach, W. Gelletly, et al., *Antineutrino spectra from ^{241}Pu and ^{239}Pu thermal neutron fission products*, Phys. Lett. **218B** (1989), 365–368.

[Ham98] W. Hampel, G. Heusser, J. Kiko, et al., *Final results of the ^{51}Cr neutrino source experiments in GALLEX*, Phys. Lett. B **420** (1998), no. 1–2, 114–126.

[Ham15] Hamamatsu Photonics, *Brochure Electron Multipliers – EMT TPMH1354E*, 2015.

[Ham98] Hamamatsu Photonics, *Data sheet Photomultiplier Tube R5912*, 1998.

[Han12] S. Hannestad, I. Tamborra, and T. Tram, *Thermalisation of light sterile neutrinos in the early universe*, Journal of Cosmology and Astroparticle Physics **2012** (2012), no. 07, 025.

[Han14] S. Hannestad, R.S. Hansen, and T. Tram, *How Self-Interactions can Reconcile Sterile Neutrinos with Cosmology*, Phys. Rev. Lett. **112** (2014), 031802.

[Hay14] A.C. Hayes, J.L. Friar, G.T. Garvey, Gerard Jungman, and G. Jonkmans, *Systematic Uncertainties in the Analysis of the Reactor Neutrino Anomaly*, Phys. Rev. Lett. **112** (2014), 202501.

[Hay15] A.C. Hayes, J.L. Friar, G.T. Garvey, et al., *Possible origins and implications of the shoulder in reactor neutrino spectra*, Phys. Rev. D **92** (2015), 033015.

[Hee13] K.M. Heeger, M.N. Tobin, B.R. Littlejohn, and H.P. Mumm, *Experimental parameters for a reactor antineutrino experiment at very short baselines*, Phys. Rev. D **87** (2013), 073008.

[Hig64a] P.W. Higgs, *Broken Symmetries and the Masses of Gauge Bosons*, Phys. Rev. Lett. **13** (1964), 508–509.

[Hig64b] P.W. Higgs, *Broken symmetries, massless particles and gauge fields*, Physics Letters **12** (1964), no. 2, 132 – 133.

[Hub11] P. Huber, *Determination of antineutrino spectra from nuclear reactors*, Phys. Rev. C **84** (2011), 024617.

[Hub16] P. Huber and P. Jaffke, *Neutron Capture and the Antineutrino Yield from Nuclear Reactors*, Phys. Rev. Lett. **116** (2016), 122503.

[Hub17] P. Huber, *NEOS Data and the Origin of the 5 MeV Bump in the Reactor Antineutrino Spectrum*, Phys. Rev. Lett. **118** (2017), 042502.

[IN20] ILL website IN20 instrument description, *https://www.ill.eu/instruments-support/instruments-groups/instruments/in20/description/layout-of-the-instrument/*, May 2017.

[Jan80] Z. Janout, S. Pospíšil, and M. Vobecký, *Observation of a Doppler broadening of the 4438 keV gamma-line of 12C in processes 12C(n, n'γ)12C and 9Be(α, nγ)12C*, Journal of Radioanalytical Chemistry **56** (1980), no. 1, 71–81.

[Jan08] M. Janecek and W.W. Moses, *Optical Reflectance Measurements for Commonly Used Reflectors*, IEEE Transactions on Nuclear Science **55** (2008), 2432.

[JEF17] Website of the Joint Evaluated Fission and Fusion File, *https://www.oecd-nea.org/dbdata/jeff/*, May 2017.

[JEND17] Web reference of the Japanese Evaluated Nuclear Data Library, Nuclear Data Center of the Japanese Atomic Energy Agency, *http://wwwndc.jaea.go.jp/jendl/jendl.html*, 2017.

[Joo16] K.K. Joo, *Proceedings of the 27th International Conference on Neutrino Physics and Astrophysics, Neutrino 2016, London*, 2016, p. (to be published).

[JUN15] JUNO Collaboration, *JUNO Conceptual Design Report*, arXiv:1508.07166 (2015).

[Kae10] F. Kaether, W. Hampel, G. Heusser, J. Kiko, and T. Kirsten, *Reanalysis of the Gallex solar neutrino flux and source experiments*, Phys. Lett. B **685** (2010), no. 1, 47–54.

[Kib67] T.W.B. Kibble, *Symmetry Breaking in Non-Abelian Gauge Theories*, Phys. Rev. **155** (1967), 1554–1561.

[Kno00] G. F. Knoll, *Radiation Detection and Measurement*, 3rd ed., John Wiley & Sons, Inc, 2000.

[Ko17] Y.J. Ko, B.R. Kim, J.Y. Kim, et al., *Sterile Neutrino Search at the NEOS Experiment*, Phys. Rev. Lett. **118** (2017), 121802.

[Koc80] H.R. Koch, G.G. Börner, J.A. Pinston, et al., *The curved crystal gamma ray spectrometers 'GAMS 1, GAMS 2, GAMS 3' for high resolution (n,γ) measurements at the high flux reactor in Grenoble*, Nucl. Instr. Meth. **175** (1980), 401–423.

[Kon14] G. Konrad, F.A. Guardia, S. Baeßler, et al., *The magnetic shielding for the neutron decay spectrometer aSPECT*, Nucl. Instr. Meth. A **767** (2014), 475 – 486.

[Kop04] Kopeikin, V.I. and Mikaelyan, L.A. and Sinev, V.V., *Reactor as a source of antineutrinos: Thermal fission energy*, Phys. At. Nucl. **67** (2004), no. 10, 1892–1899.

[Kop13] J. Kopp, P.A.N. Machado, M. Maltoni, and T. Schwetz, *Sterile neutrino oscillations: the global picture*, JHEP **2013** (2013), no. 5, 50.

[Kro85] D. Krofcheck, E. Sugarbaker, J. Rapaport, et al., *Gamow-Teller Strength Function in* ^{71}Ge *via the* (p, n) *Reaction at Medium Energies*, Phys. Rev. Lett. **55** (1985), 1051–1054.

[Kwo81] H. Kwon, F. Boehm, A.A. Hahn, et al., *Search for neutrino oscillations at a fission reactor*, Phys. Rev. D **24** (1981), 1097–1111.

[Led98] D. Lederer and A. Kost, *Modelling of Nonlinear Magnetic Material using a Complex Effective Reluctivity*, IEEE Transactions on Magnetics, **34** (1998), 3060 – 3063.

[Lhu12] D. Lhuillier, D. Benchekroun, C. Buck, et al., *Proposal of a search for sterile neutrinos at ILL: the STEREO experiment*, Proposal STEREO Experiment (2012).

[Lhu16] D. Lhuillier, *Light collection*, STEREO collaboration, internal note (2016), stereo–doc–180–v4.

[Lhu17] D. Lhuillier, *Metrology*, STEREO collaboration, internal note (2017), stereo–doc–433–v1.

[Ma13] X.B. Ma, W.L. Zhong, L.Z. Wang, Y.X. Chen, and J. Cao, *Improved calculation of the energy release in neutron-induced fission*, Phys. Rev. C **88** (2013), 014605.

[Maj37] E. Majorana, *Theory of the Symmetry of Electrons and Positrons*, Il Nuovo Cimento **14** (1937), 171–184.

[Mam78] W. Mampe, K. Schreckenbach, P. Jeuch, et al., *The double focusing iron-core electron-spectrometer „BILL“ for high resolution (n, e-) measurements at the high flux reactor in Grenoble*, Nucl. Instr. Meth. **154** (1978), no. 1, 127–149.

[Man16] L. Manzanillas, *Development of the source calibration system of the STEREO experiment and search for sterile neutrinos at the ILL*, 2016, PhD Thesis, Université Grenoble Alpes.

[McC11] R.J. McConn, Jr, C.J. Gesh, R.T. Pagh, R.A. Rucker, and R.G. Williams III, *Compendium of Material Composition Data for Radiation Transport Modeling - Revision 1* , PNNL-15870 Rev. 1 (2011).

[Men11] G. Mention, M. Fechner, Th. Lasserre, et al., *Reactor antineutrino anomaly*, Phys. Rev. D **83** (2011), 073006.

[Min17] A. Minotti, *Summary on Light Leaks*, STEREO collaboration, internal note (2017), stereo–doc–228–v1.

[Moh04] R.N. Mohapatra, et al., *Theory of Neutrinos*, arXiv:hep-ph/0412099v2 (2004).

[Mue11] Th.A. Mueller, D. Lhuillier, M. Fallot, et al., *Improved predictions of reactor antineutrino spectra*, Phys. Rev. C **83** (2011), 054615.

[MUR17] Digital User Guide of the MURE code, Version 1.9, *http://lpsc.in2p3.fr/MURE/html/UserGuide/UserGuide.html*, August 2017.

[Pé13] M. Péquignot, *Etudes du flux neutronique et photonique aux sorties du guide de neutron H6-H7 par simulation MCNPX*, 2013, internal report, STEREO collaboration.

[Pé14] M. Péquignot, *Summary of STEREO background measurements, July 2014*, STEREO collaboration, internal note (2014), stereo–doc–21–v1.

[Pé15] M. Péquignot, *Les expériences Nucifer et Stéréo: étude des antineutrinos de réacteurs à courte distance*, 2015, PhD Thesis, Université Paris-Sud.

[Pat16] C. Patrignani, et al., *Particle Data Group, Reviews: 29. Cosmic Rays*, Chin. Phys. C **40** (2016), 100001.

[Pau91] W.E. Pauli, *"On the earlier and more recent history of the neutrino" (1957) in 'Neutrino Physics', edited by K. Winter*, Camebridge University Press, 1991.

[Pel11] D.B. Pelowitz, Ed., *MCNPX users Manual Version 2.7.0*, LA-CP-11-00438, 2011.

[Per75] M.L. Perl, et al., *Evidence for Anomalous Lepton Production in e^+-e^- Annihilation*, Phys. Rev. Lett. **35** (1975), 1489–1492.

[Pla16] Planck Collaboration, Ade, P. A. R., Aghanim, N., et al., *Planck 2015 results - XIII. Cosmological parameters*, A&A **594** (2016), A13.

[Rea16] J.S. Real, *Light Leaks determination using neutrino runs*, STEREO collaboration, internal note (2016), stereo–doc–165–v6.

[Reu08] P. Reuss, *Neutron Physics*, EDP Sciences, 2008.

[Ryd15] N. Ryder, *First results of the deployment of a SoLid detector module at the SCK•CEN BR2 reactor*, PoS EPS-HEP (2015), 071.

[Sal59] A. Salam and J.C. Ward, *Weak and electromagnetic interactions*, Il Nuovo Cimento **11** (1959), no. 4, 568–577.

[Sal17] T. Salagnac, *Recherche d'un neutrino stérile avec l'expérience STEREO: Developpement de l'électronique et identification des neutrinos*, 2017, PhD Thesis, Université Grenoble Alpes - to be published.

[SAN17] ILL – Service for Advanced Neutron Environment (https://www.ill.eu/instruments-support/sample-environment/about-us/), *private communication*, May 2017.

[Sav13] N. Saviano, A. Mirizzi, O. Pisanti, et al., *Multimomentum and multiflavor active-sterile neutrino oscillations in the early universe: Role of neutrino asymmetries and effects on nucleosynthesis*, Phys. Rev. D **87** (2013), 073006.

[Sch81] K. Schreckenbach, H.R. Faust, F. von Feilitzsch, et al., *Absolute measurement of the beta spectrum from ^{235}U fission as a basis for reactor antineutrino experiments*, Phys. Lett. **99B** (1981), 251–256.

[Sch85] K. Schreckenbach, G. Colvin, W. Gelletly, and F. von Feilitzsch, *Determination of the antineutrino spectrum from ^{235}U thermal neutron fission products up to 9.5 MeV*, Phys. Lett. **160B** (1985), 325–330.

[Ser13] A.P. Serebrov, A.K. Fomin, V.G. Zinoviev, et al., *„Neutrino–4" experiment: preparations for search for sterile neutrino at 100 MW reactor SM-3 at 6-13 meters*, arXiv:1205.2955 [hep-ph] (2013).

[Ser15] A.P. Serebrov, V.G. Ivochkin, R.M. Samoylov, et al., *Neutrino-4 experiment on the search for a sterile neutrino at the SM-3 reactor*, Journal of Experimental and Theoretical Physics **121** (2015), no. 4, 578–586.

[Ser17] A.P. Serebrov, V.G. Ivochkin, R.M. Samoilov, et al., *Experiment NEUTRINO-4 Search for Sterile Neutrino*, arXiv:1702.00941v2 [physics.ins-det] (2017).

[Sir67] A. Sirlin, *General Properties of the Electromagnetic Corrections to the Beta Decay of a Physical Nucleon*, Phys. Rev. **164** (1967), 1767–1775.

[Sir11] A. Sirlin, *Radiative correction to the $\overline{\nu}_e(\nu_e)$ spectrum in β decay*, Phys. Rev. D **84** (2011), 014021.

[Son16] A.A. Sonzogni, E.A. McCutchan, T.D. Johnson, and P. Dimitriou, *Effects of Fission Yield Data in the Calculation of Antineutrino Spectra for ^{235}U$(n, fission)$ at Thermal and Fast Neutron Energies*, Phys. Rev. Lett. **116** (2016), 132502.

[Stu14] A. Stutz, *Summary of gamma background measurements during cycle 172*, STEREO collaboration, internal note (2014), stereo–doc–30–v1.

[Stu15a] A. Stutz, *Impact of magnetic field on Stereo PMTs*, STEREO collaboration, internal note (2015), stereo–doc–95–v1.

[Stu15b] A. Stutz, *Summary of Stereo gamma background measurements, cycle 173, november 2014*, STEREO collaboration, internal note (2015), stereo–doc–90–v1.

[Ten89] O. Tengblad, K. Aleklett, R. Von Dincklage, et al., *Integral $\bar{\nu}$-spectra derived from experimental β-spectra of individual fission products*, Nuclear Physics A **503** (1989), no. 1, 136 – 160.

[vF82] F. von Feilitzsch, A.A. Hahn, and K. Schreckenbach, *Experimental beta-spectra from ^{239}Pu and ^{235}U thermal neutron fission products and their correlated antineutrino spectra*, Phys. Lett. **118B** (1982), 162–166.

[Vog81] P. Vogel, G. K. Schenter, F. M. Mann, and R. E. Schenter, *Reactor antineutrino spectra and their application to antineutrino-induced reactions. II*, Phys. Rev. C **24** (1981), 1543–1553.

[Vog84] P. Vogel, *Analysis of the antineutrino capture on protons*, Phys. Rev. D **29** (1984), 1918–1922.

[Vog99] P. Vogel and J.F. Beacom, *Angular distribution of neutron inverse beta decay, $\overline{\nu}_e + \vec{p} \rightarrow e^+ + n$*, Phys. Rev. D **60** (1999), 053003.

[Wei67] S. Weinberg, *A Model of Leptons*, Phys. Rev. Lett. **19** (1967), 1264–1266.

[Wil90] D.H. Wilkinson, *Evaluation of beta-decay*, Nucl. Instr. Meth. A **290** (1990), no. 2, 509–515.

[Wu57] C. S. Wu, E. Ambler, R. W. Hayward, D. D. Hoppes, and R. P. Hudson, *Experimental Test of Parity Conservation in Beta Decay*, Phys. Rev. **105** (1957), 1413–1415.

[X-503] X-5 Monte Carlo Team, *MCNP - A General Monte Carlo N-Particle Transport Code, Version 5, Vol. I: Overview and Theory*, LA-UR-03-1987, 2003.

[XCO17] NIST, XCOM: Photon Cross Sections Database, *https://www.nist.gov/pml/xcom-photon-cross-sections-database*, August 2017.

[Zho12] B. Zhou, X. Ruan, Y. Nie, et al., *A study of antineutrino spectra from spent nuclear fuel at Daya Bay*, Chin. Phys. C **36** (2012), no. 1, 1.

[Zso16] S. Zsoldos, *Recherche d'un neutrino stérile avec l'expérience STEREO: Construction du veto à muons et estimation du bruit de fond corrélé*, 2016, PhD Thesis, Université Grenoble Alpes.

[Zub12] K. Zuber, *Neutrino Physics*, 2nd ed., CRC Press, 2012.

Acknowledgements

First of all I would like to thank Torsten Soldner for his guidance, help and advice right from the very beginning until the end of the thesis. For his availability at all stages and his willingness to dig into all details of my work in order to give advice and comments. In many long discussions and helpful explanations he helped to bring the thesis forward and to find conclusions on the addressed topics.
I would also like to thank François Montanet for being the 'directeur de thèse', for the dicussions and the good support, including many administrative questions.

I thank all members of the STEREO collaboration for their tedious work to advance the project through difficult times, so that the detector could finally go online and collect good data. Especially I want to thank David Lhuillier for bringing up this interesting project, solving many problems on the way and taking his time to discuss all important subjects in detail. Special thanks also to the collaborators from the LPSC Grenoble, for the close collaboration, their help and the many fruitful discussions. Many thanks also to all the technicians at the involved institutes, who planned, prepared and accomplished the installation of the STEREO detector.

I would also like to thank the members of the ILL's Nuclear and Particle Physics group, for their hospitality, the pleasant working atmosphere and their support in many tasks. A special thanks to Michael Jentschel and Ulli Köster, who contributed to many discussions and helped in many practical tasks.

I would like to thank Gertrud Konrad (ATI Vienna) for her explanations, support and patience with the simulations for the magnetic shielding. In the same way I'd like to thank Stephane Fuard (ILL) for the introductions to and help with MCNP, especially during the major simulation campaigns.

I thank the members of the jury of the thesis defense, especially the two referees, for accepting their tasks and taking their time to read the manuscript and attend the defense itself.

I thank all those who are not yet explicitly mentioned, but contributed directly or indirectly with their help, advice or support to the outcome ot this work.

Last but not least I am glad that I had this chance to pass my thesis at the ILL, which not only showed hospitality but also offered an interesting, vibrant and diverse research program and environment.